Karl-Franzens Universität Graz

Naturwissenschaftliche Fakultät

Institut für Physik

Abteilung Oberflächen- und Grenzflächenphysik

Titanium silicide formation by ion beam mixing

Dissertation

zur Erlangung des Doktorgrades

vorgelegt von

Paweł Szych

Graz, Juni 2008

I am among those who think that science has great beauty.
A scientist in his laboratory is not only a technician: he is also a child placed before natural phenomena which impress him like a fairy tale.

Maria Skłodowska–Curie

Contents

1 Introduction **1**

2 Fundamentals **3**

2.1 Titanium Silicides 3

2.2 Ion beam mixing 4

2.2.1 Ion-solid interactions 4

2.2.2 Ion beam mixing process 8

2.2.3 Compound formation model for IBM 10

2.2.4 Computer simulations 13

3 Experimental techniques **16**

3.1 UHV deposition 16

3.1.1 Monolayer equivalent 16

3.1.2 Tooling factor 17

3.2 Photoemission spectroscopy 19

3.2.1 XPS, depth profiling with XPS 20

3.2.2 UPS 21

3.3 LEED 21

3.4 Ex-situ investigations 23

3.4.1 GIXRD 24

3.4.2 Noncontact AFM 25

3.4.3 TLM 25

3.5 Experimental setup 26

3.5.1 Silicon substrates 26

3.5.2 SCIENTA UHV System 27

3.5.3 SPECS UHV System 35

4 Experimental results and discussion **40**
4.1 Silicon cleaning procedure 40
4.2 Ti growth on Si(111) at room temperature 41
4.3 Titanium silicide formation by thermal annealing 44
4.3.1 In-situ photoemission and LEED studies on Si(111) 44
4.3.2 In-situ photoemission and LEED studies on Si(100) 47
4.4 Titanium silicide phase identification 51
4.4.1 Detailed titanium silicide phase analysis 56
4.5 Electrical properties of the Ti/Si interface 59
4.6 Titanium silicide formation by ion beam mixing 63
4.6.1 Photoemission studies of the IBMed Ti/Si(111) 66
4.6.2 Photoemission studies of the IBMed Ti/Si(100) 68
4.6.3 IBM of the Ti/Si(100) for different Ar^+ energies 71
4.6.4 IBM of the Ti/Si(100) for different Ti coverages 78
4.7 Monte Carlo simulations of the IBMed Ti/Si system 84
4.7.1 Mixing and sputtering 85
4.7.2 Ion distribution in the target 89
4.7.3 The distribution of the absorbed energy 89
4.7.4 Collision events 94
4.8 Mixing rate 95
4.8.1 Mixing rate calculations 95
4.8.2 Mixing rate measurements 98
4.8.3 Conclusions 101
4.9 Electrical properties of the IBMed Ti/Si 103
4.10 Surface morphology of the IBMed samples 107
4.11 Thermally assisted ion beam mixing 112
4.12 IBM of the Ti/SiO_2/Si(100) interface 116
4.12.1 Photoemission studies of the IBMed Ti/SiO_2/Si(100) 117
4.12.2 Computer simulations of the IBM of the Ti/SiO_2/Si(100) 121

5 Summary **128**

Bibliography **133**

List of Figures **139**

Acknowledgments **148**

Chapter 1

Introduction

This dissertation is the result of a project that was performed in cooperation between the Surface and Interface Physics Group of the Institute of Physics of the Karl-Franzens University Graz and Infineon Technologies Austria AG company – the Infineon's Technology Development Centre in Villach. The purpose of this work was to develop a method of low temperature titanium silicide formation, which would find applications in a back side metallization process of silicon wafers at Infineon.

Titanium silicides are materials that find many applications in microelectronics. High thermal stability, low resistivity and good adhesion to silicon make them a good equivalent to currently used materials. They form an ohmic contact to silicon, so that they can be used as metallization layers and interconnections. For example they can be used as contacts on sources, gates, and drains of MOSFETs and for interconnections in logic and memory devices [34, 46].
If titanium is brought in contact with silicon and the system is heated up, a chemical reaction takes place, which results in titanium silicide formation. Depending on the applied temperature, different titanium silicides can be formed that differ in chemical composition, crystal phase, electrical and elastic properties. But when the temperature reaches $\sim 700°C$ the titanium silicides transform into a stable phase of lowest resistivity – a face centered orthorhombic C54 $TiSi_2$ (Titanium silicide phase transformations are described in details in Chapter 2).
The formation temperature of the low resistivity C54 $TiSi_2$ ($700°C$) is much to high to be applied in an industrial back side metallization process, where the maximum temperatures allowed cannot exceed $350°C$, because the high temperature could destroy the structures fabricated at the front side of the wafer. Therefore in this work a room temperature tita-

nium silicide formation was investigated by an innovative method called ion beam mixing (IBM). In this process the titanium deposited onto the silicon surface is subsequently bombarded with Ar^+ ions. The incident Ar^+ ions transfer their kinetic energy to the Ti atoms enabling their diffusion at the Ti/Si interface and the formation of the silicide (Chapter 2 gives more explanations). Titanium silicide formation was studied under ultra high vacuum (UHV) conditions using surface sensitive techniques, like XPS, UPS and LEED. The crystal phase of the silicides was checked by GIXRD in the Siemens Laboratories in Munich, Germany. The properties of the electrical contact and the adhesion to silicon were studied at Infineon in Villach. Chapter 3 describes in details the UHV systems were the experiments were performed and the principles of the measurement methods.

In Chapter 4 the experimental results are presented and discussed. Titanium growth at room temperature on Si(111) is presented in section 4.2. Titanium silicide formation by thermal annealing was studied in order to investigate the titanium silicide phase transformations and the electrical properties of the formed contact – the results are presented in sections 4.3, 4.4 and 4.5.
Titanium silicide formation by ion beam mixing is described in section 4.6. Such aspects of the silicide formation by IBM as mixing rate (4.8) and surface morphology of the IBMed samples (4.10) were studied. Electrical properties of the IBMed Ti/Si contact are presented in 4.9.
Computer calculations of the ion beam mixing process based on Monte Carlo algorithms were applied to perform 'virtual experiments', which simulated the real experiments in the laboratories. The results are shown in section 4.7.
Thermally assisted ion beam mixing - an interesting experiment that combines the ion beam mixing and the thermal annealing was performed at the temperature of $200°C$ and it is described in section 4.11.
Also the ion beam mixing of titanium evaporated onto silicon covered by a native SiO_2 layer was studied. In the semiconductor processing it can happen, that the silicon cleaning procedure is not performed in the UHV chamber, where the titanium evaporation and IBM takes place. In this case the silicon wafer is exposed to the atmosphere for some time, which causes the oxidation of the silicon. Therefore the IBM of $Ti/SiO_2/Si$ system was investigated and the results are presented in section 4.12.
Finally, section 5 gives a summary and a collection of the results obtained.

Chapter 2

Fundamentals

2.1 Titanium Silicides

Titanium silicides are the materials that are formed when the silicon and titanium are brought into contact and the chemical reaction between them is thermally initiated. At room temperature there is no titanium silicide formation observed, but when the temperature exceeds $300°C$ the metal rich silicides (Ti_3Si, Ti_5Si_2, Ti_5Si_3, Ti_5Si_4 [44]) are created [15, 69, 75, 17, 14]. With further annealing, when the temperature is increased to $\sim 450°C$, the $TiSi$ is formed. Once the $TiSi$ is formed and the temperature rises to $\sim 550°C$ the $TiSi_2$ nucleates and it forms the $C49$ crystal phase. The $C49$ $TiSi_2$ is a metastable phase and when the heating temperature reaches $\sim 700 - 750°C$ the $C49$ $TiSi_2$ phase transforms into the low resistivity $C54$ $TiSi_2$ [39, 46]. The $C54$ is the final phase of the $TiSi_2$ and once it is formed no further phase transformation is observed [39, 27, 46, 32]. The titanium silicide reaction sequence is presented in Fig. 2.1 and the crystal structure of the C49 and C54 is shown in Fig. 2.2. Both C49 and C54 phases are low resistivity materials (Table 2.1) with good adhesion to silicon and the C54 shows a very good thermal stability. These properties make them a great equivalent for currently used materials in microelectronics, especially in all the applications that require the formation of metalizations and interconnections [46, 34, 32].

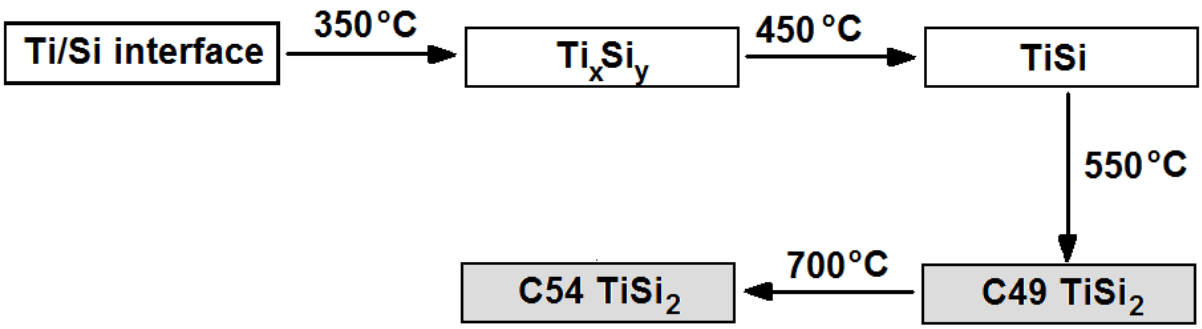

Figure 2.1: *The chemical reaction sequence of the titanium silicides.*

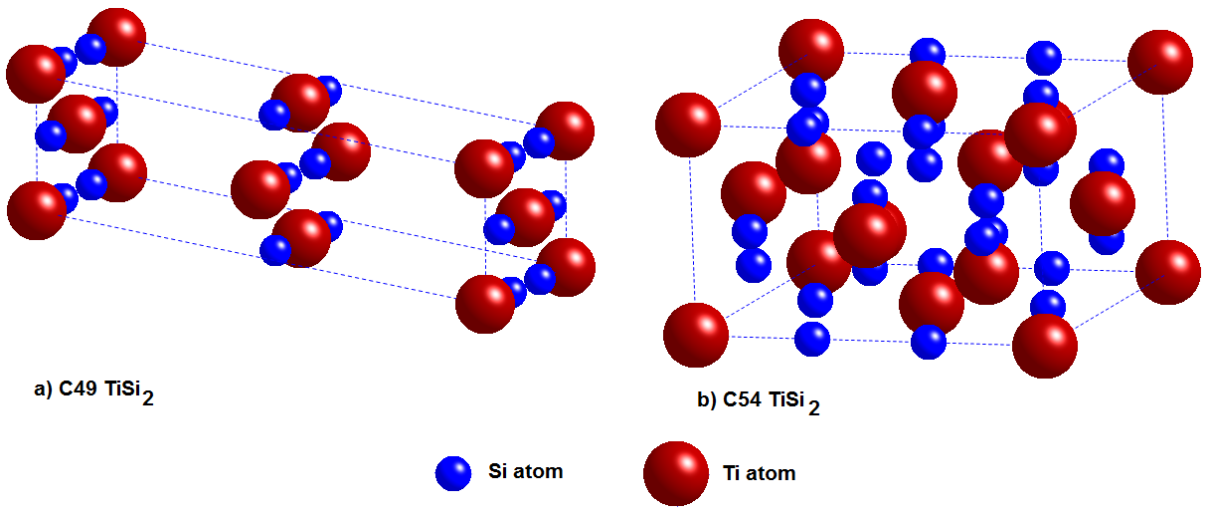

Figure 2.2: *Two crystal phases of the $TiSi_2$: the base centered orthorhombic C49 silicide phase a) and the face centered orthorhombic C54 silicide phase b).*

2.2 Ion beam mixing

2.2.1 Ion-solid interactions

Let's assume that under UHV conditions an energetic ion impinges on the solid target surface. The Fig. 2.3 presents the possible ion-solid interactions that may occur during the ion-target surface collision.

Sputtering

The sputtering process, also called ion etching, occurs as the result of a series of elastic atomic collisions where the kinetic energy is transferred from the incident ions to the

properties	**C49 $TiSi_2$**	**C54 $TiSi_2$**
crystal structure	base centered orthorhombic	face centered orthorhombic
cell parameters [47, 44]		
a	3.62Å	8.252Å
b	13.76Å	4.783Å
c	3.605Å	8.540Å
formation temperature	550°C	650-700°C
melting point [46]		1540°C
resistivity [$\mu\Omega cm$]	60-80	12-15
Young modulus, E [GPa] [62]	192	252
Poisson's ratio, ν [62]	0.29	0.26
Hall coefficient, $R_H[10^5 cm^3/C]$	-21.2	-4.0

Table 2.1: *Properties of the C49 and C54 titanium silicides. Hall coefficients were measured at room temperature at the field of 1.5T*

target atoms, which results in ejecting target particles from the target surface [54, 26, 77]. The sputtering process is characterized by the sputtering yield Y, which is defined by:

$$Y = \frac{number\ \ of\ \ sputtered\ \ atoms}{number\ \ of\ \ incident\ \ ions} \tag{2.1}$$

The sputtering yield Y depends on the structure and the composition of the target material, the parameters of the incident ion beam and the geometry of the experimental system. The typical values of Y range from 1 to 10 [54].

Energy loss

An incident ion after hitting the target surface penetrates into the target and while traveling through the matter it looses continuously its energy due to two mechanisms [54, 26, 24]:

1. nuclear collisions, collisions with atoms in the target material,
2. electronic collisions, in which the moving ion excites (excitation process) or ejects (ionization process) the electrons from the target atoms.

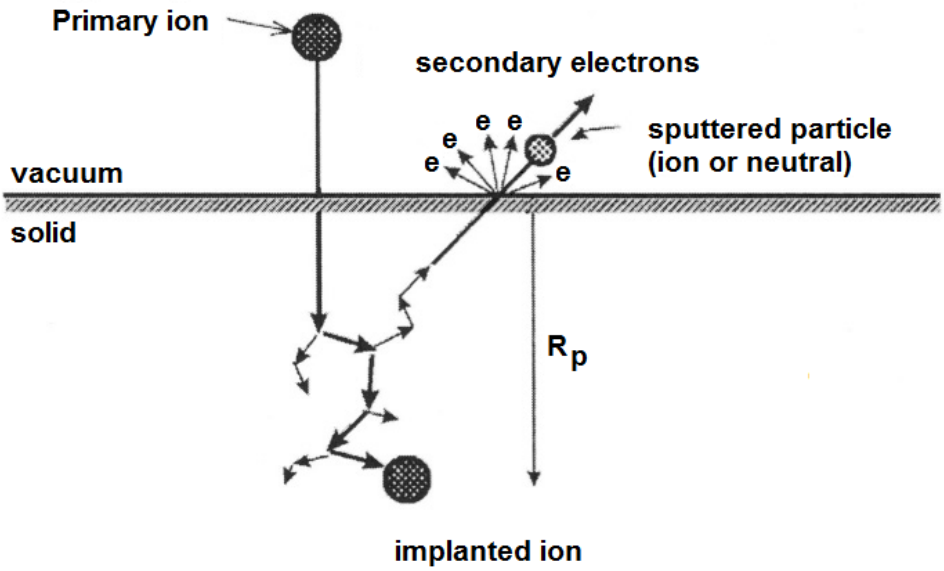

Figure 2.3: *The picture [54] presents the possible ion-solid interactions. The R_p is the projected range of a single ion.*

The energy-loss rate dE/dx of an energetic ion penetrating the matter is called the **stopping power** and can be expressed by the following equation:

$$\frac{dE}{dx} = \left.\frac{dE}{dx}\right|_n + \left.\frac{dE}{dx}\right|_e \tag{2.2}$$

where the subscript n represents the nuclear stopping power, and the subscript e denotes the electronic stopping power.
Additionally to the stopping power it is also convenient to speak about the stopping cross-section, which is defined as:

$$S \equiv \frac{dE/dx}{N} \tag{2.3}$$

where N is the atomic density.

By a single nuclear collision an ion transfers kinetic energy to the target atom. The transfered energy ratio between the incident ion and the recoiling atom for nuclear stopping is [54]:

$$\frac{E_2}{E_0} = \frac{4M_1M_2}{(M_1+M_2)^2}E_0 cos^2\phi \tag{2.4}$$

where the E_0 is the initial kinetic energy of the incident ion, E_2 is the kinetic energy of the recoiling target atom, ϕ is the recoil angle, and M_1 and M_2 are the atomic masses of the ion and the atom.

The energy transferred by the ion to the target electrons (electronic stopping) is considered separately for low and high ion energies. Electronic stopping for low ion energies is described as [54]:

$$\left.\frac{dE}{dx}\right|_e = \frac{8\pi e^2 a_0}{4\pi\epsilon_0}\frac{Z_1^{7/6}Z_2}{(Z_1^{2/3}+Z_2^{2/3})^{3/2}}\left(\frac{v}{v_0}\right) \tag{2.5}$$

where v is the ion velocity, v_0 is the Bohr velocity of an electron in the innermost orbit of a hydrogen atom ($v_0 \cong 2.2 \times 10^8 cm/s$), M_1 and M_2 are the masses of the two interacting elements in the atomic mass units, Z_1 and Z_2 are the atomic numbers of the two interacting elements.

Electronic stopping for high ion energies is given by [54, 76]:

$$\left.\frac{dE}{dx}\right|_e = \frac{2\pi Z_1^2 e^4}{E} N Z_2 \left(\frac{M_1}{m_e}\right) ln \frac{2m_e v^2}{I} \tag{2.6}$$

where m_e is the electron mass, I represents the average excitation energy of an electron, $E = M_1 v^2/2$ and $n_e = NZ_2$, with N given by the atomic density in the stopping medium, M_1 and M_2 are the mass of two interacting elements in atomic mass units, Z_1 and Z_2 are the atomic numbers of two interacting elements.

A recoil atom is produced when an energetic ion collides with it and permanently relocates it from its lattice site. If the energy transfered to the recoil is larger than its displacement threshold energy E_d, it can continue to knock other atoms and produce secondary recoils, which can also displace another atoms. Such an phenomenon results in many collision and displacements events and is called a collision cascade.
The displacement threshold energy E_d is defined as the minimum energy required to produce a stable interstitial-vacancy (Frenkel) pair, and the typical values of the E_d range from 20-30eV [49].
A collision cascade may result in transferring a large amount of energy into a cluster of atoms which could create a thermal spike. The thermal spike causes the local melting of the material and destroys significantly the crystal structure. The duration of a thermal spike is approximately $10^{-11}s$ and for materials with average atomic number less than 20 no thermal spikes are expected [49, 54].

Ion range

An ion, while penetrating the solid, experiences many collisions with atoms and electrons, it looses its energy and finally gets implanted into the target material. The distance travelled between the collisions and the amount of energy lost per each collision are

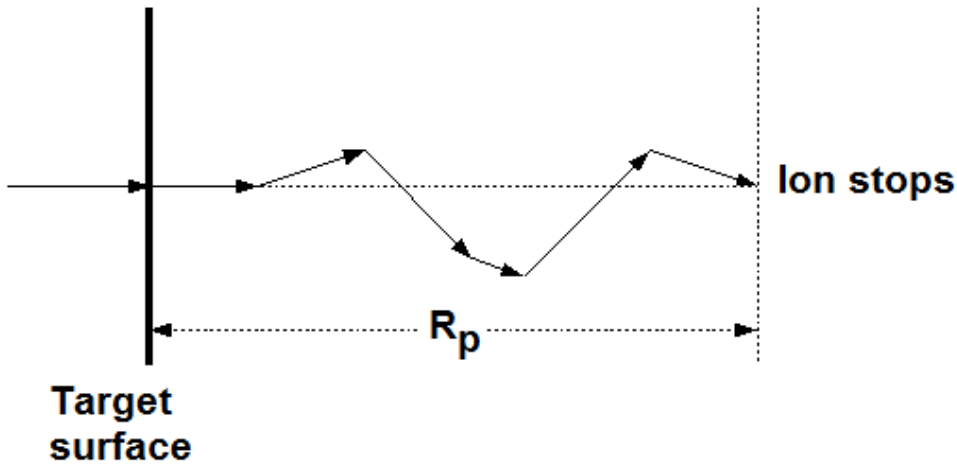

Figure 2.4: *The path of an energetic ion in a solid during an ion implantation process. The picture shows the total ion path R and the projected ion range R_p. As the ion moves through the solid it collides into the stationary target atoms, which changes its direction.*

random processes and are different for every ion. The penetration depth, or the ion range R, are dependent on the rate of energy-loss along the ion path [26]:

$$R = \int_{E_0}^{0} \frac{dE}{dE/dx} = \int_{E_0}^{0} \frac{dE}{NS(E)} \tag{2.7}$$

where E_0 is the ion incident energy as it penetrates the solid.
Usually in ion implantation the total distance R travelled by an ion is not important, but the projection of R normal to the surface, called the projected range R_p. The difference between the ion range R and the projected ion range R_p is illustrated in Fig. 2.4.

2.2.2 Ion beam mixing process

The target that is being bombarded by ions undergoes many atomic rearrangements. When this process takes place at the boundary of two materials the interface mixing appears (Fig. 2.5). This phenomenon is known as the **I**on **B**eam **M**ixing (IBM) [7, 11, 12].

The IBM process governed by the transferring of the energy to both atoms and electrons of the target solid is called the **ballistic mixing**. If an energetic ion hits the target atom, the atom recoils many lattice sites away from its initial location. The process results in atomic mass transport through the repeated collisions and this is the simplest form of the ballistic mixing, called the **recoil mixing**. In order to make the recoil mixing as effective as possible, the recoil should travel the largest range possible. The maximum

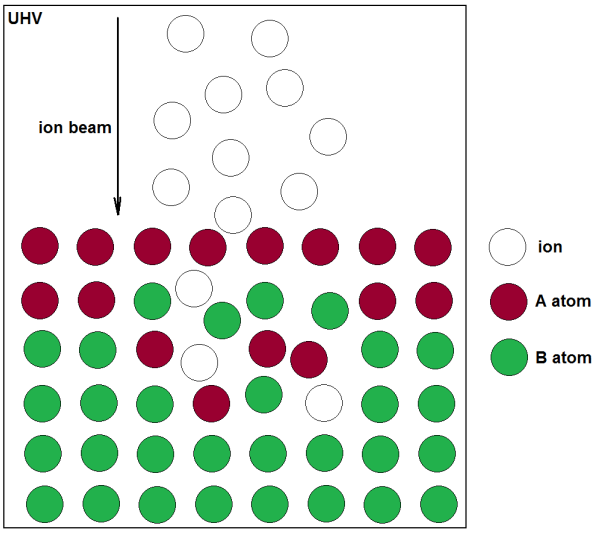

Figure 2.5: *The graphical interpretation of the Ion Beam Mixing (IBM) at the interface of two materials.*

range of the recoil will be obtained when the collision between the ion and the atom is a perfect head collision (maximum kinetic energy transfer from the ion to the atom is obtained, Eq.2.4). Usually only few collisions are the perfect head collisions, so the recoils produced in such a process will have lower energy and their trajectory will not be in forward direction. During the IBM experiment one should increase the probability of the head collisions by positioning the ion gun normal to the target surface.
The efficiency of the recoil mixing can by significantly improved when multiple displacements of the target atoms occur from a single incident ion - a collision cascade appears. The ballistic mixing dominated by the collision cascades is called the **cascade mixing**. Unlike in the recoil mixing, when a recoil receives a large amount of energy in a single displacement, the atoms in collision cascades experience many uncorrelated relocation events. The thermal spikes may occur during the cascade mixing.

Mass transport mechanisms

The ballistic mixing dominates for low ion energies and heavy ions (nuclear stopping is dominant) [54]. In this case the collision cascades are the real driving force of the mass transport, because they cause the relocations of the target atoms [8, 67]. But if the target is bombarded with high-energetic ions (hundreds of keV and more), the nuclear stopping power is negligible and the electronic stopping dominates the process. In this case the

nuclear collisions contribute only a little to the energy loss, because the ion energy is lost by electronic interactions (electronic excitation and ionization) with the target electrons. Here the initiation of atomic transport by the incident ion is much less obvious. In order to explain what really causes the mixing in the electronic mixing regime the idea of the **nuclear track** was introduced [10, 8, 9, 11]. If a high energy ion penetrates a solid it leaves behind a highly excited electronic system in a small cylindrical zone around its path, with a high electron deficiency in its centre - a nuclear track [10]. This electronic excitation energy could be transferred into the kinetic energy of the target atoms by two different mechanisms: an **electron-phonon coupling** or a **Coulomb explosion**.
The Coulomb explosion concept assumes that the electrostatic repulsion between the positively charged atoms in the centre results in an explosion-like atomic motion perpendicular to the track [8].
The electron-phonon coupling concept presumes that electron-phonon coupling results in heating of the lattice and the generation of a Gaussian-like temperature profile around the ions path. For sufficiently large energy loss of the ion, the temperature may rise above the melting point and a molten cylinder of some nanometers in diameter forms [9].

2.2.3 Compound formation model for IBM

IBM is a diffusion-like process that supports the intermixing of the two elements. It was also observed that the IBM process can initiate the chemical reaction between the two mixed reactive elements.
In 1993 a theoretical model for compound formation during the ion beam mixing was introduced by J. Desimoni and A. Traverse [19], and in 1996 an extension to this model in the thermal spike mixing regime was proposed by S. Dhar, Y. N. Mohapatra and V. N. Kulkarni [20].

The target configuration as assumed for the ion beam mixing model in case of a compound formation [19] is presented in Fig. 2.6. So let us assume that after the ion irradiation fluence ϕ, the sample has a configuration as presented in Fig. 2.6.

There are three layers: the first layer of atoms A with the atomic concentration C_A, a mixed layer with the compound A_aB_b with the thickness X and the atomic concentration of C, and the third layer of atoms B with the atomic concentration C_B. Let us consider A and B as the infinite reservoirs of atoms, and that under the ion irradiation only A atoms penetrate into the mixed layer A_aB_b (only A atoms are mobile). The A_aB_b layer is saturated with the A atoms, so the A atoms can only diffuse through the A_aB_b and

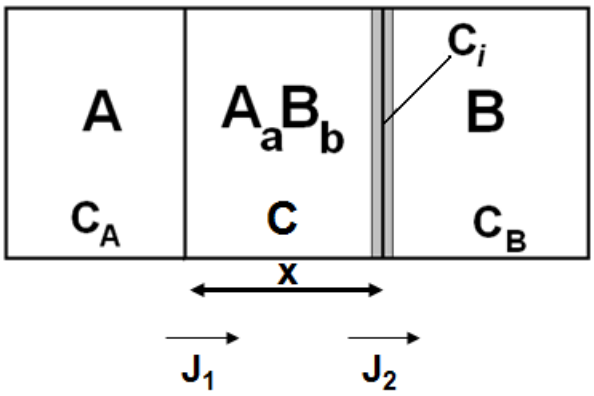

Figure 2.6: *Target configuration assumed for the ion beam mixing model for compound formation [19]. Both A and B layers are the infinite reservoirs of atoms (C_A and C_B are the atomic concentrations of A and B atoms). J_1 is the diffusion flux according to the 1. Fick Law of Diffusion, and J_2 is the flux caused by the chemical reaction rate k for the A_aB_b compound. X is the thickness of the mixed layer.*

finally arrive at the A_aB_b/B interface with the atomic concentration C_i. At this interface the A atoms can chemically react with the B atoms and form a new layer of the A_aB_b/B compound. Let us define the two fluxes J_1 and J_2 as shown in Fig. 2.6. J_1 is the diffusion flux of A through the A_aB_b/B layer, and according to Fick's First Law of Diffusion we have:

$$J_1 = -D\frac{dC}{dX} = D\frac{C_A - C_i}{X} \tag{2.8}$$

where D is the diffusion coefficient induced by the ion irradiation. The flux J_2 is defined as:

$$J_2 = kC_i \tag{2.9}$$

where k is the chemical reaction rate. The growth rate of the mixed layer can be represented by:

$$N_A\frac{dX}{dt} = N_A\phi'\frac{dX}{d\phi} \tag{2.10}$$

where N_A is the number of A atoms per unit volume presented in A_aB_b equal to $aC/(a+b)$. We assume that during the ion irradiation the ion flux ϕ' is kept constant, so the time t can be replaced by ϕ/ϕ'.

The material flow through the sample must be constant, so:

$$N_A \phi' \frac{dX}{d\phi} = J_1 = J_2 \tag{2.11}$$

and

$$D(C_A - C_i)/X = kC_i \tag{2.12}$$

Eliminating C_i in terms of Eq. 2.12 and integrating Eq. 2.11 with the assumption that $X = 0$ for $\phi = 0$ we obtain the equation:

$$N_A \phi' k X^2 + 2N_A \phi' D X - 2C_A D k \phi = 0 \tag{2.13}$$

Equation 2.13 is a standard quadratic equation, where X is the variable. Depending on the fluence range we can obtain different solutions. Let us define a critical ϕ_c such that:

$$\phi_c = 2\left[\frac{a}{a+b}\right]\frac{CD\phi'}{C_A k^2} \tag{2.14}$$

For $\phi >> \phi_c$ the squared thickness X^2 changes lenearly with ϕ

$$X^2 = 2\left\{C_A/\left[a/(a+b)\right]C\right\} D\frac{\phi}{\phi'} \tag{2.15}$$

and for $\phi << \phi_c$ the squared thickness X^2 varies as ϕ^2

$$X^2 = \left\{kC_A/\left[a/(a+b)\right]C\right\}^2 \left(\frac{\phi}{\phi'}\right)^2 \tag{2.16}$$

The coefficient D in the Eq. 2.15 is the diffusion coefficient described as:

$$D = (0.2F_d\phi'/C)(\mu^{1/2})(\lambda^2/E_d) \tag{2.17}$$

and represents the diffusion coefficient in in the case of low F_d (density of the deposited energy deposited in nuclear collisions corresponding to the collision cascade regime), where $\mu = (4M_A M_B)/(M_A + M_B)^2$ with M_A and M_B the atomic masses of the components. The λ constant is the stable distance between a vacancy and an interstitial, usually taken as $1nm$ [5] and E_D is the displacement threshold energy.

Mixing rate

The mixing rate is a very important parameter that describes the IBM process. By definition the mixing rate is the square thickness of the mixed layer X^2 divided by the ion dose ϕ [19]:

$$mixing\ \ rate \equiv \frac{X^2}{\phi} \tag{2.18}$$

Considering the compound formation, thus combining the equations 2.15 and 2.17 we end up with the expression for the mixing rate in the collision cascade mixing regime in case of one mobile atom A:

$$\frac{X^2}{\phi} = \left\{ \frac{2C_A}{[a/(a+b)]\,C} \right\} \cdot \left[\frac{0.2F_d(\mu^{1/2})\lambda^2}{CE_d} \right] \tag{2.19}$$

For high densities of the deposited energy F_d, the influence of the thermal spikes must be considered. In the compound formation model [19] the following expression was proposed for the mixing rate in the thermal spike regime:

$$\frac{X^2}{\phi} = \left\{ \frac{2C_A}{[a/(a+b)]C} \right\} \cdot \left[\frac{K_1 F_d^2}{C^{5/3}\Delta H_{coh}^2} \right] \tag{2.20}$$

where ΔH_{coh} is the cohesive energy, and $K_1 = 0.0035nm$ is the parameter which value was deduced from the the experimental results [19].

2.2.4 Computer simulations

Computer calculations are an important tool that can simulate the ion-solid interactions very precisely. The simulations enable us to estimate by calculations some parameters that are impossible to be studied experimentally. As an addition to the experimental results the simulations can give us a much better understanding of the investigated process.

Monte Carlo simulations

Monte Carlo is a well-known city of Monaco that is especially famous for casinos, where so called 'luck' depends very often on the roulette (a very primitive random number generator) and is governed by the laws of statistics and probability. Monte Carlo also gave its name to the computational method that tries to solve each problem according to the following algorithm:

1. initiate randomly the input conditions, then
2. execute the deterministic calculations on them,
3. repeat 1 and 2 n-times and when it's done,
4. gather the results of all the calculations into the final result.

The randomly repeated action and the unpredictable nature of each single result reminds a little bit of gambling in a casino.
Because of the reliance on the random numbers and the repeated calculations, the Monte Carlo (MC) method is very suitable for computers. MC algorithms started being important especially in the second half of the 20th century, when the computers became more accessible and their computing power grew significantly, so they allowed to perform complicated calculations in reasonable time. They quickly found many applications in many areas of science and engineering.
Ion-solid interactions are very suitable to be simulated using the Monte Carlo method. The result of the calculation requires averaging over many simulated particle trajectories and can give the information about the ion range, energy distribution, sputtering process, energy loss and many more. A large number of MC programs has been developed until now. The software package SRIM (the **S**topping and **R**ange of **I**ons in **M**atter) [77] was chosen for all the computer calculations presented in this work. The SRIM package contains the TRIM code (TRIM stands for the **Tr**ansport of **I**ons in **M**atter) that is one of the most commonly cited programs for ion-solid interactions. It has been developed since the 1980s by J. F. Ziegler and J. P. Biersack in the USA and is distributed freely in the internet under http://www.srim.org/. The program allows the user to define the target materials, to set up the ion beam parameters and for the given number of ions it follows each ion into the target and makes the detailed calculations of the energy transferred to every target atom. It tracks the collision cascades that every ion caused and also the sputtering phenomenon, ionization and phonon production. It also calculates the 3D ion distribution and the target damage, and many more parameters of the ion bombardment process that are impossible to be measured. It all makes the TRIM code a very interesting tool to study the ion beam mixing of the Ti/Si interface. The only disadvantage of the TRIM is that it does not consider the titanium silicide formation under the ion bombardment.
All the calculations in this work were performed with SRIM-2006.02 package with the Stopping Power code version 2003. The simulations were run on a desktop PC with Intel Pentium 4 1.70GHz CPU and 256MB of RAM with Microsoft Windows XP operating system.

Molecular dynamics simulations

Molecular dynamics (MD) calculations may be also applied to study the ion-solid interactions. In principle the MD calculation involves modeling the system where atoms are

allowed to interact for some period of time under the specified conditions and governed by the specified laws of physics. In the ion-solid bombardment process the molecular dynamics simulations may be used for example to model the real-time collision cascade evolution, the defects evolution, liquid-like effects in the solid (during the thermal spike) and final defect states. The real-time evolution of the collision cascade can not be measured experimentally for many reasons, for example because of its very short time scale ($10^{-12}s$), but it could be modeled with MD methods.
It was observed with MD simulations, that a collision cascade consists of three phases [54, 49, 67]:

1. Collisional phase - lasts for a few tenths of a picosecond, this phase lasts while all recoiling atoms are capable of producing any further displacements.

2. Thermal spike phase - represents a special condition of a collision cascade when a thermal spike appears and a local melting of the substrate is observed.

3. Relaxational phase [66] - the last phase of the collision cascade when close unstable Frenkel pairs recombine.

The effects of 5keV collision cascades on defects in crystal structure of silicon were already studied by the means of molecular dynamics calculations [55, 56, 60]. The simulations revealed that the 5keV collision cascades are broken down into subcascades and then form isolated liquid-like areas. When theses zones cool down (when the atoms reach the thermal equilibrium) they form amorphous-like 'damage pockets'. At high temperatures these pockets anneal out rapidly, but at room temperature they remain stable.

In this work no Molecular Dynamics simulations were performed. This was due to the fact, that there is no available code that could be easily adopted to the Ti/Si interface. So the MD simulation would require the development of a dedicated computer program and it would reach far beyond the time scale of this work.

Chapter 3

Experimental techniques

3.1 UHV deposition

A silicon crystal under atmospheric pressure is always covered with a 15-20Å [61] thick layer of SiO_2, because of the oxidation process - the chemical reaction between the silicon and the oxygen, that occurs at room temperature if only an O_2 molecule hits the silicon surface. Moreover, the surface is always contaminated with carbon, or other atoms that have accidentally struck the surface and have been adsorbed. Also the atmospheric gasses (e.g. CO_2) may diffuse into the bulk of the crystal. So the silicon's surface under the atmospheric pressure is very far away from the ideal surface. There is the same problem with the titanium: in the atmosphere the titanium reacts immediately with the oxygen and forms a thin layer of the TiO_2 on its surface. Since the aim of this work is to study the chemical reactions at the silicon/titanium interface, it is crucial to have very clean silicon surfaces covered with pure titanium layers. It is also necessary to deposit titanium onto silicon with the precision of atomic layers. All these conditions may be fulfilled only under ultra high vacuum (UHV) conditions.

3.1.1 Monolayer equivalent

In this work all the titanium coverages are given in equivalent monolayers (MLE). A monolayer by definition is a single layer of atoms (or molecules) that covers the substrate crystal surface.
The deposition rate is measured by the quartz microbalance which measures the change of the resonant frequency related to the deposited mass per cm^2. The microbalance control

unit displays this frequency change in digits and the sensitivity of one digit is set to $1 \cdot 10^{-8} g/cm^2$.

1 MLE Ti on Si(111)

The Si(111) surface has the surface density of $1.18 \cdot 10^{15} atoms/cm^2$.

$$1 \text{ mol of Ti} = 6.022 \cdot 10^{23} atoms \text{ (Avogadro constant)}..... \ 47.867g$$
$$1.18 \cdot 10^{15} atoms/cm^2 .....x[g]$$

$$x = \frac{1.18 \cdot 10^{15} atoms/cm^2 \cdot 47.867g}{6.022 \cdot 10^{23} atoms}$$
$$x = 9.37 \cdot 10^{-8} g/cm^2$$

If 1 digit corresponds to $1 \cdot 10^{-8} g/cm^2$ it means that it is necessary to measure 9.37 digits in order to evaporate 1 MLE of Ti onto Si(111).

1 MLE Ti on Si(100)

The Si(100) surface has the surface density of $0.69 \cdot 10^{15} atoms/cm^2$.

$$1 \text{ mol of Ti} = 6.022 \cdot 10^{23} atoms \text{ (Avogadro constant)}..... \ 47.867g$$
$$0.69 \cdot 10^{15} atoms/cm^2 .....x[g]$$

$$x = \frac{0.69 \cdot 10^{15} atoms/cm^2 \cdot 47.867g}{6.022 \cdot 10^{23} atoms}$$
$$x = 5.48 \cdot 10^{-8} g/cm^2$$

So if 1 digit represents $1 \cdot 10^{-8} g/cm^2$ of the deposited mass, it means that it is necessary to measure 5.48 digits in order to evaporate 1 MLE of Ti onto Si(100).

3.1.2 Tooling factor

Sometimes the geometry of the vacuum chamber may prevent positioning the quartz microbalance exactly at the same position and exactly in the same way as the sample is. Let's consider that the quartz microbalance crystal is tilted 45° against the vapour beam like presented in the Fig. 3.1

Let's further assume that the microbalance spot area is a circle and the cross-section area of the vapour beam is also a circle. If the microbalance crystal is perpendicular to the vapour beam the evaporated particles bombard the whole microbalance surface evenly.

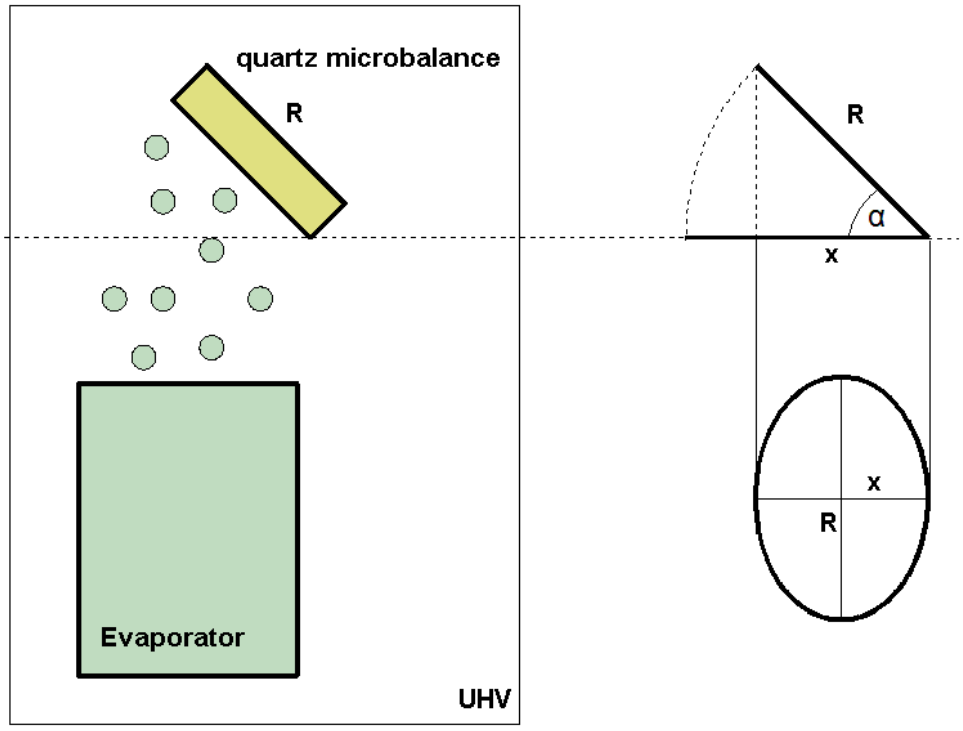

Figure 3.1: *Tilted quartz microbalance and its projection (ellipse)*

But if the microbalance is tilted, the cross-section area of the bombarded microbalance area changes into an ellipse.
Let's assume the diameter of the quartz microblalnce is R, so its area is:

$$S_1 = \pi(\frac{R}{2})^2 = \frac{1}{4}\pi R^2 \tag{3.1}$$

and when the microbalance tilts at 45° the area of the cross-sectional area (ellipse) is:

$$S_2 = \pi\frac{x}{2} \cdot \frac{R}{2} = \frac{1}{4}\pi R^2 cos\alpha \tag{3.2}$$

so the ratio T is:

$$T = \frac{S_1}{S_2} = \frac{1}{cos\alpha} \tag{3.3}$$

and we call it the tooling factor. If the $\alpha = 45°$ than $T \approx 1.41$.
So the deposition rate measured with the microbalance must be multiplied by the tooling factor T in order to obtain the relevant deposition rate on the sample.

3.2 Photoemission spectroscopy

The photoelectric effect was first described by Albert Einstein in 1905 and it refers to the phenomenon in which the electron is ejected from the solid, after the absorption of the electromagnetic radiation energy. Such an ejected electron is called a photoelectron. The photoelectric effect is described by the following equation:

$$E_{kin} = h\nu - E_B - \phi \tag{3.4}$$

where E_{kin} is the kinetic energy of the ejected photoelectron, $h\nu$ is the kinetic energy of the incident photon (h is the Planck constant and ν is the photon wave length), E_B is the binding energy of the electron and ϕ is the work function of the material.
If the energy $h\nu$ of the incident photon and E_{kin} of photoelectron is known, it is possible to obtain the information about the chemical composition, electronic structure and the valence band of the material from which the photoelectron was emitted. This investigation techniques are generally known as a photoemission spectroscopy or a photoelectron spectroscopy. [4]
So the photoemission spectroscopy requires a special apparatus that at least consists of: light source, electron detector and the electron analyzer. In most cases the photoemission spectroscopy is performed with monochromated light, and the light sources are the helium discharge lamp (for ultra-violet light emission) and the X-ray source (for the X-ray light emission).

The mean free path of the electrons in the solids depends strongly on their kinetic energy and forms a 'universal curve' presented in Fig. 3.2 In the discussed photoemission spectroscopy the photoelectrons gain kinetic energy not greater than 1200eV so their penetration depth should not exceed $\sim$ 20Å. That makes photoemission spectroscopy surface sensitive and suitable to study the growth of the materials on a substrate.

Usually, the studied sample is a couple of centimeters away from the electron analyzer, so it is absolutely necessary to run the measurement under the ultra high vacuum conditions, in order to prevent the photoelectrons from colliding with other gas particles.

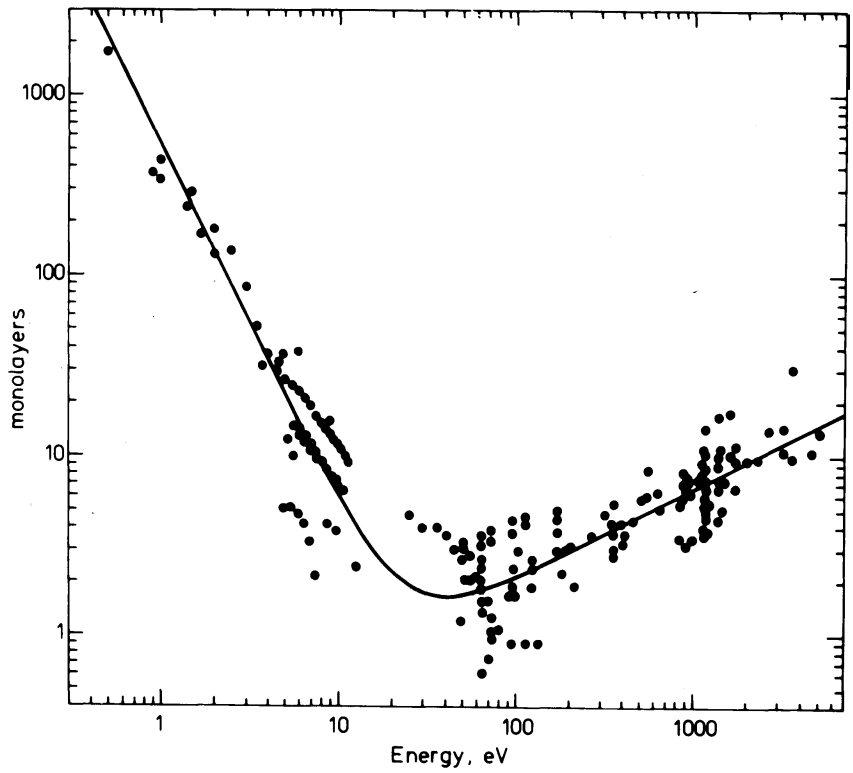

Figure 3.2: *Mean free path of the electrons as a function of their kinetic energy [43]*

3.2.1 XPS, depth profiling with XPS

XPS [57] stands for the **X**-ray **P**hotoemission **S**pectroscopy, because in this technoque the x-ray gun is used as a light source. It is also known as ESCA (**E**lectron **S**pectroscopy for **C**hemical **A**nalysis).

The x-ray source emits the electromagnetic radiation of $h\nu = 1253.6eV$ for the $MgK\alpha$ anode and $h\nu = 1486.6eV$ for the $AlK\alpha$ anode. The XPS technique is used to determine the chemical composition and the electronic core level states of the investigated sample. It is very surface sensitive because it excites the electrons in the studied solid that lay not deeper than $10 - 20$Å.

A typical XPS spectrum is plotted as the number of detected photoelectrons versus their binding energy. Each chemical element creates a specific set of XPS peaks that differ in height and shape at specific binding energies, so it is possible to identify every element that lies on the surface of the investigated sample.

Depth profiling with XPS

As discussed above the XPS is a technique that excites the electrons in the very surface region, but very often it is necessary to study the chemical composition of the layers that lay much deeper in the bulk. Such studies may be performed using the method called depth profiling [57]. In the depth profiling the surface of the sample is subsequently investigated by the means of XPS and sputtering. XPS reveals the chemical composition of the sample and the sputtering process removes the atoms (or molecules) from the surface layers, so it is possible to explore deeper layers in the bulk. The ion beam used for sputtering can be optimized and calibrated so that it is possible to estimate the depth of the sputtered crater. With all this knowledge it is possible to obtain the depth profile - a plot with the target depth on the x axis versus the atomic concentration of the identified chemical elements on the y axis.
Depth profiling is especially needed when one wishes to study the buried interface at the boundary of two materials.
The disadvantage of the depth profiling is that it is a destructive method that destroys the investigated sample (sputtering).

3.2.2 UPS

UPS [57] stands for the **U**ltra-violet **P**hotoemission **S**pectroscopy and it is the technique that uses the ultra-violet (UV) light in order to obtain the photoelectric effect.
A helium discharge lamp provides the UV radiation for both He1 ($h\nu = 21.2eV$) and He2 ($h\nu = 40.8eV$) lines. The technique is even more surface sensitive than XPS and allows to study layers not thicker than $2-6$Å. Due to the low energy of photons it is not possible to excite the deep core levels of the atom and only the electrons from the valence band and the shallow core levels can be ejected. So UPS finds applications in determining the valence band states of the studied material.

3.3 LEED

The diffraction is a common method for the investigation of the periodic structures. If an electron beam incident on a surface is diffracted by the atom of the surface, the diffracted beams, collected on a fluorescent screen, give a particular diffraction pattern (Fig. 3.3). This surface investigation method is known as the Low Energy Electron Diffraction (LEED) [36, 57, 72, 58].

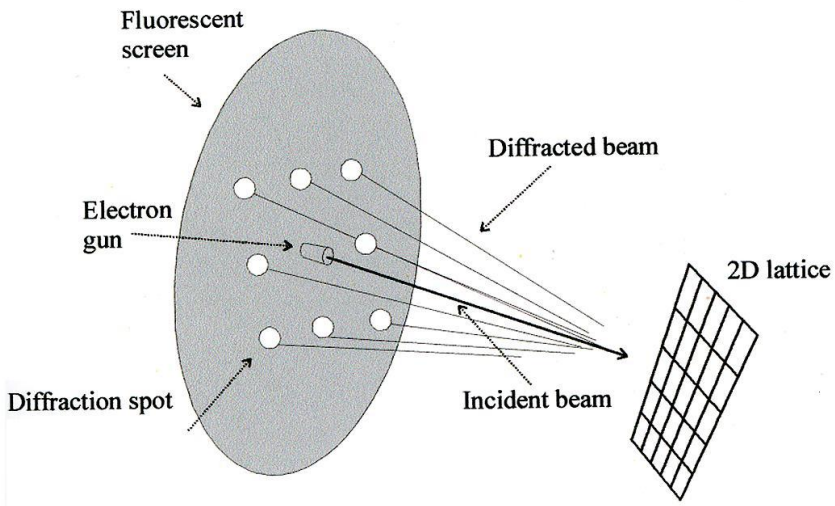

Figure 3.3: *Schematic drawing of the LEED system [72]. A beam of electrons is directed on the crystal surface. The diffracted beams are collected on a fluorescent screen (the LEED pattern is observed).*

The conditions under which a diffraction pattern is obtained are defined by the two equivalent principles of von Laue and Bragg [36]. These conditions predict the formation of a diffraction pattern if the incident beam is specularly reflected by the atoms of the surface and if they interfere constructively.

In order to be able to interpret the diffraction pattern it is good to recall the concept of the reciprocal space [36, 58]. In 2-dimensional space the 2-dimensional reciprocal space is spanned by the 2 unit vectors of the reciprocal unit mesh:

$$\vec{b}_1 = 2\pi \frac{\vec{a}_2 \times \vec{n}}{\vec{a}_1 \left(\vec{a}_2 \times \vec{n}\right)} \tag{3.5}$$

$$\vec{b}_2 = 2\pi \frac{\vec{a}_1 \times \vec{n}}{\vec{a}_2 \left(\vec{a}_1 \times \vec{n}\right)} \tag{3.6}$$

and

$$\vec{G} = h\vec{b}_1 + k\vec{b}_2 \tag{3.7}$$

where $\vec{a}_1$ is the first real space unit cell vector, $\vec{a}_2$ is the second real space unit cell vector, $\vec{b}_1$ is the first reciprocal space unit cell vector, $\vec{b}_2$ is the second reciprocal space unit cell vector, and $\vec{n}$ is the vector normal to surface.
It can be also represented as:

$$\left|\vec{b}_1\right| = 2\pi \frac{1}{|\vec{a}_1 sin\gamma|} \tag{3.8}$$

$$\left|\vec{b}_2\right| = 2\pi \frac{1}{|\vec{a}_2 sin\gamma|} \tag{3.9}$$

where γ is an enclosed angle between $\underline{a}_1^*$ and $\underline{a}_2^*$. This construction is very useful upon considering the 2 dimensional Laue conditions which state:

$$\vec{a}_1 \Delta\vec{k} = 2\pi h \tag{3.10}$$

$$\vec{a}_2 \Delta\vec{k} = 2\pi k \tag{3.11}$$

and $\Delta\underline{k} = \underline{k}' - \underline{k}$. They principally represent the conservation of energy and momentum between the incident wave vector $\underline{k}$ and the emerging wavevector $\underline{k}'$. These equations can be fulfilled whenever $\Delta\underline{k}$ equals a reciprocal lattice vector $\underline{G}$. So the LEED pattern is the Fourier transformation of the surface structure in real space. By back transforming the reciprocal lattice via the equations given above it is possible to analyze the surface structure.

3.4 Ex-situ investigations

All the previously described techniques were used in in-situ experiments, which means all the silicon samples preparation, modification and investigation was done in one UHV chamber. But it was also necessary to study the samples with other techniques that were not available in the vacuum chambers, or it was not possible to apply them under UHV conditions. That is why it was needed to perform ex-situ investigations: to take samples out of the vacuum and transport them into another systems.
GIXRD measurements were performed by Siemens Laboratories in Munich (Germany) in order to study the crystal phase of the titanium silicides.
TLM measurements were done at Infineon Technologies in Villach in order to investigate the electrical parameters of the formed titanium silicides – silicon contact.
Non contact atomic force microscopy was done in AFM System in the Institute of Physics of Karl-Franzens University Graz and its purpose was to study the surface topography of the titanium silicides formed by different methods.

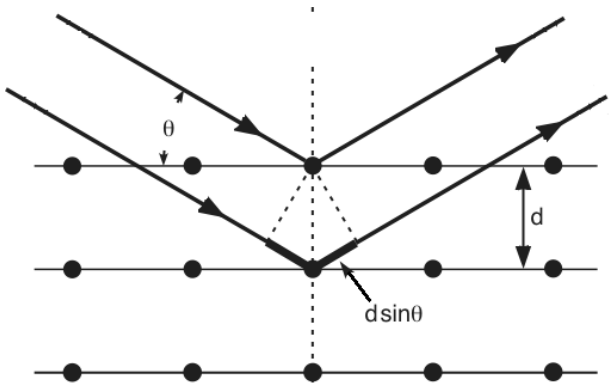

Figure 3.4: *Derivation of the Bragg Equation:* $2dsin\theta = n\lambda$

3.4.1 GIXRD

When the X-rays pass through the matter, the radiation interacts with the atoms in the solid which results in scattering of the radiation. In the crystalline materials the atoms are organized in planes and the distance between the planes is similar to the X-ray wave length. This means that interference can take place. As a result one observes a diffraction pattern where the X-rays are emitted from the solid at different angles. Those characteristic angles are based on the spaces between the atoms which are specific for different materials. This phenomenon is described by the Bragg Law [36]. The Bragg Law was derived from the experiments with the diffraction of X-rays on different crystal substrates and is mathematically expressed as:

$$2dsin\theta = n\lambda \tag{3.12}$$

where

- n an integer,
- λ is a wavelength of the incident electromagnetic radiation,
- d is the spacing between the planes in the atomic lattice,
- θ is the angle between the incident rays and the scattering planes.

The graphical representation of the equation 3.12 is presented on the Fig. 3.4. According to the phenomenon described by the Bragg Law a new technique, called **G**razing **I**ncidence **X**-**R**ay **D**iffraction (GIXRD), was developed. In this technique the

crystal sample is irradiated by the X-rays at grazing angles and the intensity of the reflections for different angles is detected. The grazing incidence of the X-rays make this technique surface sensitive. With GIXRD it is possible to identify the crystallographic structure of the studied crystal and also the preferred orientation in the polycrystalline samples. Each material gives its characteristic diffraction pattern so it is easy to identify the material by comparing the diffraction data against the already existed and maintained databases.
All the GIXRD diffraction patterns presented in this work were measured ex-situ by Siemens Laboratories in Munich (Germany).

3.4.2 Noncontact AFM

Atomic **F**orce **M**icroscopy (AFM) [52] was invented by Gerd Binning, Calvin F. Quate and Christopher Herbe in 1986 and it is a very important tool for measuring and manipulating the matter at the nanoscale. The AFM is called 'microscopy' which reminds of 'looking at the surface' like it is performed by optical microscopes, but in fact the AFM principle relies on 'sensing' the surface with a mechanically controlled probe. The operational principle and the AFM apparatus is shown in the Fig. 3.5 If the tip of the cantilever is approached to the sample surface, the forces between the tip and the surface cause the deflection of the cantilever. The deflection of the cantilever is detected by the laser-photodiode system in that way, that the laser light is shone onto the cantilever and then is reflected onto the array of photodiodes. The photodiodes detect the changes in the position of the laser spot and the computer transforms this data into the length units. In this study the noncontact AFM mode with the frequency modulation was used, which means the cantilever was constantly vibrating over the investigated surface. The vibration was caused by the piezoactuators embedded into the console.
The result of the AFM presents the topography of the studied surface and also the roughness of the surface can be obtained.

3.4.3 TLM

TLM stands for the **T**ransmition **L**ine **M**ethod and it is a very widely used method in semiconductor physics for measuring the contact resistance between a metal and a semiconductor. The method involves patterning the metallization layer of the investigated sample. The pattern should form separated contacts (pads) and the resistance between them is measured by attaching four probes to a pair of contacts, applying the voltage

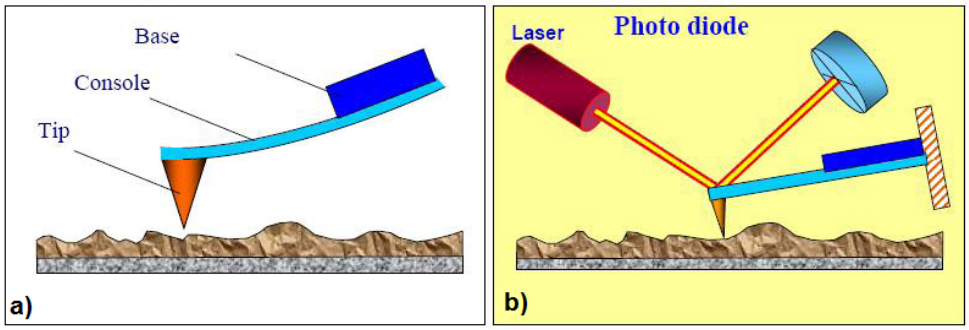

Figure 3.5: *Image of an AFM cantilever approaching the surface (a) and the optical method for detection of the console bending (b) [40]*

between two probes and measuring the resulting current with two other probes (Fig. 3.6). The current flows from the first current probe through the metalization layer, the metal-semiconductor junction, through the bulk of the semiconductor, the second metal-semiconductor junction, the second metalization layer to the second current probe. So the resistance obtained from the current and voltage measurement is the sum of the contact resistance of the first and the second contact and the resistance of the bulk semiconductor between the contacts. If such a measurement is repeated for the couple of next neighbouring contacts one can obtain a plot of resistance versus the contact distance. This plot must be linear, because the resistance changes linearly with the length according to the $R = \rho\frac{l}{A}$ (l - length, A - cross-sectional area of the resistor) formula. The slope of the plot is the sheet resistance.
If one applies the voltage to a pair of contacts, then changes it and also measures the current, it is possible to obtain the current-voltage (I-V) characteristic of the contact. Its shape gives information about the type of the created metal-semiconductor contact (linear for ohmic contact and exponential for Schottky contact in case of a forward bias).

3.5 Experimental setup

3.5.1 Silicon substrates

The silicon crystals used for the titanium silicide formation studies were cut from the silicon wafers delivered by Infineon Technologies Austria A.G. company by the chip plant in Villach. The wafers were 6” n-type Si(111) and 8” n-type Si(100).
The wafers were cut into samples using a pencil with a diamond tip. Each silicon sample was a rectangle with the dimensions of $\sim 1cm \times 0.5cm$.

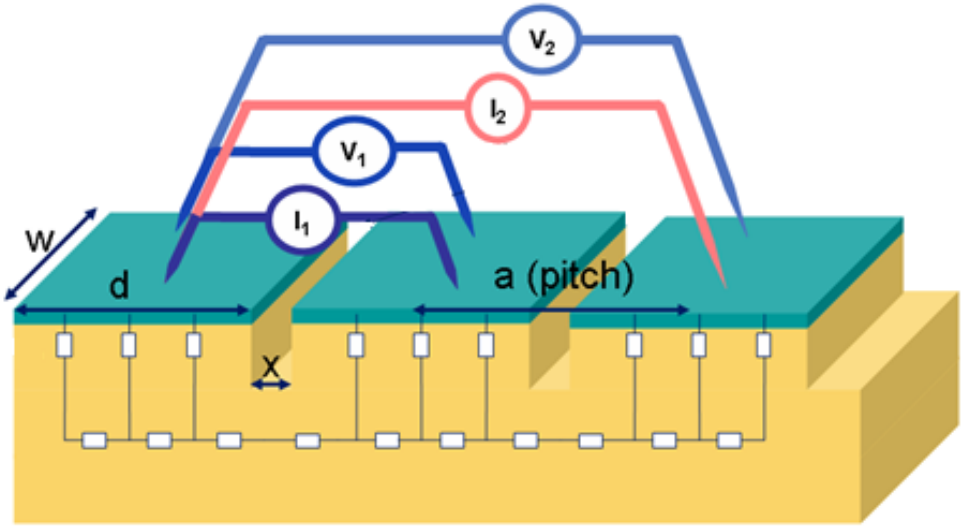

Figure 3.6: *The illustration of the contact resistance measurement by the TLM method*

In order to introduce the silicon samples into the ultra high vacuum chamber it was necessary to mount them on the Omicron-type sample plates that are compatible with most of the sample holders used in the institute. The sample plates were made of molybdenum, because the silicon does not form compounds nor alloys with the molybdenum in the temperature range (up to $750°C$) used during the titanium silicide investigations. The sample plates have also four small tantalum studs so it is possible to attach the silicon sample to the sample plate by spot-welding tantalum clamps to the tantalum studs and clamping the silicon crystal. The tantalum clamps were cut from high purity (99.9%) 0.100mm thick tantalum foil. The sample plates were made by the fine precision mechanics Workshop in the Institute of Physics of Karl-Franzens University Graz.

3.5.2 SCIENTA UHV System

Most of the experimental results presented in this work were done in the ultra high vacuum system called the "SCIENTA System", Fig 3.7

The system consists of three chambers: preparation, analysis and the fast-entry chamber, that are separated by gate valves. In order to obtain the UHV conditions the SCIENTA system is constantly pumped by a set of pumps: turbomolecular pump, roughing pumps, ion pumps and sublimation pumps. The exact position of the pumps in the chambers is presented in Fig. 3.8. The base pressure in the system is kept in the $10 \times 1^{-10} mbar$ range and such conditions can be obtained after about 12 hours of the system bake-out. The sample transportation in the system is carried out by the Omniax 600 sample ma-

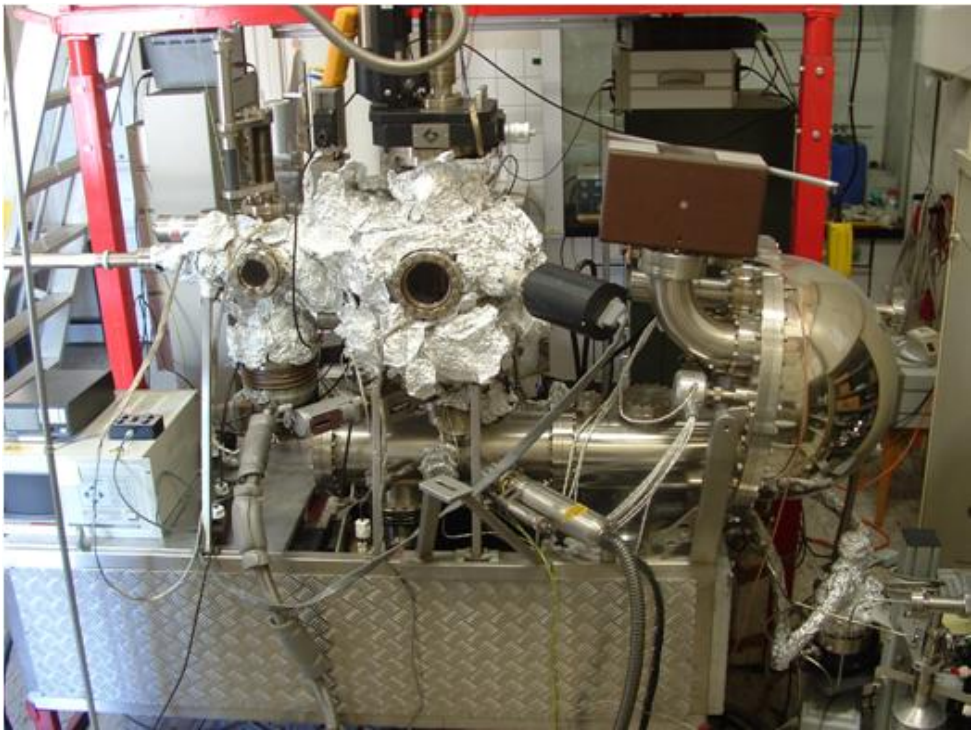

Figure 3.7: *SCIENTA Lab in 2007*

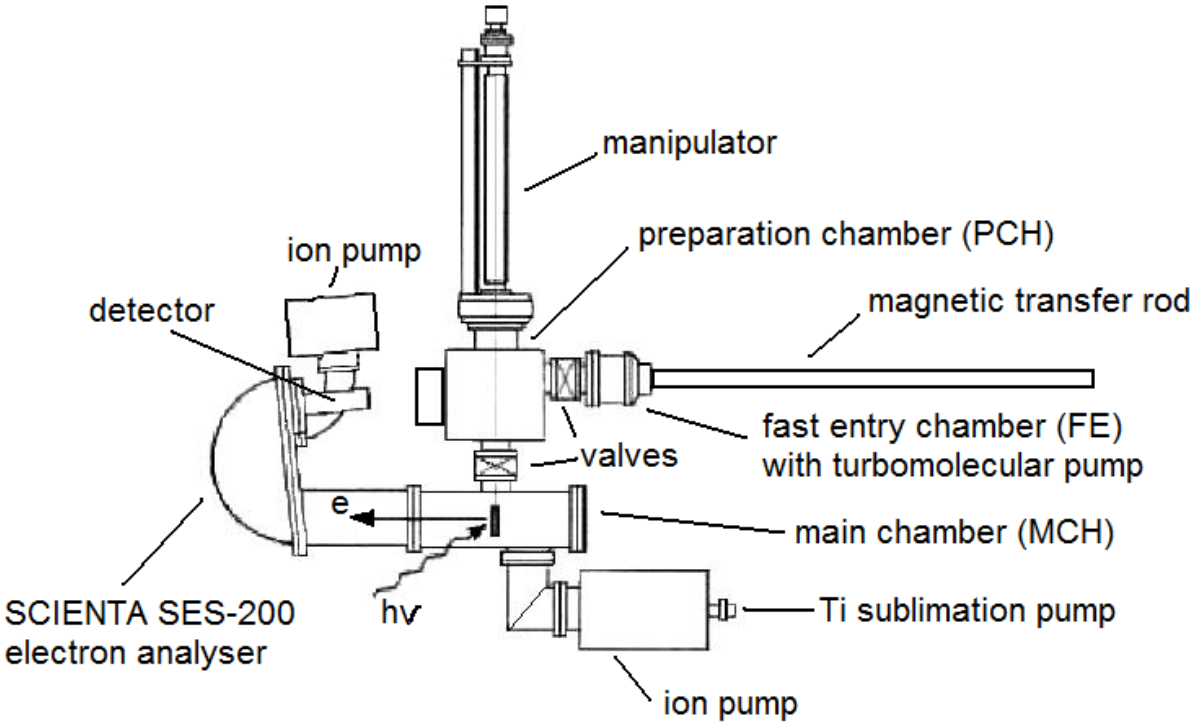

Figure 3.8: *SCIENTA UHV System.*

nipulator and a magnetic transfer rod. The magnetic transfer rod transfers the samples in the horizontal direction between the fast-entry chamber and the preparation chamber. The sample manipulator enables to move the sample between the preparation chamber and the analysis chamber in the vertical direction. It has also a sample holder that was designed and made by Prof. Michael G. Ramsey and Ing. Kurt Ansperger in the Institute of Physics of the Karl-Franzens University Graz. The manipulator rod can be also rotated what enables positioning of the sample against different devices in the chambers.
It is also possible to heat the samples attached to the manipulator by indirect heating. The sample head is electrically isolated from the sample plate and has a spot-welded spiral shaped tungsten filament (grounded at one side) behind the sample plate. The indirect heating is possible when the current of about 2.0A flows through the tungsten filament and a positive high voltage (up to 1000V) is applied to the sample plate. The high voltage attracts the electrons from the filament and the electrons emitted from the filament hit the sample plate what increases its temperature. There is a chromel-alumel thermocouple mounted on the sample head that can be used for measuring the temperature.

The fast-entry chamber is used as a sample magazine that can store up to five samples. This chamber is valved off from the preparation chamber so it can be vented and opened without any influence on the pressure in the preparation and analysis chambers. It is pumped by a roughing pump and a turbomolecular pump. After opening and replacing the samples the chamber must be baked-out for about seven hours.

The preparation chamber is equipped with:

- the ion gun with the ion source (ISE10 by Omicron Vakuumphysik GmbH) - used for the argon ion bombardment of the samples in order to sputter-clean them or for the IBM process. The ion gun operates in an argon pressure of the order of $3.0-6.0\times10^{-6}mbar$ (measured by the ionization gauge in the preparation chamber) and accelerates the argon ions up to 5keV.
- the EGN4 electron beam evaporator manufactured by Oxford Applied Research company, which was used for the precise titanium deposition. Titanium was evaporated from high purity (99.99+%) 2mm thick titanium rods. The titanium evaporation takes place when the rod is bombarded by the electron beam with a power of $13-16W$. The electron beam bombardment causes local melting of the titanium rod and also partly the ionization of the evaporated particles. The measured ion

current ranged from 11-15nA. During the evaporation the system pressure rose but was never higher than $2.0 \times 10^{-9} mbar$.

- a quartz microbalance to control the titanium deposition rate
- a LEED optics for low energy electron diffraction to study the surface structure of the investigated crystals
- a mass spectrometer to monitor the pressure of th residual gases in the chamber
- an ionization gauge to measure the system pressure.

The analysis chamber is used for photoemission measurements, so it contains:

- the high resolution SCIENTA SES-200 hemispherical electron analyzer. The SES-200 is equipped with an electron detector with a CCD camera for electron imaging and the computer software package for data acquisition, processing, storage and analysis.
- twin anode water-cooled x-ray gun for XPS studies. The gun was mounted on the linear motion facility so it was possible to approach the gun to the sample to the distance of $\sim 2cm$ during the XPS measurement. The X-ray source was mounted in that way that there was an angle of 45° with respect to the analyzer lenses, when the sample was positioned for normal emission. The gun was always operated at the power of 300W (15kV of voltage and the emission current of 20mA) with the Mg anode. During the XPS measurement the pressure in the analysis chamber increased, but was never higher than $7.0 \times 10^{-10} mbar$.
- UV discharge lamp used in UPS studies. It is possible to excite He I and He II radiation by controlling the partial pressure in the discharge lamp. The discharge conditions for He I were obtain by the partial pressure of $3 \times 10^{-1} mbar$ in the first pumping stage. The helium flow through the lamp also caused the rising of the He pressure in the analysis chamber to $\sim 1.5 \times 10^{-8} mbar$. The UV lamp was mounted that the angle between the lamp and the analyzer lenses was 45°, when the sample was positioned for normal emission. By rotating the sample on the manipulator it was possible to measure the UPS spectra at normal emission and at normal incidence.
- ionization gauge to control the the chamber pressure

Temperature calibration in SCIENTA

In order to study titanium silicide formation by thermal annealing it was necessary to measure the sample annealing temperature very precisely. The sample manipulator in SCIENTA UHV system is equipped with a thermocouple embedded in the sample head, so the thermocouple does not measure the temperature exactly on the sample surface. Therefore it was necessary to calibrate it - to find out how the temperature on the sample surface depends on the electron beam power and the electron bombardment time.
A silicon sample was prepared that a chromel-alumel thermocouple was squeezed between the surface of the silicon crystal and the spot-welded tantalum strap that holds the silicon sample. The thermocouple was in direct contact with the silicon crystal so it measured the temperature exactly on its surface. The sample was annealed for 30 min for different electron beam powers (ranging from 5W to 30W) and both thermocouple readings were compared and transformed into a heating time versus heating power plot. So in the future experiments with thermal annealing it was not necessary to mount a thermocouple on the sample surface, it was only necessary to keep constant heating power and measure the annealing time and read the temperature from the previously obtained heating time versus heating power plots.

Ion flux measurement in SCIENTA

In the IBM process it is crucial to control not only the energy but also the fluence of the incident ions.
The argon ion current was measured in the configuration schematically presented in Fig. 3.9.

The ion bombarded sample is grounded and the current is measured with a multimeter. But the value of the measured current depends not only on the number of the incident ions. During the bombardment process many ion-atom collisions appear on the target surface what results not only in sputtering of the target atoms but also ionization process of the target atoms may take place. The free electrons from the ionized target atoms may be supplied with enough kinetic energy to leave the surface of the target, and this would be measured by the multimeter as an additional plus charge in the target. So the value of the measured current would be the superposition of the ion current and the ejected electrons current. To avoid this misleading measurement the sample is biased with the 9V battery so the positive voltage is on the sample. The positive plus charge should attract the ejected electrons and pull them back to the target or just prevent the electrons from leaving the surface. On the other hand the positive voltage is low enough not to repel

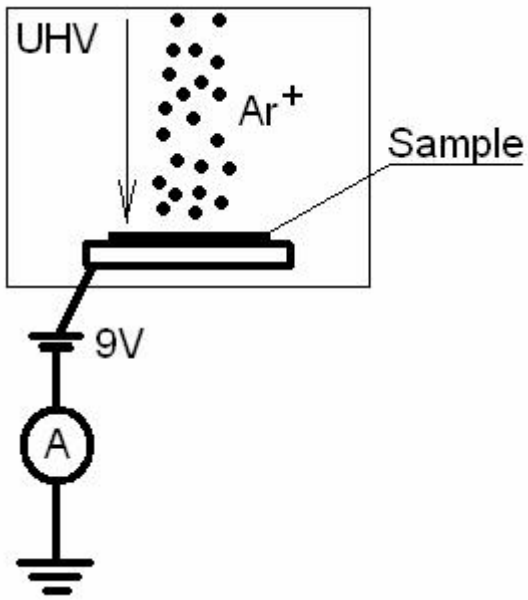

Figure 3.9: *Ion current measurement in SCIENTA Lab*

significantly the plus charged ions reaching the surface.
The ionization process of the target is significant and can be simulated with the TRIM code. In Fig. 3.10 and in Fig. 3.11 the results of the calculations are presented. The simulations were run for 60Å of Ti on 150Å of Si for 100 000 ions bombarding the surface at 0° with different kinetic energies: 1.30, 1.80 and 2.30keV.

In figures 3.10 and 3.11 one can see that the ionization process takes places mostly in the near surface region. The argon ions loose, depending on the energy, approximately 5-7eV/Å in ionizing the target about 10Å deep. Deeper in the target the process rapidly looses its intensity due to the general loss of the kinetic energy of ions. The recoiled target atoms also partly loose their energy in ionization processes and they loose maximum 6-9eV/Å at the target depth of 17Å. The maximum peak height is shifted in case of the recoils deeper into the target. It all means one can expect many free electrons in the surface region from the ionized target atoms that could be ejected from the surface if only supplied with enough kinetic energy.
During the current measurement in SCIENTA Lab in the configuration of the Fig. 3.9 the ion current under the Ar pressure of $4.0 \times 10^{-6} mbar$ ranges from 2.5 - 3.5μA depending on Ar ion energy (energy range: 1.30 - 2.30keV). If the battery is removed from the system the current increases to 5.0 - 6.0μA due to above described phenomenon.

In order to estimate the ion dose it is required to know not only the ion current, but

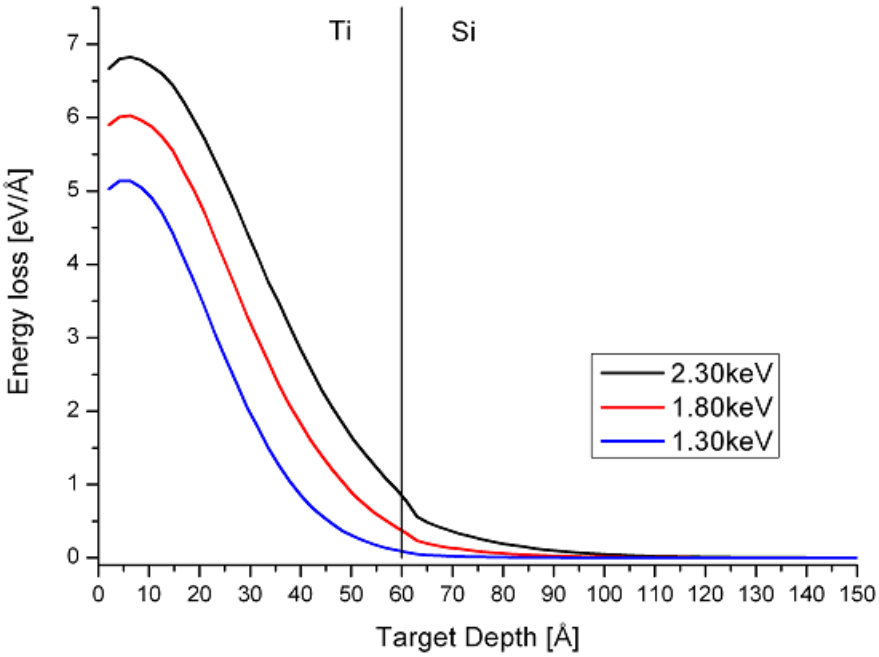

Figure 3.10: *Ion energy loss on ionization as the function of the target depth*

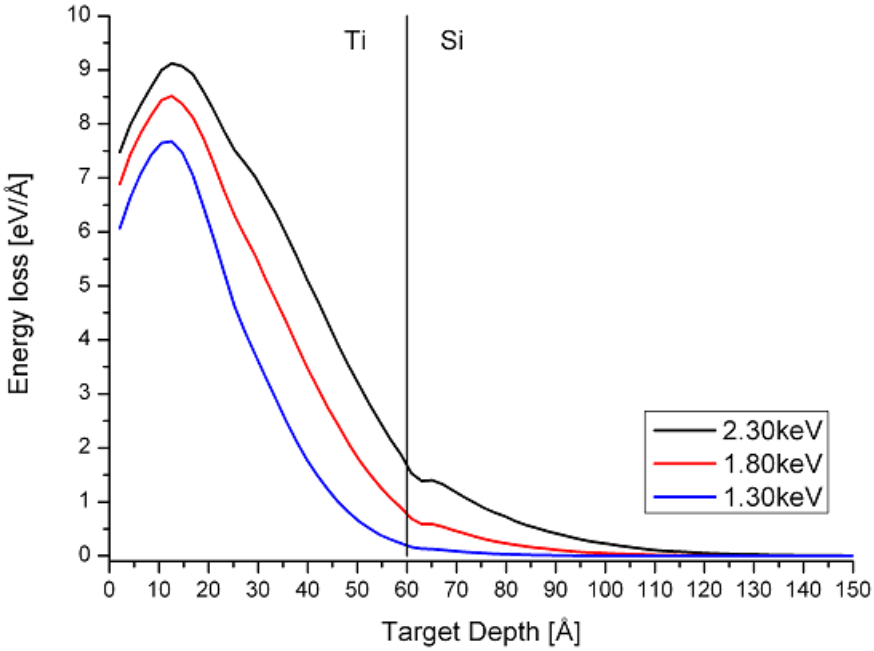

Figure 3.11: *Recoil energy loss on ionization as the function of the target depth*

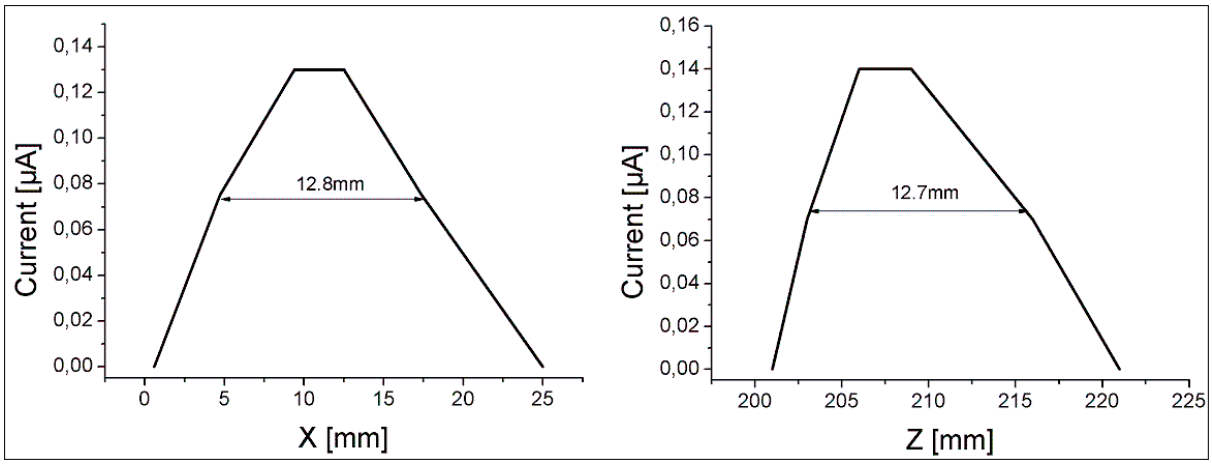

Figure 3.12: *Ion current as the function of the filament position (in horizontal and vertical direction).*

also the area of the ion bombarded spot. It was calculated according to the following procedure: ion beam was directed at the tungsten filament of the manipulator and the filament current was measured. By moving the manipulator in vertical and horizontal directions and measuring the changes in the ion current, the spot size was estimated. In Fig. 3.12 it is shown how the ion current changes by changing the filament position in horizontal and vertical direction.

The spot width is considered to be the width at FWHM which is about 12.8mm in horizontal direction and about 12.7mm in vertical direction. The spot area was estimated to be a circle with a diameter of approximately $r = 12.75mm$.

With the precise knowledge of the ion current and of the ion bombarded spot area it is finally possible to calculate the ion dose.
The ion dose for $5min$ of ion bombardment with the ion current kept constant at $2.5\mu A$ can be calculated as follows.
The spot area is $A = \pi \cdot (6.375)^2 mm^2 = 1.26cm^2$. A single argon atom becomes an ion when it looses at least one electron, which means its electrical charge is equal to $q = +1.602 \cdot 10^{-19}C$. In $5min$ time the sample receives the electrical charge from ions that is equal to:

$$q = 2.5 \cdot 10^{-6}A \cdot 300s = 7.5 \cdot 10^{-4}C \tag{3.13}$$

If the overall electrical charge carried by all the ions during 5min time of the ion bombardment is $7.5 \cdot 10^{-4}C$ and one argon ion carries the electrical charge of $q = +1.602 \cdot 10^{-19}C$,

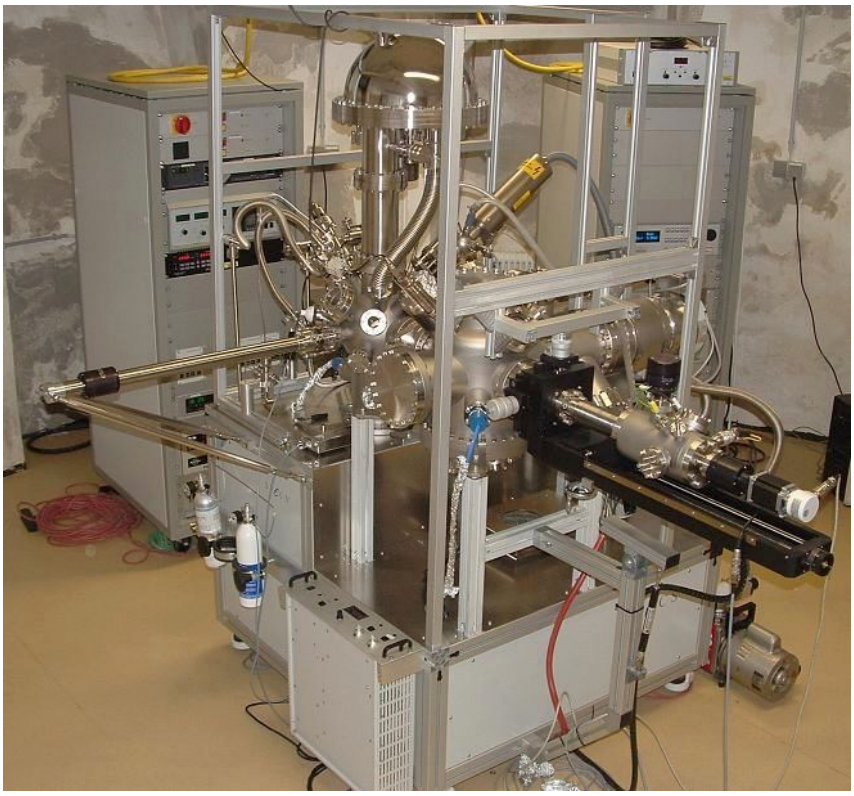

Figure 3.13: *SPECS Lab in 2007*

it is easy to calculate that the total number of ions that hit the target per cm^2 (ion dose ϕ) was:

$$\phi = \frac{7.5 \cdot 10^{-4}C}{1.602 \cdot 10^{-19}C} \cdot \frac{1}{1.26cm^2} = 3.7 \cdot 10^{15} ions/cm^2 \tag{3.14}$$

Using the above method it is possible to calculate the ion dose ϕ for different bombardment times and different ion currents.

3.5.3 SPECS UHV System

All the depth profiling experiments and also the studies of the Ti/SiO_2/Si interface were done in another UHV system called the "SPECS System" (Fig. 3.13). The system consists of three chambers: the fast-entry chamber, the analysis chamber and the preparation chamber and they are separated from each other by gate valves. The base pressure in the system is lower than $2.0 \times 10^{-10} mbar$ and such conditions may be obtained after about 12 hours of the system bake-out. The geometry of the system and the position of all its components is presented in Fig. 3.14.

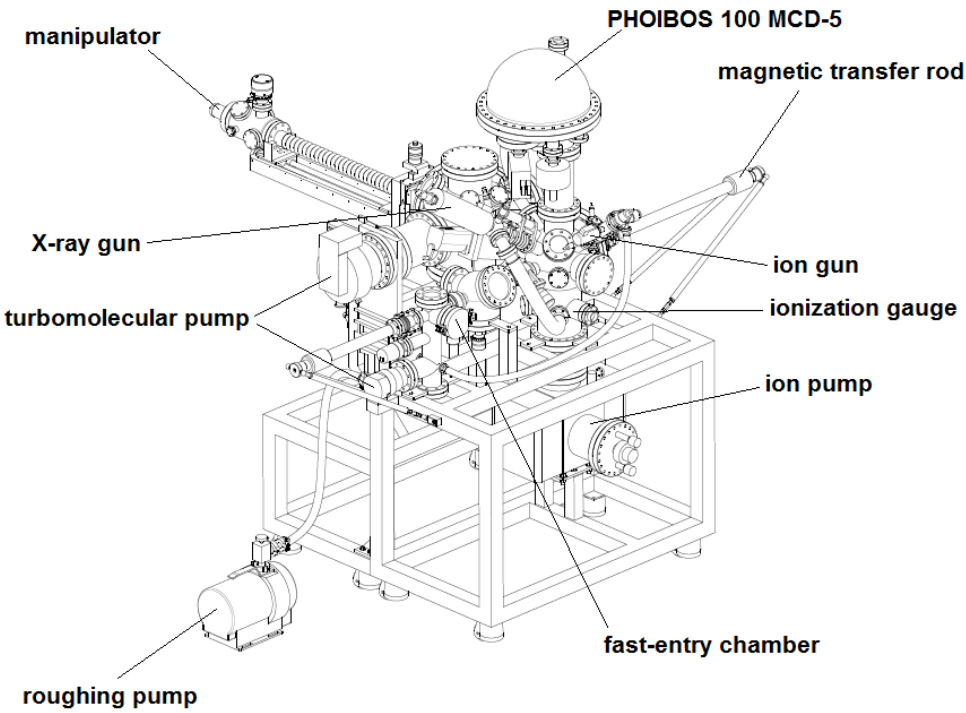

Figure 3.14: *SPECS UHV System*

The small fast-entry chamber is used only for inserting the samples into the vacuum without any need of the bake-out. The chamber is pumped out by the roughing pump and the turbomolecular pump and the pressure is monitored by the ionization gauge. The chamber may be valved off from the analysis chamber so it can be easily vented and opened without disturbing the pressure in the overall system. When the new sample is inserted it takes about $30min$ of pumping to reach the high vacuum conditions ($p \approx 10^{-7}mbar$). The samples may be stored on a sample carousel which may hold up to six samples. In order to transport the sample from the fast-entry chamber into the analysis chamber it is necessary to open the valve between the two chambers which always leads to a very short pressure rise in the analysis chamber up to $\sim 10^{-9}mbar$.

The analysis chamber is used for the photoemission studies of the samples and also for sputter-cleaning the samples and the ion beam mixing process. It is equipped with:

- PHOIBOS 100 MCD-5 hemispherical photoelectron energy analyzer. The data acquisition and processing is computer controlled and supported by the SpecsLab (version 2.32) software package.

- SPECS-XR50 twin anode water-cooled X-ray source for the XPS measurements. The x-ray gun is mounted on a linear motion facility so it is possible to approach the gun to the sample during the measurement to about 2cm. The gun is positioned at the angle of about 45° to the sample, when the sample is positioned for the normal emission. During all the measurements done in this work the x-ray gun operated at the power of 300W (anode voltage 10kV, emission current 30mA) with the Mg anode which gave a reasonable number of counts in XPS spectra. During the x-ray gun operation the pressure in the analysis chamber rises, but it is never higher than $4.0 \times 10^{-10} mbar$.

- SPECS IQE-11/35 ion gun for the ion bombardment of the samples used for sputter cleaning and the ion beam mixing purposes. The ion gun consists of an ion source that operates under the argon pressure of about $4.0 \times 10^{-7} mbar$ and repels the ions to the sample with the kinetic energy up to 5keV. With the ion gun control unit it is possible to set up precisely the area bombarded by the ion beam (ion beam scans through this area). For the ion beam mixing experiments this area was set to $10.00mm \times 10.00mm$ and for the depth profiling experiments the area was set to $4.00mm \times 4.00mm$.

- ionization gauge to monitor the system pressure.

- ion pump

The preparation chamber is used for the titanium deposition so it contains:

- electron beam evaporator for titanium evaporation. The titanium was evaporated from the high purity titanium rod (99.99+%) of the diameter of 2mm. Titanium evaporation took place, when the titanium rod was bombarded by the electron beam with the power of $P \approx 13 - 15W$. During the titanium deposition process the pressure in the chamber rose, but it was always lower than $3.0 \times 10^{-9} mbar$.

- quartz microbalance to control the titanium deposition rate. The microbalance was mounted on a linear motion facility and is positioned at the angle of 45° against the evaporator. Such a mounting of a microbalance was forced by the geometry of the preparation chamber and the distribution of the flanges in the chamber. The angle of 45° between the microbalance and the evaporated titanium beam influences the evaporation rate, so the measured rate by the microbalance must be multiplied by the tooling factor of ~ 1.41.

- ionization and pirani gauge to monitor the pressure in the chamber.

- pumps: roughing pump, turbomolecular pump, titanium sublimation pump (TSP)

The sample transportation between the analysis chamber and the preparation chamber is carried out by the magnetic transfer rod presented in Fig. 3.14. It is also possible to rotate the sample on the transfer rod. This feature enables to position the sample at different angles against the ion gun what is crucial for sputtering and the ion beam mixing experiments.

The manipulator enables the sample transportation between the analysis and the preparation chamber. The manipulator is equipped with a sample head compatible with the sample plates used in SCIENTA system. It also contains a heating system for indirect heating and a chromel-alumel thermocouple embedded in the sample head to control the temperature.

The ion current in SPECS system was measured in the configuration from Fig. 3.9. The ion current depends strongly on the argon pressure and the chosen ion energy like presented in Fig. 3.15. The area of the ion bombarded spot was fixed and equal to $1cm^2$, so it is possible to calculate the ion dose as previously described in the section about the SCIENTA system. The ion dose was needed for the IBM of the Ti/SiO_2/Si experiments described in the experimental part of this thesis.

Depth profiling in SPECS Lab

The main purpose of the experiments in SPECS Lab was to investigate the mixing rate of the Ti/Si bilayers, and therefore it was necessary to perform depth profiling experiments. In the depth profiling experiments the sputtering of Ti/Si samples was performed by Ar^+ bombardment 45° to the sample surface, and the kinetic energy of ions was 3.0keV. The area of the ion bombarded spot was fixed and equal to $1cm^2$. After each sputtering step the sample surface was studied with XPS. It was needed to perform about 40 sputtering steps in order to completely remove the mixture of Ti_xSi_y layer and to reach clean silicon. The argon pressure during the sputtering was kept constant and was equal to $2.0 \cdot 10^{-7} mbar$. The whole depth profiling experiment was computer controlled by a dedicated computer program (SpecsLab version 2.30.44), which task was to steer the sputter gun and XPS control units, and also to do the measurement data acquisition. In order to provide an efficient information flow between the computer and the control units, a small local network based on a standard TCP/IP data transmission protocol was built. Such an infrastructure made the depth profiling process fully automated: sputtering parameters

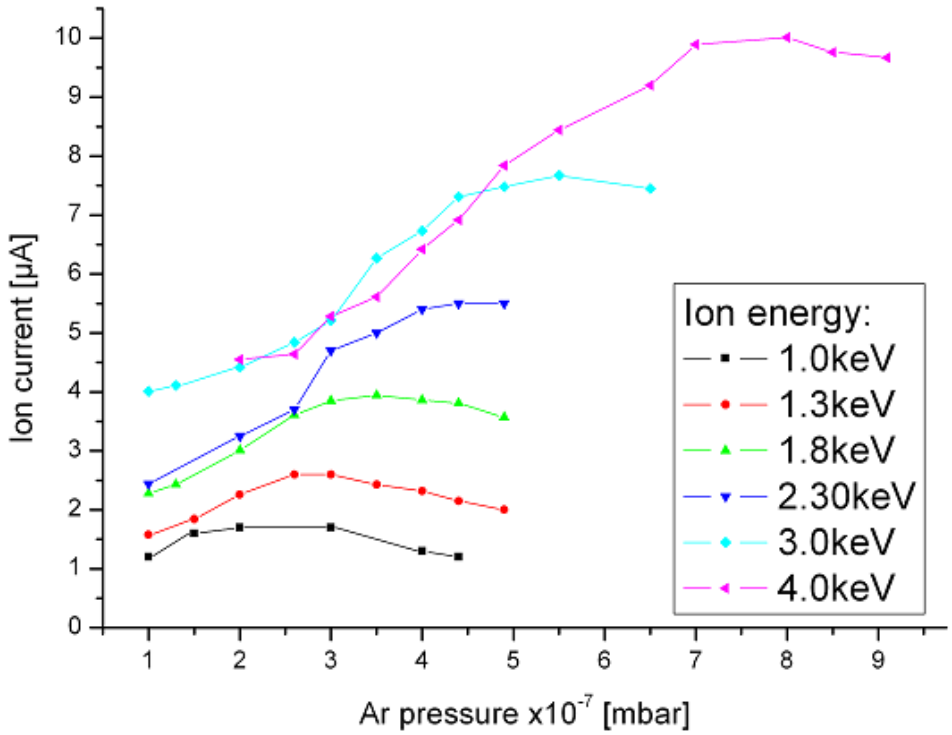

Figure 3.15: *Ion current as the function of the argon pressure, emission 10.00mA (SPECS UHV system).*

and XPS measurement parameters were set up at the beginning of the experiment and then the whole process was run automatically by the computer.

Chapter 4

Experimental results and discussion

4.1 Silicon cleaning procedure

All the silicon samples before inserting them into the vacuum were rinsed in deionized water and then dipped in alcohol and ultra-sonic cleaned. After taking the samples from the alcohol bath, the surface of the silicon was dried with the high purity pressurised air. Then the samples were inserted into the vacuum system and there degassed for 5-6h at a temperature lower than $600°C$. The heating temperature was increased slowly in steps in that way, so that the system pressure was always in low $10^{-9}mbar$ range. At the temperature of $600°C$ the native oxide layer is still preserved and protects the silicon surface from contaminants [72]. In order to remove the layer of the native silicon dioxide from the silicon, the samples were sputter-cleaned with Ar ions. The ion energy was as low as $1.0keV$ and the sputtering time was $15 - 20min$. In SCIENTA Lab the sputtering angle (the angle between the sample and the sputter gun) was 70° and in SPECS Lab the sputtering angle was 45°. According to the sputtering simulations of SiO_2/Si with the TRIM code (Fig. 4.1) the best sputtering angle is $70 - 75°$ because it gives the highest sputtering yield possible for the ion energy of 1.0keV ($Y \approx 7.5$). The ion energy was set to 1.0keV because the argon ions do not penetrate very deeply into the target material (ion range about 15Å) and do not cause any significant damage to the crystal structure.

After the sputtering process the samples were flashed to $\sim 1000°C$ for a few seconds in order to remove the shallow implanted argon and to reconstruct the crystal structure of the clean silicon. During flashing the system pressure was always in $10^{-10}mbar$ range. After flashing the cleanliness of the silicon was checked with XPS and/or LEED (in SCIENTA Lab). In case of the LEED, the Si(111)-(7x7) and the Si(100)-(2x1) reconstructions were observed. Fig. presents the LEED pattern of the Si(111)-(7x) surface after the cleaning

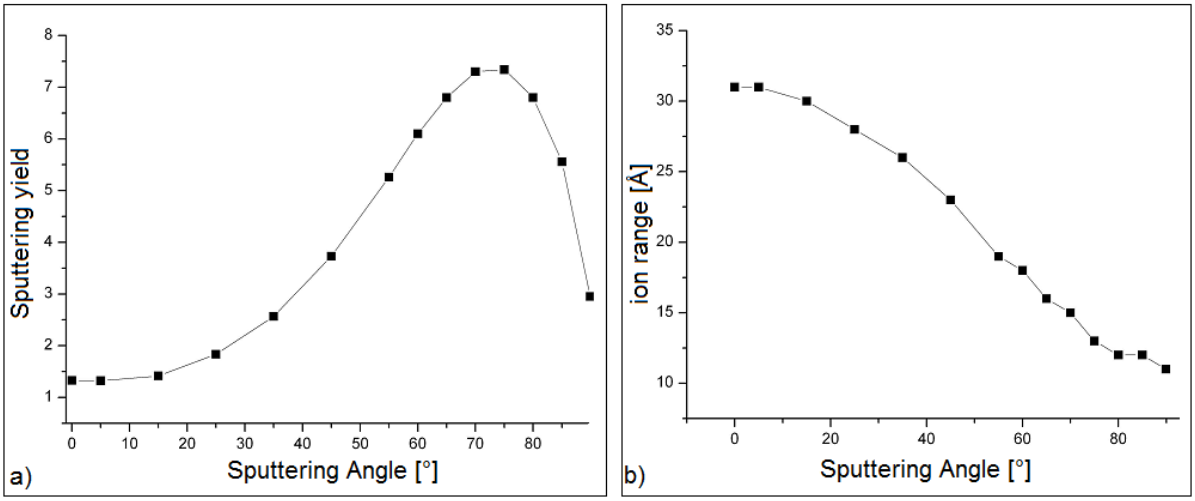

Figure 4.1: *The sputtering yield vs. the sputtering angle (a) and the Ar ion range vs. the sputtering angle (b), obtained from the TRIM code. The target material is defined as* $15Å$ *of* SiO_2 *on the* $45Å$ *of Si. The ion dose is 100000 Ar ions and the ion energy is* $1.0keV$*. The density of the* SiO_2 *is set to* $2.533g/cm^3$ *[59].*

procedure.

4.2 Ti growth on Si(111) at room temperature

Titanium was deposited in steps onto the clean Si(111)–(7x7) surface at room temperature in order to study the titanium growth and the titanium silicide formation at room temperature. After each titanium evaporation step the XPS spectra of Si 2p and Ti 2p regions were taken. The experiment was done up to two different titanium coverages:

- 8 ML of Ti - in order to investigate the titanium silicide formation at the very Ti/Si interface,
- 20ML of Ti - in order to study the titanium growth.

The results of both experiments are presented in Fig. 4.3 and Fig. 4.4.

Fig. 4.3 presents XPS spectra of the Si 2p and Ti $2p_{3/2}$ peaks taken after the indicated titanium evaporation steps. The Si 2p peak decreases in height with the increasing Ti coverage (Fig. 4.4), it does not loose its symmetry. The binding energy of the Si 2p peak does not change significantly for the Ti coverage of 1-8ML. For the Ti coverage of 10-20ML it shifts by $\sim 0.1eV$ into lower binding energies. The Ti $2p_{3/2}$ peak increases in

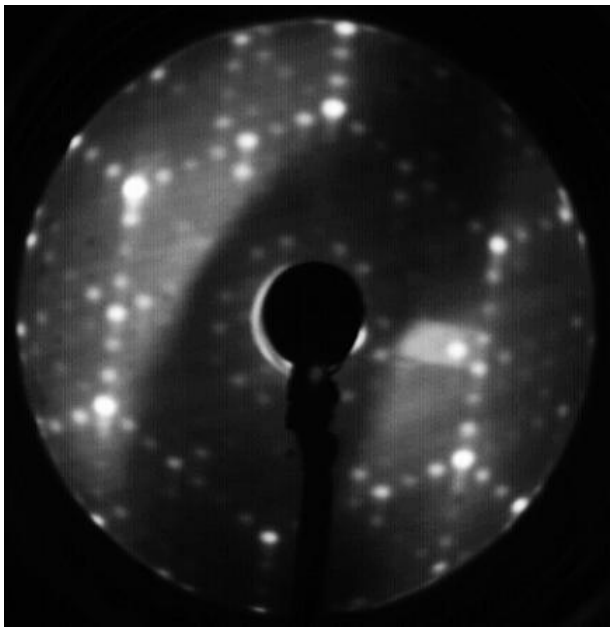

Figure 4.2: *LEED pattern of the Si(111)-(7x7) surface (E=60eV).*

height with the increasing Ti coverage (Fig. 4.4). With the increasing Ti coverage the Ti $2p_{3/2}$ shifts by $\sim 0.1eV$ into lower binding energies.

The above mentioned properties of the Si 2p and the Ti $2p_{3/2}$ peaks during the Ti evaporation suggest, that there is no significant titanium silicide formation at room temperature. The small binding energy shifts ($\sim 0.1eV$) for the Si 2p are observed only for high titanium coverages (more than 8ML) when the Si 2p peak is low and broad, due to the lower number of detected photoelectrons. Under such conditions the energy shift of only $\sim 0.1eV$ could be considered as a statistical error. For the Ti $2p_{3/2}$ peak the energy shifts of $\sim 0.1eV$ are observed for very low Ti coverages. For the same reasons as in the case of the Si 2p, the peak shifts of Ti $2p_{3/2}$ should not be considered as a sufficient proof of a titanium silicide formation. These conclusions stay in a good agreement with the literature [15, 17, 69, 75].

For the titanium coverages up to 4ML the Ti $2p_{3/2}$ growths linearly with the titanium coverage and the Si 2p decreases in height linearly (Fig. 4.4). For higher Ti coverages both peaks show non-linear behaviour. From the literature it is known that for the low Ti coverages (up to 4ML) the titanium growths in layer-by-layer mode and then in Stranski-Krastanov mode [3]. So the change from the linear to non-linear behaviour in growth observed for Si 2p and Ti $2p_{3/2}$ peaks in Fig. 4.4 suggests the change in the growth mode from the layer-by-layer mode to Stranski-Krastanov mode.

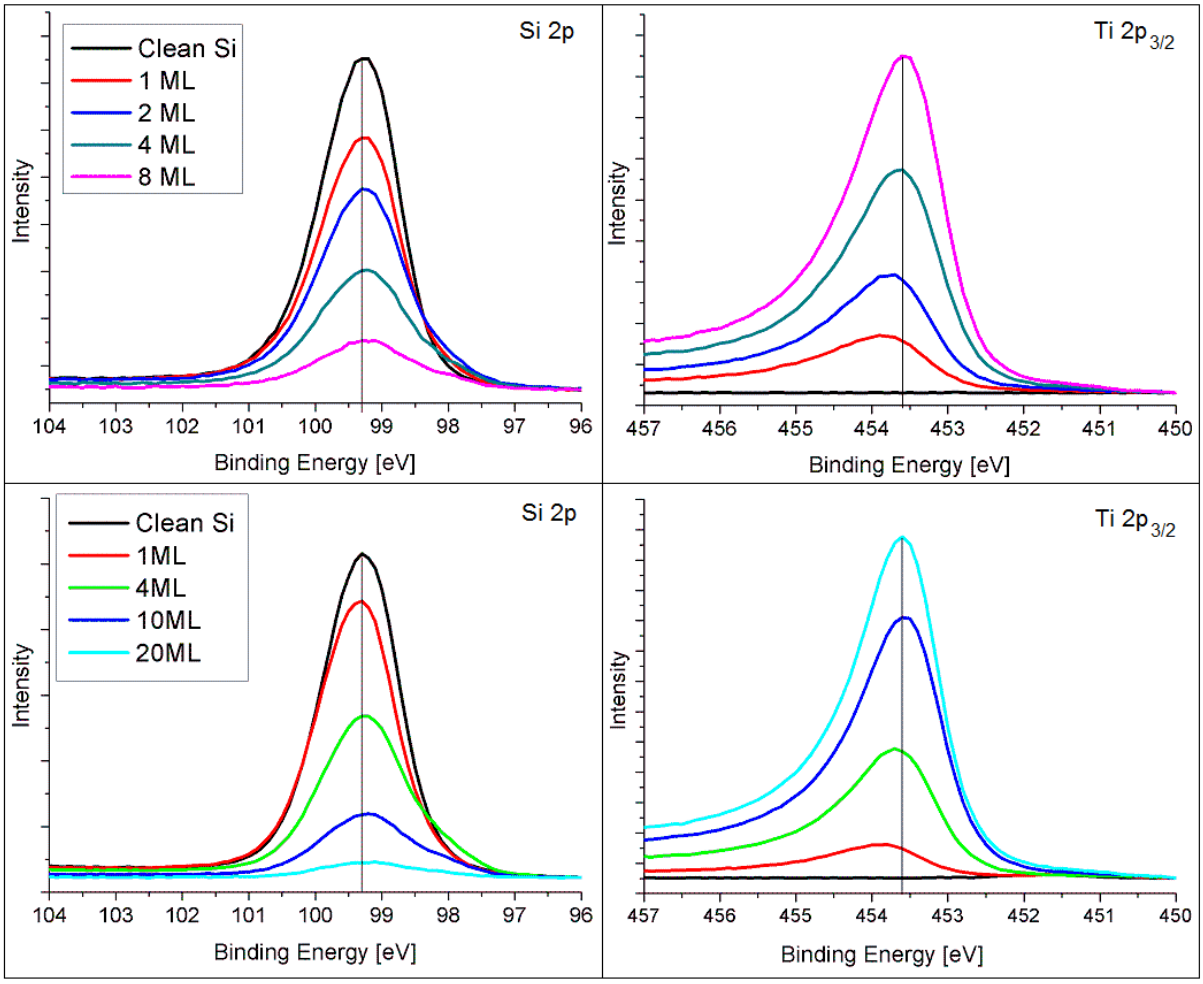

Figure 4.3: *Ti growth on Si(111) at room temperature. XPS spectra of the Si 2p and Ti $2p_{3/2}$ regions taken for different Ti coverage.*

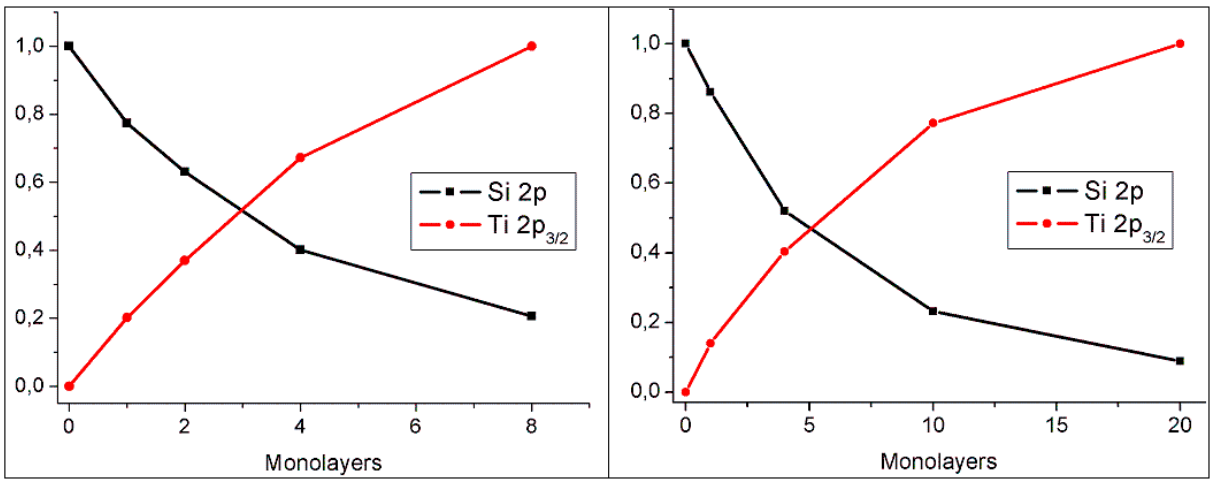

Figure 4.4: *Ti growth on Si(111) at room temperature. The XPS Si 2p and Ti $2p_{3/2}$ peak heights normalized to 1 and plotted against the Ti coverage (in monolayers).*

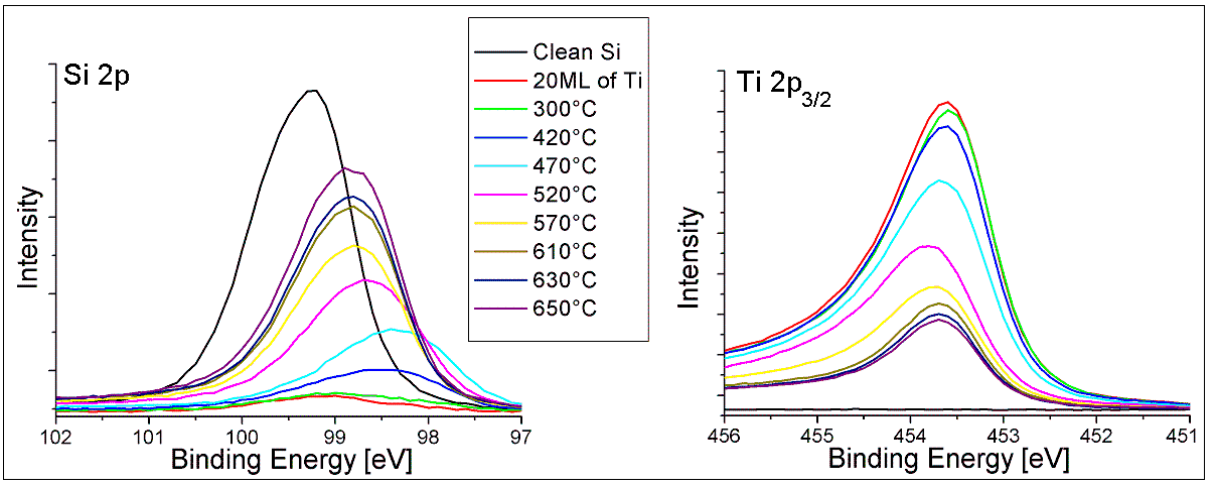

Figure 4.5: *The evolution of the Si 2p and Ti $2p_{3/2}$ XPS peaks during the thermal annealing of the Ti/Si(111) interface (Ti coverage: 20ML).*

4.3 Titanium silicide formation by thermal annealing

As it was discussed above there is no chemical reaction between the silicon and titanium at room temperature, and therefore the titanium silicide formation by thermal annealing was investigated.

4.3.1 In-situ photoemission and LEED studies on Si(111)

20 ML of Ti were deposited at room temperature onto the clean Si(111) crystal. After the titanium deposition the sample was annealed in steps and after each annealing step the XPS and UPS spectra were taken. During the heating the system pressure rose, but it was always in $10^{-9} mbar$ range. Fig. 4.5 presents the results of the XPS measurements as a function of the measured temperature.

After the evaporation of the 20 ML of Ti the silicon peak is very small and starts growing when the temperature rises and at the same time the Ti $2p_{3/2}$ decreases in size. Such a behaviour indicates the interdiffusion between the two elements.
The described experiment was repeated many times and it was observed that both peaks shift in binding energy position. The detailed analysis of the peak shifts is presented in Fig. 4.6. Fig. 4.6 presents the average peak shifts for a series of five experiments. For the temperature lower than $\sim 400°C$ the Si 2p peak shifts to the lower binding energy and reaches its minimum at $\sim 98.4eV$. For higher temperatures it shifts back to higher binding energies and stops at $\sim 99.1eV$. The Ti $2p_{3/2}$ moves almost linearly to higher

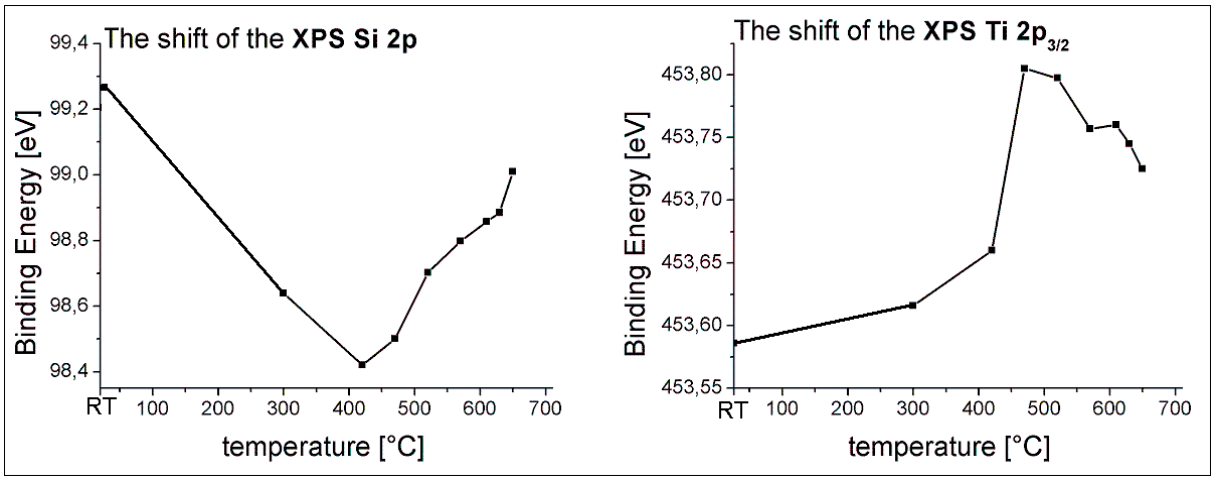

Figure 4.6: *The average XPS peak shifts of the Si 2p and Ti 2p$_{3/2}$ during the thermal annealing of the Ti/Si(111) interface (Ti coverage: 20ML).*

binding energies, when the applied temperature does not exceed $\sim 420°C$. With further annealing up to $\sim 470°C$, the peak moves very rapidly to higher binding energies and reaches its maximum at $\sim 453.8eV$. With further annealing the Ti 2p$_{3/2}$ peak shifts to lower binding energies and at $650°C$ it reaches $\sim 453.7eV$. It is important to notice that the Si 2p XPS peak shifts are much more significant than those of the Ti 2p$_{3/2}$. The maximum binding energy difference for the Si 2p peak is $0.8 - 0.9eV$ and for the Ti 2p$_{3/2}$ it's only 0.2eV. The XPS peak shifts with binding energies give the information that a new chemical state between the titanium and the silicon was formed. The detailed analysis of the titanium silicide phases is presented in the next section.

The changes in XPS peak heights (Fig. 4.5) of Ti and Si indicate that the surface atomic concentrations of the two elements change. The changes of the atomic concentrations on the surface were calculated using the XPS atomic sensitivity factors (ASF) and the XPS peak areas. The peak areas were calculated with the SCIENTA analysis software and the ASF for the Si 2p was taken as 0.27 and for the Ti 2p$_{3/2}$ as 1.2. The result is presented in Fig. 4.7 and shows how the Si to Ti concentration ratio changes with the annealing temperature. For temperatures up to $\sim 300°C$ the Si to Ti concentration rises linearly with temperature and is less than 0.25. In the temperature range $300 - 450°C$, where the formation of the TiSi is expected, the Si/Ti ratio rises to 0.5. With further annealing the Si concentration with respect to Ti rises linearly much faster and at about $570°C$ (which is the formation temperature of the C49 $TiSi_2$) reaches ~ 2. Then the Si/Ti ratio is almost constant and its value is a little more than 2, even if the temperature is

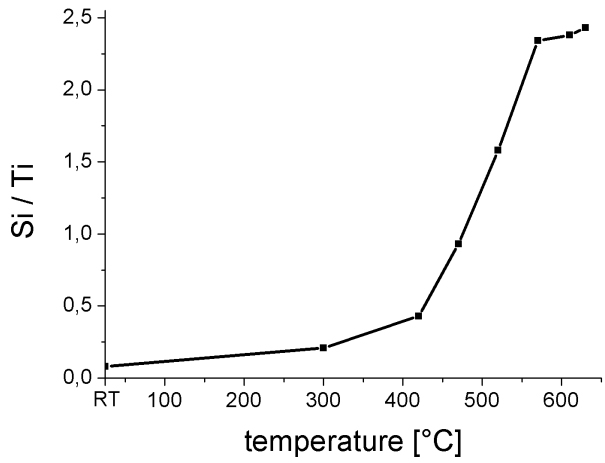

Figure 4.7: *The ratio of the XPS Si 2p to Ti $2p_{3/2}$ peaks. It was calculated using the measured XPS peak areas and the atomic sensitivity factors.*

further increased and reaches $650°C$. 2/1 is the ratio of Si to Ti in the perfect $TiSi_2$ silicide, so the results presented in Fig. 4.7 suggest that above $570°C$ the $TiSi_2$ is formed. The above presented method of estimating the atomic concentration with ASF factors is subjected to a certain error::

1. ASF factors are estimated for the pure elements (e.g. Ti or Si) and they might be different when the two elements form a compound (like it happens in case of this system).

2. There is always a calculation uncertainty in peak areas of about 10%.

During the thermal annealing of the Ti/Si(111) interface, UPS spectra were also taken and they are presented in Fig. 4.8. The last two spectra were taken in the temperature range that is high enough to form the C54 $TiSi_2$ (up to $650°C$). These spectra do not change its shape - the peaks are at the same energy position and the ratio between them does not change. So it means that the C54 phase was formed and it does not transform into any other silicide phase.

The titanium silicide formation during the thermal annealing was also studied by the means of the LEED. After the cleaning of the Si(111) the LEED pattern of the Si(111)-(7x7) was observed. After the room temperature titanium deposition the pattern disappeared. After each annealing step the sample was examined with LEED, but no diffraction pattern was observed. So it means that no ordered titanium silicides are formed

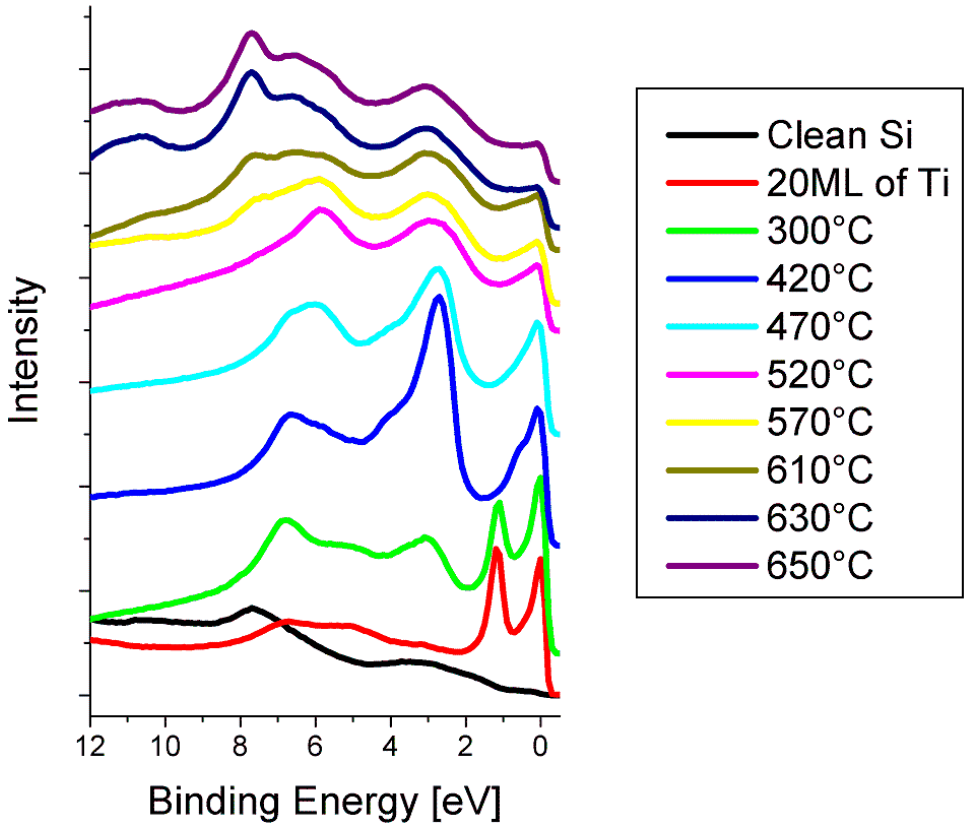

Figure 4.8: *UPS spectra of the thermally annealed Ti/Si(111) interface (Ti coverage: 20ML)*

on Si(111) by thermal annealing when they are heated up to $700°C$. This conclusion was already mentioned in the literature [42].

4.3.2 In-situ photoemission and LEED studies on Si(100)

Titanium silicide formation by thermal annealing was studied on the Ti/Si(100) interface by means of XPS, UPS and LEED. The Si(100) was cleaned and 20ML of titanium were deposited onto it at room temperature. Then the sample was thermally annealed by increasing the temperature in steps and between the annealing steps the XPS, UPS and LEED measurements were performed. The system pressure during the thermal annealing increased but always stayed in $10^{-9} mbar$ range.

Fig. 4.9 presents the experimental results of the XPS measurements. The silicon is completely covered with 20ML of Ti and when the temperature rises, it starts diffusing to the sample surface (Si 2p peak increases its height). At the same time the Ti $2p_{3/2}$ decreases in height. Such changes in concentration of these two elements on the sample surface prove there is an intensive intermixing of Si and Ti induced by the temperature. The

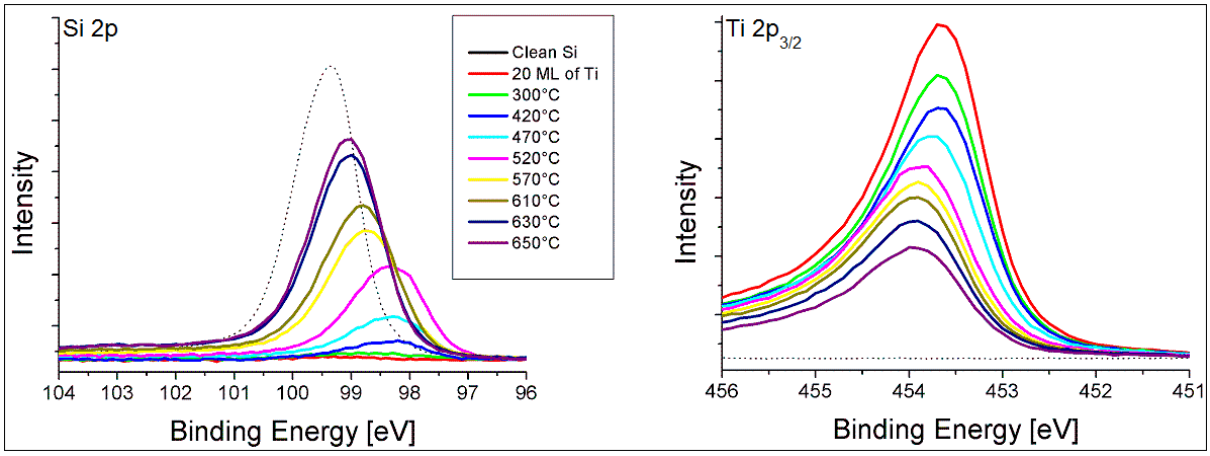

Figure 4.9: *The evolution of the Si 2p and Ti 2p$_{3/2}$ XPS peaks during the thermal annealing of the Ti/Si(100) interface (Ti coverage: 20ML).*

changes in atomic concentration on the sample surface were estimated using the XPS ASF factors of Si and Ti and the area of both peaks and are presented in Fig. 4.10. At low temperatures (room temperature to 300°C) the change in Si/Ti ratio is very small (very small diffusion). But when the temperature is increased to 470°C the concentration changes linearly and faster, and for higher temperatures it changes significantly fast also in a linear way. In the temperature range $600 - 650°C$ the atomic concentration ratio between the Si and Ti is very much like 2. It shows that $TiSi_2$ was formed and the measured temperature suggests that it could be the C54 crystal phase. In this temperature range the concentration ratio does not change so abruptly, because the C54 $TiSi_2$ is the final crystal phase and it does not nucleate into any other phase, so the Ti/Si ratio is almost constant.

The shape of the plot presented in Fig. 4.10 for Si(100) is very similar to that presented in Fig. 4.7 for Si(111). It means that the intermixing between Si and Ti during the thermal annealing does not depend significantly on the silicon surface orientation. For both silicon surfaces the intermixing is very low for $< 300°C$ where only metal reach titanium silicide formation is expected. For the $300°C < T < 470°C$ the intermixing speeds up and the TiSi is expected to be formed. If the temperature is above 600°C the Si/Ti ratio stabilizes at ~ 2 and slows down significantly. It suggests that $TiSi_2$ is formed and it does not change its phase any more.

The XPS peak shifts were studied in details and the analysis is presented in Fig. 4.11. When the temperature is increased from room temperature to about 470°C the XPS Si 2p peak moves by $\sim 1.0eV$ in binding energy to lower energies. For $\sim 470°C$ it reaches its

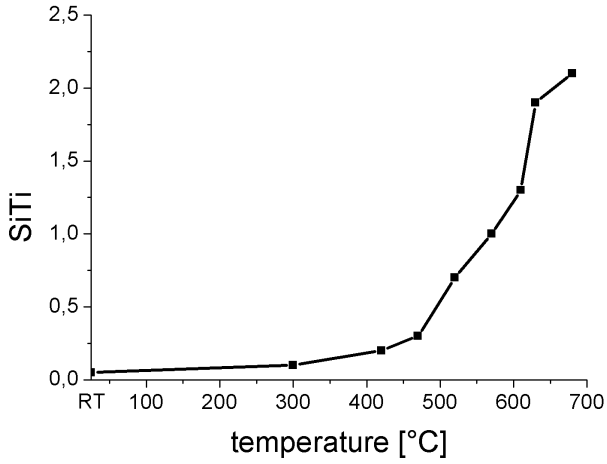

Figure 4.10: *The ratio of the Si to Ti concentration during the thermal annealing of the Ti/Si(100) interface. The atomic concentration ratio was calculated using the measured XPS peak areas and the atomic sensitivity factors.*

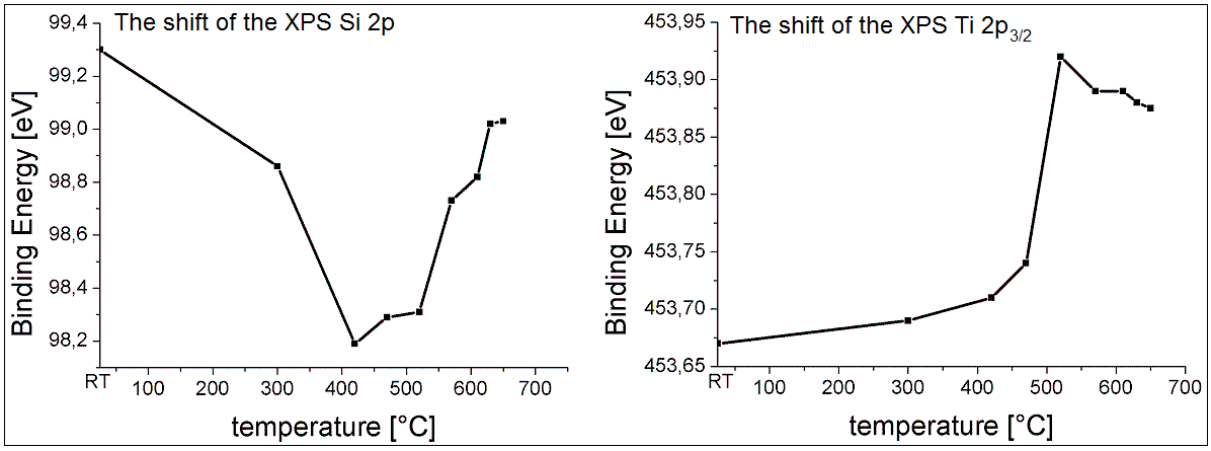

Figure 4.11: *The XPS peak shifts of the Si 2p and Ti $2p_{3/2}$ during the thermal annealing of the Ti/Si(100) interface (Ti coverage: 20ML). RT stands for 'room temperature'.*

minimum and with further annealing it shifts back to higher binding energies and stops at $\sim 99.1eV$. The Ti $2p_{3/2}$ shifts to higher binding energies until the temperature reaches $510°C$ (maximum energy shift). Then the Ti $2p_{3/2}$ peak moves to lower binding energies and stops at $\sim 453.8eV$ when the temperature reaches $650°C$.

The XPS peak shifts observed for the thermally annealed Ti/Si(100) (Fig. 4.11) are very comparable to those observed for the Ti/Si(111) system (Fig. 4.6). So they are not significantly dependent on the silicon surface orientation. The shifts in binding energy of the XPS peaks are due to the change in chemical environment of the studied elements.

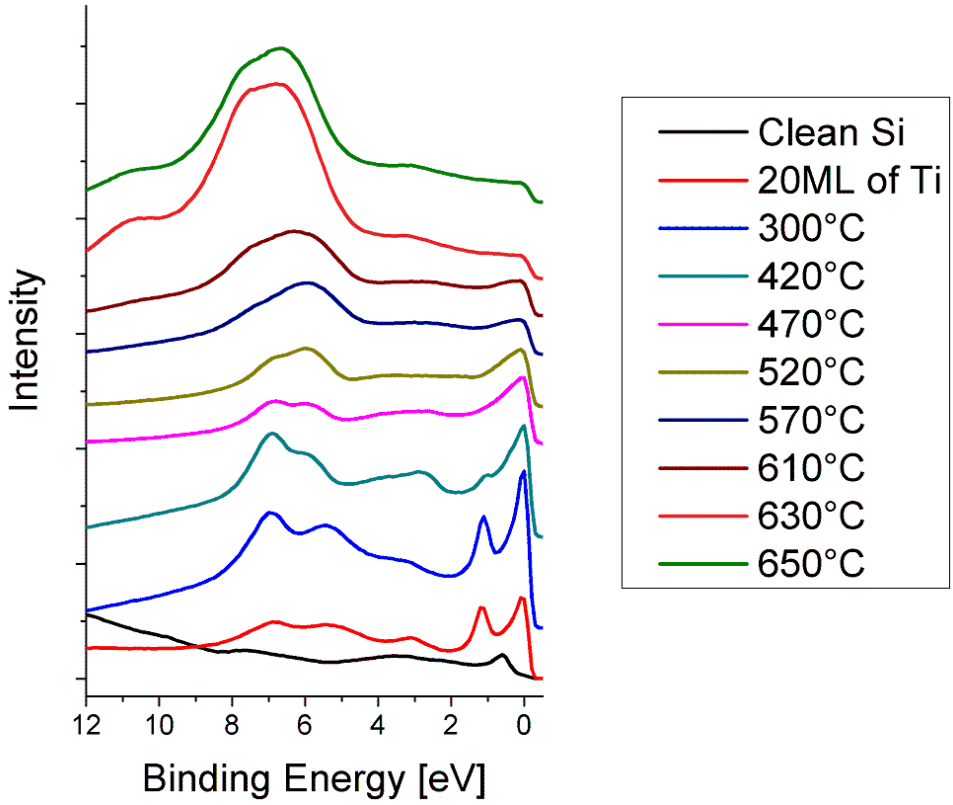

Figure 4.12: *UPS spectra of the thermally annealed Ti/Si(100) interface (Ti coverage: 20ML)*

Ti and Si form silicides that change from Ti_xSi_y to TiSi and finally into $TiSi_2$, which is observed by the XPS peak shifts in binding energy. The detailed analysis of the XPS peak binding energy position with respect to the titanium silicide phase is presented in the next section.

The annealing process of the Ti/Si(100) was also studied with UPS and the results are presented in Fig. 4.12. It shows the evolution of the valence band of the formed materials. The last two spectra measured for the temperatures higher than $600°C$ are expected to be $TiSi_2$.

LEED was used to study the structure and orientation of the formed titanium silicides. The clean Si(100) covered with 20ML of Ti did not give a diffraction pattern. After each annealing step of the Ti/Si(100) the sample was studied with LEED, but no diffraction pattern was observed. It leads to the conclusion that the titanium silicides formed by thermal annealing on Si(100) are disordered in the temperature range up to $\sim 650°C$.

4.4 Titanium silicide phase identification

The previous investigations of the thermally annealed Ti/Si interface have shown that the heating induces the intermixing of the Si and Ti and also supports the silicide formation. It would be very useful to assign the XPS peak position to the respective titanium silicide phase. In order to identify the phase of the formed titanium silicides, the GIXRD technique was used.

GIXRD is the technique in which the X-rays penetrate much deeper into the bulk of the crystal than in case of UPS or XPS. As it is a less surface sensitive technique, it was necessary to prepare samples covered with much thicker Ti layers. So 90.5ML of Ti were deposited at room temperature onto clean Si(100) crystal. Then the sample was annealed for 20min at $700°C$. The system pressure during the annealing process was monitored and it was always in $10^{-9}mbar$ range. The temperature of $700°C$ is sufficient to allow the C54 $TiSi_2$ formation. And it was experimentally checked that the annealing time of 20min is long enough to allow the diffusion of Si through the thick Ti layer to the sample surface (Si/Ti ratio on the surface is 2/1, Fig. 4.13).

It is very important that the whole volume of the deposited titanium reacts with the silicon, so the bulk and the surface of the sample are homogeneous. The titanium layer of 90.5ML thickness corresponds to $\sim$ 271Å. The XPS penetrates the sample up to 20Å and UPS only up to $\sim$ 6Å, but the XRD gets into the bulk as far as $\sim$ 100Å. So if the annealing time was relatively short, the silicon would react with the titanium near the buried Ti/Si interface only. In this case the XRD would show the titanium silicides formed in the bulk near the interface region, but it would be no use to study the sample with XPS and UPS, because the surface would differ significantly from the bulk.

After the annealing the chemical composition of the sample surface was studied with XPS (Fig. 4.14) and the valence band was studied by the means of UPS (Fig. 4.15). Then the sample was taken out from the vacuum chamber and transported to Siemens Labs in Munich (Germany) were the GIXRD measurement was done (Fig. 4.16).

Fig. 4.13 presents the XPS survey spectra right after the annealing process. Although the system pressure during the heating process was low (in $10^{-9}mbar$ range) there is a low carbon contamination visible (C 1s peak on the spectra), and also a small amount of oxygen was found on the surface (O 1s peak). The Si to Ti ratio was estimated using the XPS ASF factors and the Si 2p and Ti $2p_{3/2}$ peak areas obtained by the computer analysis of the detailed spectra of these two peaks (Fig. 4.14). The Si/Ti ratio turned out to be 1.96, which is almost exactly the atomic concentration ratio in $TiSi_2$.

Fig. 4.14 shows the detailed XPS spectra of the Si 2p and the Ti $2p_{3/2}$ taken immediately

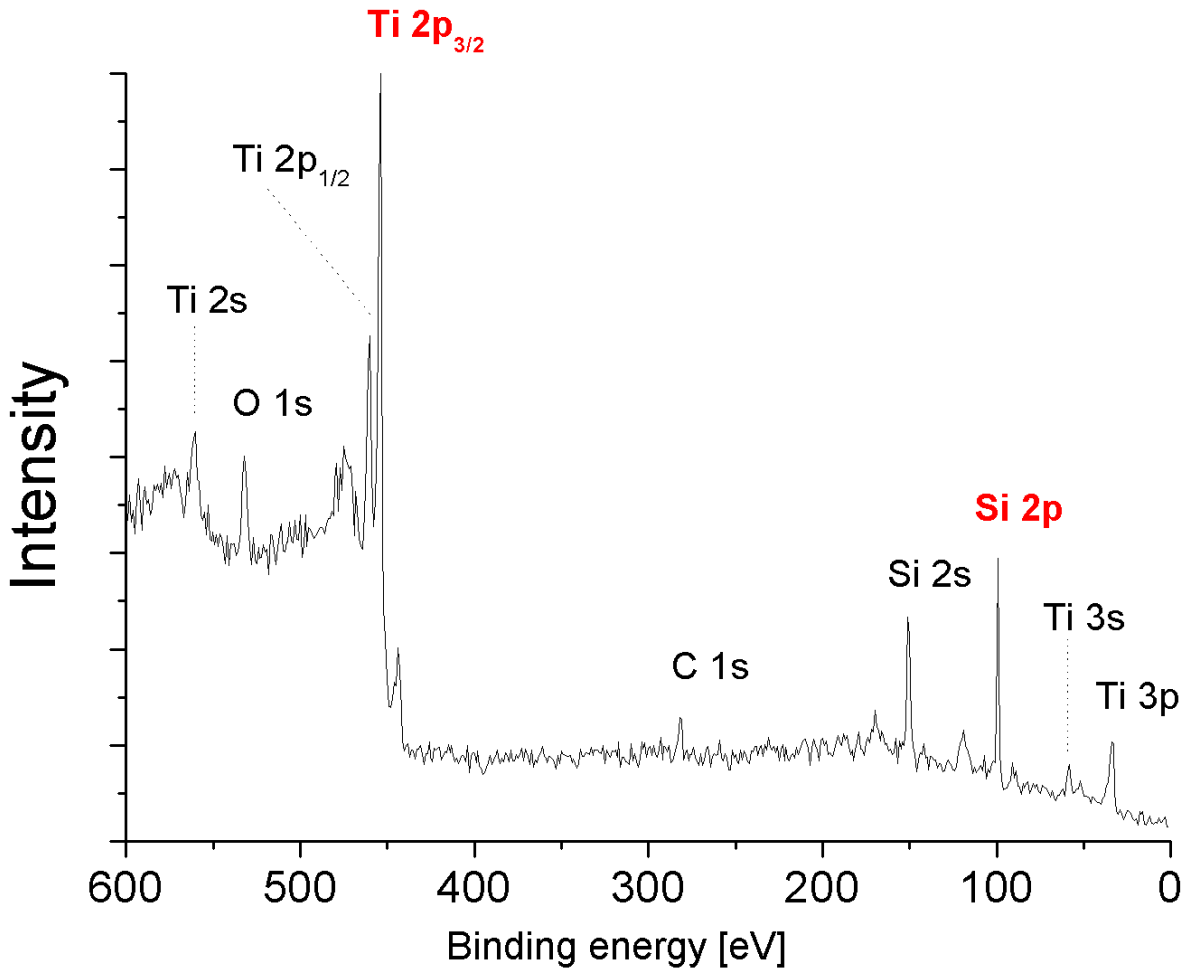

Figure 4.13: *XPS survey spectra of the annealed Ti/Si(100) sample. Annealing temp. 700°C, annealing time: 20min, Ti coverage: 90.5ML. The Si/Ti atomic concentration ratio is 1.96.*

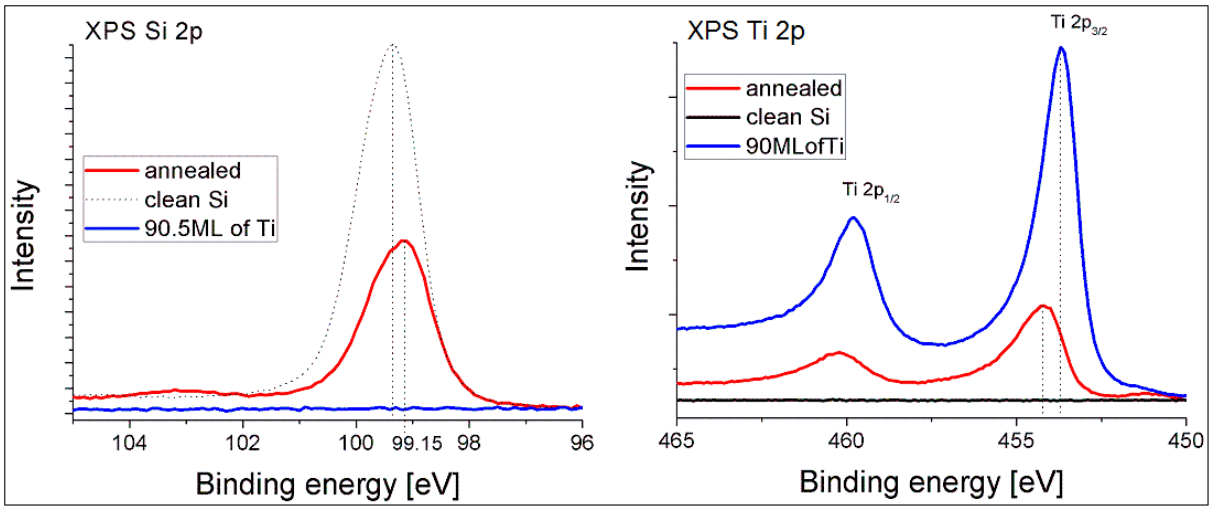

Figure 4.14: *XPS Si 2p and Ti 2p spectra of the annealed Ti/Si(100) sample. Annealing temp. 700°C, annealing time: 20min, Ti coverage: 90.5ML*

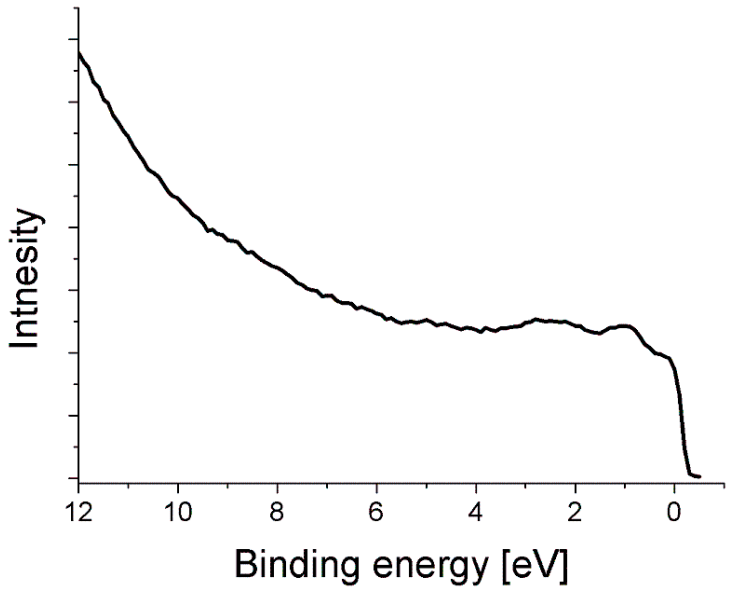

Figure 4.15: *UPS spectra of the annealed Ti/Si(100) sample. Annealing temp.* $700°C$*, annealing time: 20min, Ti coverage: 90.5ML*

after the thermal annealing process. The Si 2p binding energy position is 99.15eV, which means it is shifted by $\sim 0.15eV$ to lower binding energies with respect to the pure silicon. The peak is symmetric and its shape is very comparable to the shape of a pure Si 2p peak. At the binding energy of $\sim 103eV$ a very small peak is visible, what indicates that the silicon is a little oxidized by the oxygen that contaminates the surface (see Fig. 4.13). The 'annealed' Ti 2p consists of the two spin orbit split doublets which do not differ in shape (distance in binding energy between doublets, height ratio of the two doublets) from the pure Ti 2p. But the whole Ti 2p is shifted in binding energy by $\sim 0.3eV$ with respect to the pure Ti 2p to higher binding energy.
The XPS peak shifts of Si 2p and Ti $2p_{3/2}$ are comparable to the peak shifts observed during the thermal annealing experiments with the lower (20ML) titanium coverage.

The UPS spectrum of the annealed sample is presented in Fig. 4.15. The spectrum is very featureless and differs significantly from the UPS spectra obtained from the previous experiments with the low (20ML) titanium coverage. It is so, because during the intermixing of the Ti and Si, the material looses its surface orientation features. The surface orientation features are not lost in case of the low Ti coverages.

Fig. 4.16 presents the results of the GIXRD measurement of the studied sample. The sample had to be transported to the Siemens Labs in Munich and therefore it had been exposed to the atmosphere for about one week, before it was investigated by GIXRD. It

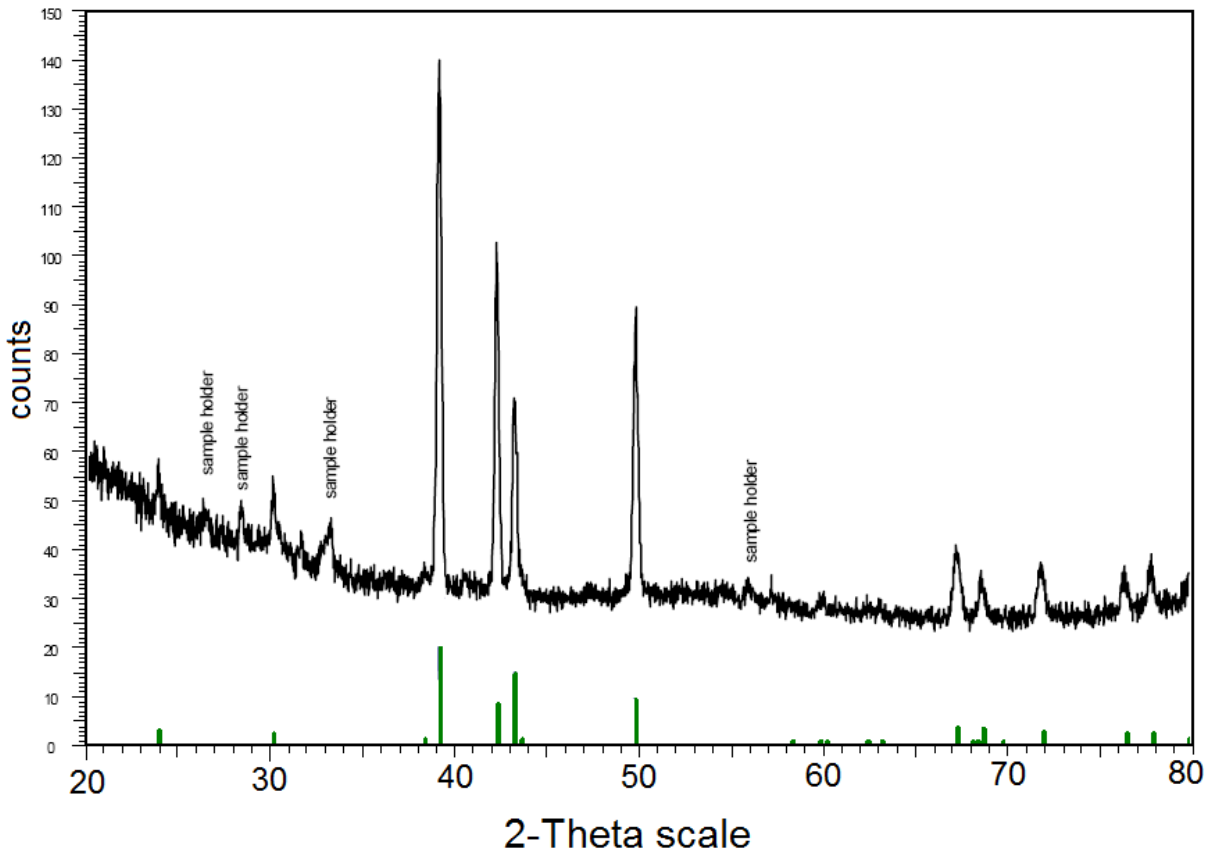

Figure 4.16: *GIXRD spectra of the annealed Ti/Si(100) sample. Annealing temp.* 700°*C, annealing time: 20min, Ti coverage: 90.5ML*

is unclear what the influence of the atmosphere on the sample was. The surface of the sample must have been contaminated with carbon and the oxygen must have oxidised the silicon and TiO_2 maybe formed at the surface. Fortunately the GIXRD penetrates deeply into the bulk, so that the surface signal is only a fraction of the detected signal. That is why the exposure to the atmosphere should not have a significant influence on the detection of the titanium silicide phase. The sample, after it had arrived to Siemens Labs, was not cleaned, nor modified in any way. It was only inserted into the GIXRD system and studied with GIXRD. The result of the measurement (Fig. 4.16) shows that the C54 $TiSi_2$ is identified as the dominant phase. The peaks which are the reflections from the C54 $TiSi_2$ are marked with the green lines at the bottom. The green lines represent the reference peaks heights and positions for the C54 phase and they were taken from the computer data base, so that the identification of the GIXRD peaks is possible. Other peaks in the spectra were identified as the reflections from the sample holder and they do not origin from the sample itself. No presence of other titanium silicide phases was detected. Probably they exist in such low amounts that the detection was not possible

(it was impossible to distinguish the corresponding peaks from the background noise).

It was also interesting to repeat the experiment described above, but with lower annealing temperatures, and detect with GIXRD also the C49 $TiSi_2$ phase. Such experiments were performed according to the following procedure: Si(100) was cleaned and 90.5ML of Ti were deposited at room temperature, the sample was annealed at $550°C$, because the formation of the C49 phase was intended. The experiment did not succeed, because it was not possible to obtain the 2:1 Si to Ti ratio on the surface (according to the XPS measurements). The experiment was repeated many times and the annealing time was prolonged up to 2 hours, but the results were not successful. The explanation of this phenomenon is based on the diffusion theory. As it is known from the literature, that silicon is the main diffusive species in the Ti/Si system [64]. The silicon crystal may be considered as an infinite source of atoms, because it is much thicker than the titanium layer. So in this case the Fick's First Law of diffusion (Eq. 2.8) may be applied to describe the diffusion process. The diffusion flux is reciprocally proportional to the thickness of the diffusion path, so the thicker the layer the lower the diffusion flux. For the Ti coverage of 20ML, the Ti thickness is so low that the diffusion is possible even low low temperatures. For the temperatures as high as $\sim 650°C$ the temperature is high enough to support the diffusion of the silicon through the thick 90.5ML. But at the temperature of $\sim 550°C$ the diffusion coefficient is not high enough to support the diffusion through 90.5ML of Ti.

Since was proven with GIXRD that the C54 $TiSi_2$ was formed, so it is possible to assign the XPS Si 2p peak position to the appropriate titanium silicide phase, and use this result as a reference for next investigations. For this reason only the Si 2p peaks will be analysed and Ti $2p_{3/2}$ will be skipped, because its shifts are much less pronounced. It has been shown in the literature [38] that the Si 2p in titanium silicide can be fitted using doublets, which represent the spin orbit split Si $2p_{1/2}$ and Si $2p_{3/2}$ states. Each doublet should have the same parameters (peak height ratio, binding energy difference) as the pure Si 2p doublet. According to the literature [31] the pure Si 2p doublet consists of two peaks separated from each other by 0.6eV in binding energy and the height ratio between them is $\frac{Si2p_{1/2}}{Si2p_{3/2}} = \frac{1}{2}$. So the titanium silicide Si 2p peak should be successfully fitted with the discussed doublet that differs only in binding energy position. The energy of 99.12eV should be assigned to the C54 $TiSi_2$, 98.80eV to the metastable C49 $TiSi_2$ and 98.54eV to the TiSi [38]. The binding energy difference between the C49 and C54 crystal phases is $\sim 0.3eV$.

Fig. 4.17 shows the fitted Si 2p peak of the previously identified (GIXRD) C54 $TiSi_2$. The

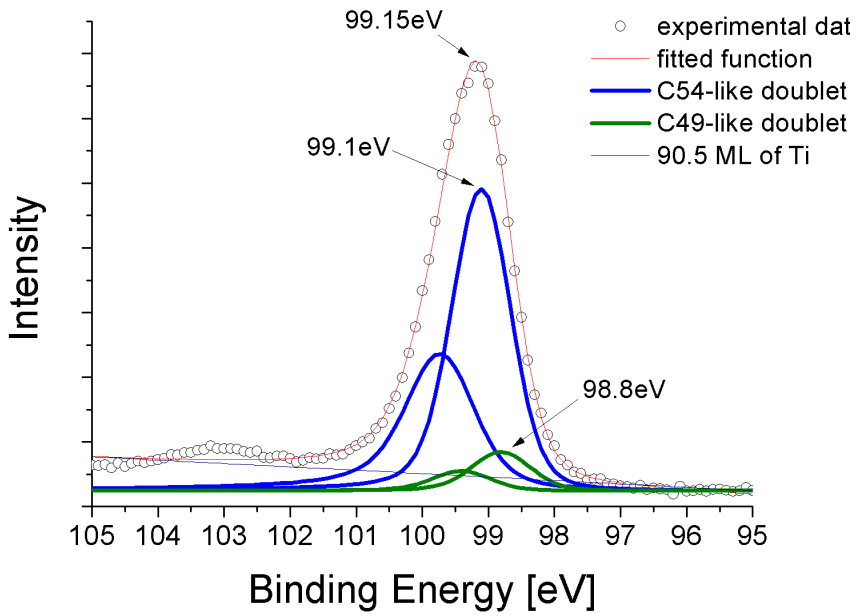

Figure 4.17: *Fitted XPS Si 2p spectra of the annealed Ti/Si(100) sample (annealing temp. 700°C, annealing time: 20min, Ti coverage: 90.5ML). Si 2p fitted with two doublets that correspond to the different titanium disilicide phases: 99.1eV - C54 $TiSi_2$, 98.80eV - C49 $TiSi_2$.*

fitting was done using the fitXPS 2.12 computer program [2]. On the measured spectra (open circles in the Fig. 4.17) the Si 2p is positioned at 99.15eV binding energy. The peak was fitted with two doublets that differ in binding energy, which proves the co-existence of two components: the doublet at 99.1eV correspond to the C54 $TiSi_2$ and the doublet at 98.80eV corresponds to the C49 $TiSi_2$. It was not possible to fit the Si 2p peak with more doublets. The peak height of the C49 component is significantly lower than the height of the C54. So the investigated sample consists of a mixture of $TiSi_2$ silicides, but the C54 phase is dominant. These conclusions from the Si 2p fitting agree with the theory [39, 46](it is expected to form C54 $TiSi_2$ by thermal annealing at $\sim 650°C$) and the GIXRD measurement (C54 was identified, other phases [if exist] are the minority).

4.4.1 Detailed titanium silicide phase analysis

It was shown that the XPS peak positions may be assigned to respective titanium silicide phases, and that the peak height of the fitted doublets corresponds to the amount of its compound. With this knowledge a detailed phase analysis of the XPS peaks of the thermally annealed samples (Ti coverage of 20ML) was done. Let's analyse the titanium silicide phase transformations of the thermally annealed Ti/Si(111) interface according

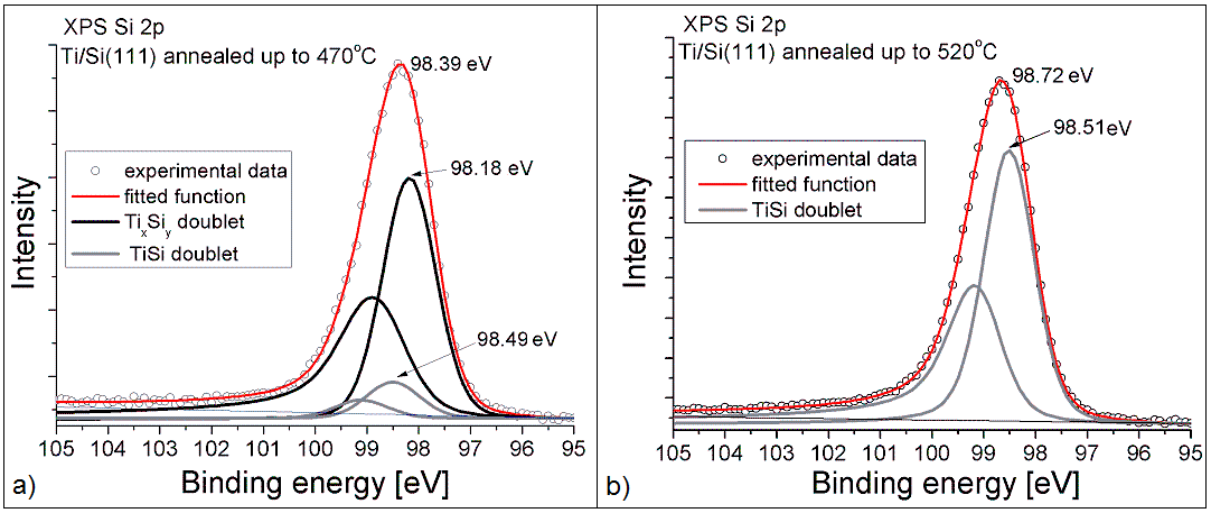

Figure 4.18: *The fitted Si 2p XPS spectra of the thermally annealed Si/Ti(111) sample at lower temperatures (up to* $\sim 520°C$*).*

to the XPS measurements (Fig. 4.5). Fig. 4.18 presents the XPS fitting results of the Si 2p peak measured after annealing the Ti/Si(111) interface at low temperatures (up to $520°C$). The Si 2p peak measured on the sample surface annealed at $470°C$ (Fig. 4.18a) is at 98.39eV, and it could be fitted with two doublets. This is the Si 2p peak that is the most shifted one to the lower binding energy during the whole annealing process. The small doublet with the $2p_{3/2}$ peak at 98.49eV corresponds to the TiSi silicide. The second doublet is significantly bigger in height and it is positioned at 98.18eV, so this peak should be assigned to a mixture of metal-rich titanium silicides (Ti_xSi_y). Thus, after annealing the sample up to $470°C$ there is a mixture of titanium silicides at its surface, the metal-rich silicides are dominant and the TiSi phase starts to be formed. When the sample was further annealed to $520°C$ (Fig. 4.18b) the Si 2p peak moved to higher binding energies and its maximum intensity is at 98.72eV. This peak shift indicates a significant phase transition that can be investigated by the XPS fitting. The Fig. 4.18b shows the fitted Si 2p with one doublet. The position of the higher peak in the doublet is 98.51eV, which is the binding energy position of TiSi. The attempts of fitting more doublets into the Si 2p did not succeed, which indicates that the sample is very homogeneous at this stage and consists mainly of TiSi silicide.

The presented data analysis agrees well with the theoretical predictions [15, 69, 75, 17, 14]: at $470°C$ the sample consists mainly of metal-rich silicides with a little amount of TiSi, at $520°C$ the metal rich silicides are fully transformed into the metastable TiSi phase, which is the major phase.

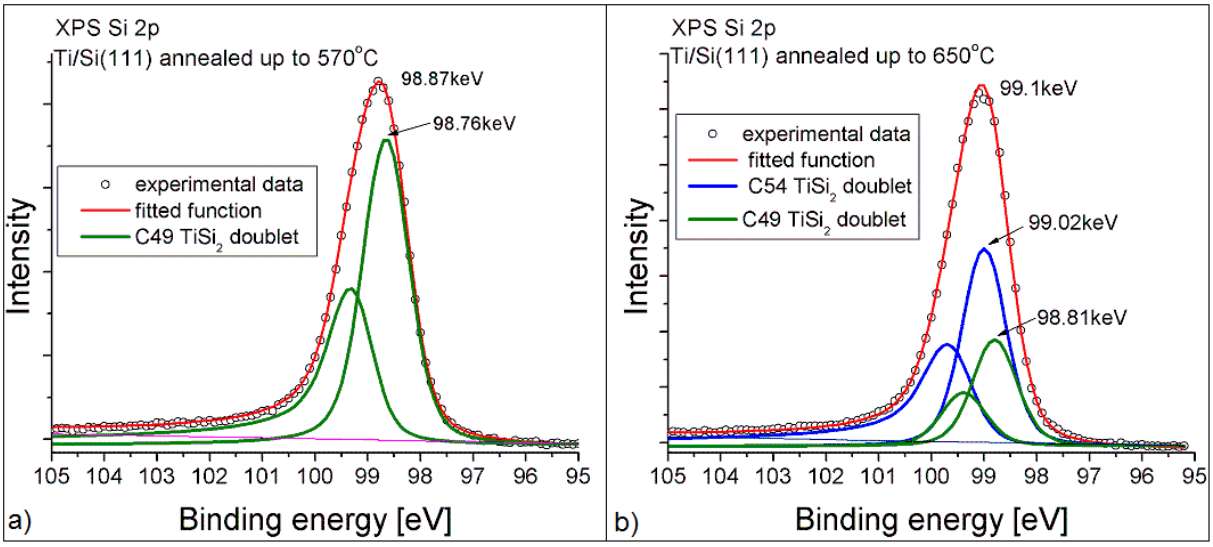

Figure 4.19: *The fitted Si 2p XPS spectra of the thermally annealed Si/Ti(111) sample at high temperatures (570°C and 650°C).*

The phase analysis of the Ti/Si(111) interface at high temperatures was also done. Fig. 4.19 presents the fitting results of the XPS Si 2p peak measured when the Ti/Si(111) sample was annealed up to 570°C (Fig. 4.19a) and 650°C (Fig. 4.19b). Fig. 4.19a shows the Si 2p peak at 98.87eV fitted with one doublet. The binding energy of the fitted doublet is 98.76eV, so the doublet should represent the C49 $TiSi_2$. The attempts of including more doublets did not result in a good fitting, so the C49 is the only phase here. The second XPS Si 2p peak (Fig. 4.19b) was measured after heating up to 650°C, it is positioned at 99.1eV and was fitted with two doublets. The C49 $TiSi_2$ doublet (at 98.81eV) is much smaller than the second doublet at 99.02eV of binding energy. This binding energy (99.02eV) is very similar to the theoretically predicted binding energy for the C54 $TiSi_2$ (99.1eV), so the doublet should be considered as the C54 $TiSi_2$ doublet. So the sample consists of a mixture of the $TiSi_2$ silicides in two crystal phases: C49 and C54, but according to the fitted doublet heights, the C54 is the dominant phase.
The results of the phase analysis presented above are in a good agreement with the theory: at 570°C the metastable C49 $TiSi_2$ is the only phase, and when the sample is annealed up to 650°C the C49 $TiSi_2$ nucleates into the stable C54 $TiSi_2$, which becomes the dominant phase. The two phases co-exist and if only the sample were annealed for a longer time, the C49 would fully transform into the C54 phase.
The binding energy peak positions of the fitted doublets are not always exactly the same as those theoretically predicted. In case of TiSi the binding energy difference between the theoretically calculated peak position and the fitted peak position is never higher

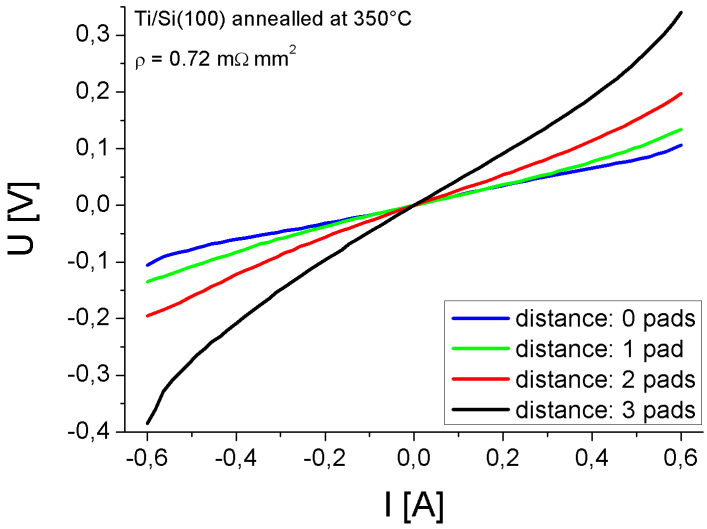

Figure 4.20: *TLM results of the Ti/Si(100) annealed to* $350°C$ *(Ti coverage: 90.5ML). The specific contact resistance of the interface is* $\rho_c = 0.72 m\Omega \cdot mm^2$.

than 0.05eV. In case of C49 $TiSi_2$ the binding energy difference between the theoretically calculated peak position and the fitted peak position is never higher than 0.04eV. In case of the C54 $TiSi_2$ this energy difference is 0.1eV. Theoretically the C49 and C54 doublets should be separated from each other by $\sim 0.3eV$ of binding energy. In the experimental data they are separated from each other by 0.21eV.

4.5 Electrical properties of the Ti/Si interface

The electrical properties of the Ti_xSi_y/Si interface formed by the thermal annealing where studied ex-situ by the means of the TLM method and the titanium silicide phase was identified by the GIXRD.

90.5ML of Ti were deposited at room temperature onto the in-situ cleaned Si(100) substrate. The sample was then annealed in vacuum for 11 min at $350°C$. It was taken out from the vacuum chamber and transported to Infineon Technologies company in Villach in order to examine the formed interface by the TLM. The Fig. 4.20 shows the results of the TLM measurements for different pads. All the characteristics are linear, what proves a good ohmic behaviour of the contact. The specific contact resistance of the interface is $\rho_c = 0.72 m\Omega \cdot mm^2$. According to the previous experiments and the titanium phase analysis of the thermally annealed Ti/Si(100) interface, the silicides formed at $350°C$ are

a mixture of the metal-rich silicides (Ti_xSi_y). TLM results (Fig. 4.20) show that Ti_xSi_y form ohmic contacts with the silicon.
One should not forget that the Ti_xSi_y is a metastable phase and that it would transform into other titanium silicide phases, if only higher temperature was applied to the sample. The silicides during the phase transformations change not only the resistivity, but also the crystal structure. So if the Ti_xSi_y layer is used as a contact material to silicon and it is also covered with other materials that form a capping layer (as it often happens in metalization layers used in microelectronics), the phase transformation could result in changing the resistivity of the interface and it could also give an additional mechanical stress to the layers that it is covered with.

The electrical properties of the $TiSi_2$/Si interface were also studied by TLM. Two samples were prepared in-situ in the following, that 90.5ML of Ti were deposited at room temperature onto the clean Si(100) crystal. Then the samples were annealed, the first one for 12min at $720°C$ and the second one for 18min also at $720°C$. The system pressure during the annealing process was monitored and it was always in $10^{-9}mbar$ range. After the annealing the samples were taken out from the vacuum chamber and sent for GIXRD and TLM measurements.

The results of the GIXRD measurements are presented in Fig. 4.21 and Fig. 4.22. According to the GIXRD measurements, the sample that was annealed for 12min (Fig. 4.21) consisted of a mixture of C49 and C54 $TiSi_2$ silicides, but the C49 phase was the dominant phase. In Fig. 4.21 the GIXRD spectrum is presented and the red lines on the spectrum correspond to the identified C49 $TiSi_2$. The green lines are at the 2Θ position of the C54 $TiSi_2$. Although the annealing temperature ($720°C$) was high enough to form the C54 phase, the annealing time was to short to transform the previously formed C49 phase fully into the C54.
The GIXRD spectra shown in Fig. 4.22 is the spectrum measured on the sample that was thermally annealed for 18min at $720°C$. The sample consists exclusively of the C54 $TiSi_2$. The green lines marked on the spectra correspond to the identified C54 phase. No other phase was detected, which means that the annealing temperature and the annealing time were sufficient enough to allow the titanium silicides to nucleate into the C54 crystal phase and the sample is homogeneous.
On both GIXRD spectra there are the peaks marked as 'sample holder'. These reflections come from the sample holder material only and they do not origin from the studied sample.

Both samples after the GIXRD measurements were studied by TLM. Fig. 4.23 presents the TLM measurements of the C49-$TiSi_2$/Si(100) interface. The V-I characteristics were

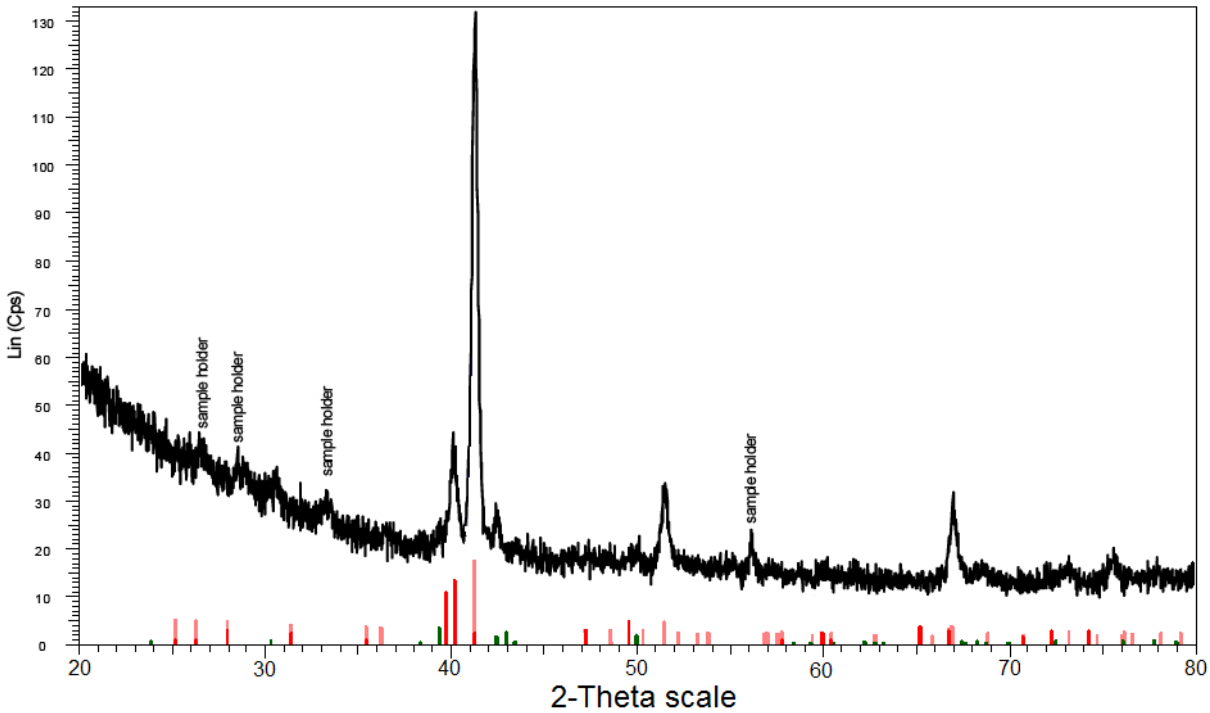

Figure 4.21: *GIXRD spectra of the annealed Ti/Si(100) sample (12min at 720°C). C49 $TiSi_2$ phase was identified as the dominant phase.*

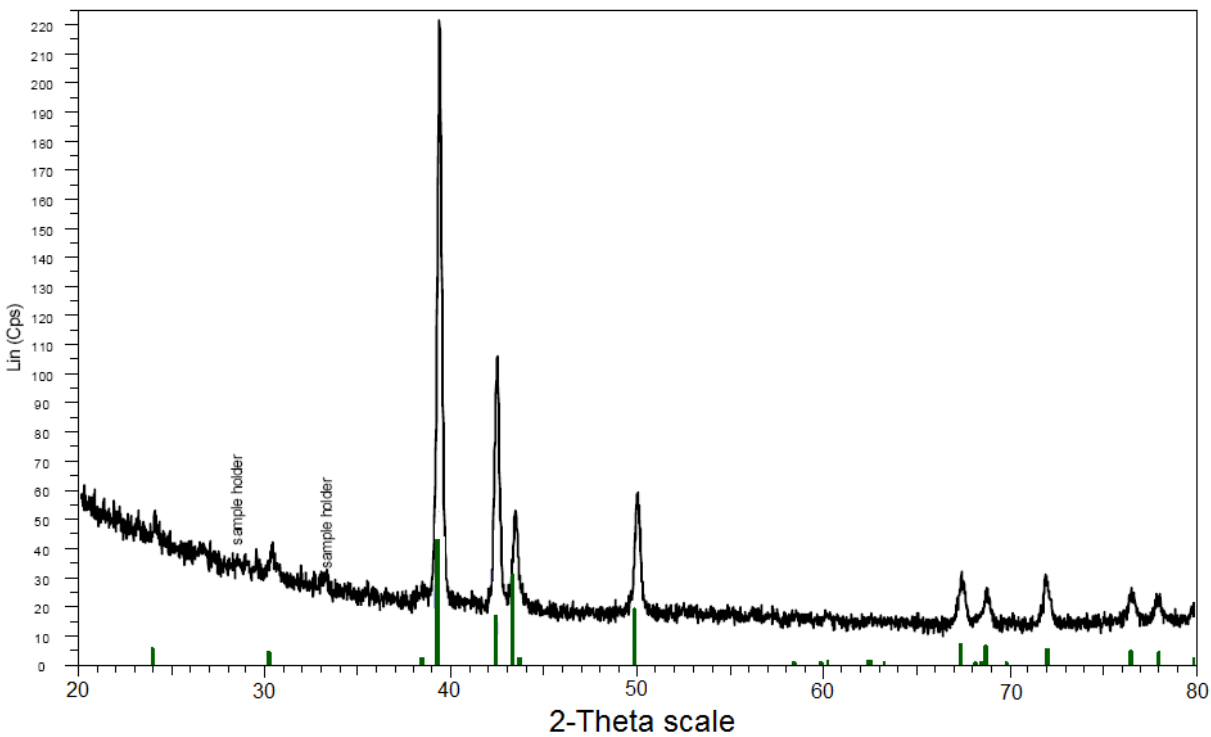

Figure 4.22: *GIXRD spectra of the annealed Ti/Si(100) sample (18min at 720°C). C54 $TiSi_2$ was identified as the dominant phase.*

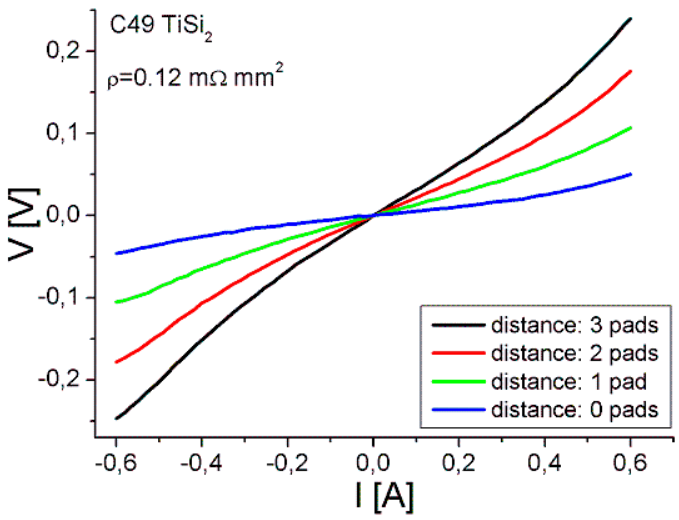

Figure 4.23: *TLM results of the C49 $TiSi_2$/Si interface prepared by thermal annealing at 720°C for 12min of the in-situ prepared 90.5ML-Ti/Si(100) interface. The GIXRD spectra of the sample is presented in Fig. 4.21. The specific contact resistance is* $\rho_c = 0.12 m\Omega \cdot mm^2$.

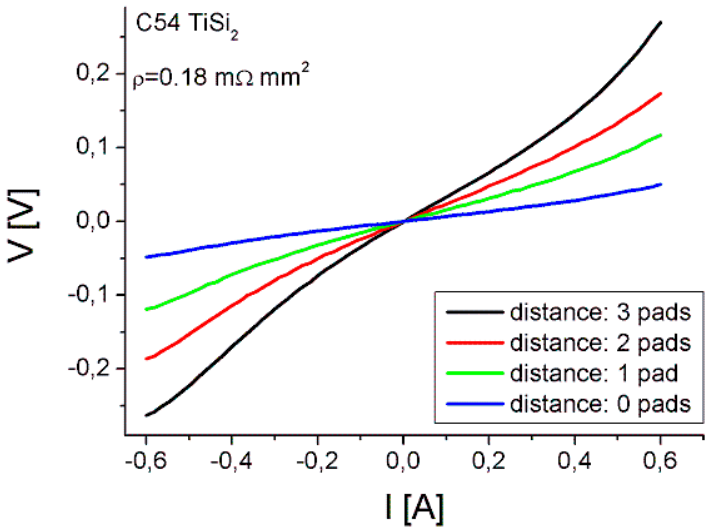

Figure 4.24: *TLM results of the C54 $TiSi_2$/Si interface prepared by thermal annealing at 720°C for 18min of the in-situ prepared 90.5ML-Ti/Si(100) interface. The GIXRD spectra of the sample is presented in Fig. 4.22. The specific contact resistance is* $\rho_c = 0.18 m\Omega \cdot mm^2$.

measured for the very neighbouring pads and for the next three pads. The contact shows a good ohmic behaviour - all characteristics are linear on the full current scale. The measured specific contact resistance is $\rho_c = 0.12 m\Omega \cdot mm^2$. Fig. 4.24 shows the measured V-I characteristics of C54–$TiSi_2$/Si(100) interface. The TLM was done for the neighbouring pads and for the three next pads. All the characteristics are linear (ohmic contact) and the obtained specific contact resistance is $\rho_c = 0.18 m\Omega \cdot mm^2$.

The TLM measurements show that the resistance of the C49 phase ($0.12 m\Omega \cdot mm^2$) is very comparable to that of the C54 phase ($0.18 m\Omega \cdot mm^2$). The difference in resistance is only $0.06\Omega \cdot mm^2$, so both values are of the same order of magnitude. The difference in the results of the TLM is rather the measurement uncertainty which could appear because of the samples treatment: they were measured ex-situ, after exposing them to the atmospheric pressure they got oxidized, before the TLM measurement they were not cleaned. Besides the sample with C49 consists of a mixture of C49 and C54 silicides, what could also change the resistance.

Summarizing thus, it was shown in these experiments that Ti_xSi_y and $TiSi_2$ silicides are low resistivity materials that form an ohmic contact to the silicon. The specific contact resistance of both $TiSi_2$ crystal phases is approximately 4-6 times lower than that of the Ti_xSi_y.

4.6 Titanium silicide formation by ion beam mixing

The previously described investigations have shown that the titanium silicides are suitable materials for low resistivity ohmic contacts. Unfortunately the formation temperature of the stable C54 $TiSi_2$ phase is as high as $\sim 650°C$, what makes the C54 formation by thermal annealing unsuitable for the back side metallization process. It would be best if there was a possibility to initiate the chemical reaction at the Ti/Si interface and to mix Ti and Si bilayers at room temperature. As it is shown in this chapter, the ion beam mixing is a method, that could give such results and could be used as a substitution to thermal annealing.

In all the IBM experiments the ion gun used was the Ar sputter gun, which limited the kinetic ion energy to 5.0keV. It is useful to consider the stopping power that slows down the Ar ions penetrating the Ti and Si layers, because the Ar ions interact with

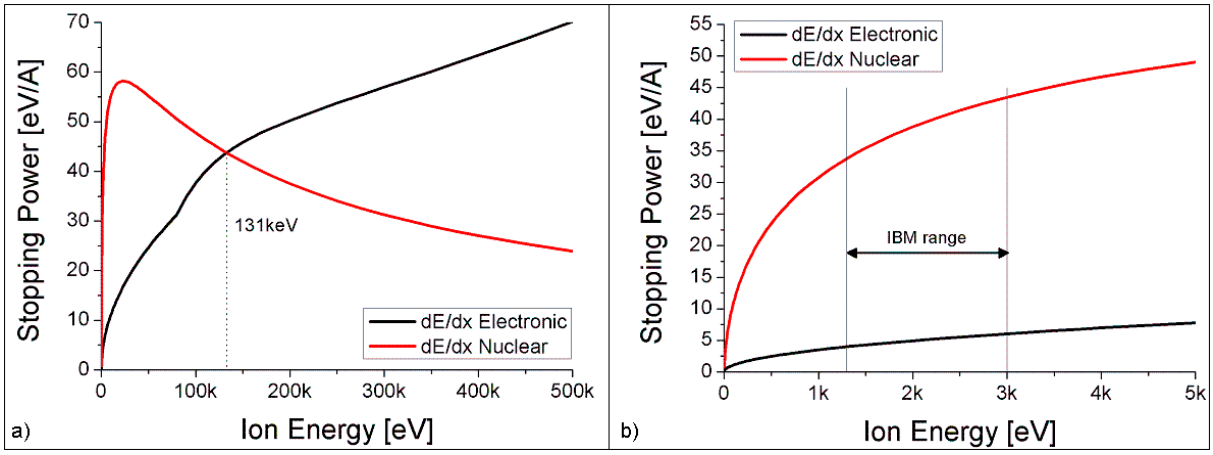

Figure 4.25: *The stopping power of Ar penetrating the Si obtained from the TRIM code. The stopping power plots are presented for high kinetic energies of Ar (a) and for ion energies up to 5.0keV (b). The IBM ion kinetic energy range that was used in this work is marked in (b).*

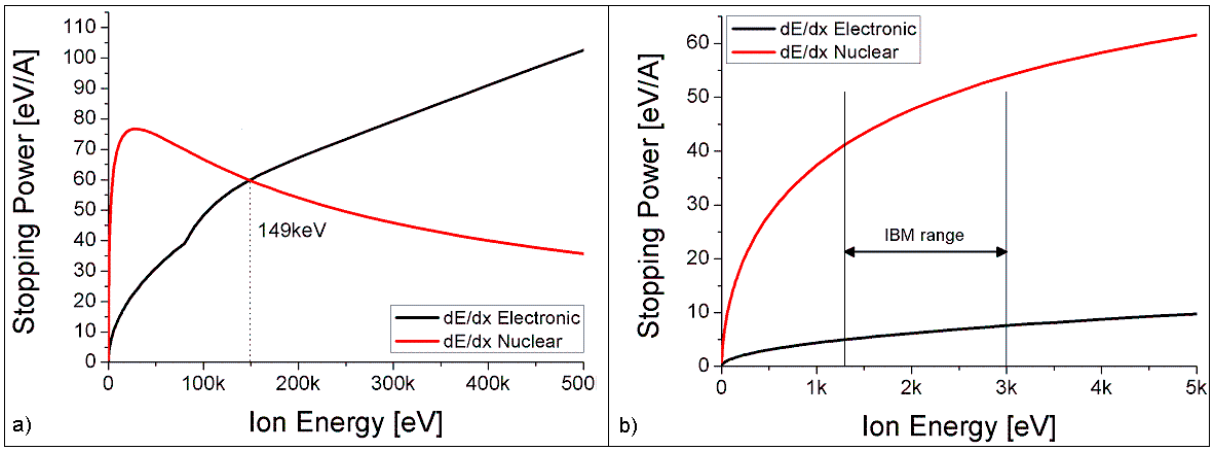

Figure 4.26: *The stopping power of Ar penetrating the Ti obtained from the TRIM code. The stopping power plots are presented for the high Ar kinetic energies (a) and for the ion energies up to 5.0keV (b) IBM ion kinetic energy range that was used in this work is marked.*

both Ti and Si atoms during the IBM process. Figures 4.25 and 4.26 show the stopping power that slows down the Ar ions penetrating the Si (Fig. 4.25) and the Ti (Fig. 4.26) calculated using the TRIM code.

Fig. 4.25a shows that for the low energetic Ar ions that penetrate the Si, the nuclear stopping dominates the process. It reaches its maximum at $\sim 22.0keV$ and then starts to decrease. The electronic stopping power does not have a maximum, but it growths exponentially-like up to $\sim 131keV$, where the values of the nuclear stopping and the electronic stopping are equal. From this point the electronic stopping growths linearly. Fig. 4.25b presents the stopping power plot in the ion energy scale used in the studies

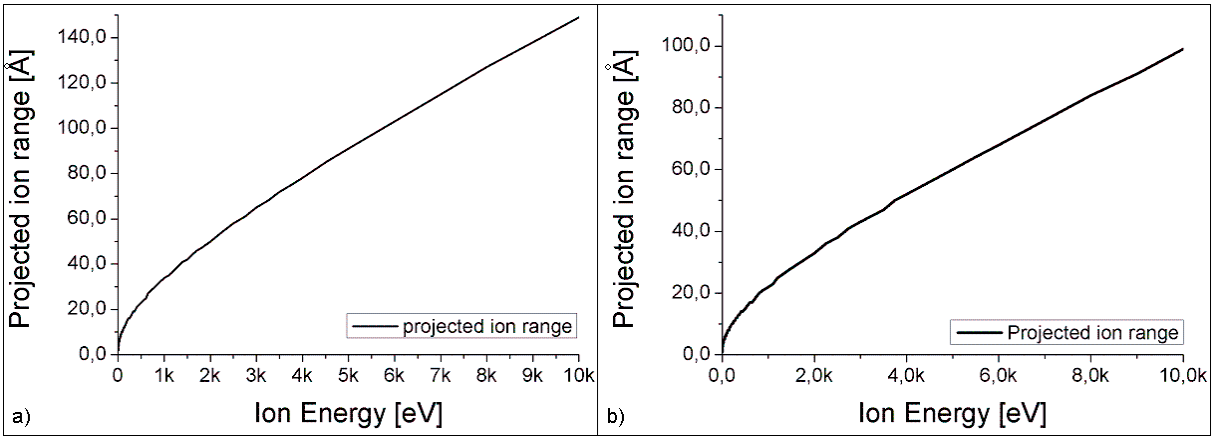

Figure 4.27: *Projected Ar range vs. the Ar kinetic energy in Si (a) and in the Ti (b).*

presented in this work. For the ion energies up to 5.0keV the nuclear stopping power significantly dominates over the electronic stopping power. The IBM ion energy range, in which all the IBM experiments were done, is marked on the plot. In this plot the nuclear stopping power is 6-8 times higher than the electronic stopping power.

If a low energetic Ar ion travels through the thick Ti layer, it mainly looses its energy due to the nuclear stopping power (Fig. 4.26a. The nuclear stopping power increases up to $\sim 30keV$ and then starts decreasing. The electronic stopping increases and for $\sim 149keV$ it is equal to the nuclear stopping. Fig. 4.26b shows that for the ion energies used in this work (IBM range is marked on the plot) the nuclear stopping power significantly dominates over the electronic stopping and its value is 8-10 times higher.

According to the presented TRIM calculations the Ar ions of $E_{kin} < 5.0keV$ slow down mainly due to the nuclear collisions while traveling through Ti/Si bilayers. The value of the nuclear stopping power for Ti is higher than for the Si in the discussed ion energy range. The titanium has higher material density ($4.52g/cm^3$) than silicon ($2.32g/cm^3$) and the titanium atom has a higher atomic weight (47,9 amu) than a silicon atom (28,08 amu), which means the amount of lost energy in nuclear collision is greater for Ar-Ti collisions, and the probability of an Ar-atom collision in Ti is higher than in Si. It all results in a higher nuclear stopping power for Ti.

Fig. 4.27 presents the projected ion range for Ar ions penetrating the Si (a) and Ti (b), calculated with the TRIM code. For Ar kinetic energies $E_{kin} > 1.0keV$ the projected ion range growths linearly-like with the ion energy. The Ar ions of energies from 1.0-3.0keV (ion energy range used for investigations in this work) should not penetrate the pure Si

deeper than $\sim$ 70Å and the pure Ti deeper than $\sim$ 50Å.

4.6.1 Photoemission studies of the IBMed Ti/Si(111)

The IBM experiment was performed on Si(111) covered in 20ML of Ti, deposited at room temperature. The Ar^+ ion beam was directed at the sample surface at normal incidence. The Ar^+ ions bombard the surface with a kinetic energy of $E_{kin} = 1.30keV$ and the ion dose was precisely controlled by the ion current measurement and the ion bombardment time (this procedure has been described in details in the previous chapter). After irradiating the sample with a specific ion dose, the photoemission studies (XPS and UPS) were performed in order to monitor the changes in the chemical composition, to investigate the titanium silicide phases, and to observe the valence band evolution.

Fig. 4.28 presents the XPS spectra taken after the IBM process of the Si 2p and the Ti $2p_{3/2}$ as a function of ion dose. At the beginning, when the Si is covered in 20ML of Ti, the Si 2p intensity is very low. With increasing ion dose, the Si 2p increases in height and also shifts in binding energy. The Ti $2p_{3/2}$ has the highest intensity right after the Ti evaporation, and its height decreases with the ion irradiation. Also an energy shift for Ti $2p_{3/2}$ is visible. Such peak behaviour proves there is an intermixing of Si and Ti, because the surface concentration of silicon increases and the one of titanium decreases. The both peaks evolve in a very comparable way, like the Si 2p and Ti $2p_{3/2}$ peaks during the thermal annealing experiment (Fig. 4.5).

A detailed XPS peak shift analysis was done, according to the XPS data from Fig. 4.28, and the results are presented in Fig. 4.29. When the ion dose increases, the Si 2p peak shifts into lower binding energies in almost linear way, and it reaches its minimum value of $\sim 98.3eV$. Then it moves back to higher binding energies and it reaches about 99.1eV. So, the maximum energy difference observed for the Si 2p shift is $\sim 0.9eV$. This peak behaviour is very similar to the Si 2p peak shifts observed during the thermal annealing experiments (Fig. 4.6). The Ti 2p3/2 first shifts to higher binding energies, when the ion dose increases, and reaches its maximum value at $\sim 453.96eV$. Then the peak shifts back to lower binding energy and stabilizes at $\sim 453.90eV$. The maximum binding energy shift observed is $\sim 0.35eV$. The Ti $2p_{3/2}$ peak shifts in the presented IBM experiment are very comparable to the shifts of the Ti $2p_{3/2}$ observed during the thermal annealing process (Fig. 4.6).

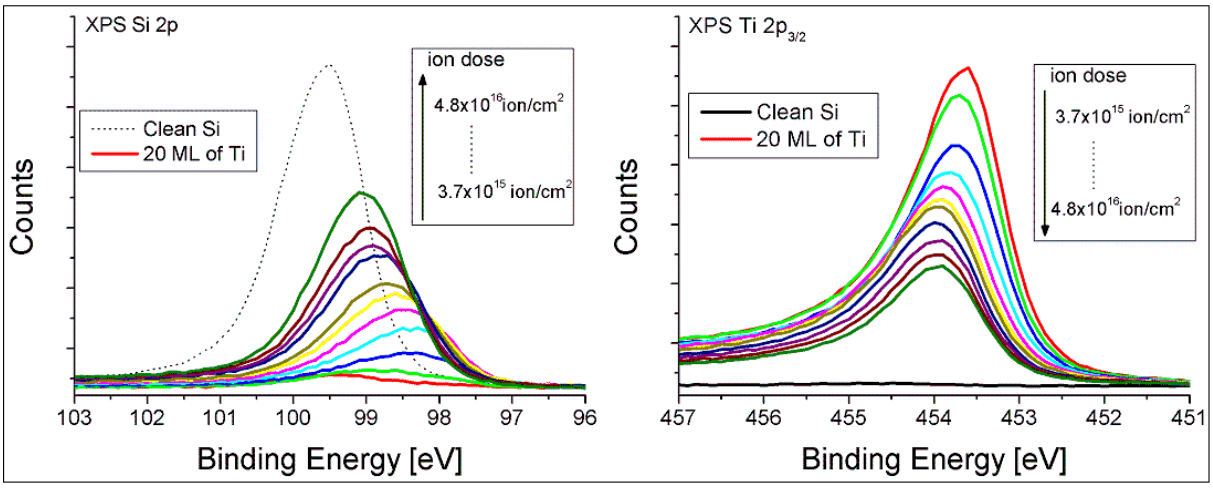

Figure 4.28: *Ion beam mixing of the 20ML–Ti/Si(111) bilayers at room temperature with the Ar beam at 1.30keV normal to the target surface. The XPS spectra show how the Si 2p and the Ti $2p_{3/2}$ change with the ion dose.*

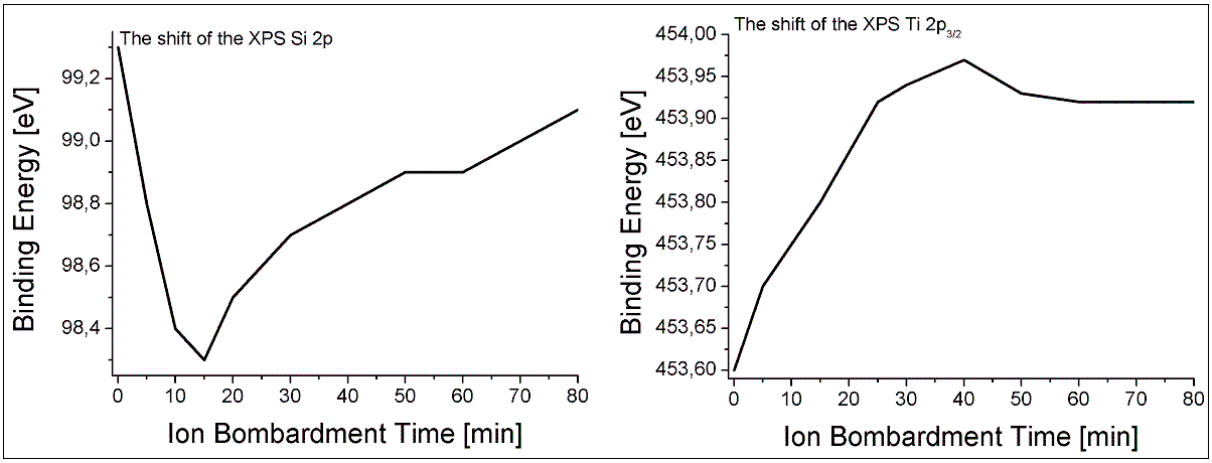

Figure 4.29: *The XPS peak shifts of the Si 2p and Ti $2p_{3/2}$ during the IBM of the Ti/Si(111) interface (Ti coverage: 20ML) at room temperature. Ar beam is normal to the surface, Ar kinetic energy is $E_{kin} = 1.30keV$.*

The valence band evolution of the ion-beam bombarded sample was studied by means of UPS, and the results are presented in Fig. 4.30. The peaks in the last three spectra do not change significantly, which indicates there is not much change in the chemical composition of the sample surface. For the same ion dose the XPS Si 2p peak position is $\sim 99.1eV$, which corresponds to the C54 $TiSi_2$ phase (mixture of silicides, where C54 dominates in quantity) according to the previous phase analysis with XPS peak fitting. The peak at $\sim 9eV$, which appears after the sample has received the ion dose of $\sim 18.5 \cdot 10^{15} ion/cm^2$, is the peak related to the presence of Ar on the sample surface.

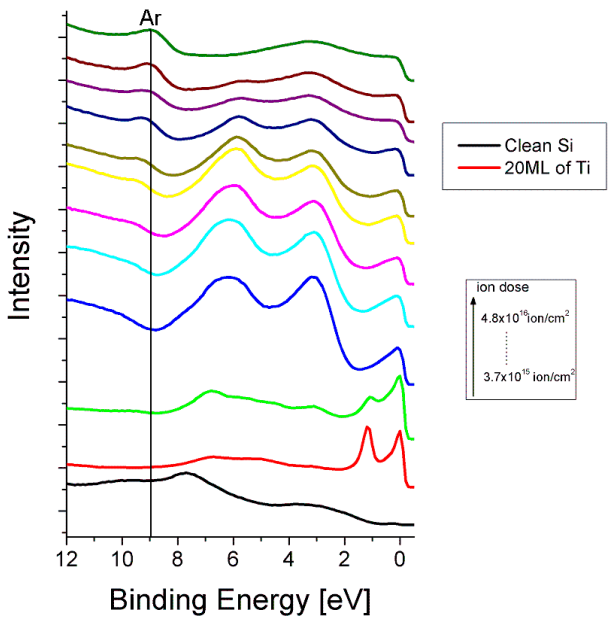

Figure 4.30: *The evolution of the valence band of the Ti/Si(111) sample during the IBM process at room temperature (irradiation with Ar^+ ions at the kinetic energy of 1.30keV, normal to the surface).*

The sample was also studied with the LEED, but no LEED pattern was observed during the whole IBM process, which indicates that the surface was disordered. Also, the silicides formed by the thermal annealing did not give any diffraction pattern. For the IBM process the appearance of an ordered LEED pattern is less expected, because the Ar^+ ions destroy the surface structure.

The described experiment has shown that the titanium silicide formation on the Ti/Si(111) system by IBM is similar to the silicide formation by thermal annealing. The changes in the intensities of the XPS peaks indicate the intermixing of the two elements. The XPS peak shifts of the Si 2p and the Ti $2p_{3/2}$ during the IBM are very similar to the shifts during annealing, so the silicide phases change in the same sequence.

4.6.2 Photoemission studies of the IBMed Ti/Si(100)

Titanium silicide formation by IBM was also studied on the Ti/Si(100) interface by the means of XPS, UPS and LEED. 20ML of Ti were deposited at room temperature onto the clean Si(100) crystal, and the sample was IBMed with the Ar^+ beam normal to the sample surface. The Ar^+ ion energy was set to 1.30keV, and the ion dose was precisely controlled.

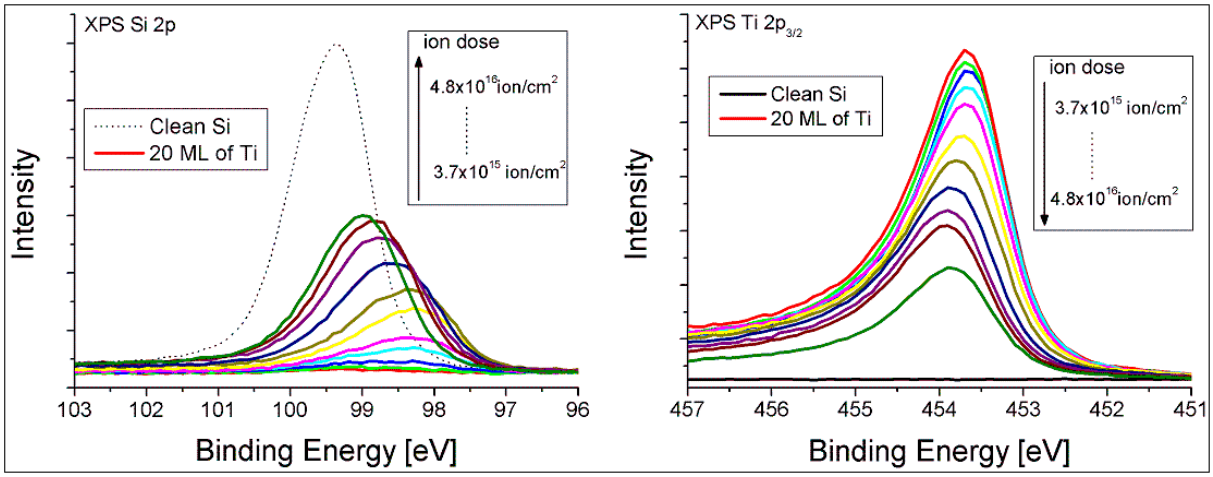

Figure 4.31: *Ion beam mixing of the 20ML–Ti/Si(100) bilayers at room temperature with the Ar beam at 1.30keV normal to the target surface. The XPS spectra show how the Si 2p and the Ti 2p$_{3/2}$ change with the ion dose.*

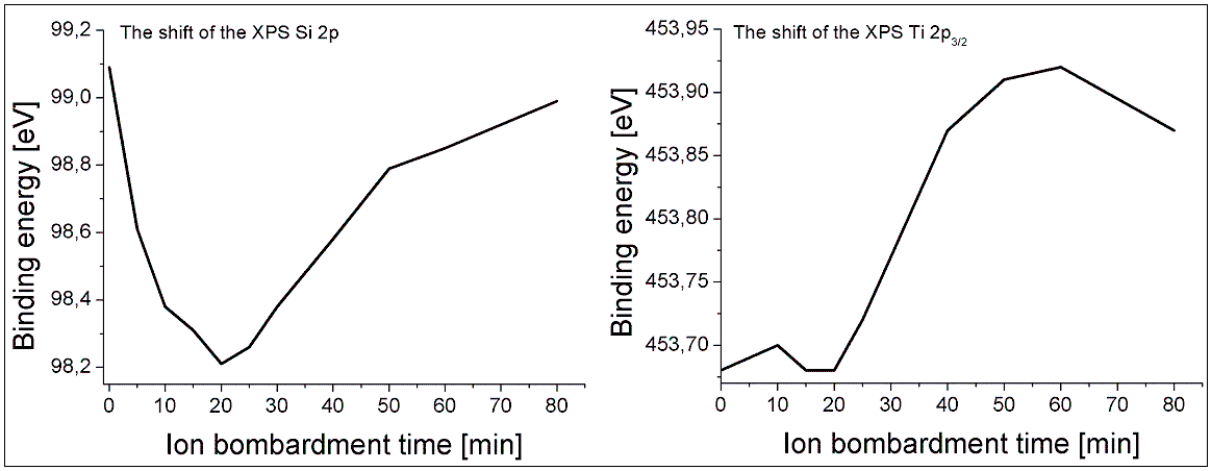

Figure 4.32: *The XPS peak shifts of the Si 2p and the Ti 2p$_{3/2}$ during the IBM process of the Ti/Si(100) interface (Ti coverage: 20ML) with Ar ions at 1.30keV, bombarding the sample at normal incidence.*

During the IBM process the XPS and UPS spectra were taken in order to examine the changes in chemical composition on the sample surface, to observe the titanium silicide phase transformation (according to the XPS peak shifts) and also to study the valence band evolution.

The XPS spectra taken during the IBM are presented in Fig. 4.31. It is shown how the Si 2p and the Ti 2p$_{3/2}$ change with the ion dose. Such peaks behaviour was already observed during the thermal annealing experiment of the Ti/Si(100) system (Fig. 4.9).

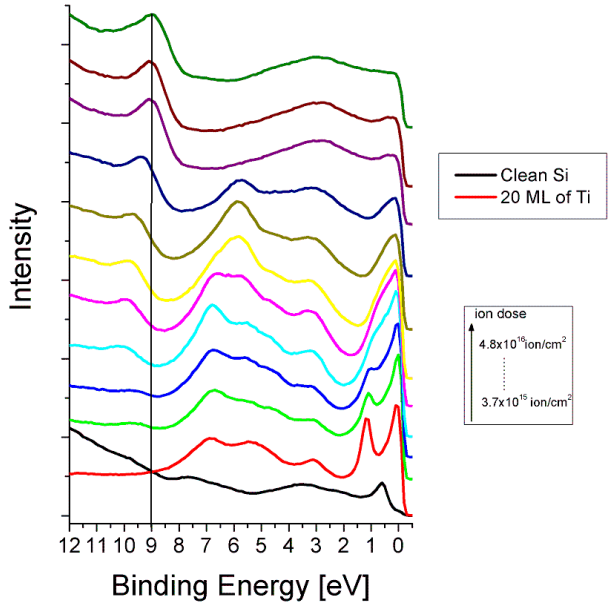

Figure 4.33: *The evolution of the valence band of the Ti/Si(100) sample during the IBM process at room temperature (irradiation with Ar^+ ions at the kinetic energy of 1.30keV, normal to the surface).*

The XPS peaks also shift in binding energy, and the analysis of the Si 2p and the Ti $2p_{3/2}$ peak shifts is presented in Fig. 4.32. The presented XPS peaks behaviour and the energy shifts are almost the same as the shifts observed for the Ti/Si(100) during the thermal annealing process (Fig. 4.11).

Fig. 4.33 shows the UPS spectra measured for different ion doses during the IBM experiment. The last three spectra do not differ much - there is no more peak transformation. At the binding energy of $\sim 9eV$ a peak develops, which is related to the Ar presence on the sample surface.
The UPS spectra of the thermally annealed Ti/Si(111) (Fig. 4.8) and the Ti/Si(100) (Fig. 4.12) differ in the peak evolution, and also the final spectra are different. But the UPS spectra of the IBMed Ti/Si(111) (Fig. 4.30) and the Ti/Si(100) (Fig. 4.33) also differ in the peak evolution, but they final 2-3 spectra are much the same in shape. These spectra are very featureless with one flat peak at $\sim 2.5eV$ and a pronounced Ar-related peak at $\sim 9eV$. The thermal annealing process of a thick 90.5ML Ti layer on Si(100) at $700°C$ for 20min also resulted in a similar featureless UPS spectra (Fig. 4.15), but without the Ar peak at 9.0eV (there was no argon bombardment). This sample was studied by the GIXRD and the C54 $TiSi_2$ phase was identified. So the annealed 90.5ML-thick Ti on Si(100) and the IBMed Ti/Si(111) and Ti/Si(100) give very similar, almost featureless

UPS spectra. This phenomenon is due to the fact, that the IBM process destroys locally the crystal structure, due to the ion-target atoms collisions. Since the UPS is also sensitive to the surface structure (the UPS spectra of the annealed 20ML–Ti/Si(111) and the 20ML–Ti/Si(100) are different), the IBMed samples are similar in UPS, due to the destroyed crystal structure of the silicon. Also the annealed 90.5ML-Ti/Si(100) surface looses its silicon surface properties, because of the very thick titanium coverage and a long-term intense diffusion/intermixing process.

The Ti/Si(100) sample was also investigated with the LEED during the ion beam mixing. After each ion bombardment step the sample surface was examined with the LEED. No diffraction pattern was observed for any ion dose, what means that the formed titanium silicides had no particular orientation. Also the thermally annealed Ti/Si(100) did not give any diffraction pattern at the temperature ranging from the room temperature up to $650°C$. During the IBM process the ion beam additionally disturbs the surface structure, and therefore no diffraction pattern is expected.

The described experiment has shown that with the IBM it is possible to obtain the same results like with the thermal annealing, but at room temperature. The room temperature IBM causes the Ti/Si bilayers to mix at their interface and it initiates the chemical reaction between them.

4.6.3 IBM of the Ti/Si(100) for different Ar^+ energies

It was an interesting task to find out how the ion energy influences the titanium silicide formation during the IBM process. Therefore the IBM of the Ti/Si(100) bilayers was studied for three different Ar^+ energies. The 20ML of Ti were deposited in UHV onto the clean Si(100) substrate. Then each sample was irradiated with the same dose of Ar^+ ions normal to the sample surface, but at different ion energies: 1.30keV, 1.80keV and 2.30keV. During the IBM process the sample was examined by the means of the XPS and UPS.

Fig. 4.34 presents the XPS measurements during the IBM with the Ar^+ ions at the kinetic energy of $E_{kin} = 1.80keV$. Fig. 4.35 shows the experimental results of the XPS measurements during the IBM process for the 2.30keV of Ar^+ kinetic energy. When the IBM process starts, the Si 2p peak increases in height, and the Ti $2p_{3/2}$ decreases. This peak behaviour is identical to the peak behaviour observed for the lower 1.30keV ion

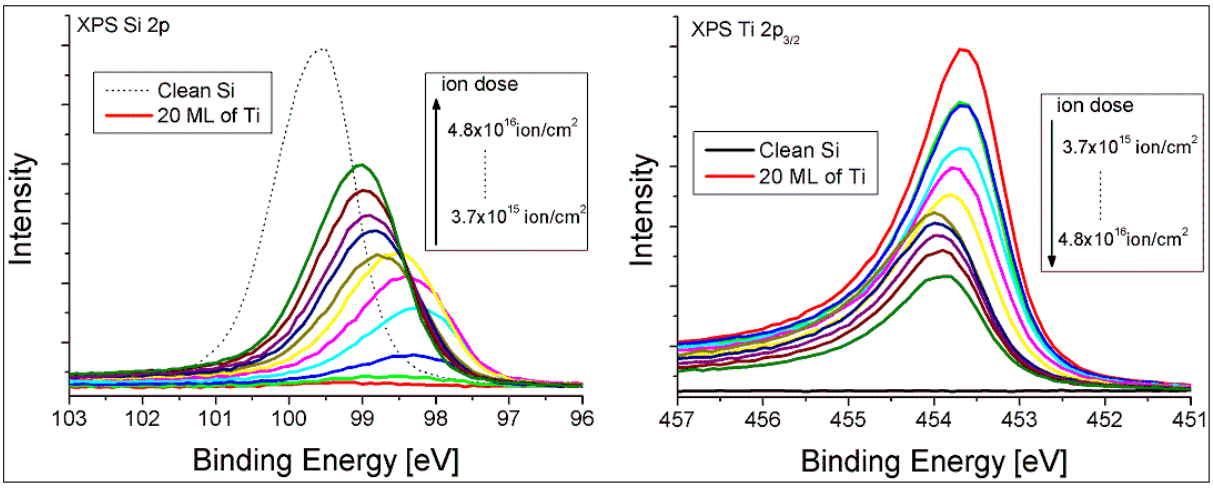

Figure 4.34: *Ion beam mixing of the 20ML–Ti/Si bilayers at room temperature with the Ar beam at 1.80keV normal to the target surface. The XPS spectra show how the Si 2p and the Ti* $2p_{3/2}$ *change with the ion dose.*

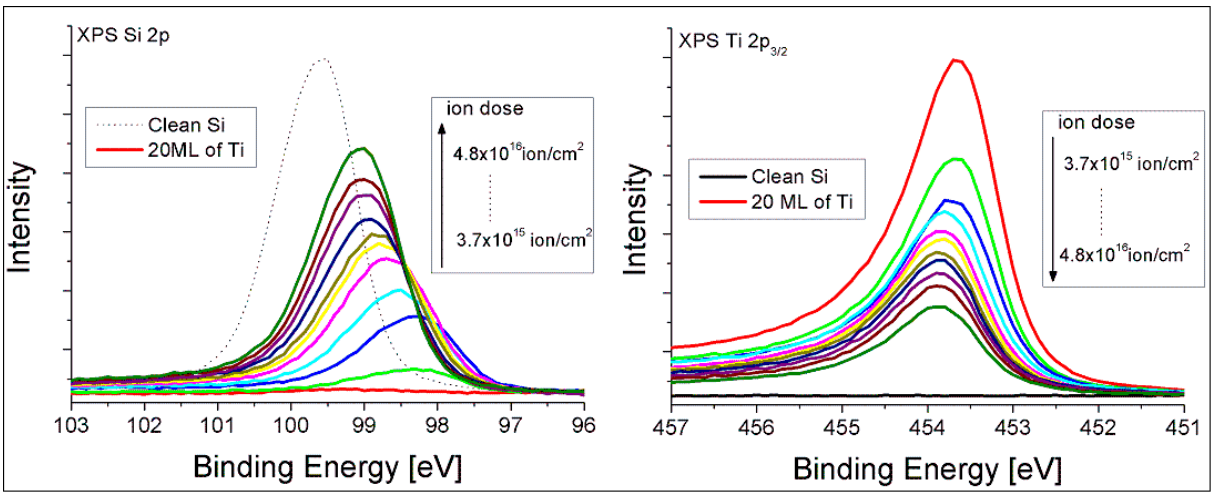

Figure 4.35: *Ion beam mixing of the 20ML–Ti/Si bilayers at room temperature with the Ar beam at 2.30keV normal to the target surface. The XPS spectra show how the Si 2p and the Ti* $2p_{3/2}$ *change with the ion dose.*

energy.

Both peaks also shift in the binding energy, as the ion dose increases. For both ion energies the Si 2p peak shifts to the lower binding energies and reaches the minimum value of $\sim 98.3eV$. Then it shifts back into the higher binding energies. The Ti 2p3/2 moves first in higher binding energies, when the IBM process starts. It reaches its maximum value of $\sim 453.9eV$ and then moves back to lower binding energies. This behaviour is

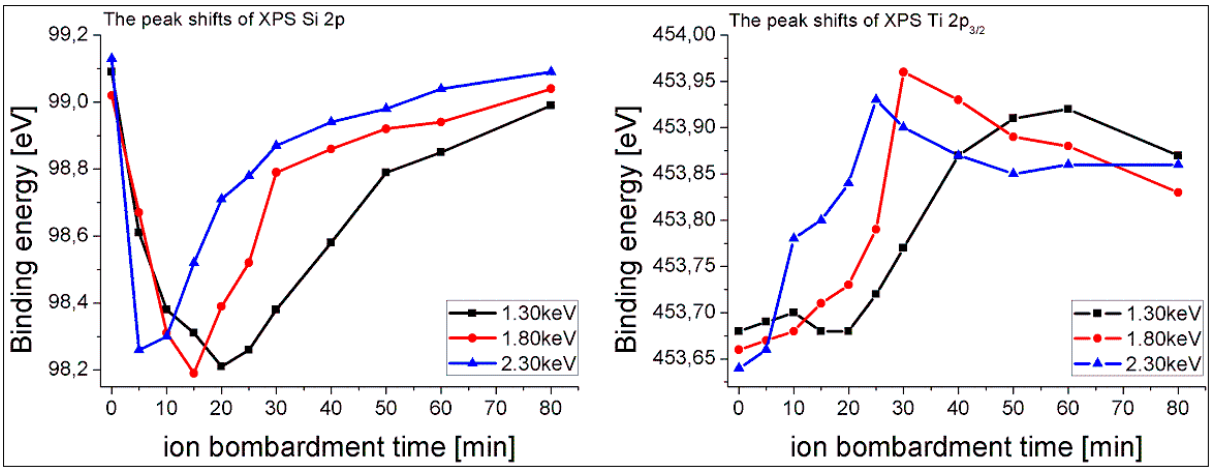

Figure 4.36: *XPS peak shits of the Si 2p and the Ti 2p$_{3/2}$ during the room temperature IBM process for different Ar$^+$ energies.*

observed for 1.80keV and 2.30keV. The peak movements are the same, like the movements observed for 1.30keV.

Fig. 4.36 presents the peak shifts of the Si 2p and the Ti 2p$_{3/2}$ during IBM process for the three different Ar$^+$ energies - 1.30keV, 1.80keV and 2.30keV. As one compares the shifts of both peaks for different binding energies, it is clearly visible that the higher Ar$^+$ energy, the faster the peaks shift. For 2.30keV the Si 2p reaches its minimum binding energy after only $\sim 5min$ of IBM, and for 1.30keV it reaches its minimum after $\sim 20min$. The Ti 2p$_{3/2}$ shifts to its maximum binding energy position only after $\sim 25min$ of IBM with 2.30keV, and it takes about 50min for the same shift, while bombarding the sample with Ar$^+$ at 1.30keV. As the peak shifts are related to the titanium silicide phase formation, it means that the phase transformation happens faster for the higher Ar$^+$ kinetic energies.

Fig. 4.37 shows the valence band evolution studied by the means of the UPS during the Ar$^+$ ion bombardment for two different energies: 1.80keV and 2.30keV. On both UPS series the peak at $\sim 9.0eV$ develops, which is the peak that proves the Ar presence on the studied surface. The UPS spectra evolution ends with the featureless spectra with a flat peak at $\sim 2.5eV$ and $\sim 9eV$ (Ar). Also the UPS spectra taken for the 1.30keV finish their evolution with such a spectrum.

If one compares the UPS spectra from the Fig. 4.37 and the Fig. 4.33, it is clear that the spectra for the same ion dose consist of different peaks for different ion energies. So it means, that the speed of the titanium silicide phase transformation is different for different ion energies.

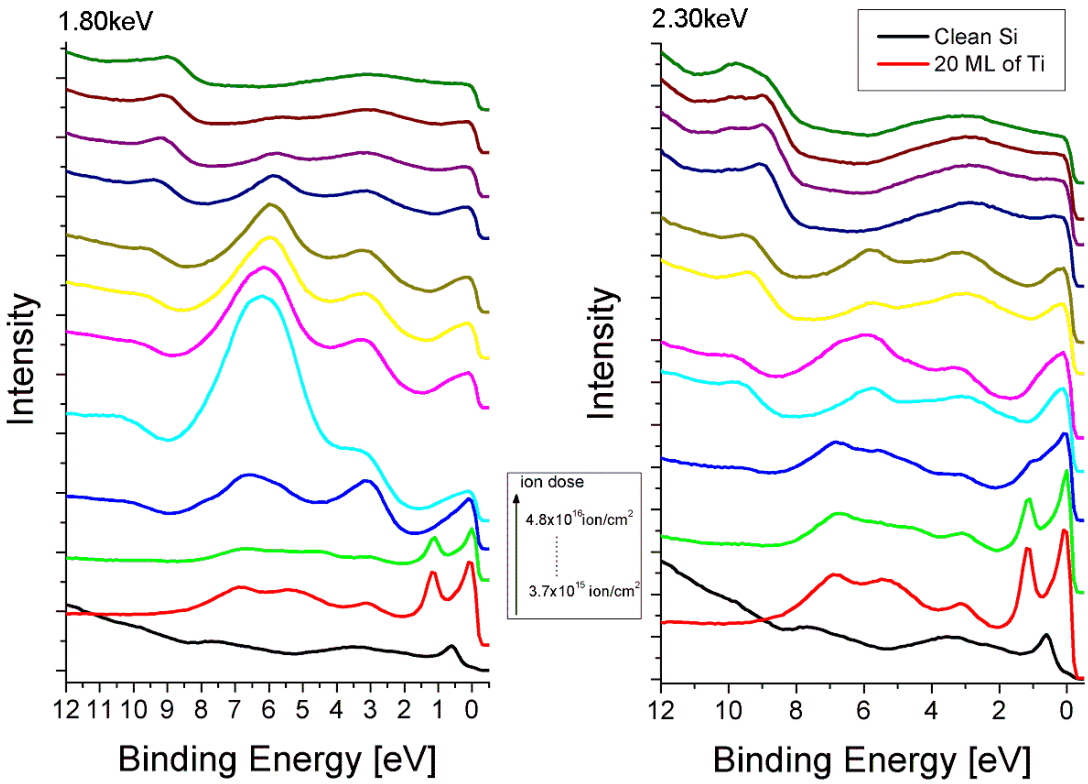

Figure 4.37: *The evolution of the valence band of the Ti/Si(100) sample during the IBM process at room temperature (irradiation with Ar^+ ions at the kinetic energy of 1.80keV and 2.30keV, normal to the surface)*

Let us compare the XPS and the UPS spectra for a specific ion dose for the three different Ar^+ energies, in order to analyse the titanium silicide phase transformation and the intermixing in more details.

Fig. 4.38 shows the comparison of the XPS spectra for the three samples irradiated by different Ar^+ ion energies for the same ion dose of $29.6 \times 10^{15} ions/cm^2$, and the spectra of the clean Si and the 20ML of Ti on the Si are given as a reference. The Si 2p peaks differ in intensity and peak position: the higher the ion energy, the higher the intensity. The Ti $2p_{3/2}$ peaks are smaller for higher ion energies. The interdiffusion at the Si/Ti interface is greater for higher ion energies.

The peaks are not only different in height, but they are also shifted in binding energy, so different titanium silicides were formed. The lower the ion energy, the more the Si 2p peak is shifted to the lower binding energy with respect to the clean silicon. The Ti $2p_{3/2}$ shifts to higher binding energies for the ion energies of the 1.30keV and 1.80keV, but it shifts back to the higher binding energy for the argon energy of 2.30keV.

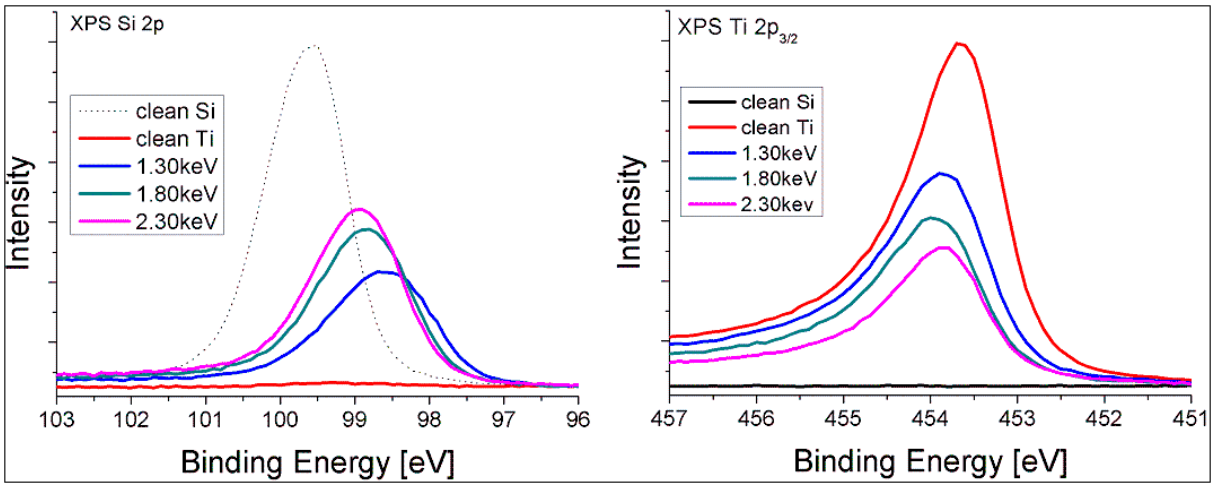

Figure 4.38: *The comparison of the XPS spectra showing the Si 2p and the Ti $2p_{3/2}$ peaks taken for the samples irradiated with the ion dose of* $29.6 \times 10^{15} ions/cm^2$ *and for different* Ar^+ *ion energies (1.30, 1.80 and 2.30keV).*

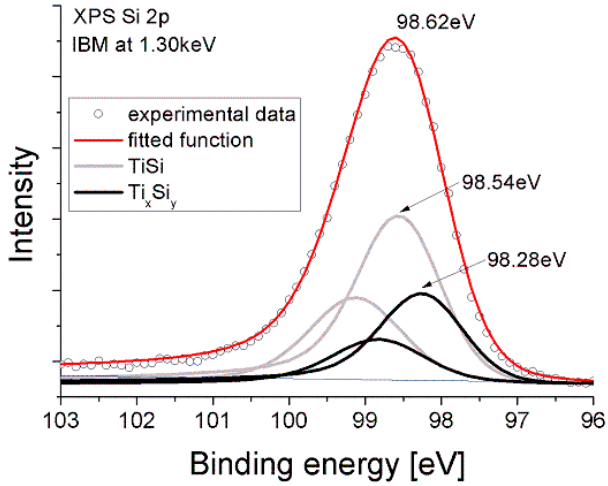

Figure 4.39: *XPS fitting of the Si 2p, the 20ML–Ti/Si(100) sample bombarded with* Ar^+ *at 1.30keV, the ion dose* $29.6 \times 10^{15} ions/cm^2$.

The detailed titanium silicide phase analysis of the XPS Si 2p peaks is shown in Fig. 4.39, 4.40 and 4.41. The peaks were fitted with the Si 2p doublets, and the binding energy position of the doublets was assign to the appropriate titanium silicide phase. The Si 2p peak measured on the sample bombarded with the lowest ion energy (1.30keV) is positioned at 98.62eV, and was successfully fitted with two doublets (Fig. 4.39). The largest peak represents the TiSi (98.54eV), and the smaller the Ti_xSi_y (98.28eV). It was not possible to fit the Si 2p peak with more doublets, so the sample consists only of two titanium silicide phases.

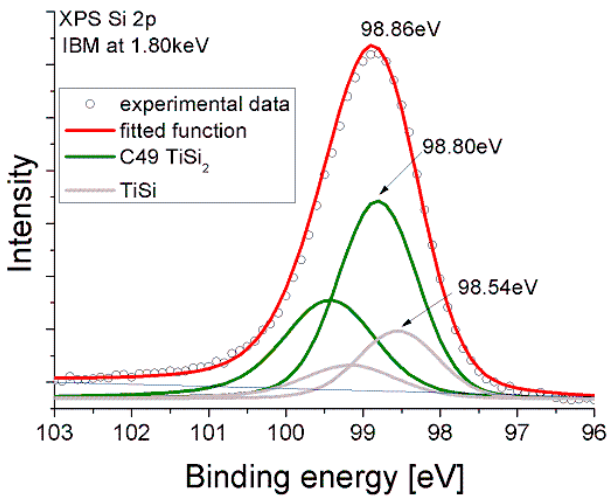

Figure 4.40: *XPS fitting of the Si 2p, the 20ML–Ti/Si(100) sample bombarded with* Ar^+ *at 1.80keV, the ion dose* $29.6 \times 10^{15} ions/cm^2$.

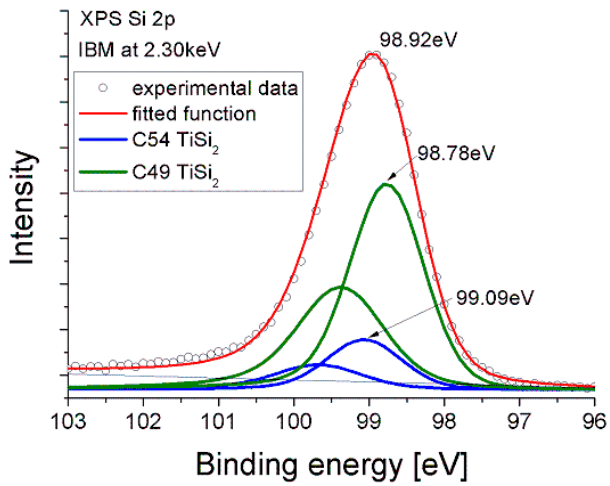

Figure 4.41: *XPS fitting of the Si 2p, the 20ML–Ti/Si(100) sample bombarded with* Ar^+ *at 2.30keV, the ion dose* $29.6 \times 10^{15} ions/cm^2$.

The Si 2p peak of the sample bombarded with Ar^+ at 1.80keV is positioned at 98.86eV, and it was fitted also with two doublets (Fig. 4.40). The binding energy of the largest Si 2p3/2 is 98.80eV, what means it is a C49 $TiSi_2$. The second doublet with its binding energy of 98.54eV represents the TiSi silicide, which is the minority phase.

Fig. 4.41 shows the fitting of th Si 2p of the sample irradiated with the Ar^+ ions at 2.30keV. The Si 2p peak position is 98.92eV and it was fitted with the two doublets. The dominating phase is the C49 $TiSi_2$, which is represented by the tallest peak at 98.78eV. The very small doublet at 99.09eV corresponds to the C54 $TiSi_2$.

As the phase analysis shows, there the ion energy has a significant impact on the titanium

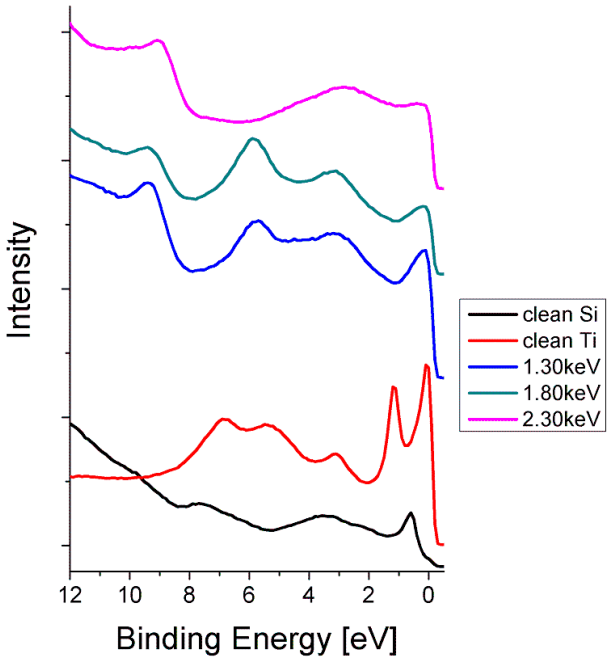

Figure 4.42: *The comparison of the UPS spectra taken for the samples irradiated with the ion dose of* $29.6 \times 10^{15} ion/cm^2$ *and for different* Ar^+ *ion energies (1.30, 1.80 and 2.30keV).*

silicide phase transformations. The samples that received the same ion dose but at different energies consist of different titanium silicides. The phase transformation happens faster for higher ion energies. The sample irradiated with the ions of 1.30keV represents the early stage of the silicide formation, that is comparable to the thermal annealing at $\sim 450°C$, where the TiSi is the dominant phase. The sample bombarded with the higher energetic ions (1.80keV) already consists mostly of the C49 $TiSi_2$ phase. The TiSi already transformed into the C49, and only very little of it can be detected. This sample is comparable to the thermally annealed one at $\sim 550°C$. In the third sample (2.30keV) the whole TiSi has transformed into the C49 $TiSi_2$ and the C49 phase started to transform into the stable C54 $TiSi_2$ phase. The C54 $TiSi_2$ exists in a very small quantity, which means that the nucleation process has just started.

In Fig. 4.42 the UPS spectra are compared taken for the samples bombarded with the same ion dose of $29.6 \times 10^{15} ion/cm^2$, but for the different kinetic energies of the incident argon ions. Each spectrum contains the peak at $\sim 9eV$, which is due to argon. The spectrum for the highest argon energy (2.30keV) consists of only one flat peak at $\sim 3eV$. This spectrum is very much like the UPS spectrum in the end of the silicide nucleation process, observed for the all previous IBM experiments, and it represents the mixture of the C49 and C54 $TiSi_2$ silicides. That agrees well with the phase analysis presented above

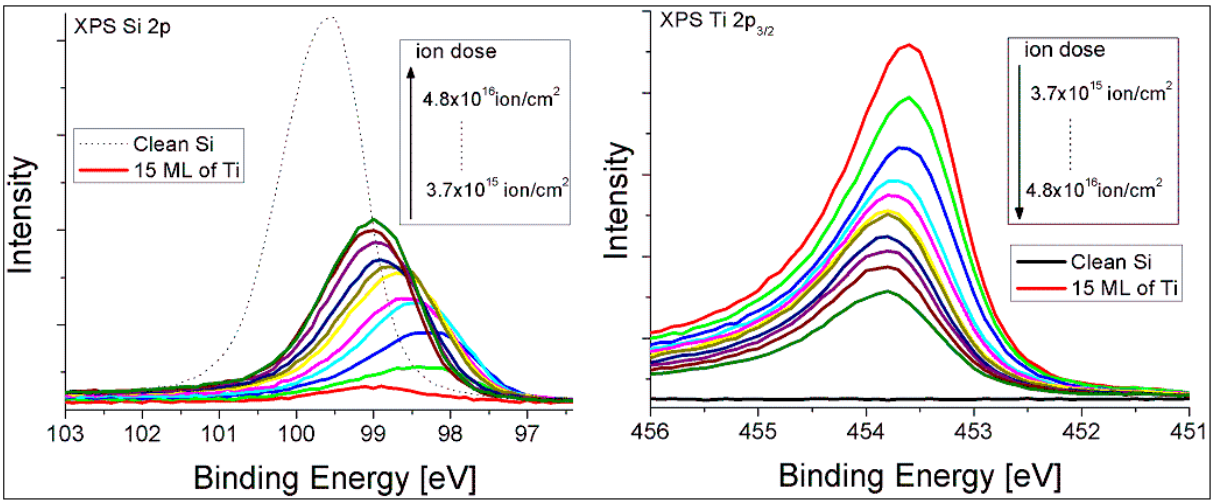

Figure 4.43: *Si 2p and the Ti $2p_{3/2}$ XPS spectra of the Ti/Si(100) sample IBMed with the Ar^+ ions at 1.30keV. Titanium coverage is 15ML.*

(Fig. 4.41), where the $TiSi_2$ was the only silicide detected. The UPS spectra for 1.80keV and 2.30keV are similar in shape, but the peak at $\sim 6eV$ is more pronounced for the Ar^+ 1.80keV. Both samples consist of the TiSi, but in different quantity (more TiSi for the 1.30keV sample). But the second component is different for each sample - Ti_xSi_y for the 1.30keV sample, and the C49 $TiSi_2$ for the 1.80keV sample. The second component causes the change in the UPS spectra between the two samples.

4.6.4 IBM of the Ti/Si(100) for different Ti coverages

All the previous IBM experiments were performed on the silicon substrates covered with 20ML of titanium. The results of the experiments presented in this section show, how the IBM changes, when the Si is covered with different titanium coverage. So additionally to the IBM at 1.30keV of the 20ML–Ti/Si(100) system, two other experiments were performed under the same conditions, but with the titanium coverage of 15ML and 10ML. During the IBM experiment the samples were studied by the means of the XPS and the UPS. The samples were irradiated with Ar^+ ions in steps and the ion dose was precisely controlled. After each ion bombardment step the XPS and UPS spectra were taken.

Fig. 4.43 presents the XPS spectra of the Si 2p and the Ti $2p_{3/2}$ binding energy regions for the IBMed 15ML-Ti/Si(100) sample, IBMed with Ar^+ at 1.30keV. With the increasing ion dose, the Si 2p peak increases its height and also shifts in binding energy in the way that was observed also for the 20ML–Ti/Si(100) sample (Fig. 4.31). Simultaneously the

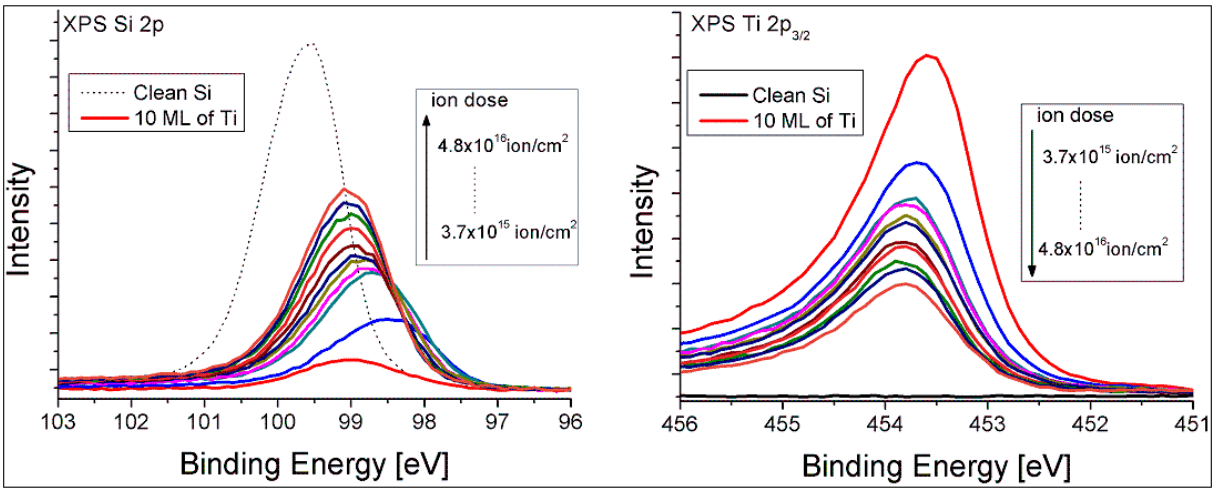

Figure 4.44: *Si 2p and the Ti $2p_{3/2}$ XPS spectra of the Ti/Si(100) sample IBMed with the Ar^+ ions at 1.30keV. Titanium coverage is 10ML.*

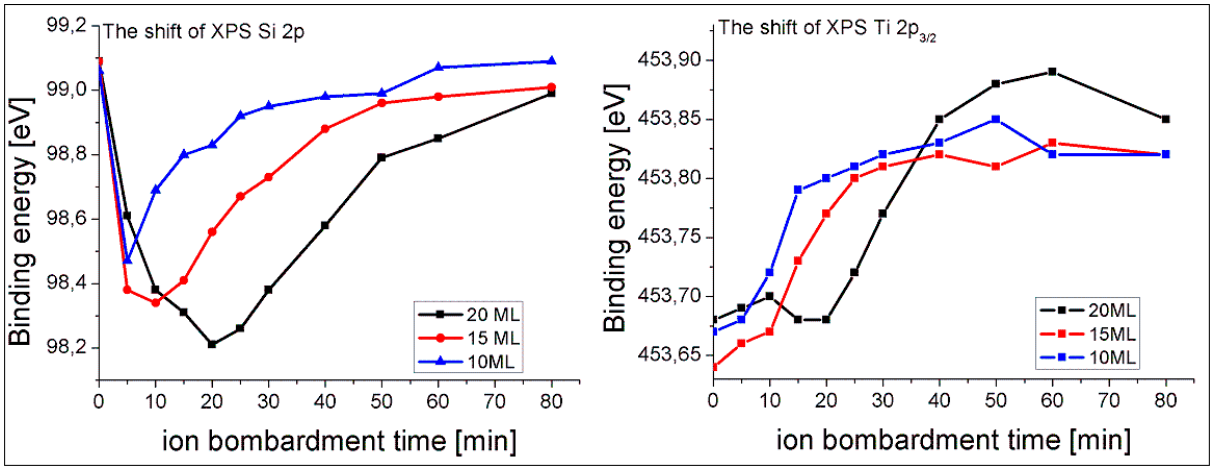

Figure 4.45: *XPS peak shits of the Si 2p and the Ti $2p_{3/2}$ during the room temperature IBM process for different titanium coverages (10-20ML) at constant Ar^+ energy of 1.30keV. Substrate: Si(100).*

Ti $2p_{3/2}$ decreases in height and also shifts in binding energy like it was observed for the 20ML sample.

In Fig. 4.44 the XPS spectra of the IBMed 10ML-Ti/Si(100) sample are presented. The behaviour of the Si 2p and the Ti $2p_{3/2}$ peaks is very comparable to the peak behaviour observed for the samples with the thicker titanium coverage.

As one compares the Si 2p growth for the three different Ti coverages, it is noticeable that the Si 2p grows fastest for the thinnest Ti coverage (10ML). So the interdiffusion takes place more intensively for the lower titanium coverages.

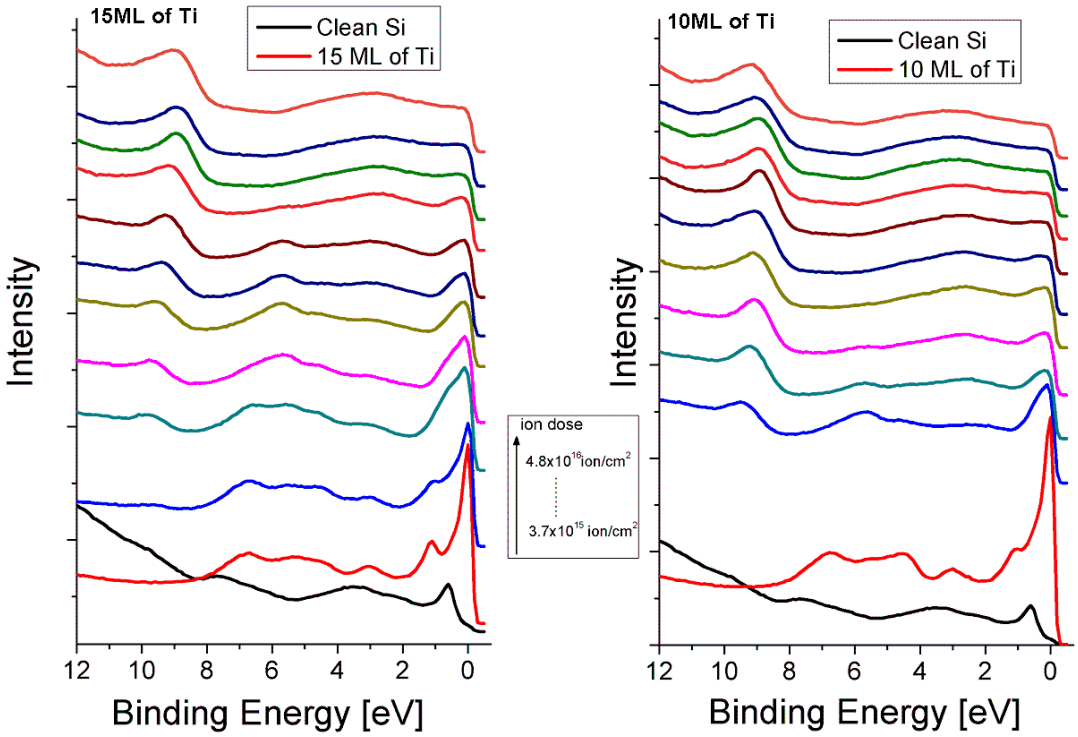

Figure 4.46: *The evolution of the valence band of the Ti/Si(100) sample during the IBM process at room temperature with Ar^+ at 1.30keV. Ti coverage is 15ML and 10ML.*

The XPS peak shifts of the Si 2p and the Ti $2p_{3/2}$ for different titanium coverages and constant Ar^+ kinetic energy (1.30keV) were analysed. The peak shifts in binding energy versus the IBM time are presented in Fig. 4.45. For all the titanium coverages the Si 2p peak moves first to the lower binding energy, and than it shifts back to the higher binding energy. So the sequence of the titanium silicide transformation is the same for all the Ti coverages. The Si 2p peak of the 10ML sample reaches the minimum binding energy faster than on the other two samples. The Si 2p peak of the 15ML sample moves to its minimum binding energy position after $\sim 10min$ of IBM, and the Si 2p peak of the 20ML sample reaches the minimum position after $\sim 20min$. This difference in the speed of the Si 2p peak movements shows clearly that the titanium silicide phase transformation happens faster for the samples with lower Ti coverages.

All the Ti $2p_{3/2}$ binding energy shifts presented in Fig. 4.45 are very similar for all the titanium coverages. Peaks move in a comparable way: first to the higher binding energy, then after reaching the maximum, they move slightly back to the lower binding energies. So the titanium silicide phase transformation takes place in the same sequence for all the investigated titanium coverages.

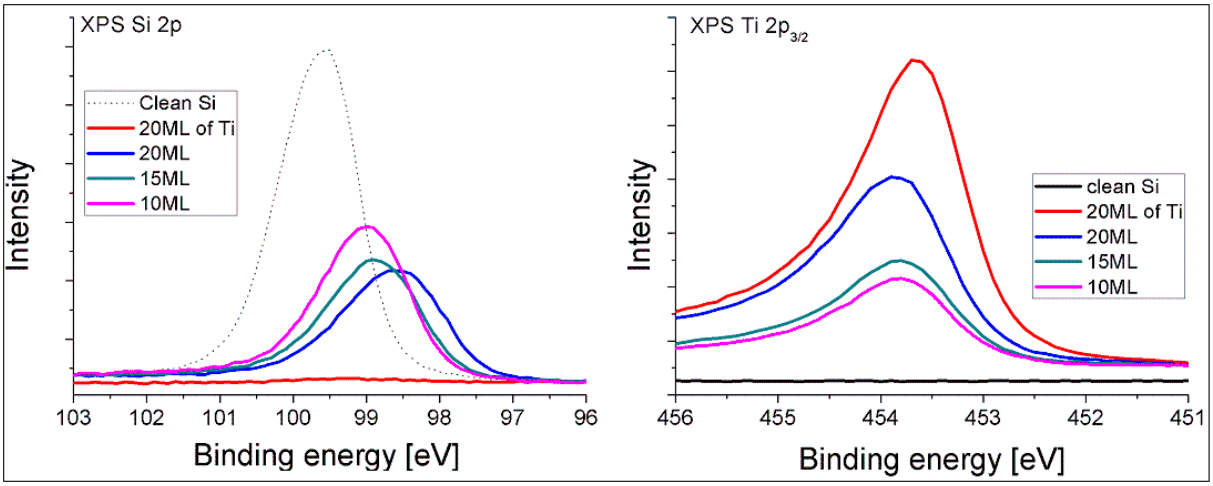

Figure 4.47: *The comparison of the XPS spectra of the Si 2p and the Ti 2p$_{3/2}$ peaks taken for the samples irradiated with the ion dose of $\phi = 29.6 \times 10^{15} ions/cm^2$ at 1.30keV, but for different Ti coverage: 20ML, 15ML and 10ML on Si(100).*

Fig. 4.46 presents the UPS spectra taken during the IBM with Ar^+ at 1.30keV of the two Si(100) samples covered in 15ML and 10ML of Ti. Both series of UPS spectra end up with a flat spectrum consisting of an argon peak at 9eV and a flat peak at $\sim 3eV$. Such a spectrum also exists for the sample covered by 20ML of Ti (see Fig. 4.33), but the evolution of the spectra is fastest for the lowest Ti coverage sample (10ML). It agrees well with the XPS results, which have shown that the XPS peak move faster (silicide phase changes faster) for the low coverage samples.

Let us now analyse the titanium silicide transformation in more details, and let us compare the XPS and UPS measurements for the specific ion dose. Fig. 4.47 shows the XPS spectra of the three samples covered in 20ML, 15ML and 10ML of Ti, irradiated with Ar^+ at 1.30keV with the ion dose $\phi = 29.6 \times 10^{15} ions/cm^2$. The lower the titanium coverage, the more Si 2p peak is shifted to the higher binding energy. The lower the titanium coverage, the smaller the Ti 2p$_{3/2}$ peak. The Ti 2p$_{3/2}$ peaks also differ in the binding energy position. The Ti 2p$_{3/2}$ of the 20ML sample is positioned at 453.87eV, the 15ML Ti 2p$_{3/2}$ at 453.79eV and the 10ML Ti 2p$_{3/2}$ at 453.7eV. So the three samples received the same ion dose, but they have different atomic concentration on the surface (different XPS peak heights) and a different titanium silicide phase was formed (different XPS peak shifts).

Figures 4.48, 4.49 and 4.50 present the fitted XPS Si 2p peaks from Fig. 4.47. Each

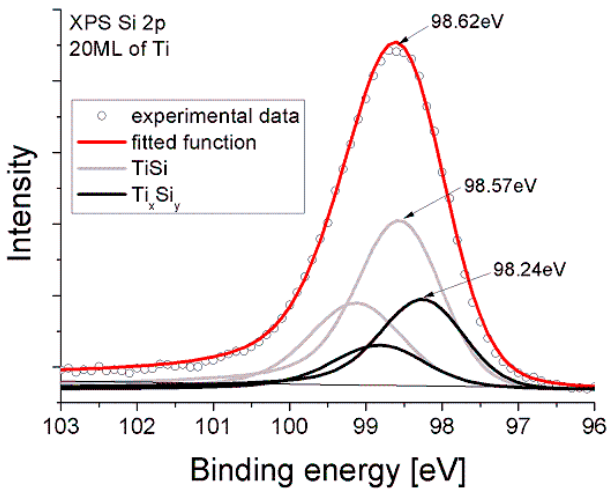

Figure 4.48: *The fitted XPS spectra of the Si 2p for the 20ML–Ti/Si(100) sample. The ion dose* $\phi = 29.6 \times 10^{15} ions/cm^2$ *and the* Ar^+ *energy* $E_{kin} = 1.30keV$.

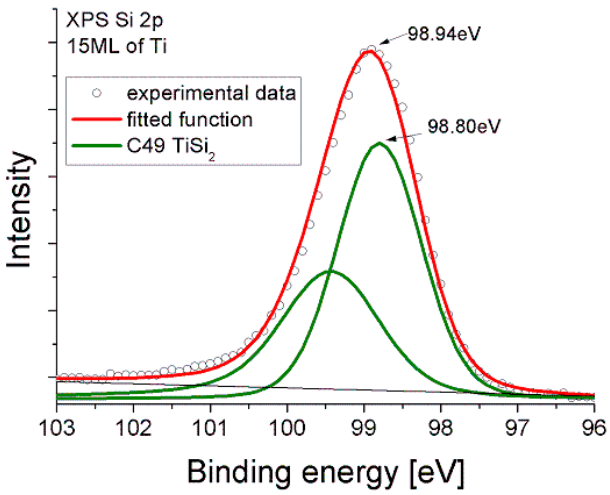

Figure 4.49: *The fitted XPS spectra of the Si 2p for the 15ML–Ti/Si(100) sample. The ion dose* $\phi = 29.6 \times 10^{15} ions/cm^2$ *and the* Ar^+ *energy* $E_{kin} = 1.30keV$.

Si 2p peak was fitted with the FitXPS 2.12 program [2] with the silicon doublets. The binding energy of each silicon doublet corresponds to the appropriate titanium silicide phase, and the doublet height corresponds to the quantity of the silicide phase.

Fig. 4.48 presents the fitted Si 2p peak of the 20ML–Ti/Si(100) sample. The binding energy of the measured Si 2p peak is 98.62eV, and it was successfully fitted with two doublets. The largest peak is positioned at 98.57eV, which corresponds to the TiSi silicide. The second doublet represents the metal-rich titanium silicides (Ti_xSi_y) and its binding energy position is 98.24eV. It was not possible to fit more doublets. So the sample consists of the two titanium silicides: TiSi (dominant) phase and a little bit of the Ti_xSi_y.

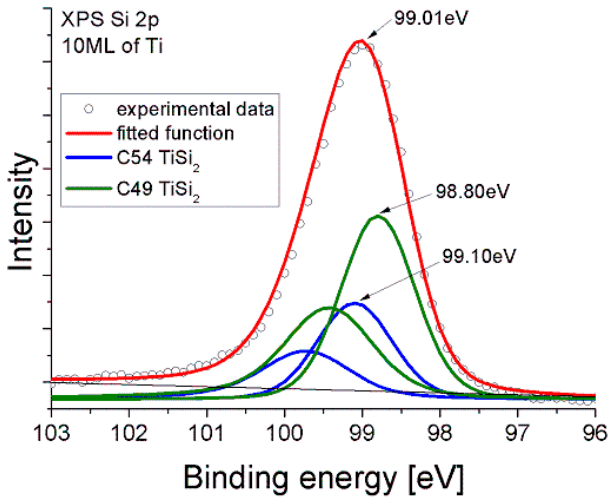

Figure 4.50: *The fitted XPS spectra of the Si 2p for the 10ML–Ti/Si(100) sample. The ion dose* $\phi = 29.6 \times 10^{15} ions/cm^2$ *and the* Ar^+ *energy* $E_{kin} = 1.30keV$.

Fig. 4.49 shows the fitted Si 2p peak of the 15ML-Ti/Si(100) sample. The measured peak is positioned at 98.94eV and it was fitted only with one silicon doublet at 98.80eV. The binding energy of the doublet suggests it is a good C49 $TiSi_2$.
Fig. 4.50 presents the obtained fitting results of the sample with the thinnest titanium coverage (10ML). The binding energy of the measured Si 2p peak is 99.01eV. It was fitted with the two doublets: a larger one at 98.80eV, and the smaller one at 99.10eV. So the sample consists of a mixture of two titanium silicides. The dominant phase is the C49 $TiSi_2$, and the other phase is the C54 $TiSi_2$.
These fitting results show that the thinner the titanium coverage, the faster the titanium silicide phase changes. The three samples that differ in Ti coverage, but were IBMed with the same conditions, have slightly different chemical composition. The 20ML sample consists of mainly the TiSi phase. In the 15ML sample only the C49 $TiSi_2$ was detected, so the TiSi had been fully converted. In the sample with the thinnest titanium coverage, the C49 and the C54 $TiSi_2$ phases coexist. So the same ion dose of $29.6 \times 10^{15} ions/cm^2$ initiated the C54 $TiSi_2$ nucleation for the 10ML sample, but it formed only the TiSi in the 20ML sample.

Fig. 4.51 presents the UPS spectra taken for the three sample bombarded with the same ion dose ($29.6 \times 10^{15} ions/cm^2$) with the same Ar^+ kinetic energy (1.30keV), but the samples had different Ti coverage: 20ML, 15ML and 10ML. The spectra for 10ML and 15ML consist of the argon peak and also at the flat peak at $\sim 3eV$. These two spectra are very much like the UPS spectra in the end of the silicide nucleation process, observed

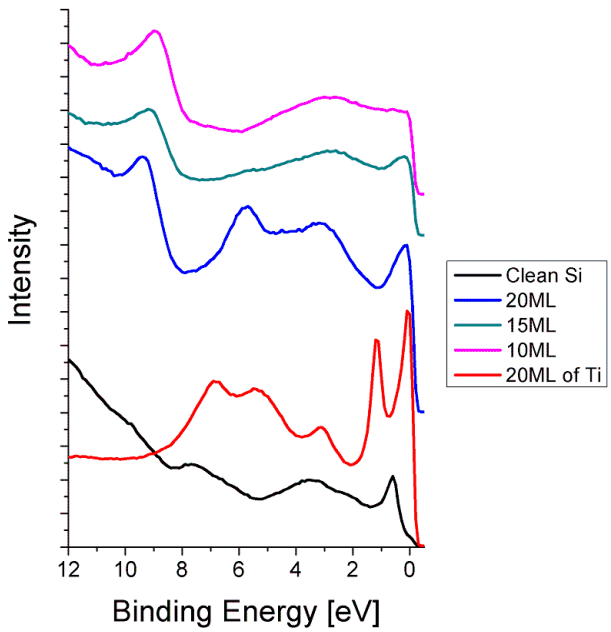

Figure 4.51: *The comparison of the UPS spectra taken for the samples irradiated with the ion dose of* $29.6 \times 10^{15} ions/cm^2$ *at 1.30keV, but for different Ti coverage: 20ML, 15ML and 10ML on Si(100).*

for the all previous IBM experiments, and it represents the mixture of the C49 and C54 $TiSi_2$ silicides. This agrees very well with the presented above phase analysis with XPS fitting. The analysis proves the existence of these two titanium silicide phases: C54 and C49 $TiSi_2$ in the 10ML sample, and C49 $TiSi_2$ in the 15ML sample. The UPS spectrum of the 20ML sample consists of different peaks at $\sim 0.5eV$, $\sim 3eV$ and $\sim 6eV$. This spectrum is the spectrum of the TiSi, which was detected as the dominant phase by the analysis with the XPS fitting.

4.7 Monte Carlo simulations of the IBMed Ti/Si system

This section presents the Monte Carlo simulations of the ion beam mixing of the Ti/Si bilayers, performed with the TRIM program. The purpose of the calculations was to simulate the IBM process under the same conditions, as the real experiments performed in the UHV. The results of these virtual experiments give better understanding of the IBM process, and also give the information about many IBM parameters that are not possible to be measured. The parameters of the calculations (e.g. incident ion angle, ion energy,

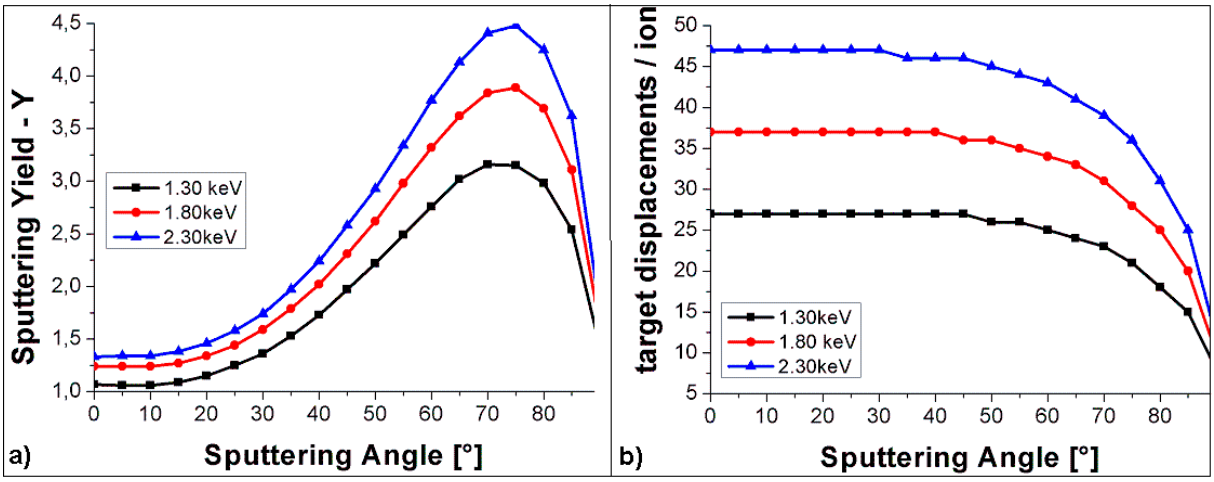

Figure 4.52: *The results of the TRIM simulations presenting the sputtering yield (Y) vs. the sputtering angle (a), and the total target displacements vs. the sputtering yield (b). The target material was titanium and it was bombarded with the Ar^+ ions at 1.30keV, 1.80keV and 2.30keV.*

target material) were set up as in the real laboratory experiments, in order to simulate the experiments as precisely as possible.

4.7.1 Mixing and sputtering

During the IBM process the kinetic energy of the impinging ions is used not only for mixing of the two elements, but it can also lead to the sputtering effect. So every IBM process consists of mixing and sputtering, but the sputtering effect in the IBM process is not desired, because it leads to the material loss. What is more: the energy absorbed by the target atoms is not used for mixing, but it is wasted on ejecting the particles from the sample surface. So the sputtering yield should be as low as possible in the IBM process. The sputtering yield depends on many parameters, such as the ion energy, angle of ion incidence, atomic mass of ions and target atoms [54]. Atomic masses of ions and target atoms are defined by the chemical elements, that take part in the experiment (Ar, Si, Ti), and, of course, they cannot be changed. But the ion energy and the angle of the ion incidence are the parameters that can be set up, and the sputtering yields can be calculated. Fig. 4.52a presents the results of the TRIM calculations of the sputtering yield Y versus the sputtering angle, for the Ar^+ ions bombarding the titanium surface with 1.30keV, 1.80keV and 2.30keV. The angle of 0° means, that the ion beam is normal to the target surface. The maximum sputtering angle is 89.9°, because the ions bombarding the surface at 90° would, in ideal case, only slide on the target surface. In Fig. 4.52a it is shown, that

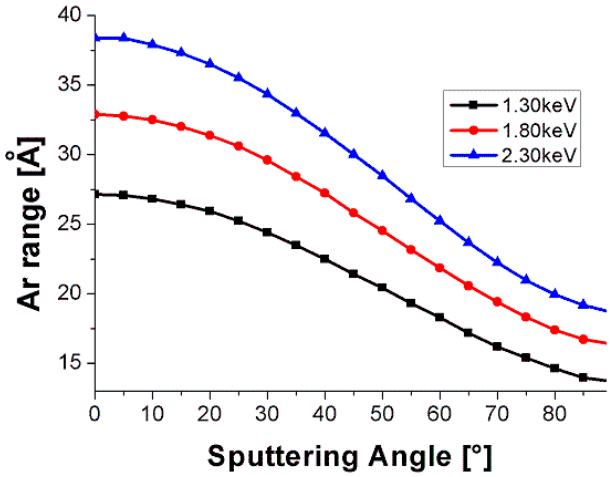

Figure 4.53: *Projected argon range (Ar^+ bombarding the titanium surface) as a function of the sputtering angle. The plot obtained by the means of the TRIM code.*

the sputtering yield depends strongly on the sputtering angle. For all the ion energies the lowest value of the sputtering yield is in the $0 - 10°$ range, and it is lower than 1.4. The highest value of the sputtering yield is in the $70 - 75°$ range. The Y depends also on the Ar^+ energy, and the higher the energy, to higher the sputtering yield Y.
Fig. 4.52b shows the calculations of the total target displacements caused by an impinging ion as the function of the sputtering angle. The displacement is every collision that causes a permanent dislocation of the target atom from its lattice site. The number of target displacements depends on the Ar^+ energy in that way that the higher the energy, the more target displacements per ion. In the range of $0 - 45°$, the number of target displacements is constant and it has the highest value. For the sputtering angles $> 45°$, the number of target displacements decreases for all the ion energies. It is crucial in the IBM to have the greatest number of the target displacements, because the target displacements are responsible for the mixing effect.
The sputtering angle of 0° is the best angle for the IBM purposes, because it results in the lowest sputtering yield Y, and it also provides the greater number of target displacements possible. That is why all the previously described IBM experiments were performed with the ion beam bombarding the target normal to its surface.
One could also consider the IBM at $\sim 85 - 89°$, because it gives a very low sputtering yield. But such an angle is not advisable, because it causes a very small number of the target displacements, so the mixing efficiency would be very low.

If Ar^+ ions bombard the target surface, they can penetrate into the bulk and get im-

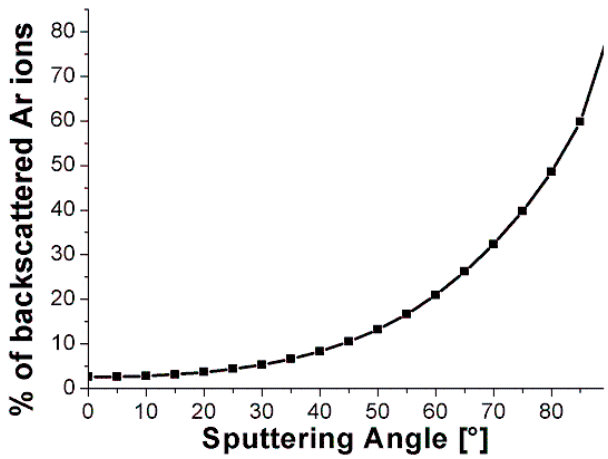

Figure 4.54: *The percentage of the backscattered argon ions as a function of the sputtering angle. The graph was obtained by the TRIM code.*

planted, or they can also be backscattered into the vacuum, because the ion-atom collision could change the ion direction and backscatter it. Both discussed effects - implantation and backscattering, depend on the sputtering angle and the ion energy. They also depend on the atomic masses of the ions and target atoms.
Fig. 4.53 presents the results of the TRIM calculation of the projected range of the implanted argon ions/atoms for three different argon energies: 1.30keV, 1.80keV and 2.30keV. The projected argon range depends strongly on the ion energy, and the higher the energy, the longer the ion range. The longest projected ion range is for the angle of $\sim 0°$, so one should expect relatively deep argon implantation during the IBM process.

The ion backscattering process is also considered by the TRIM calculations and Fig. 4.54 shows the number of backscattered ions (as the % of all the incident ions) as a function of the sputtering angle. The plot is an average taken for the three Ar^+ energies (1.30keV, 1.80keV and 2.30keV). At the sputtering angle of 0° there is less then 5% of all the incident argon ions backscattered into the vacuum. So during the IBM process the majority of Ar^+ ions (equal to $\sim 95\%$ of the ion dose) is implanted into the target material. Such an implantation supports the mixing process, because the more ions penetrate the bulk of the target, the more energy is transfered into the target atoms.
Summarizing: the best angle of ion incidence for the IBM is 0° (normal incidence), because it results in the lowest sputtering yield, greatest number of target displacements (efficient mixing), and only few per cent of the ions are backscattered. The best angle of ion incidence for the sputtering is $70 - 75°$, because it results in the highest sputtering yield, lower number of target displacements (so it does not disturb the crystal structure

	20ML	20ML	20ML	15ML	10ML
	2.30keV	1.80keV	1.30keV	1.30keV	1.30keV
Y	1.328	1.230	1.065	1.060	0.975
Ion range [Å]	41	34	28	30	35

Figure 4.55: *TRIM calculations of the sputtering yield and the projected ion range for different Ti/Si systems, that were studied experimentally.*

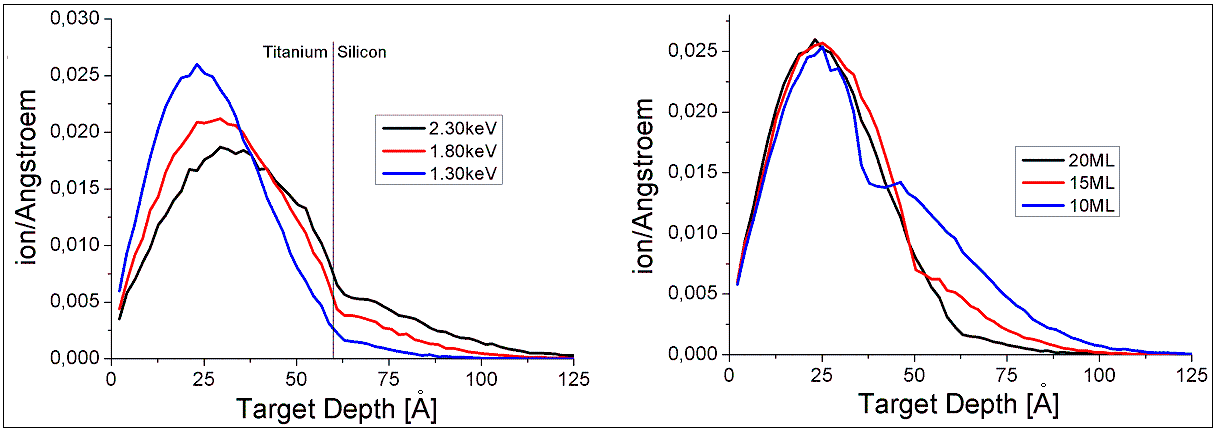

Figure 4.56: *Argon ion/atom distribution in the target for the constant Ti coverage (20ML) but different Ar^+ energy (a) and for the constant Ar^+ energy of 1.30keV and the different titanium coverage (b). The graph was obtained by the TRIM code.*

of the bulk) and a very low range of the implanted ions.

The Fig. 4.55 shows the detailed calculations of the sputtering yield and the projected ion range for the experimentally studied Ti/Si systems. For the Ti/Si systems with the same titanium coverage of 20ML the highest sputtering yield Y=1.328 was obtained for the highest Ar^+ energy $E = 2.30keV$, and the lower the Ar^+ energy, the lower the sputtering yield. For the Ti/Si systems bombarded with the constant Ar^+ energy of 1.30keV and covered with the different thickness of the Ti, the sputtering yield changes in such a way, that the lower the Ti coverage, the lower the sputtering yield.

4.7.2 Ion distribution in the target

Fig. 4.56 presents the calculated final Ar distribution in the target (after the samples have been irradiated with the 100000 ions). The calculations were performed for a constant Ti coverage (20ML) but different Ar^+ energy (a), and for a constant Ar^+ energy, but different titanium coverage (b). The thickness of the 20ML of Ti was estimated to be $\sim$ 60Å and the interface between the Ti and the Si is marked in Fig. 4.56a. All the plots presented in this figure have a significant peak in the Ti region, which corresponds to the projected ion range. The highest projected ion range have the ions with the highest 2.30keV energy ($\sim$ 41Å). For the lower Ar^+ energies the projected ion range is shorter - 34Å for 1.80keV, 28Å for 1.30keV (see Fig. 4.55). The peaks for higher ion energies are also broader, which indicates that the argon concentration is more homogeneous. At the interface between the Ti and the Si all the graphs have a shoulder. The shoulder is due to the difference in the bulk density between the titanium and the silicon. Titanium bulk density is $4.5189 g/cm^3$ and it is larger than that of the Si - $2.3212 g/cm^3$. So it is much easier for the Ar^+ ions to travel through the silicon than through the titanium, because argon ions experience less nuclear collisions in silicon. That is why the shoulder in the silicon region has a more gentle slope.

Fig. 4.56b presents the ion distribution for the same ion energy (1.30keV), but different Ti coverages. All the graphs also have shoulders at the interface of the Ti and the Si. All the peaks are located also in the titanium region, even for the thinnest Ti layers. So the titanium acts as a good barrier for the ions and prevents them from penetrating into the silicon. The projected ion ranges are very similar for all the coverages: 20ML - 28Å, 15ML - 30Å, 10ML - 35Å.

The TRIM simulations presented in Fig. 4.56 show that for all the performed IBM experiments the titanium acts as a barrier for the ions, and most of the Ar is implanted shallow in the Ti region. The advantage of this phenomenon is that the Ar^+ ions do not penetrate deeply into the bulk of the silicon and they do not destroy its crystal structure.

4.7.3 The distribution of the absorbed energy

Fig. 4.57 presents the calculated distribution of the ion energy absorbed by the target atoms. The graph presents the calculations performed for the same titanium coverage of 20ML, but different Ar^+ energies, and the same ion energy, but different Ti coverages. All the graphs show that most of the kinetic energy of the ions is always absorbed in the very surface region, approximately up to 10Å. So the Ar^+ ions lose their kinetic energy by the nuclear collisions with the surface atoms, because the nuclear stopping power dominates

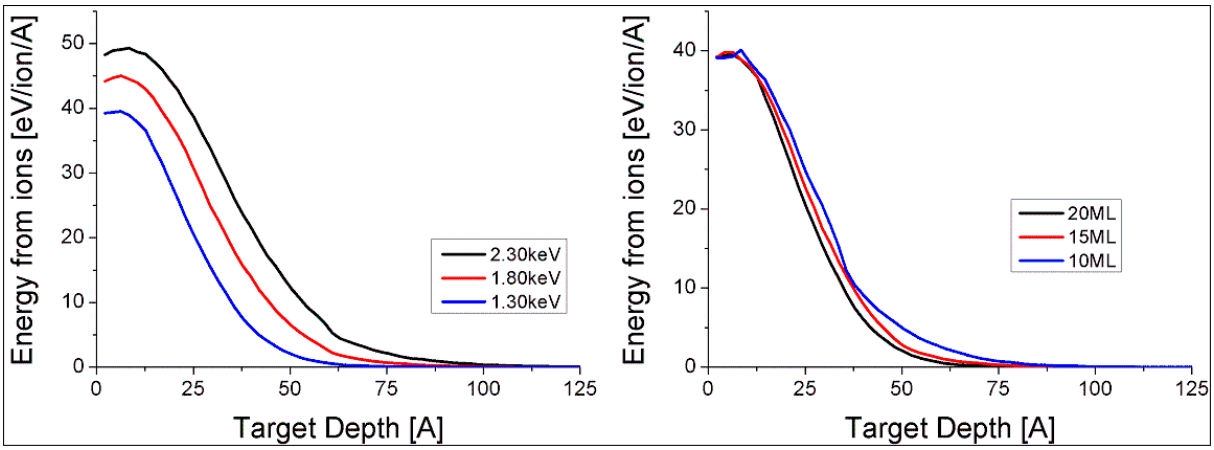

Figure 4.57: *Energy from ions absorbed by the target atoms calculated with the TRIM code. The graphs show the calculations for the same Ti coverage of 20ML and different ion energies, and the same ion energy (1.30keV) but different Ti coverage.*

this process (Fig. 4.26). Such an energy loss prevents the ions from penetrating deeply into the bulk, so their projected ion range is short (Fig. 4.56). The target atoms absorb the kinetic energy and then they can form collision cascades that transfer the kinetic energy toward the Ti/Si interface and they contribute to the mixing process.

As it has been already discussed, the Ar ions loose their kinetic energy mainly due to the nuclear collisions with the target atoms. Such a collision may result in the relocations of the target atoms, but the ion energy could be also used to increase the energy of the phonons. If a target atom was hit by another atom (or ion) it could be relocated from its lattice site, if the gained energy is greater than the displacement energy. If the gained energy is lower than the displacement energy, the atom will only oscillate around its equilibrium state and would not be able to move one atomic spacing away from its original site. In this case the atom energy contributes to the phonon energy of the studied crystal. The phonon energy can be increased not only by the native target atoms, but also by the ions that are implanted into the target during the IBM process.

Fig. 4.58 presents the distribution of the ion energy loss (Fig. 4.58a) and the recoil energy loss (Fig. 4.59b) on phonons calculated with the TRIM code for the 20ML–Ti/Si system for the three different Ar^+ kinetic energies. The ions produce the phonons mainly in the near surface region. For all the three Ar^+ energies the ion energy loss peaks have maxima not deeper than 25Å and the higher the energy, the broader and the lower the peak. The recoils also contribute to the phonons (Fig. 4.58b), but they loose the energy

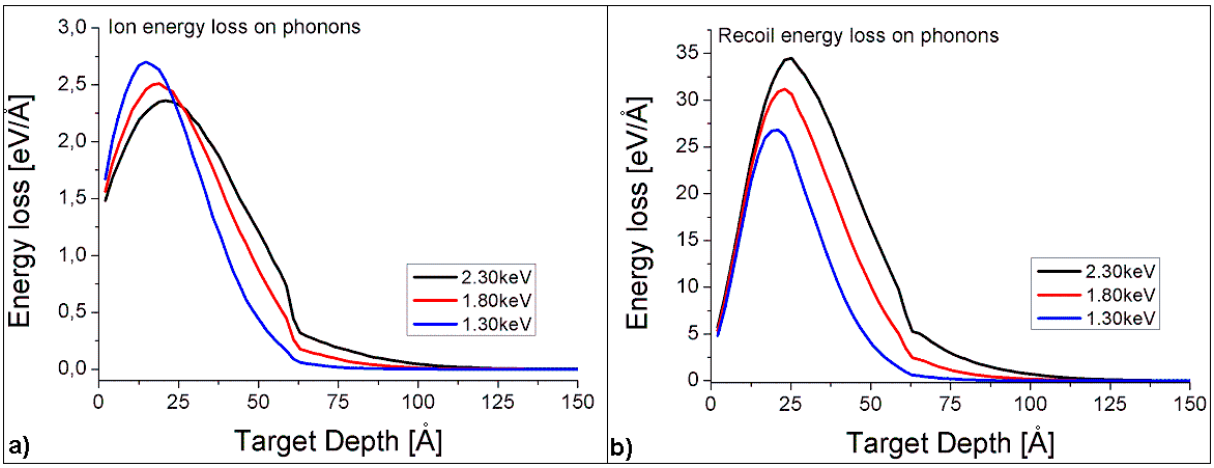

Figure 4.58: *Ion energy loss on phonons (a) and recoil energy loss on phonons (b) calculated for the three different Ar^+ kinetic energies (1.30keV, 1.80keV and 2.30keV) for the IBMed 20ML–Ti/Si bilayers.*

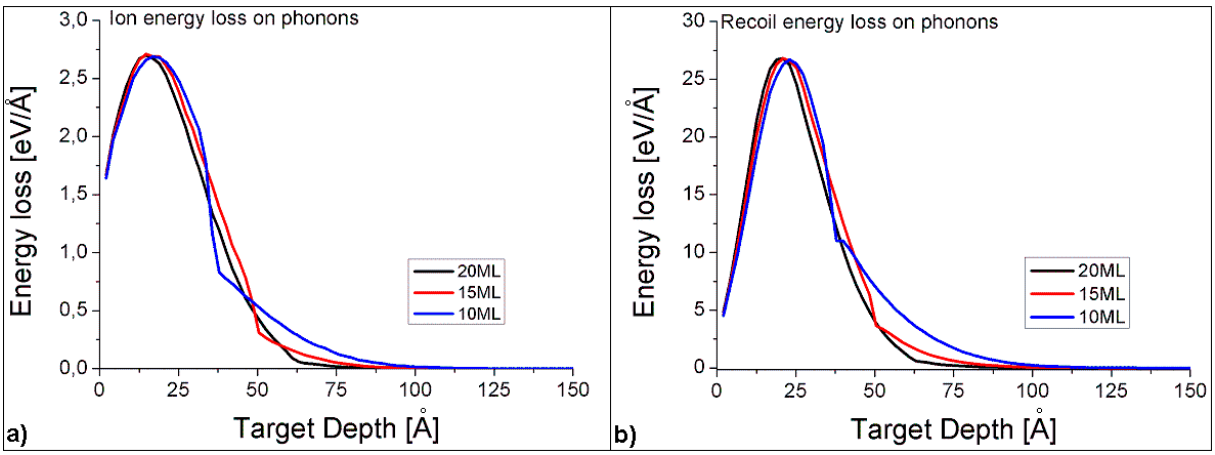

Figure 4.59: *Ion energy loss on phonons (a) and recoil energy loss on phonons (b) calculated for the different titanium coverages (20ML, 15ML and 10ML) for the Ti/Si system IBMed with Ar^+ at 1.30keV*

on phonons deeper than ions - the maxima of the energy lose peaks are deeper than 25Å. The recoils transfer on average 10 times more energy to the phonons, than the ions do. Fig. 4.59 shows the distribution of the ion energy loss (Fig. 4.59a and the recoil energy loss (Fig. 4.59b on phonons calculated with the TRIM code for the Ti/Si system bombarded with the Ar^+ at 1.30keV for different titanium coverage. The ion energy loss and the recoils energy loss does not depend significantly on the titanium coverage. The ions lose maximum energy on phonons at $\sim$ 16Å, which is always in the titanium region for all the simulated systems. The maximum value of the recoil energy loss is at $\sim$ 22Å

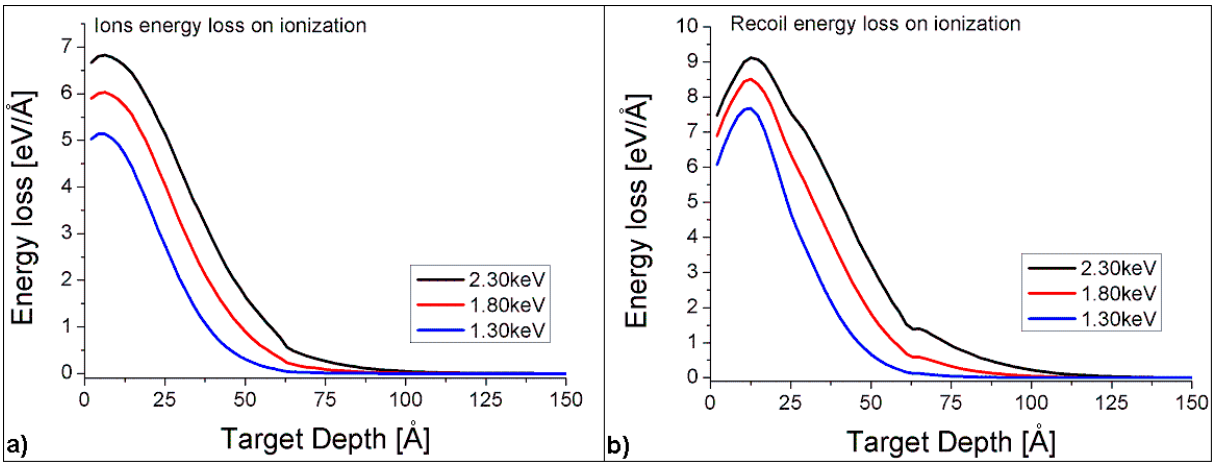

Figure 4.60: *Ion energy loss on ionization (a) and recoil energy loss on ionization (b) calculated for the three different Ar^+ kinetic energies (1.30keV, 1.80keV and 2.30keV) for the IBMed 20ML–Ti/Si bilayers.*

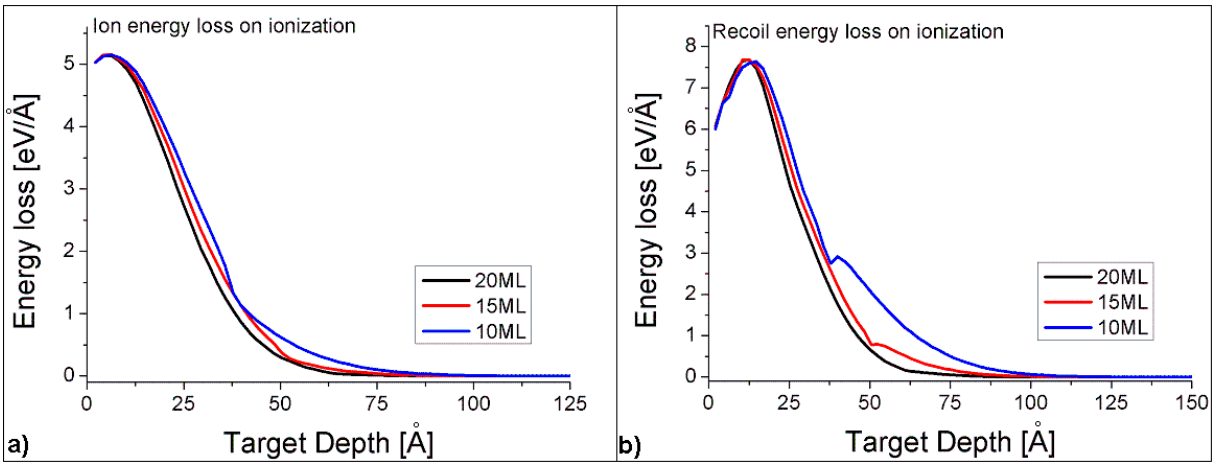

Figure 4.61: *Ion energy loss on ionization (a) and the recoil energy loss on ionization (b) calculated for the different titanium coverages (20ML, 15ML and 10ML) for the Ti/Si system IBMed with Ar^+ at 1.30keV*

and this is also independent on the titanium coverage. Also in this case the recoils loose approximately 10 times more energy on phonons than the ions.

The ion energy transfered into the target material may be also used to create secondary ions. An argon ion, while penetrating the target, may collide into an atom, and the collision process may result in ejecting an electron from the atom (ionization). The ionization process may be also supported by the recoils, which also take part in the collision process in the target.

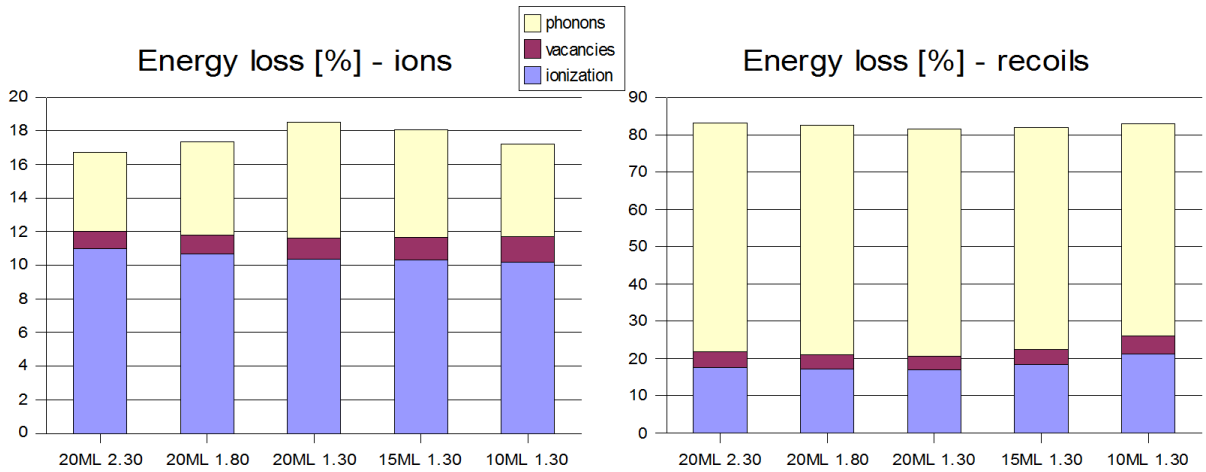

Figure 4.62: *Energy loss for ions and recoils.*

Fig. 4.60 shows the calculation of the energy loss on ionization, performed for the 20-Ti/Si target bombarded with the three different Ar^+ kinetic energies. For all the three Ar^+ energies, the ions create the ions mainly at the surface (Fig. 4.60a). The deeper into the target, the ion energy loss on ionization decreases in a linear-like way. The maximum of the recoil energy loss is at $\sim$ 12Å (Fig. 4.60b). The maximum values of the ion and recoil energy loss are of the same order, and the higher the Ar^+ energy, the higher the energy loss.
Fig. 4.61 presents the results of the calculation of the energy loss on ionization, performed for the Ti/Si system bombarded by the Ar^+ at 1.30keV, but covered in different thickness of the titanium (20ML, 15ML and 10ML). Fig. 4.61a shows the ion energy loss on ionization. The ion energy loss does not depend significantly on the titanium coverage, and the maximum value of the energy loss is at the very surface region. The recoil energy loss also does not depend strongly on the thickness of the titanium layer (Fig. 4.61b). The maximum value of the recoil energy loss is at $\sim$ 12.5Å. The graphs for 10ML and 15ML have a shoulder at the interface of the Ti and the Si. There is no shoulder for 20ML.

Fig. 4.62 gives the summary of the energy loss calculations and shows how much energy (in per cents) an average ion and an average recoil loses its energy on. The calculations were performed in order to simulate all the studied Ti/Si systems (with different Ti coverage and different Ar^+ energy). For all the examined systems an average ion loses approximately 10% of its energy on the ionization process, 4-6% is given to the phonons, and $\sim$ 2% of the energy is used to create the vacancies in the target. So the greatest amount of the ion energy is used to create other ions (ionization). It happens because

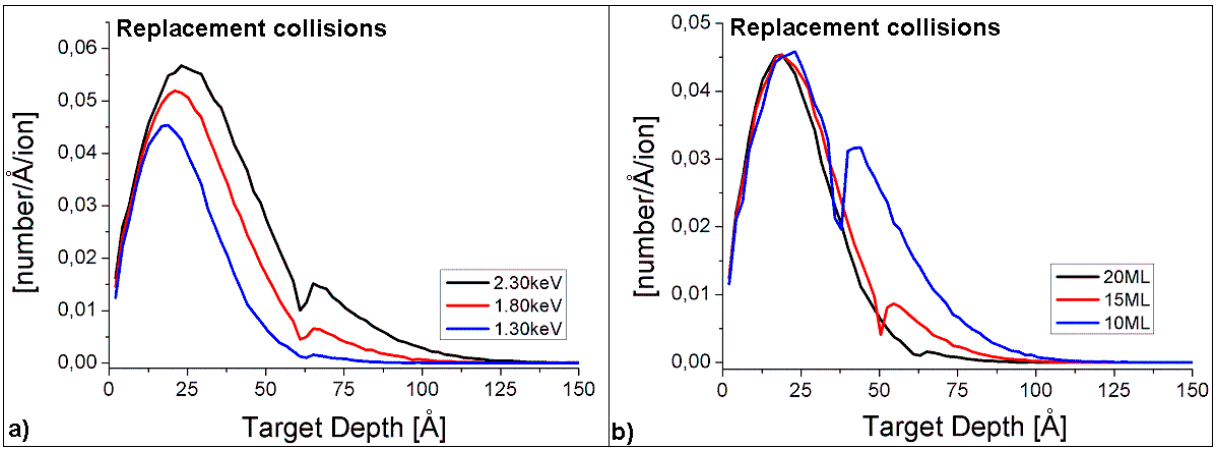

Figure 4.63: *Replacement collisions calculated for the IBMed Ti/Si system for the constant titanium coverage of 20ML, but the different Ar^+ energy (a) and for the constant Ar^+ energy, but the different Ti coverage (b).*

the positively charged Ar ion moves through the matter, attracts the electrons from the target atoms, collects them and finally becomes an atom, what is the main driving force of the ionization process.

The recoils transfer approximately 60% to phonons, they lose about 18-21% on ionization, and $\sim$ 3% on the creation of the vacancies.

The Fig. 4.62 shows, that the ions lose about 18% of their whole energy, and the recoils loose about 85% of their whole energy. The ions loose only $\sim$ 18% according to the calculations, because they contribute to the ionization process and they transform into atoms. After they have been transformed into atoms, they are not considered by TRIM in the ion statistics, but in the recoil statistics. So an average ion becomes an atom after it has lost $\sim$ 18% of its energy. An average Ar^+ ion should become an atom after it has travelled $\sim$ 10Å through the target, because the ions lose most of their energy in the very surface region (see Fig. 4.57), and the ionization process is also most intensive there (Fig. 4.60 and 4.61).

4.7.4 Collision events

The distribution of the replacement collision events in the target, caused by the ion bombardment, was calculated with the TRIM code and the results are presented in Fig. 4.63. Fig. 4.63a shows the distribution of the replacement collisions calculated for the constant Ti coverage of 20ML, but for the three different Ar^+ energies - 1.30keV, 1.80keV and

2.30keV. The higher the Ar^+ energy, the more replacement collisions in the target take place. The maximum number of the replacement collisions is in the titanium region, and the higher the Ar^+ kinetic energy, the deeper the maximum. Another peak appears at $\sim$ 64Å - almost at the Ti/Si interface. This peak appears due to the difference in the displacement energy between the titanium (25eV) and the silicon (15eV) [77]. The titanium has a bigger displacement energy, so the same amount of kinetic energy transferred into the cluster of titanium atoms would cause lower number of displacements than in the case of silicon atoms. That is why at the interface of the Ti/Si another peak appears. The existence of this peak at the Ti/Si interface is desirable, because the more collision events at the interface, the better mixing of the two elements. The highest peak at the interface is observed for the highest Ar^+ energy of 2.30keV. It agrees well with the previous experiments, in which the fastest titanium silicide phase transformation was observed also for this system (see Fig. 4.38).
Fig. 4.63b shows the distribution of the replacement collisions calculated for the constant Ar^+ energy, but for different titanium coverages (20ML, 15ML and 10ML). The highest peak (the greatest number of the replacement collisions) is at $\sim$ 19Å and it is independent on the titanium coverage. The second peak appears at the Ti/Si interface, and its position depends, of course, on the titanium thickness. This peak is the highest for the lowest titanium coverage (10ML). It stands in a good agreement with the experimental results (Fig. 4.47), where it was observed, that the fastest silicide phase transformation takes place for the thinnest titanium coverage.

4.8 Mixing rate

In this section the calculations and the measurements of the mixing rate of the Ti/Si bilayers IBMed with the Ar^+ are presented. The theoretical calculations are compared with the experimental results and the conclusions about the mixing regime are given.

4.8.1 Mixing rate calculations

The mixing rate for the Ti/Si system IBMed with the Ar^+ ions was calculated according to the compound formation model for the IBM [19], described in the 'Fundamentals' section. The calculations were performed for the mixing rate in the ballistic mixing regime and in the thermal spike regime.

Mixing rate in the ballistic mixing regime

The mixing rate in the ballistic (collision cascades) mixing regime at the boundary of the two elements is described in the Eq. 2.19. The Equation 2.19 assumes, that only one element (A atom) is a mobile species. In case of the Ti/Si system the silicon is the mobile species, because it has significantly lower displacement energy and lower the lattice binding energy [77]. The expression for the mixing rate in the ballistic mixing regime can be written as:

$$k_{ball} = \frac{X^2}{\phi} = \{2C_{Si}/[a/(a+b)]C_{54}\} \cdot [(0.2F_D/C_{54})(\mu^{1/2})(\frac{\lambda^2}{E_{dSi}})] \tag{4.1}$$

where
$a = 1$, $b = 2$ - stoichiometry of the $TiSi_2$
$E_{dSi} = 15eV$ - the displacement energy of the Si (taken from the TRIM database)
F_D - the density of the deposited energy at the Ti/Si interface calculated with the TRIM
$\lambda = 1nm$ - a stable distance between a vacancy and an interstitial [19]
$C_{Si} = 0.0489at/Å^3$ - the atomic concentration of the silicon
$C_{54} = 0.071at/Å^3$ - the atomic concentration of the C54 $TiSi_2$
and

$$\mu = \frac{4M_{Si} \cdot M_{Ti}}{(M_{Si} + M_{Ti})^2} \tag{4.2}$$

where
$M_{Si} = 28amu$ - the atomic mass of the Si
$M_{Ti} = 48amu$ - the atomic mass of the Ti

The mixing rate in the ballistic mixing regime was calculated according to the Eq. 4.1 for all the experimentally studied Ti/Si systems, and the results are presented in the Table 4.1. The value of the mixing rate is different for different Ti/Si systems, because they have different density of the deposited energy F_D (Table 4.1). The density of the deposited energy at the Ti/Si interface depends on the Ar^+ kinetic energy so that the higher the ion energy, the higher the F_D. And the lower the Ti coverage, the higher the F_D, because the titanium acts as a barrier for the ions and for the collision cascades on their way to the interface. The mixing rate is proportional to the F_D, so the higher the F_D, the higher the mixing rate k_{ball}.
For the Ti/Si systems covered by 20ML of Ti and IBMed with different Ar^+ energies, the highest values of the k_{ball} and the F_D were calculated for the system bombarded with the highest Ar^+ energy of 2.30keV. And if the Ar^+ energy decreases, so does the k_{ball} and the

F_D.
For the Ti/Si systems IBMed with the constant Ar^+ energy of 1.30keV, but covered with different titanium thickness, the highest value of the k_{ball} and the F_D was calculated for the system with the lowest Ti coverage of 10ML. The values of the k_{ball} and the F_D decrease with the increasing titanium coverage.

Mixing rate in the thermal spike regime

The mixing rate in the thermal spike regime at the interface of the two elements is given by the Eq. 2.20, according to the compound formation model for the IBM [19]. This equation in the case of the Ti/Si system can be written as:

$$k_{TS} = \frac{X^2}{\phi} = \{2C_{Si}/[a/(a+b)]C_{54}\} \cdot [K_1 F_d^2/(C_{54}^{5/3}\Delta H_{coh}^2)] \tag{4.3}$$

where
$K_1 = 0.0035nm$ - the parameter, its value suggested in [19]
$\Delta H_{coh}^2 = 22.52eV^2/at^2$ - the average cohesive energy of the Ti/Si system squared. The ΔH_{coh} was calculated as an average value of the cohesive energy of the silicon $\Delta H_{coh-Si} = 4.62eV/at$ [41] and the cohesive energy of the titanium $\Delta H_{coh-Ti} = 4.87eV/at$ [35]
and the μ is described in the Eq. 4.2.

The mixing rate in the thermal spike regime was calculated according to the Eq. 4.3 for all the experimentally studied Ti/Si systems and the results are presented in the Table 4.1.
For the Ti/Si systems covered in 20ML of Ti and IBMed with different Ar^+ energies, the highest values of the k_{TS} was obtained for the system bombarded with the highest Ar^+ energy of 2.30keV. And when the Ar^+ energy decreases, so does the mixing rate k_{TS}.
For the Ti/Si systems IBMed with the constant Ar^+ energy of 1.30keV, but covered with different titanium thicknesses, the highest value of the k_{TS} was calculated for the system with the lowest Ti coverage of 10ML. The values of the k_{TS} decrease with the increasing titanium coverage.

Ti coverage	**20ML**	**20ML**	**20ML**	15ML	10ML
Ar^+ kinetic energy	2.30keV	1.80keV	**1.30keV**	**1.30keV**	**1.30keV**
$\mathbf{F}_D[eV/\text{Å}]$	5.90	2.59	0.59	3.47	13.38
$\mathbf{k}_{ball}$ $[nm^4]$	4.57	2.01	0.46	2.69	10.36
$\mathbf{k}_{TS}$ $[nm^4]$	183.72	35.41	1.84	63.54	944.88

Table 4.1: *The calculated mixing rate of the Ti/Si in the ballistic mixing regime (k_{ball}) and in the thermal spike regime (k_{TS}). The density of the deposited energy F_D at the Ti/Si interface was calculated with the TRIM.*

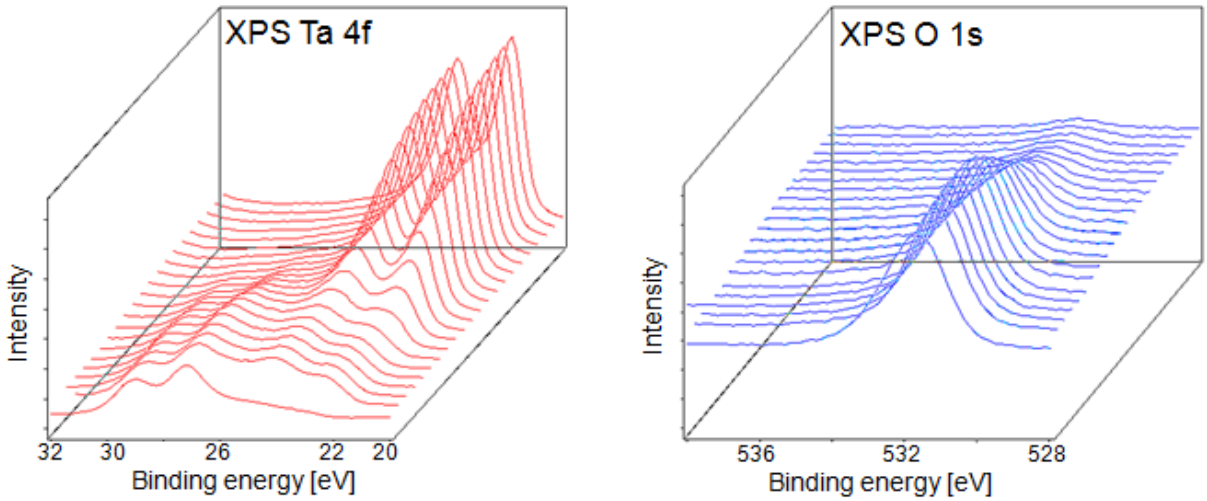

Figure 4.64: *XPS spectra of the Ta 4f and the O 1s taken during the depth profiling of the Ta_2O_5/Ta sample.*

4.8.2 Mixing rate measurements

This section presents the measurements, from which the mixing rate of the 20ML–Ti/Si IBMed with Ar^+ at 1.30keV was obtained. The mixing rate is the parameter of the IBM process that describes how the thickness of the IBMed interface changes with the ion dose. Therefore it was needed to IBM Ti/Si samples with different ion doses and then depth profile them. From the depth profiles one can obtain the thickness of the interface and compare it for different ion doses.

The depth profiling experiments were done using an Ar^+ ion beam at 3.0keV with 45° to the target surface, the argon pressure was kept constant and equal to $2.0 \cdot 10^{-7} mbar$. It was not known how the ion beam of this particular parameters sputters the crater in the

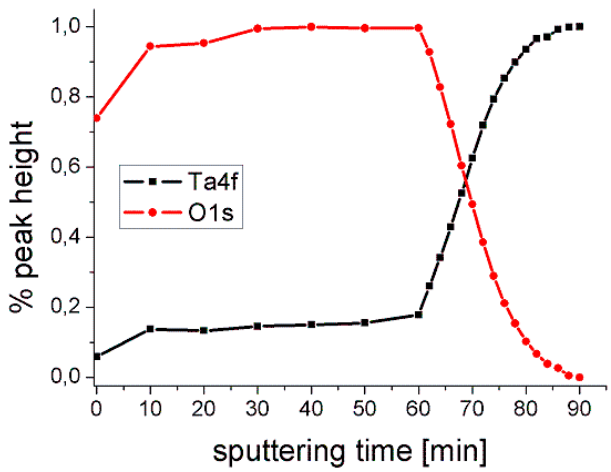

Figure 4.65: *Depth profile of the Ta_2O_5/Ta sample showing the XPS peak heights of the Ta $4f_{7/2}$ and the O 1s as a function of the sputtering time.*

target, so the reference sample of the native tantalum oxide was depth profiled in order to estimate the sputtering speed. The thickness of the native Ta_2O_5 on the Ta substrate is well known and equal to 1000Å. Fig. 4.64 shows the results of the depth profiling with the XPS of the Ta_2O_5/Ta. The XPS spectra of the Ta 4f and the O 1s were taken after each sputtering step. The sputtering step was set to $10min$ for the first six sputtering steps, and then the it was set to $2.0min$. The difference between the oxidised Ta and the pure Ta is very well pronounced, so there is no doubt when the Ta_2O_5/Ta interface was reached. The Ta $4f_{7/2}$ and the O 1s peak heights were measured after each sputtering step and they were plotted as a function of the sputtering time (Fig. 4.65). The depth profile presented in Fig. 4.65 shows that the amounts of the O 1s and the Ta $4f_{7/2}$ are almost constant in the first 60 minutes of the process, so it means the ion beam drills through the Ta_2O_5 layer. After 60 minutes of the sputtering process the amount of the O 1s decreases, and the amount of the Ta $4f_{7/2}$ increases, what indicates, that the Ta_2O_5/Ta interface was reached.

The sputtering yield of the 1000Å of the Ta_2O_5 is different than the sputtering yield of the 1000Å thick $TiSi_2$, because these two materials have different surface binding energies and the lattice binding energies (according to the TRIM database [77]). The sputtering yields of the Ta_2O_5 and the $TiSi_2$ were calculated with the TRIM and they are equal to: $Y_{Ta_2O_5} = 7.788$ and $Y_{TiSi_2} = 3.870$. The ratio $\frac{Y_{Ta_2O_5}}{Y_{TiSi_2}} = 2.012$ indicates, that a $TiSi_2$ layer would be sputtered approximately two times slower than the Ta_2O_5 layer of the same thickness. With this knowledge the thickness of the depth profiled Ti/Si samples was estimated in all the experiments shown below.

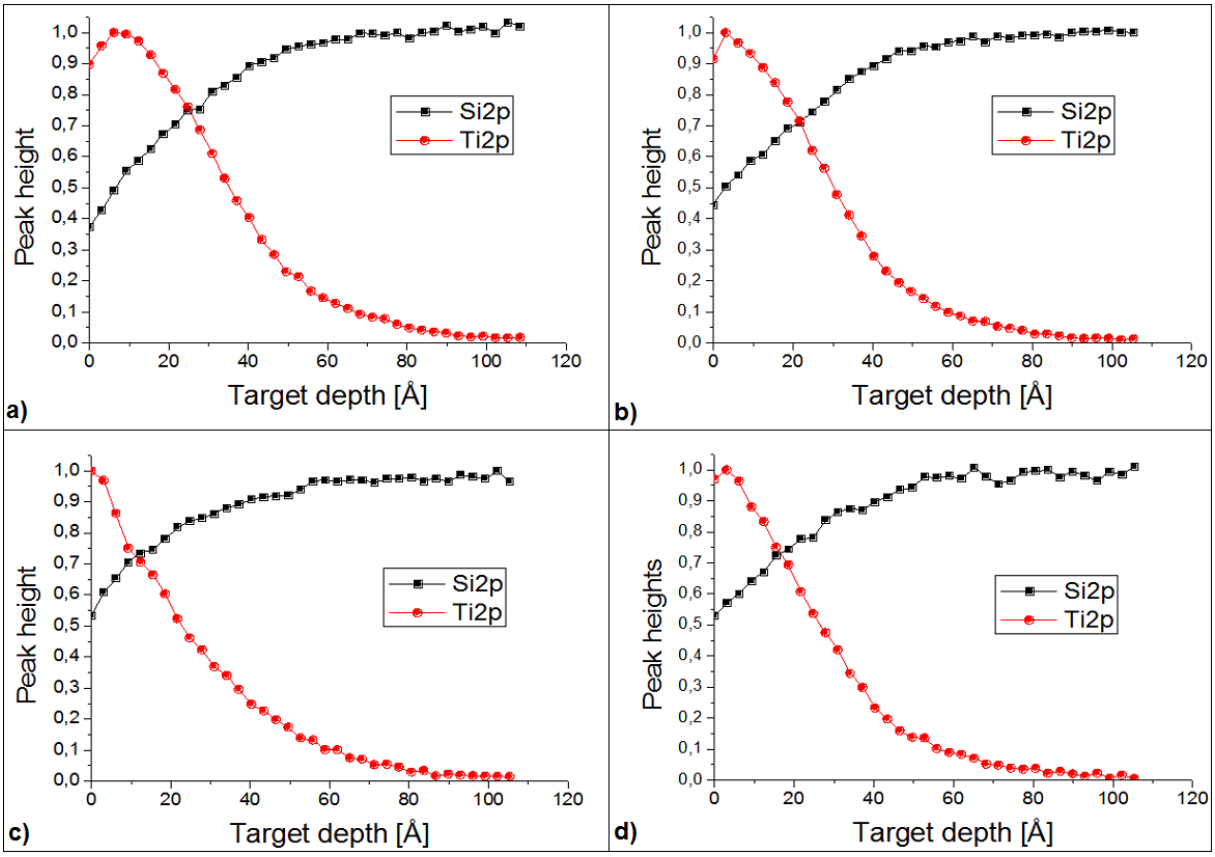

Figure 4.66: *Depth profiles of the 20ML–Ti/Si interface IBMed with the* Ar^+ *at 1.30keV with different ion doses:* $9 \cdot 10^{14} Ar/cm^2$ *(a),* $1.5 \cdot 10^{15} Ar/cm^2$ *(b),* $2.5 \cdot 10^{15} Ar/cm^2$ *(c) and* $3.5 \cdot 10^{15} Ar/cm^2$ *(d).*

Fig. 4.66 presents the results of the depth profiling of the four 20ML–Ti/Si samples, that were IBMed with Ar^+ at 1.30keV with different ion doses: $9 \cdot 10^{14} Ar/cm^2$(4.66a), $1.5 \cdot 10^{15} Ar/cm^2$(4.66b), $2.5 \cdot 10^{15} Ar/cm^2$(4.66c) and $3.5 \cdot 10^{15} Ar/cm^2$ (4.66d). From each of the depth profiles presented in Fig. 4.66 the thickness of the interface was calculated as the difference of the silicon concentration from 55% to 95%. The silicon was considered here in the calculation, because it is the mobile species in the Ti/Si system, and it diffuses into the titanium layer. So the changes in the silicon concentration are more relevant to the mixing process.

The thickness of the interface obtained from the results presented in Fig. 4.66 was squared and plotted in Fig. 4.67 as a function of the ion dose. The measurement points form a linear function, and the slop of the function is the mixing rate of the studied Ti/Si system, and it is equal to $k_{exp} = 0.647 nm^4$.

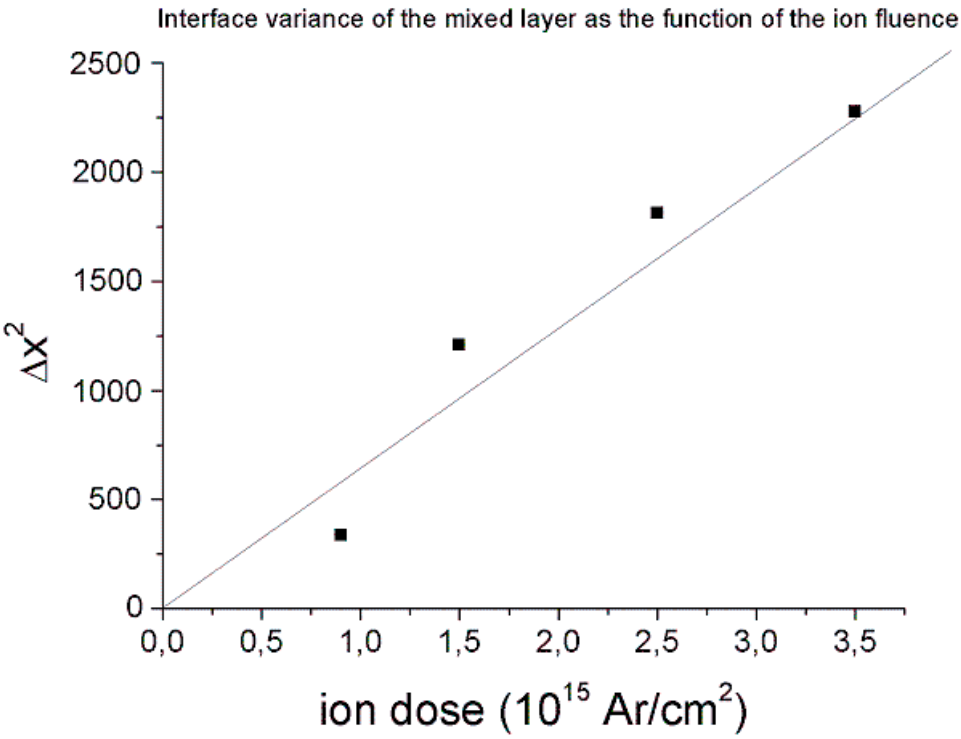

Figure 4.67: *Interface variance of the mixed Ti/Si bilayers as the function of the ion fluence.*

4.8.3 Conclusions

One should compare the theoretically calculated values of the mixing rate in the ballistic mixing regime and in the thermal spike regime of the 20ML–Ti/Si IBMed with Ar^+ at 1.30keV (Table 4.1) with the experimentally obtained value. The value of the mixing rate obtained from the experiments is $k_{ball} < k_{exp} < k_{TS}$, but the difference between the k_{exp} and the k_{TS} is $\sim 1.20nm^4$, and the difference between the k_{exp} and the k_{ball} is only $0.18nm^4$. It means the ballistic mixing dominates the process and only very few thermal spikes are expected.

The mixing process of the 20ML–Ti/Si IBMed with the Ar^+ at 1.30kV is a diffusion-controlled process, because the interface variance as the function of the ion dose is a linear function (Fig. 4.67). It means that the titanium silicide formation and the growth of the silicide layer is not influenced by the kinetics of the chemical reaction between the titanium and the silicon. The growth speed of the titanium silicide layer depends only on the diffusion of the silicon into the titanium region.

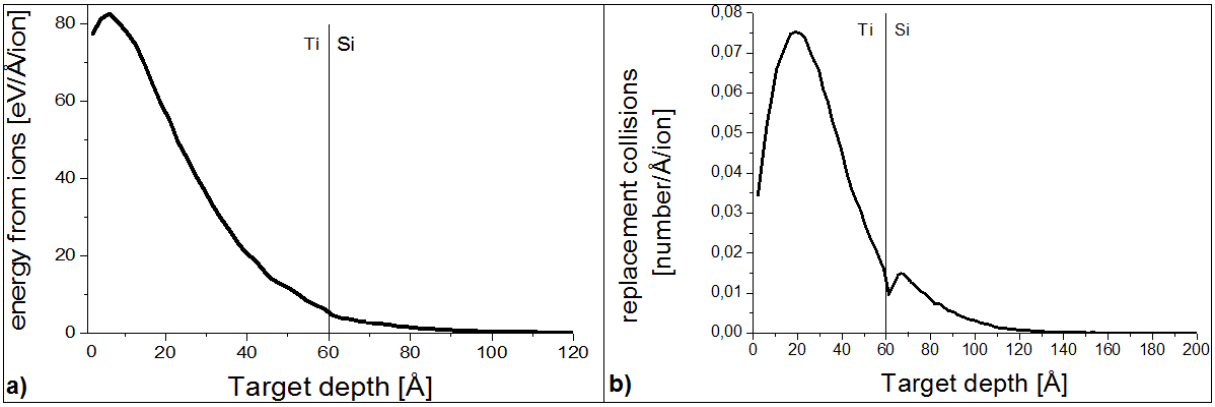

Figure 4.68: *The distribution of the energy absorbed by the target atoms from ions (a) and the distribution of the collision events (b) during the bombardment of the Ti/Si system with the* Ar^+ *ion beam at 45° to the target surface.*

Uncertainty of the depth profiling measurements

Every measurement method changes the measured objects, also in the case of the depth profiling experiments presented above. The depth profiling involves bombarding the target surface with the ions in order to sputter the material and then study the chemical composition of the uncovered layers. The ion beam in this case should cause the sputtering effect, and the ion mixing effects are not desired. In case of the depth profiling experiments presented above, the ion beam was positioned at 45° to the target surface (because of the geometry of the UHV chamber) and the Ar^+ ions bombarded the surface with the energy of 3.0keV. Some part of the ion energy in this process is used for sputtering the target atoms. But some part of the kinetic energy of the ions transferred into the target atoms would not cause the sputtering of the atom, but its movement in the direction of the interface - it would support the mixing effect. The TRIM calculations of the ion bombardment of the 20ML–Ti/Si with Ar^+ at 3.0keV at 45° to the sample surface were performed in order to simulate the depth profiling process. The simulation does not correspond exactly to the real experiment, because the samples had been IBMed before they were depth profiled, so they consist of the mixture of different titanium silicides. But the simulation gives an idea how the ion beam of such parameters influences the sample. According to the TRIM simulation, the depth profiling process results in a high sputtering yield $Y = 2.82$, and the projected range of the implanted argon ions of 36.7Å. The distribution of the energy absorbed by the target atoms from argon ions is presented in Fig. 4.68a. The greatest amount of the energy is absorbed by the target atoms in the very surface region (up to 10Å), which supports the sputtering effect. The energy absorbed by

the surface atoms is also used to relocate the atoms towards the Ti/Si interface, which results in a high number of the replacement collisions (Fig. 4.68b) deeper in the target at $\sim$ 20Å. The number of the replacement collisions decreases towards the interface, but right after the Ti/Si interface (at about 70Å) another peak appears, what indicates there is an intermixing at the interface region.
So the depth profiling process contributes to the interface mixing and to the titanium silicide formation. Since all the depth profiled samples received the same treatment (were depth profiled under the same conditions), the influence of the depth profiling should be almost the same for each sample. That is why the calculation of the changes in the interface thickness between different samples should be correct. But no titanium silicide phase analysis was done, because the depth profiling experiment supports the interface mixing and changes the titanium silicide phase.

The studied Ti/Si system differs a little bit from the A/B system proposed by J. Desimoni and A. Traverse [19] and described in the 'Fundamentals' section. The Desimoni and Traverse model assumes that the interface between the A and B elements is buried under the very thick layer of A and the ion-induced mixing appears there. The model neglects the sputtering effects that appear on the ion bombarded surface of A. In case of the studied Ti/Si system, the titanium layer is very thin, so the sputtering plays a more important role during the IBM process. The interface of the IBMed Ti/Si system is in the surface region (its evolution is studied by the surface sensitive techniques - XPS, UPS), so it broadens because of the ion-mixing effects, but at the same time it also gets thinner because of the sputtering. That is the reason why all the mixing rate measurements were performed for the relatively low ion doses, because for the low ion doses, the sputtering effect is less significant.

4.9 Electrical properties of the IBMed Ti/Si

The electrical properties of the IBMed Ti/Si interfaces were studied ex-situ by the means of TLM. The samples were prepared in-situ according to the following procedure: silicon samples were introduced into the UHV, degassed, sputter–cleaned, 20ML of Ti were deposited at room temperature and then the samples were IBMed in order to form titanium silicides. After the IBM process the samples were studied with the XPS, and then covered with 50ML of Ti. Then the samples were taken out from the UHV chamber and transported to Infineon Technologies in Villach in order to perform the TLM measurements.

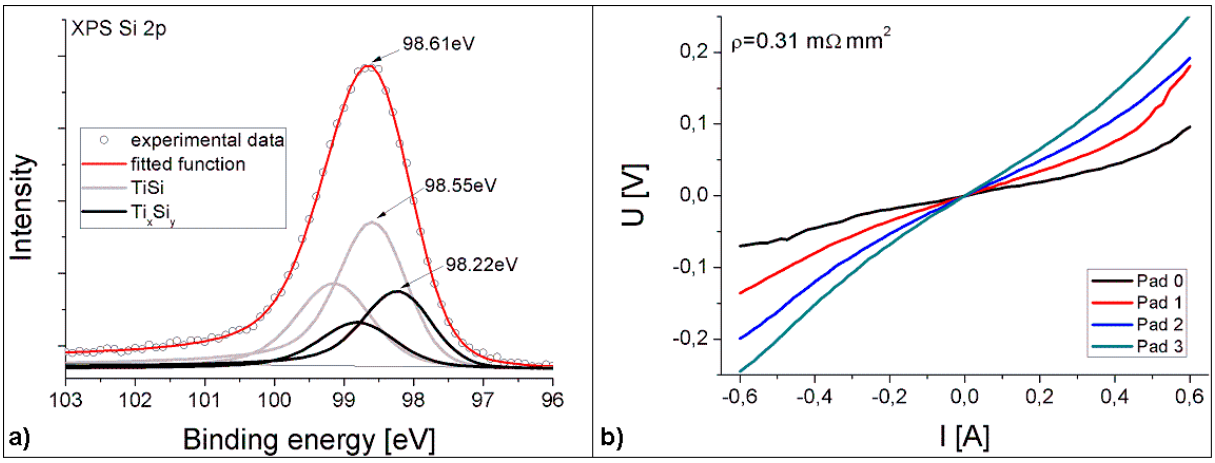

Figure 4.69: *XPS (a) and TLM (b) measurements of the 20ML–Ti/Si sample IBMed at room temperature with the Ar^+ at 1.30keV. Ion dose was $\phi = 29.6 \cdot 10^{15} ions/cm^2$, substrate: n-type Si(100).*

The 50ML-thick titanium layer acts as a capping layer that protects the titanium silicides from oxidization and contamination that would occur after the samples have been exposed to the atmosphere.

The first IBMed sample received the Ar^+ dose of $\phi = 29.6 \cdot 10^{15} ions/cm^2$ at the ion energy of 1.30keV. The results of the XPS measurement of the Si 2p are presented in Fig. 4.69a. After the ion bombardment the Si 2p is positioned at $98.61eV$. The detailed titanium silicide phase analysis by fitting the XPS Si 2p peak shows that the sample consists of a mixture of silicides, but the TiSi is a dominant phase. The second identified silicide phase represents the metastable Ti_xSi_y titanium silicide. The TLM measurements (Fig. 4.69b) show that the I-U characteristics of the electrical contact is linear, so the contact is ohmic. The obtained specific contact resistance is $\rho = 0.31 m\Omega \cdot mm^2$ and this value is of the same order as the resistance of the contacts formed by thermal annealing (see Fig. 4.20, Fig. 4.23 and Fig. 4.24), but higher than the resistance of C49 $TiSi_2$ and C54 $TiSi_2$.

The ion beam mixing process involves the ion implantation and the ion doses used in the experiments described in this work are relatively high (of the order of $10^{15} ions/cm^2$). Since argon is a noble gas, it does not react chemically with the target atoms. But does the presence of argon influence the resistivity? According to the TRIM calculations the projected ion range, in the case of the 1.30keV ion energy and the 20ML titanium coverage, is $\sim$ 28Å (Fig. 4.56), so most of the ions do not penetrate into the bulk of the silicon. Usually the argon can be removed from the sample by annealing/flashing the sample, so

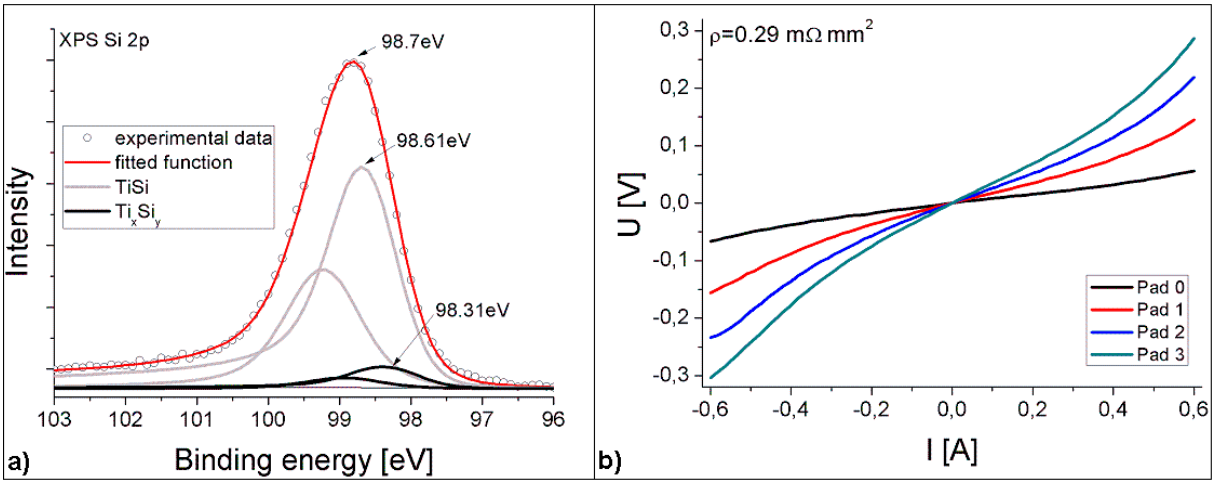

Figure 4.70: *The XPS (a) and the TLM (b) measurements of the 20ML–Ti/Si sample IBMed at room temperature with the Ar^+ at 1.30keV, and then annealed at 350° for 12min. Ion dose was $\phi = 29.6 \cdot 10^{15} ions/cm^2$, substrate: n-type Si(100).*

if the argon is not implanted very deeply, the annealing/flashing process should remove a significant amount of it.

Another sample was prepared according to the same procedure, as the sample described above (20ML–Ti/Si IBMed with Ar^+ at 1.30keV, ion dose $\phi = 29.6 \cdot 10^{15} ions/cm^2$), and then it was annealed for $12min$ at the temperature of $400°C$ in order to remove the implanted argon. The purpose of the experiment was to investigate if the argon contamination influences the resistivity. The XPS spectrum of the Si 2p after the annealing process is presented in Fig. 4.70a. The Si 2p peak is positioned at $98.7eV$, it is shifted by $\sim 0.1eV$ to higher binding energy with respect to the not-annealed sample (Fig. 4.69a). The peak could be fitted with two doublets that correspond to two different titanium silicide phases - TiSi and Ti_xSi_y, and the TiSi is the dominant phase. There is significantly more TiSi in the annealed sample, because the annealing process supported the phase transformation from the Ti_xSi_y to the TiSi. The temperature of $400°C$ was high enough to cause the $Ti_xSi_y \longrightarrow TiSi$ phase transformation, but it was not high enough to allow the transformation from the TiSi into the C49 $TiSi_2$.

XPS spectra of the Ar were taken before the annealing process and after the annealing process. The results are presented in Fig. 4.71. The argon peak is lower after the thermal annealing process so the amount of Ar has thus decreased. If the sample were annealed for a longer time, or at higher temperature, the amount of argon would decrease more significantly. But since the purpose of this experiment was to investigate the difference in the contact resistance of the samples which differ only in the argon concentration, it was

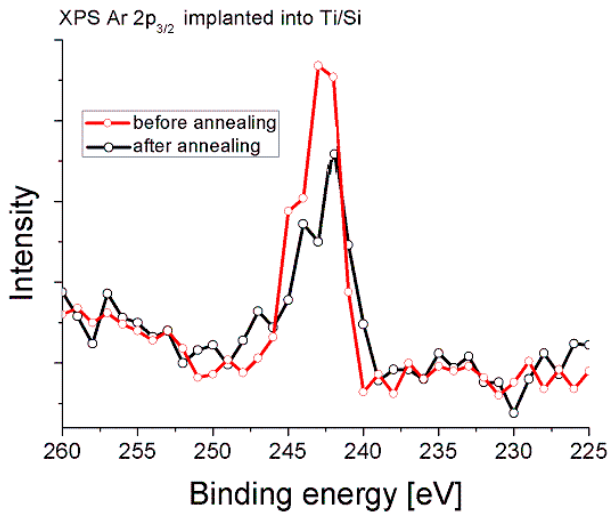

Figure 4.71: *The XPS spectra of argon on the surface of the IBMed (Ar^+ at 1.30keV, $\phi = 29.6 \cdot 10^{15} ions/cm^2$) and annealed ($400°C$ for $12min$) 20ML–Ti/Si(100) bilayers, taken before and after the thermal annealing.*

crucial not to anneal to much (so that the silicide phases do not change significantly). The contact resistance of the sample was studied by the means of TLM and the results are presented in Fig. 4.70b. The sample shows a good ohmic behaviour (linear I-U characteristics) and the obtained specific contact resistance is $\rho = 0.29 m\Omega \cdot mm^2$. The resistance of the sample depleted with argon (annealed) is only $0.02 m\Omega \cdot mm^2$ lower than the resistance of the not-annealed sample. Since the samples have a very similar composition (TiSi is a dominant titanium silicide phase), the argon has no influence on the quality of the electrical contact.

Furthermore, the C54 $TiSi_2$ was formed on the n-type Si(100) by room temperature IBM with higher ion dose (Ar^+ at 1.30keV, $\phi = 1.1 \cdot 10^{16} ions/cm^2$) and the properties of the electrical contact were studied. Fig. 4.72a shows the XPS spectrum of the Si 2p binding energy region taken right after the IBM process. The binding energy of the Si 2p peak is 99.06eV, and it was successfully fitted with the two doublets. The largest fitted peak correspond to the C54 $TiSi_2$, and the smaller peak corresponds to the C49 $TiSi_2$. The sample was covered with the capping layer (50ML of Ti) and studied ex-situ with the TLM, and the results are presented in Fig. 4.72b. The contact shows an ohmic behaviour, and the value of the obtained ρ is very comparable to the corresponding ρ value measured on the C54 $TiSi_2$ formed by the thermal annealing at $\sim 650°C$ (see Fig. 4.24).

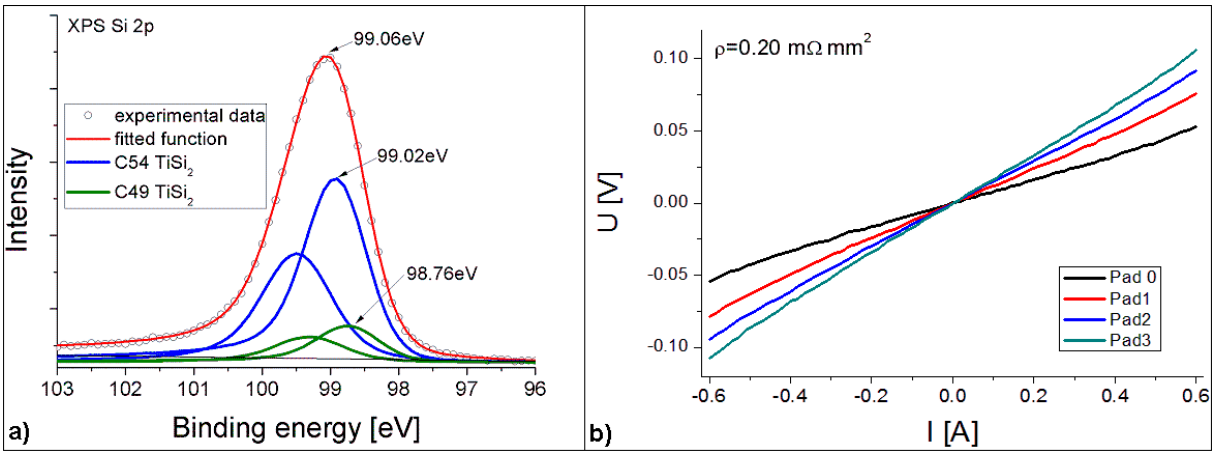

Figure 4.72: *The XPS (a) and the TLM (b) measurements of the 20ML–Ti/Si sample IBMed at room temperature with the Ar^+ at 1.30keV. Ion dose was $\phi = 1.1 \cdot 10^{16} ions/cm^2$, substrate: n-type Si(100).*

4.10 Surface morphology of the IBMed samples

The surface morphology of the 20ML–Ti/Si(100) system was investigated by the means of noncontact Atomic Force Microscopy (AFM). The purpose of these studies was to find out how the ion beam of argon influences the surface morphology, and how the morphology of the thermally annealed Ti/Si system differs from the IBMed Ti/Si system.

Four Si(100) silicon substrates were cleaned, 20ML of Ti were deposited onto them, and C54 titanium silicide was formed on their surfaces using different methods:

1. thermal annealing at 700°C for 4min
2. IBM with Ar^+ at 2.30keV ($\phi = 33.5 \cdot 10^{15} ion/cm^2$)
3. IBM with Ar^+ at 1.30keV plus annealing at 350°C for 10min ($\phi = 33.5 \cdot 10^{15} ion/cm^2$)
4. IBM with Ar^+ at 1.30keV ($\phi = 33.5 \cdot 10^{15} ion/cm^2$)

The annealing temperature and the annealing time in case of sample no. 1 were selected so that the C54 $TiSi_2$ was formed. The ion dose for the other three samples was sufficient enough to form the C54 titanium silicide phase. Sample No. 3 was annealed at low temperature (350 °C) for 10min after the IBM process in order to remove the implanted argon from its surface.
After the silicide formation process the samples were examined with XPS in order to check the Si 2p peak position - the silicide phase. All the Si 2p peaks were positioned at

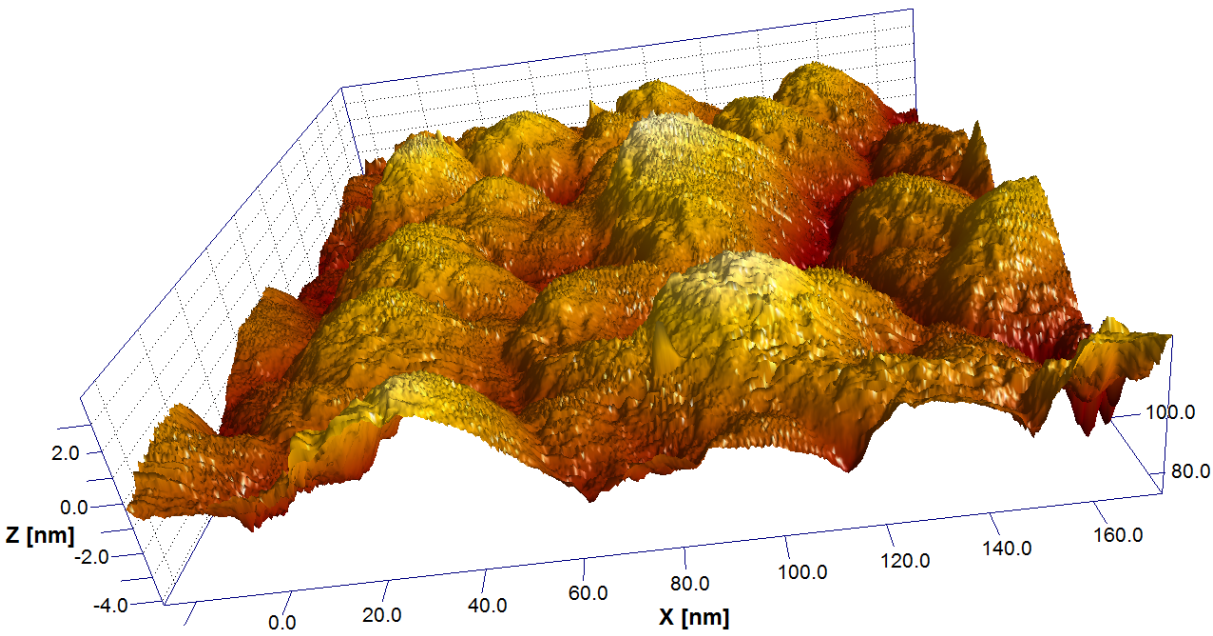

Figure 4.73: *The 3D view of the surface of the thermally annealed sample (no. 1) with the C54 $TiSi_2$ on Si(100).*

$\sim 99.1eV$, which corresponds to the C54 phase.
After the silicide formation process the samples were removed from the vacuum chamber and inserted into the AFM UHV System, where their surface roughness was studied with the AFM. During the transportation process from the SCIENTA System to the AFM System, the samples were exposed to the atmosphere. Possibly the samples surfaces were contaminated with some carbon and oxidised during the transportation and it is not known what influence this has on the surface morphology. But all the samples received the same treatment (were under the atmospheric pressure for approximately the same time) and the effect of the oxidation should be similar for all of them.

The surfaces of all the four samples were investigated with the AFM under the system pressure of the order of $10^{-10}mbar$ and the surface roughness was calculated with the SPIP [1] computer image analysis software for scanning probe microscopy. Fig. 4.73 presents the 3D view of the AFM image of the sample no. 1 (thermally annealed). Fig. 4.74 shows the 2D AFM images of the four studied samples. What is to be noticed is that the sample prepared by the thermal annealing (no. 1) has significantly larger grains on its surface as compared to the others. The heating at $700°C$ causes the surface particles to agglomerate into grains, which does not happen under the room temperature ion bombardment.
The surface roughness average S_a and the root mean square S_q were calculated by the

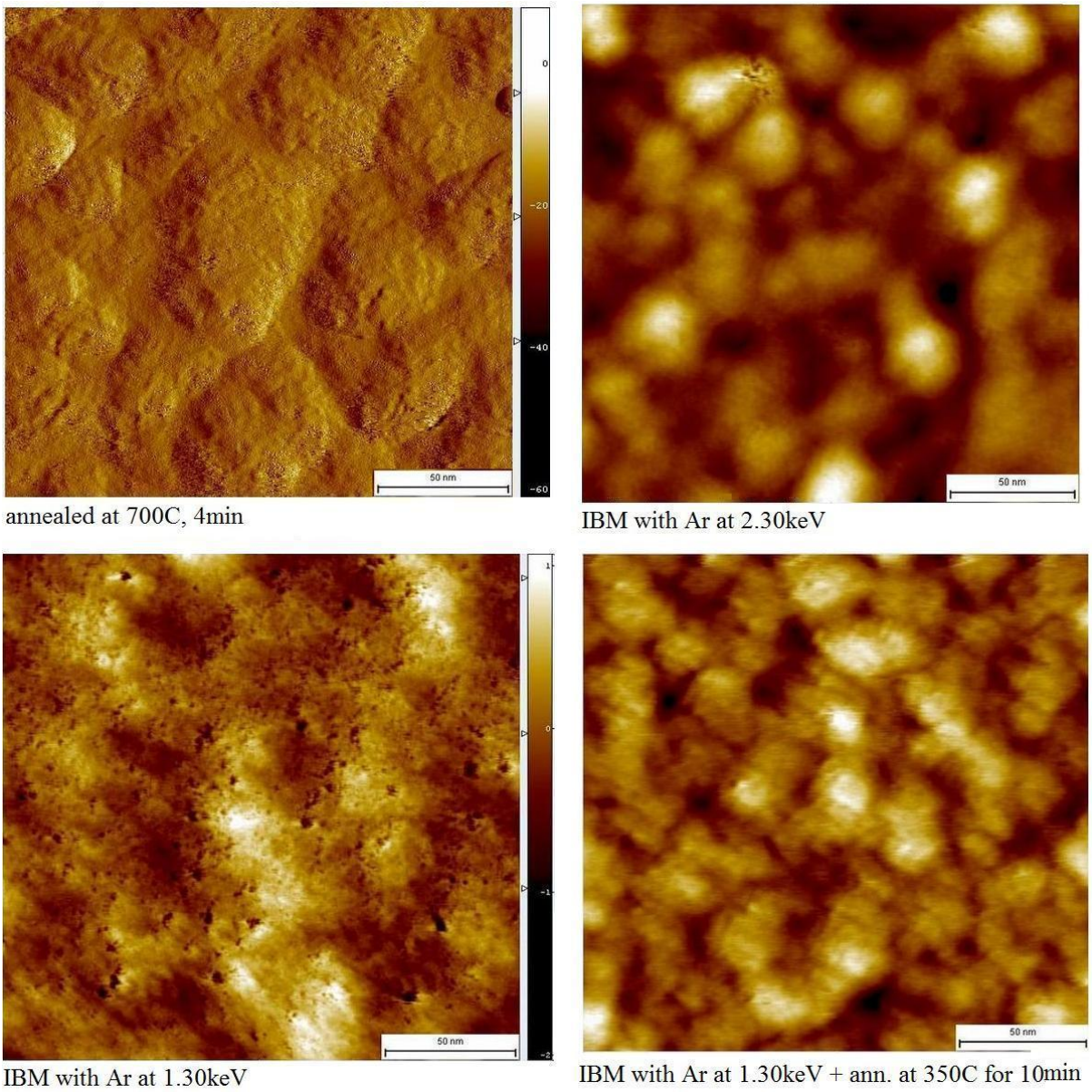

Figure 4.74: *AFM images of the C54 $TiSi_2$/Si(100) samples, where the C54 phase was formed by: thermal annealing at 700°C for 4.0min (no. 1), IBM with Ar^+ 2.30keV (no. 2), IBM with Ar^+ 1.30keV (no. 3), IBM with Ar^+ 1.30keV + annealing at 350°C for 10min (no. 4).*

SPIP, from the experimentally obtained AFM surface images (Fig. 4.74). The roughness average S_a is defined as:

$$S_a = \frac{1}{MN} \sum_{k=0}^{M-1} \sum_{l=0}^{N-1} |z(x_k, y_l) - \mu| \tag{4.4}$$

where the μ is called the mean height and it is equal to:

$$\mu = \frac{1}{MN} \sum_{k=0}^{M-1} \sum_{l=0}^{N-1} z(x_k, y_l) \tag{4.5}$$

and the M and N are the image dimensions, x and y are the coordinates of the currently calculated height.

The root mean square roughness parameter is defined as:

$$S_q = \sqrt{\frac{1}{MN} \sum_{k=0}^{M-1} \sum_{l=0}^{N-1} [z(x_k, y_l) - \mu]^2} \tag{4.6}$$

where the μ parameter is defined in Eq. 4.5, M and N are the image dimensions, x and y are the coordinates of the currently calculated height.

	Sample No. 1 (annealed 700°C)	**Sample No. 2** (IBM Ar^+ at 2.30keV)	**Sample No. 3** (IBM Ar^+ at 1.30keV +350°C for 10min)	**Sample No. 4** (IBM Ar^+ at 1.30keV)
S_a[nm]	0.838	0.393	0.47	0.277
S_q[nm]	1.03	0.498	0.59	0.352

Table 4.2: *The surface roughness of the C54 $TiSi_2$/Si(100).*

The calculated roughness parameters are given in the Table 4.2. In general all the examined surfaces are very smooth - both roughness parameters S_a and S_q are $\leq 1.03nm$. The annealed sample (no. 1) has the highest roughness of all the investigated samples. The second roughest surface is the surface from the sample no. 3 - the one that was IBMed and annealed at low temperature. The smoothest samples are the IBMed samples, and the smoothest one is IBMed one with Ar^+ at 1.30keV. The samples 3 and 4 were both IBMed at 1.30keV, but the sample no. 3 was additionally annealed and it is about 40% rougher (concerning both S_a and S_q parameters). Clearly the thermal annealing roughens the surface and the ion bombardment smoothens it. During the thermal annealing the pronounced grains are formed on the surface and they significantly increase the surface roughness. The grain formation process is very well visible at the annealing temperature of 700°C (Fig. 4.74-1), but it also appears at 350°C. The grain formation is not so clearly

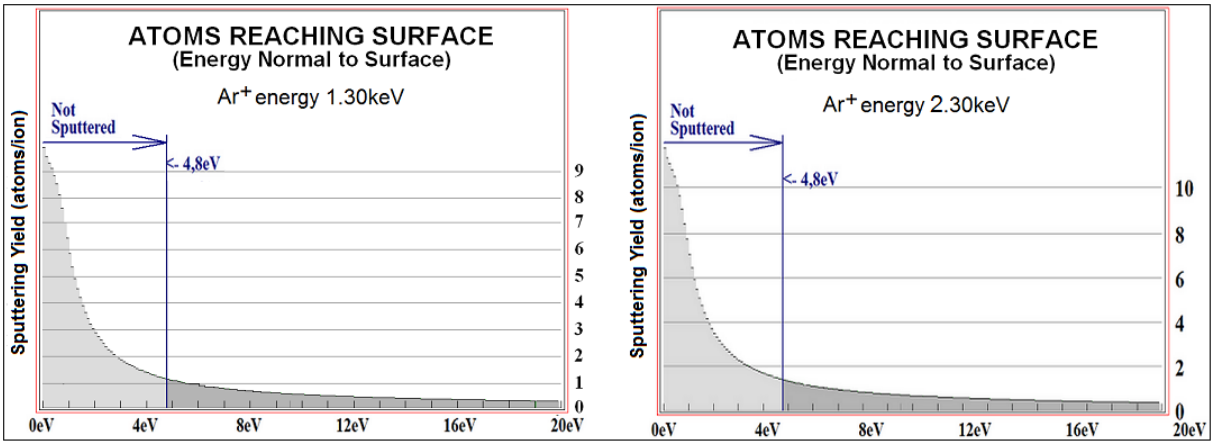

Figure 4.75: *A TRIM simulation result showing the energy distribution of the ion-beam-induced displaced target atoms reaching the surface. The atoms with the energy lower than 4.8eV (surface binding energy) cannot leave the surface and do not contribute to the sputtering yield, but they contribute to the surface diffusion leading to smoothing. The simulation was performed for the Ar^+ ions bombarding the Ti/Si surface with the energy of 1.30keV and 2.30keV normal to the surface. The ion dose was 100000 ions.*

visible, but the annealing at this temperature results in higher surface roughness in comparison to the not-annealed sample (compare the samples no. 3 and no. 4).

The ion beam smoothing effect appears when an ion beam smoothens out the surface features, and this effect is widely described in the literature [45, 28, 6]. As the AFM results have shown, this effect also appears during the IBM (Ar^+ at 1.30-2.30keV) of the 20ML–Ti/Si(100) system. The smoothing mechanism can be understood better by more detailed analysis of the ion-surface bombardment process. The Fig. 4.75 presents the results of the TRIM simulations showing the energy distribution of the ion-beam-induced displaced atoms reaching the surface. The calculation was performed for the Ar^+ ions bombarding the surface with the energy of 1.30keV and 2.30keV normal to the surface, the ion dose was 100000 ions. The kinetic energy of the atoms on the plot is the energy normal to the surface. The energy of 4.8eV, marked on the plot, is the average surface binding energy of the sample, and it was estimated by the TRIM code. So all the atoms that arrive at the surface with the energy $0eV < K_{kin} < 4.8eV$ can not be sputtered (they do not increase the sputtering yield). As it is presented in Fig. 4.75 the number of atoms reaching the surface with the energy $< 4.8eV$ is significant. These atoms can not overcome the surface binding energy, but they can translate parallel to the surface. Such a movement is called a surface diffusion and it causes the ion beam smoothing effect.

The thermal annealing also supports the surface diffusion, because it increases the mobility of the atoms. But the thermally annealed surface atoms form grains, and the IBMed atoms do not. The IBM counteracts the grain formation, because the Ar^+ ions modify the surface constantly. The ion-atom collisions crack and sputter the grains, which finally makes a very smooth surface.

Another interesting phenomenon that was observed and described in the literature [45] is the surface ripple formation caused by an ion beam. The ripples are periodic surface structures that can be described by a wave length and an amplitude. The existence and the features of the ripples depend on the chemical composition of the target material, the structure of the target surface, but also on the parameters of the ion beam (ion type, ion energy, incidence angle and also the ion dose).
The ripple formation on the argon sputtered Si(100) was studied and reported in the literature. If the argon ions bombard the Si(100) surface with the energy of 0.75keV at the angle of 67.5° normal to the surface, they shape ripples of $\lambda = 0.57\mu m$ [22, 45].
The ripples on the native SiO_2 (oxide formed on Si crystal) were also observed, when the sample was bombarded with argon ions. For argon beam at the angle of 45° to the surface, and the Ar^+ energy ranging from 0.5–2.0keV, the ripples wavelength is $0.2\mu m < \lambda < 0.55\mu m$ [25].
It is questionable if the ripple formation appears also on the Ar^+ bombarded Ti/Si target. The AFM images (Fig. 4.74) are squares of $200nm \times 200nm$ and no periodic structures are observed there. So if ripples are formed, their wavelength must be greater than the image size. One could expect that the ripple wavelength should be of the order of $\lambda \approx 200-500nm$ (according to the previous investigations on Si(100) and SiO_2 substrates), but this hypothesis was not verified in this work.

4.11 Thermally assisted ion beam mixing

All the experiments discussed in the previous sections were aimed at the titanium silicide formation by the thermal annealing or by the ion beam mixing. During the thermal annealing, the temperature is the factor that allows the intermixing of the Ti/Si bilayers by increasing the atoms mobility. As it was shown, the thermal annealing may be very well substituted by the ion beam mixing at room temperature. In the case of IBM, the kinetic energy of ions is absorbed by the target atoms in nuclear collisions and it is used for interface mixing and compound formation. What if these two different methods were

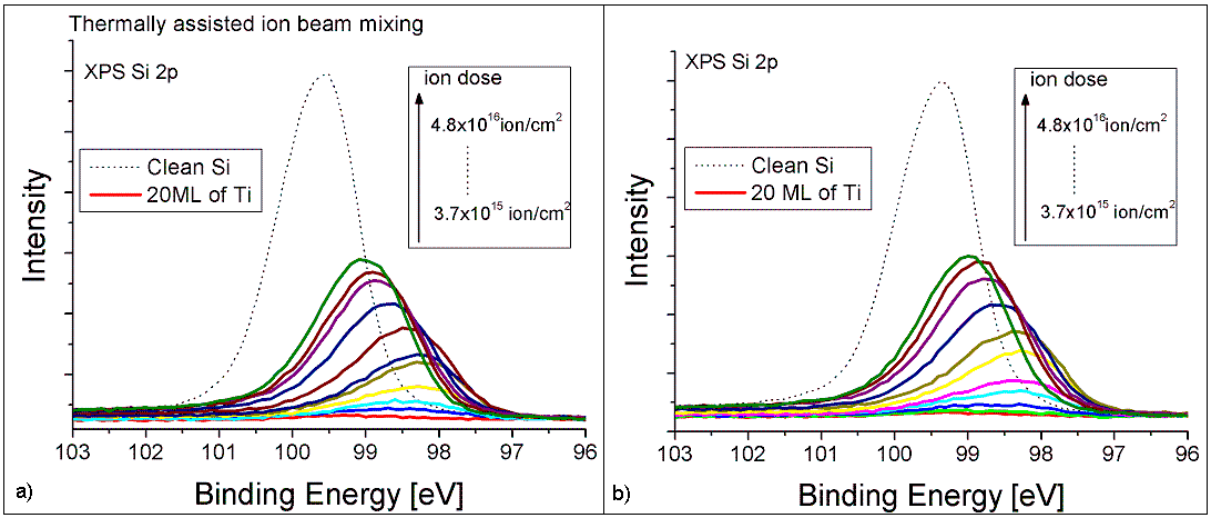

Figure 4.76: *The XPS spectra of the Si 2p taken during the TAIBM at 200°C (a) and taken during the room temperature IBM. The substrate is 20ML–Ti/Si(100), the Ar^+ energy is 1.30keV.*

combined in order to increase the mixing rate? The experiment would require heating the sample during the ion bombardment, and that is why such a method is called the **t**hermally **a**ssisted **i**on **b**eam **m**ixing (TAIBM) [54].
A TAIBM experiment, in case of the Ti/Si system, should be supported by a temperature that is not higher than about 300°C, because the purpose of this work is to create the silicides at low temperatures. Below 300°C there is no significant silicide formation at the Ti/Si interface, so it would be interesting to enhance the annealing at T< 300°C with the ion bombardment.
The TAIBM experiment was performed on the Si(100) substrate covered with 20ML of Ti, deposited at room temperature. The sample was then heated to 200°C and at the same time bombarded with Ar^+ ions with a kinetic energy of 1.30keV. After the TAIBM process the XPS and UPS spectra were taken. All the XPS and UPS spectra were taken after the same ion dose irradiations like during the room temperature IBM at 1.30keV, so the results are comparable.

Fig. 4.76a presents the XPS spectra of the Si 2p peak during the described TAIBM experiment. Fig. 4.77 shows the series of XPS peaks of the Ti $2p_{3/2}$ binding energy region. The Si 2p increases in height with the ion dose, and the Ti $2p_{3/2}$ decreases. So the intermixing between the two layers takes place. Fig. 4.76 b shows the Si 2p peak evolution for the room temperature IBM also at 1.30keV. The Si 2p peak growth is the same for the IBM and the TAIBM, which indicates the temperature has very little impact on the

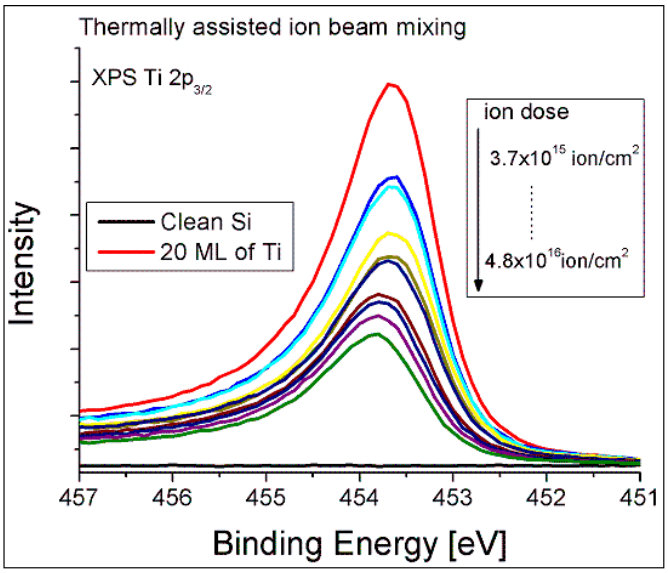

Figure 4.77: *The XPS spectra of the Ti $2p_{3/2}$ taken during the TAIBM at 200°C. The substrate is 20ML–Ti/Si(100), the Ar^+ energy is 1.30keV.*

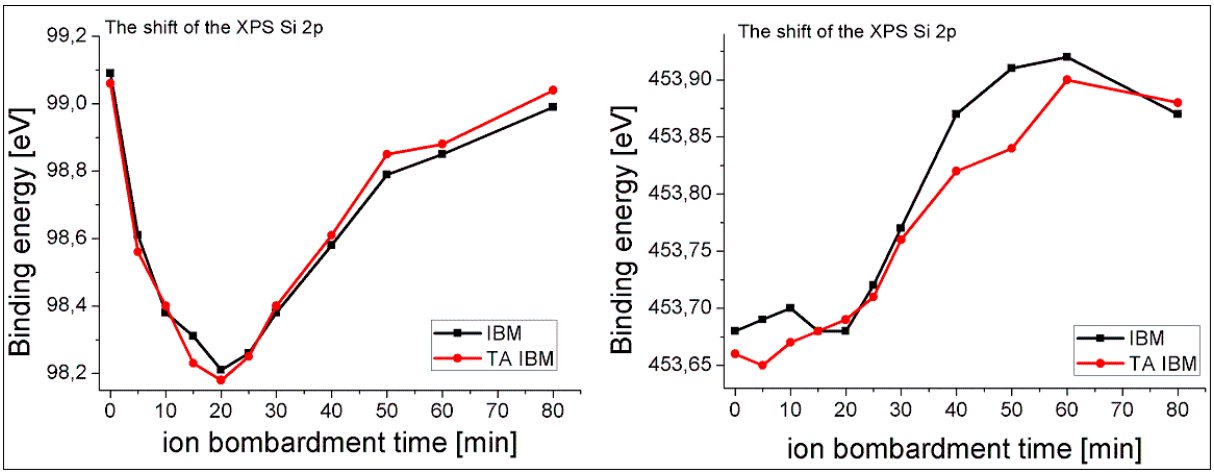

Figure 4.78: *Peak shifts of the XPS Si 2p and the Ti $2p_{3/2}$ peaks during the room temperature IBM and during the TAIBM at 200°C. The substrate is 20ML–Ti/Si(100) and the Ar^+ energy is 1.30keV.*

diffusion process. The temperature of 200°C does not increase significantly the mobility of the atoms and its contribution to the mixing process is negligible in comparison to the ion bombardment.

The detailed XPS peak analysis was done for the Si 2p and the Ti $2p_{3/2}$ and it is presented in Fig. 4.78. There are also plotted the peak shifts of the Si 2p and the Ti $2p_{3/2}$ during the room temperature IBM at 1.30keV (according to the data from the Fig. 4.76b),

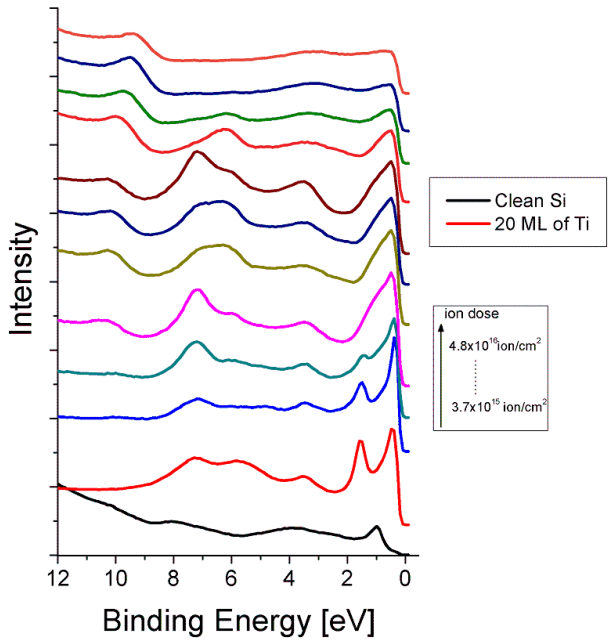

Figure 4.79: *The valence band evolution of the TAIBMed 20ML–Ti/Si(100) (Ar^+ at 1.30keV, T=200°C) obtained be the means of UPS.*

so the comparison of the peaks movements is possible. The Si 2p peaks from the IBM and the TAIBM experiments shift in exactly the same way, and the both peaks reach its minimum binding energy after they have received the same ion dose. The binding energy difference between the two Si 2p plots in never greater than 0.08eV. The XPS Ti $2p_{3/2}$ peaks also shift in the same way with the ion dose - they move to the higher binging energy first and both reach its maximum value at the same time. Then they move back to lower binding energies. The maximum difference in binding energy of the two peaks is always lower than 0.07eV.
According to the peak shift analysis there is no significant difference in the titanium silicide phase transformation between the IBM and the TAIBM. The silicide phase changes in the same sequence and with the same speed. The temperature of 200°C does not speed up the phase transformation – its contribution to the titanium silicide formation is negligible in the TAIBM process.

The evolution of the valence band of the TAIBMed Ti/Si(100) sample (Ar^+ at 1.30keV normal to the surface, $T = 200°C$) is shown in Fig. 4.79. The last three spectra do not differ from each other, and they are similar to the last three spectra measured during the standard room temperature IBM process at 1.30keV. Also the argon peak at $\sim 9eV$ appears on the spectra.

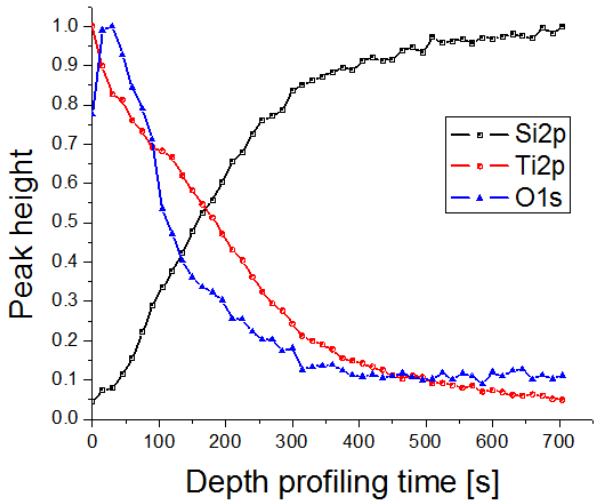

Figure 4.80: *Depth profile of the Ti/SiO$_2$/Si system formed by the room temperature deposition of the 20ML of titanium onto the Si(100) substrate covered with the native SiO$_2$ layer.*

All the described above measurements have shown that there is no difference between the room temperature IBM and the TAIBM (200°C, Ar$^+$ at 1.30keV) applied to 20ML–Ti/Si(100). The temperature of 200°C is to low to support the intermixing of the studied bilayers, or to speed up the silicide phase transformation, and its contribution to the process is negligible. No further experiments with the TAIBM were performed, because they would require increasing the annealing temperature, which is not consistent with the purpose of this work.

4.12 IBM of the Ti/SiO$_2$/Si(100) interface

It was of technological interest to investigate the ion beam mixing of the Ti/SiO$_2$/Si system, formed by the room temperature deposition of the titanium onto the silicon substrate covered with the native SiO$_2$ layer. In all the experiments presented below, the n-type Si(100) was used as a substrate material. The silicon substrates were not sputtered cleaned before the Ti evaporation, they were only degassed for 5-6 hours at the temperature $\sim$ 500°C.

4.12.1 Photoemission studies of the IBMed Ti/SiO_2/Si(100)

If titanium is evaporated onto the SiO_2, it reduces the Si replacing the Si-O bonds by the Ti-O bonds, and this chemical reaction takes place even at room temperature [14]. Thus, after the titanium evaporation onto the SiO_2/Si one should expect a TiO_x layer at the interface. In order to investigate this phenomenon, the depth profile of the Ti/SiO_2/Si (Ti coverage - 20ML) system was investigated. The depth profile was done for the Ar^+ beam incidence of 45° with an ion energy of $3.00keV$. The results (peak heights of the Si 2p, Ti $2p_{3/2}$ and the O 1s versus the Ar sputtering time) are presented in Fig. 4.80. After the first sputtering steps the amount of oxygen increases, and then the oxygen decreases in the same way, as the Ti does. It suggests that almost the whole titanium layer has reduced the SiO_2 and formed TiO_x.

The IBM of the Ti/SiO_2/Si system was studied by the means of the XPS for different Ar^+ kinetic energies. 20ML of Ti were deposited onto the degassed SiO_2, and the sample was IBMed with the Ar^+ ions bombarding the sample normal to the surface. During the IBM the XPS spectra of the sample surface were taken and the results are presented in Fig. 4.81. Three binding energy regions were investigated that correspond to the Si 2p (4.81a), Ti $2p_{3/2}$ (4.81b) and the O 1s (4.81c). Fig. 4.81d shows how the peak heights (normalized to 1) change with the ion bombardment time. The peaks for the time $t < 0min$ are the peaks from the spectra taken before the titanium evaporation (clean native SiO_2). The peaks for the time $t = 0min$ are the peaks from the spectra taken right after the titanium deposition. That is why the amount of the silicon and the oxygen decrease dramatically, and the titanium peak has the highest intensity ever. With the ion bombardment time the intensity of the Ti $2p_{3/2}$ decreases constantly. The intensity of the O 1s increases, and after $\sim 20min$ of the IBM it changes very slowly. At the same time the Ti $2p_{3/2}$ slows down to decrease. The Si 2p increases in height very slowly, and after $\sim 50min$ of the IBM it speeds up its growth (at the moment when the O 1s speeds up to decrease). The peak behaviour suggests there is no ion beam mixing, but a slow sputtering process. The silicon does not diffuse to the surface, and it starts to increase its intensity only after the mixture of the titanium and the oxygen has been sputtered away.

In the time range between $20 - 50min$ of the IBM (Fig. 4.81d) there is very little of silicon, and the amount of titanium and the oxygen changes very slowly. The XPS spectra of the Ti $2p_{3/2}$ taken at this time differ from the pure titanium spectra, because a third peak at $\sim 458.8eV$ develops. The XPS spectrum of the Ti in the pure TiO_2 consists of the

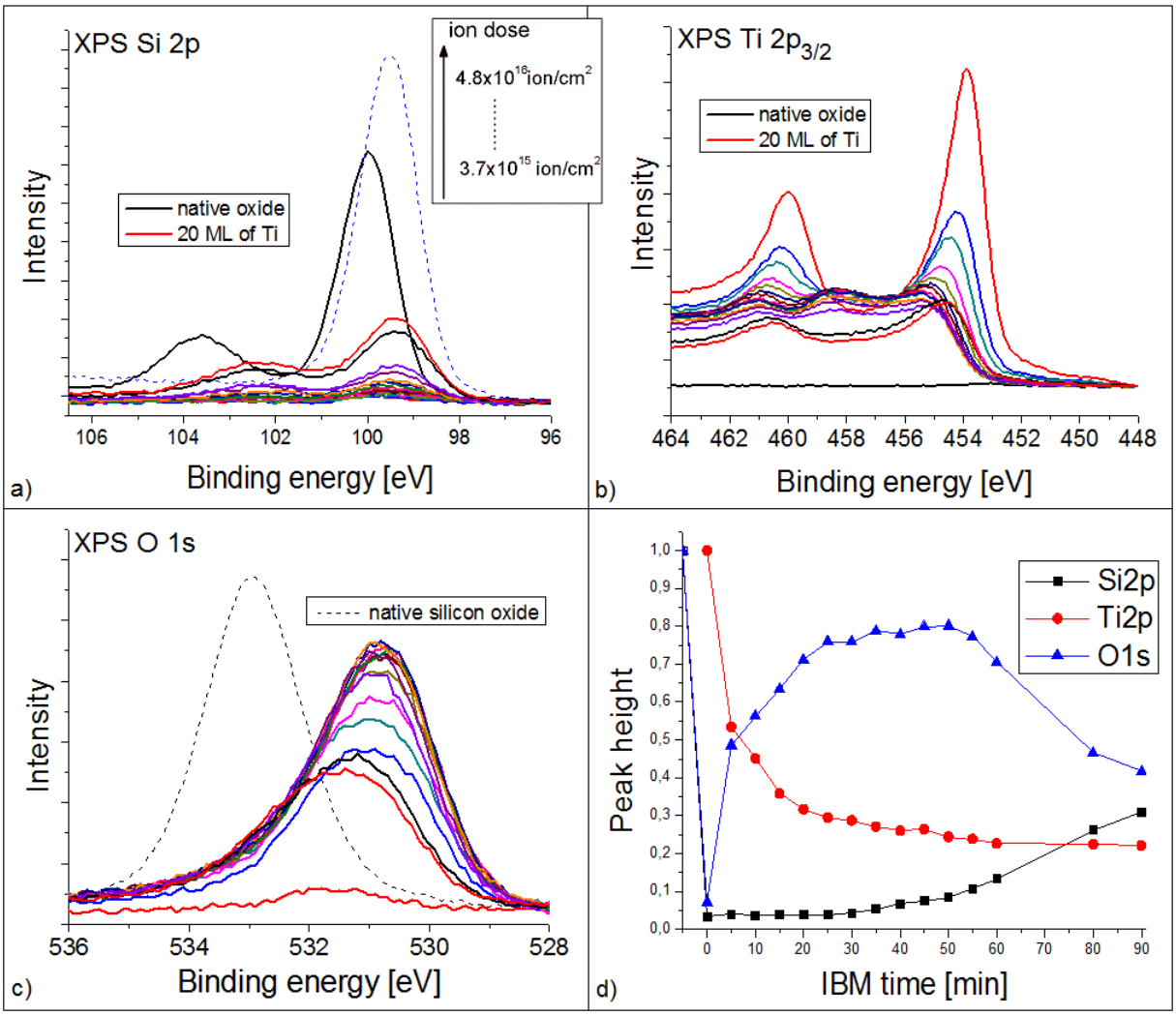

Figure 4.81: *XPS spectra of the IBMed (Ar^+ at 1.30keV) Ti/SiO_2/Si system: Si 2p (a), Ti $2p_{3/2}$ (b,) O 1s (c), and the analysis of the peak heights (d).*

Ti $2p_{3/2}$ positioned at 458.8eV and the binding energy difference between the Ti $2p_{3/2}$ and the Ti $2p_{1/2}$ is $\Delta = 5.54eV$. Fig. 4.83 presents the spectrum of the Ti $2p_{3/2}$ binding energy region during the IBM process after 25min of IBM (ion dose $\phi = 18.5 \cdot 10^{15} ions/cm^2$), which is a mixture of metallic Ti and oxidised Ti.
The IBM of the Ti/SiO_2/Si at 1.30keV does not result in the ion beam mixing. It causes slow sputtering and it additionally supports the chemical reaction between the Ti and the O what leads to the TiO_2 formation.

A similar experiment to the one described above was performed, but the ion angle of incidence was 45° to the sample surface. During the ion bombardment, the chemical composition of the sample was investigated by XPS. The results are presented in Fig.

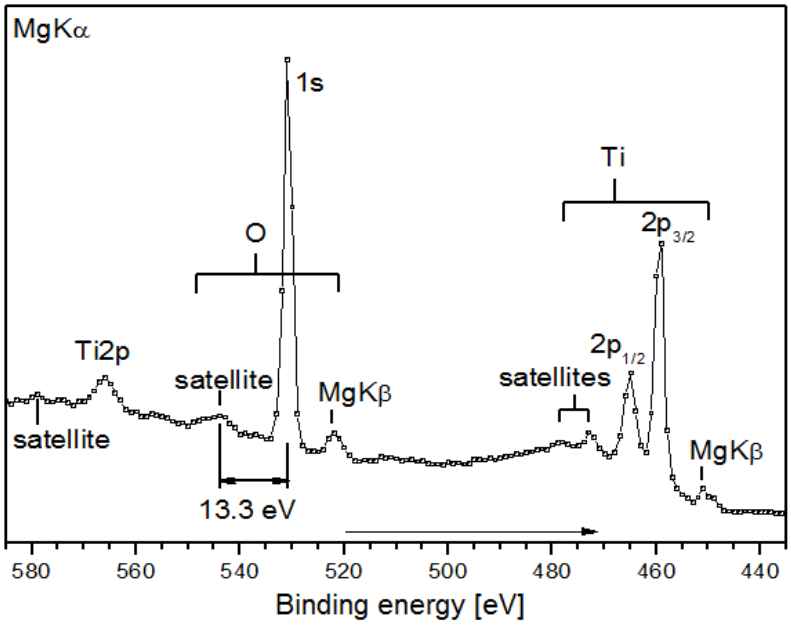

Figure 4.82: *The XPS spectrum of the clean surface of the pure TiO_2 crystal, taken by Mag. Stephen Berkebile in SCIENTA Lab.*

4.84. The peaks height analysis (Fig. 4.84d) shows that the peaks grow in the same way as did during the IBM at normal incidence to the target surface. The amount of oxygen increases, it reaches its maximum, and then decreases. At the same time the amount of titanium decreases constantly, and the amount of the silicon increases. The silicon peak during this experiment growths significantly faster than during the previous experiment (IBM at normal to the target surface). The Si 2p peak does not shift significantly in the binding energy, the titanium silicide formation is therefore not indicated. The Ti XPS peak also develops the third peak at $\sim 458.8eV$, but it decreases in height faster, then during the previous experiment. Summarizing: IBM at 45° does not cause the titanium silicide formation (no Si 2p peak shifts). It only sputters the material faster (Si 2p growths faster, Ti 2p decreases faster), because of the higher sputtering yield for the angle of 45° than for the normal incidence.

Since the ion beam mixing at 1.30keV did not result in the titanium silicide formation, it was attempted to IBM the $Ti/SiO_2/Si$ samples with the Ar^+ at higher kinetic energies. Fig. 4.85 presents the XPS spectra of the Si 2p, Ti 2p and the O 1s peaks of the IBMed $Ti/SiO_2/Si$ at Ar^+ at 1.80keV. During the IBM process, the Si 2p peak increases in height and it also shifts in binding energy (Fig. 4.85a). First it shifts to lower binding energy, and then it shifts back to higher binding energy - the behaviour typical for the titanium silicide formation, as observed previously. The Ti 2p decreases in height with the IBM

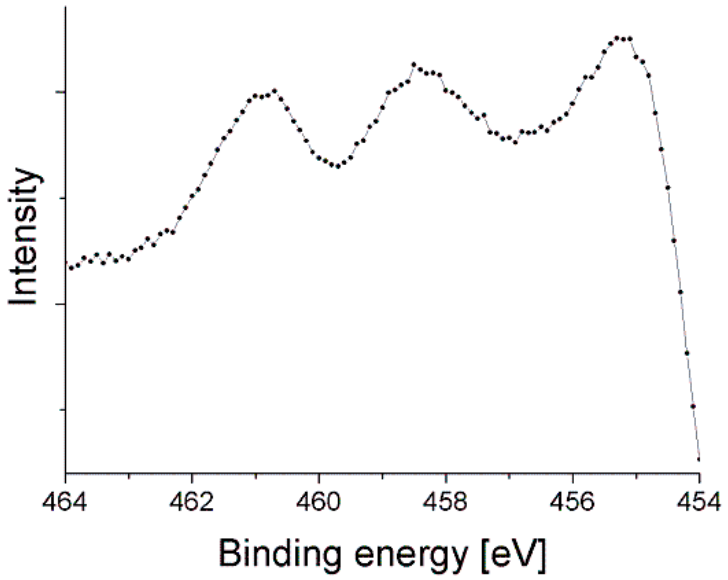

Figure 4.83: *fitted*

(Fig. 4.85d), and it consists only of the two doublets (Ti $2p_{3/2}$ and the Ti $2p_{1/2}$) and no peak typical for the TiO_2 at $\sim 458.8eV$ is formed (Fig. 4.85b). The peak also moves towards higher binding energies first, and then it shifts back - typical behaviour for the titanium silicide formation. The oxygen is removed quickly from the sample, leaving only the two elements - the Ti and the Si - on the surface.
The IBM at 1.80keV removed quickly the oxygen, and left the Ti and the Si, so the titanium silicide formation was possible. The diffusion of the silicon to the surface was more efficient.

The IBM of the $Ti/SiO_2/Si$ was also performed for the Ar^+ ion kinetic energies of 2.30keV and 3.0keV. The samples were investigated with the XPS during the ion irradiation process and the results are presented in Fig. 4.86 (for 2.30keV) and in Fig. 4.87 (for 3.0keV). In both cases the Si 2p peak increases in height with the ion dose, but it growths faster for the higher ion energy (compare the final Si 2p peak heights for the 2.30keV [Fig. 4.86a] and for the 3.0keV [Fig. 4.87]). The Si 2p peak also shifts in binding energy in a way typical for the ion induced titanium silicide formation process (it moves to lower binding energies first, and then back to higher binding energies). The Ti 2p peaks decrease in height with the ion dose and they also shift in binding energy, like during the titanium silicide formation process. The Ti 2p peaks do not change their shape significantly, and no peak at $\sim 458.8eV$ was identified, which indicates there was no TiO_x formation during the process.

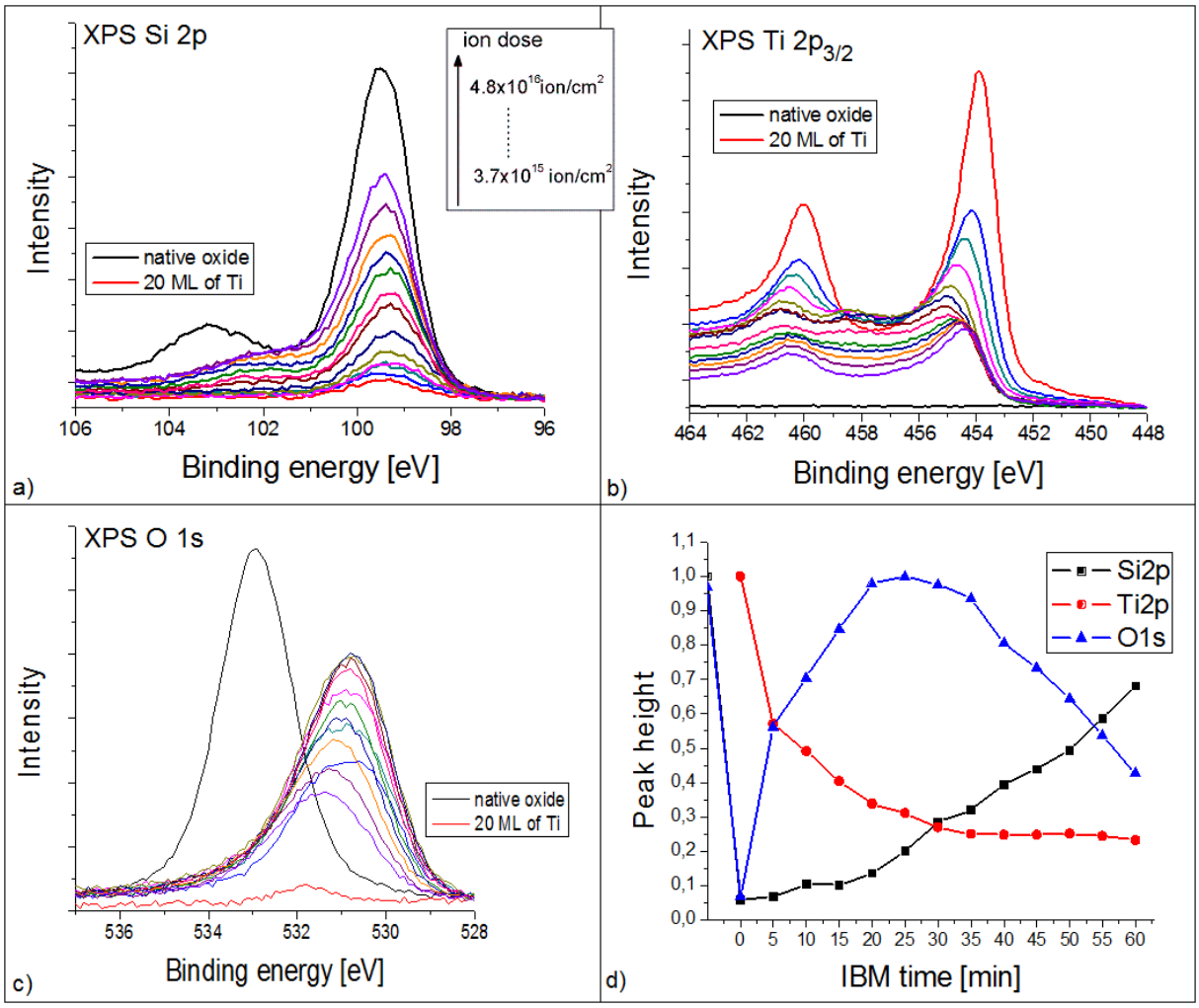

Figure 4.84: *XPS spectra of the IBMed (Ar^+ at 1.30keV at 45° to the target surface) $Ti/SiO_2/Si$ system: Si 2p (a), Ti $2p_{3/2}$ (b,) O 1s (c), and the analysis of the peak heights (d).*

According to the experiments described above, only the ion beam mixing with the Ar^+ at the kinetic energies $E_{kin} > 1.30keV$ caused the titanium silicide formation. The energy of 1.30keV did not support the Si diffusion enough, and the IBM process resulted only in the TiO_x formation and in the slow sputtering of the target material.

4.12.2 Computer simulations of the IBM of the $Ti/SiO_2/Si(100)$

The ion beam mixing process of the $Ti/SiO_2/Si$ layers was simulated with the TRIM program. In all the simulations the thickness of the native silicon dioxide was set to 20Å.

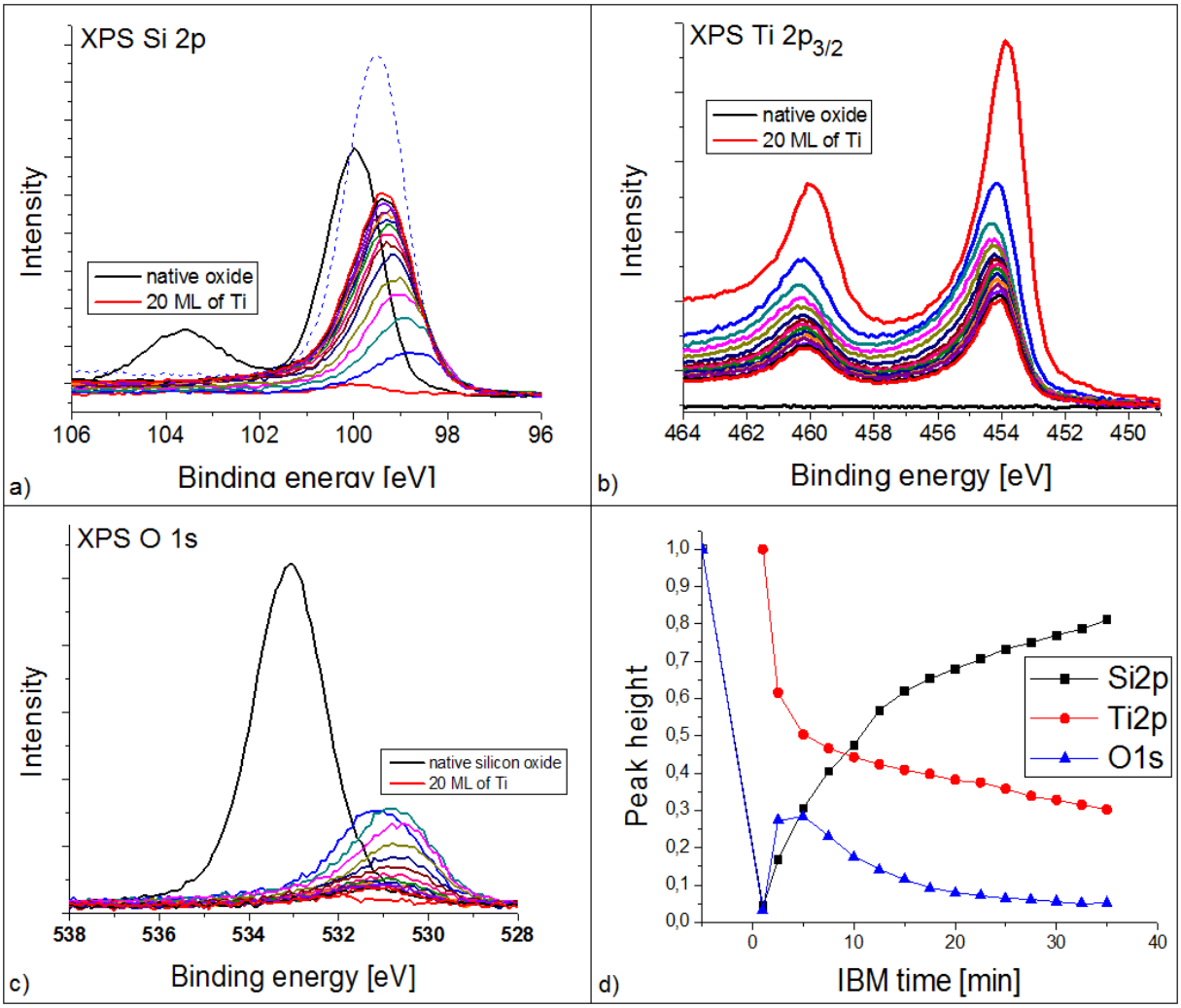

Figure 4.85: *XPS spectra of the IBMed (Ar^+ at 1.80keV normal to the target surface) $Ti/SiO_2/Si$ system: Si 2p (a), Ti $2p_{3/2}$ (b,) O 1s (c), and the analysis of the peak heights (d).*

Fig. 4.88 presents the calculated distribution of the energy absorbed from the Ar ions by the target atoms during the IBM of the $Ti/SiO_2/Si$ with Ar^+ at different kinetic energies at normal incidence. Most of the ion energy is absorbed in the very surface region – up to $\sim$ 30Å. This phenomenon does not depend significantly on the ion energy. But the ion energy influences the amount of the absorbed energy – the higher the ion energy, the more ion energy is absorbed. The energy distribution in Fig. 4.88 suggests, that argon ions lose the majority of their kinetic energy in collisions with the titanium atoms in the surface region. The titanium atoms use the absorbed ion energy to form the collision cascades that transfer the energy deeper into the sample. So the dominant driving force of the interface mixing is the collision cascade mixing.

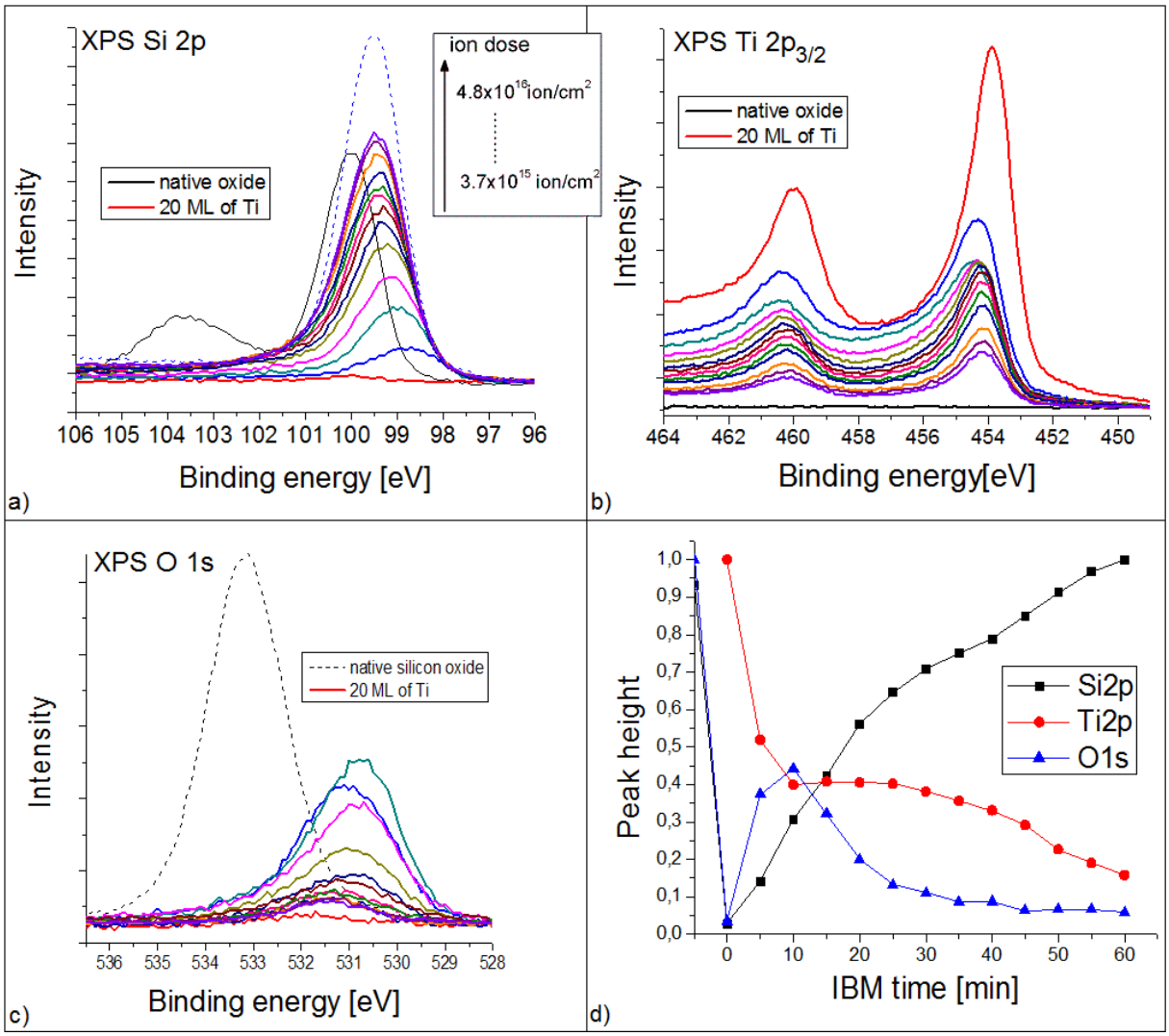

Figure 4.86: *XPS spectra of the IBMed (Ar^+ at 2.30keV normal to the target surface) $Ti/SiO_2/Si$ system: Si 2p (a), Ti $2p_{3/2}$ (b,) O 1s (c), and the analysis of the peak heights (d).*

Fig. 4.89 presents the distribution of the replacement collisions during the IBM of the $Ti/SiO_2/Si$ with Ar^+ at different kinetic energies at normal incidence. For 1.30keV there are no replacement collisions at the Ti/SiO_2, as well as at the SiO_2/Si interface. That explains why there was no interface mixing observed with the XPS for 1.30keV during the IBM experiments.

The higher the Ar^+ kinetic energy, the more the replacement collisions at the SiO_2/Si interface. That is the reason why it was experimentally observed with XPS, that the mixing process is more intense for higher argon energies.

The number of the replacement collisions decreases abruptly at the Ti/SiO_2 interface. According to the TRIM database, the SiO_2 has higher lattice displacement energy than

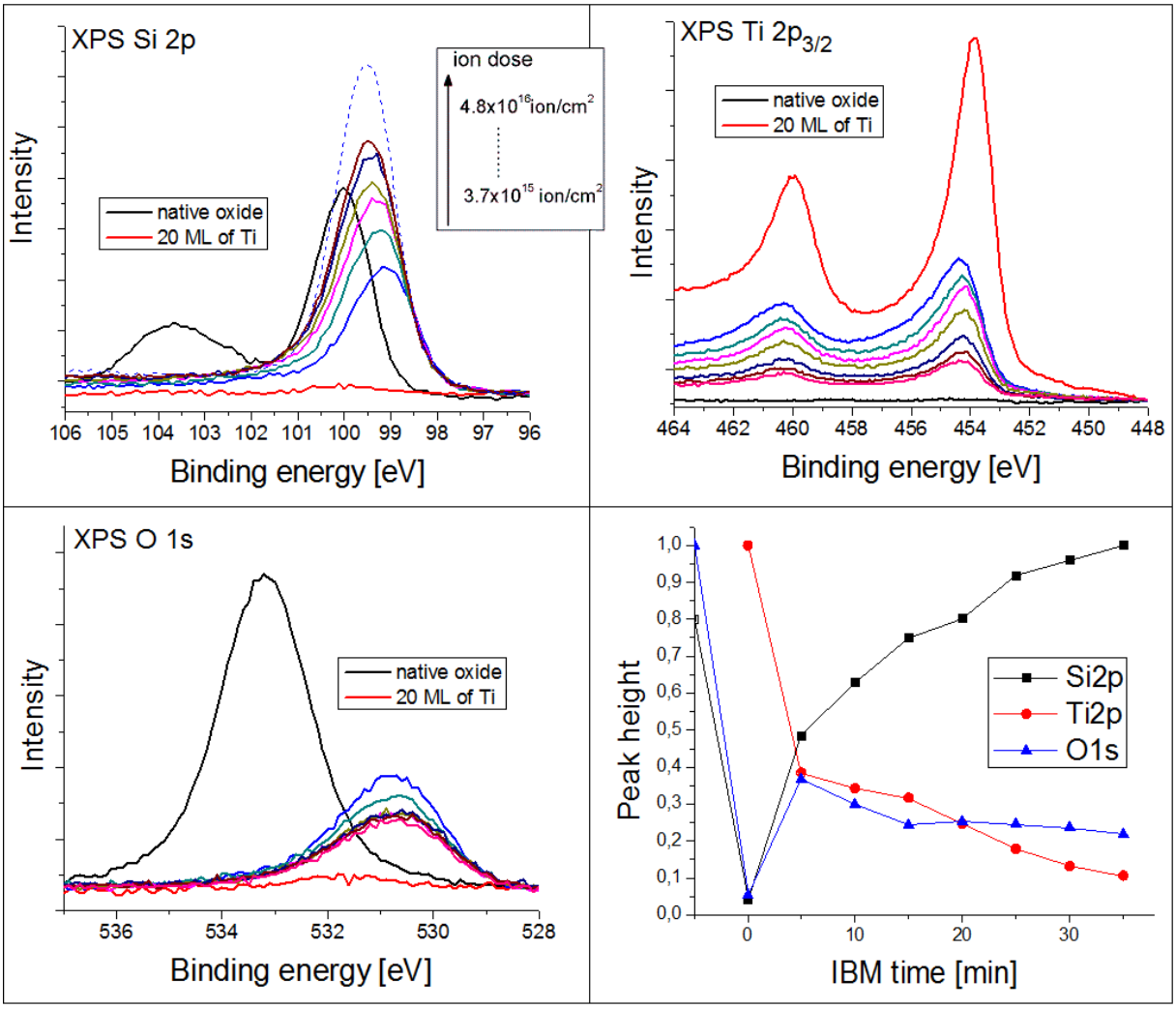

Figure 4.87: *XPS spectra of the IBMed (Ar^+ at 3.00keV normal to the target surface) $Ti/SiO_2/Si$ system: Si 2p (a), Ti $2p_{3/2}$ (b,) O 1s (c), and the analysis of the peak heights (d).*

the Ti and the Si. That is why the number of the replacement collisions decreases in the SiO_2 layer - it is necessary to provide target atoms with more energy in order to relocate them, so the relocation is less probable. The number of the replacement collisions increases again in the Si region, because the silicon atoms need less energy to be relocated and the relocation is more probable.

One should not forget, that the nuclear collisions are not the only factor that causes the mixing of the SiO_2 layer. The SiO_2 is also in direct contact with the titanium, which causes the TiO_x formation, which results in the thinning of the SiO_2 layer. But this effect (chemical reaction) cannot be simulated with TRIM.

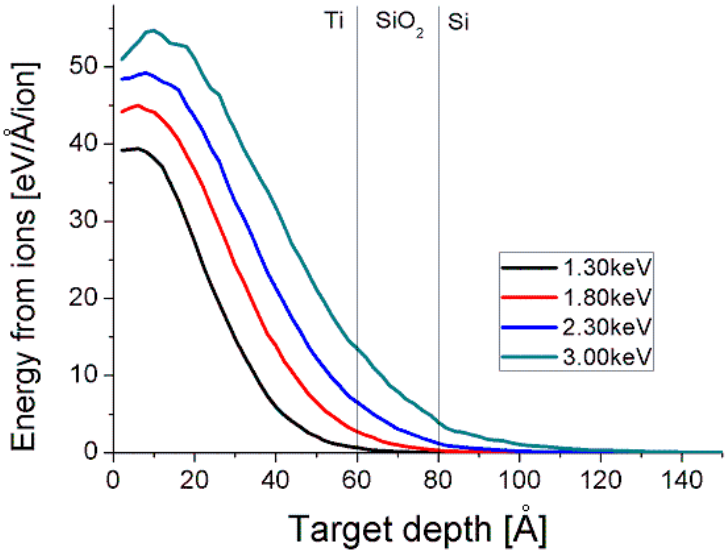

Figure 4.88: *The distribution of the energy absorbed by the target atoms during the IBM of the Ti/SiO$_2$/Si with Ar$^+$ at different kinetic energies at normal incidence.*

Fig. 4.90 shows the argon distribution after the IBM of the Ti/SiO$_2$/Si with Ar$^+$ at different kinetic energies at normal incidence. The projected ion range is always in the titanium region, and only few argons penetrate deeper into SiO$_2$ and Si. The higher the Ar$^+$ energy, the more argon ions/atoms penetrate into the silicon.

Figures 4.91 and 4.92 present the final 3D argon distribution after the IBM of the Ti/SiO$_2$/Si with Ar$^+$ at 1.30keV and 3.0keV at normal incidence. For the energy of 1.30keV the argon atoms are shallowly implanted and their spacial distribution is elliptic. For the energy of 3.0keV the argon atoms are more spread over the target volume. They are deeper implanted into the target and their spacial distribution is spherical.

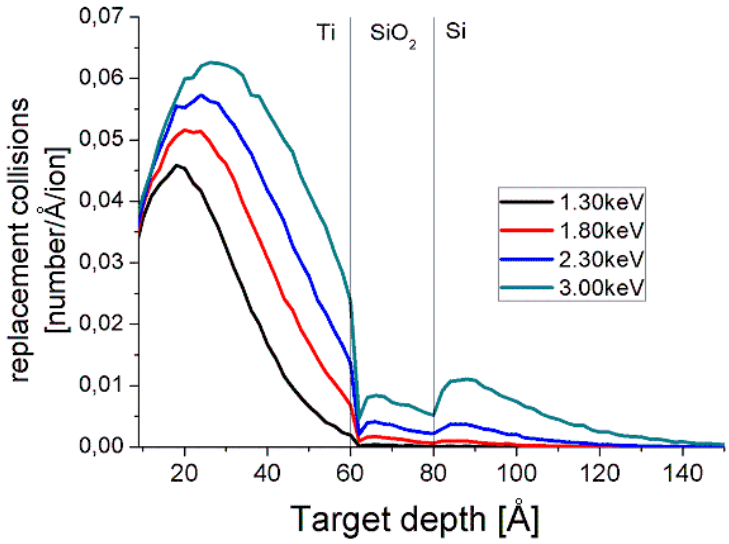

Figure 4.89: *The distribution of the replacement collisions during the IBM of the $Ti/SiO_2/Si$ with Ar^+ at different kinetic energies at normal incidence.*

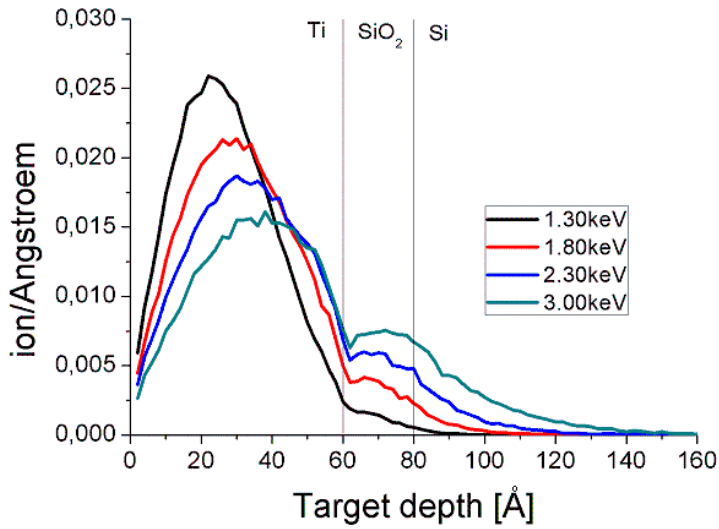

Figure 4.90: *The argon distribution after the IBM of the $Ti/SiO_2/Si$ with Ar^+ at different kinetic energies at normal incidence.*

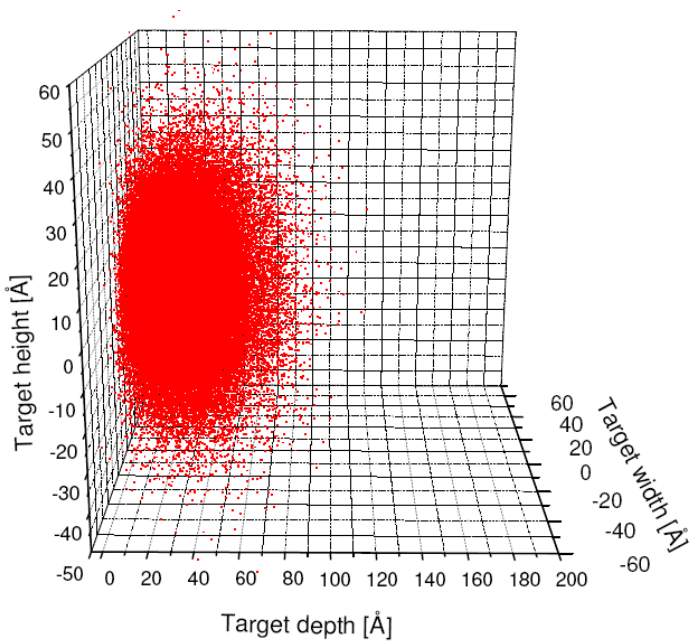

Figure 4.91: *The 3D argon distribution after the IBM of the $Ti/SiO_2/Si$ with Ar^+ at 1.30keV at normal incidence.*

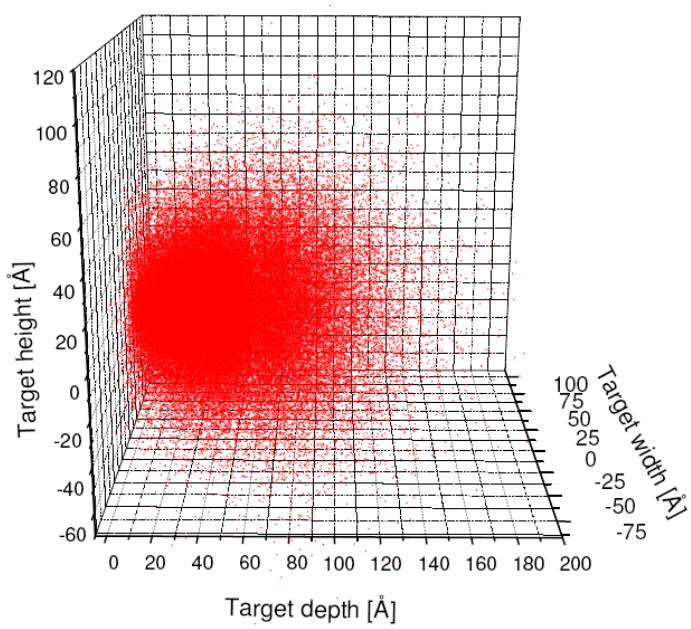

Figure 4.92: *The final 3D argon distribution after the IBM of the $Ti/SiO_2/Si$ with Ar^+ at 3.0keV at normal incidence.*

Chapter 5

Summary

The aim of this work was to form titanium silicides on a silicon substrate at the temperatures lower than $350°C$ so that it could find applications in the fabrication of the Ti-silicide/Si contacts, to be used in the backside metallization process of silicon wafers. Since the low resistivity C54 $TiSi_2$ crystal phase is formed at $\sim 650°C$, it was of scientific and technological interest to initiate the titanium silicide formation at room temperature. Therefore, the room temperature titanium silicide formation by ion beam mixing (IBM) was investigated in this work. Titanium silicide formation was studied in-situ under UHV conditions by means of the surface science techniques, like XPS, UPS and LEED, and it was also studied ex-situ by GIXRD (in the Siemens Laboratories in Munich) and non-contact AFM. The properties of the electrical contact (current–voltage characteristic and contact resistance) were investigated by TLM at the R&D Centre of Infineon Technologies in Villach.

Titanium growth at room temperature on clean n-type Si(111) substrates was studied with XPS. It was found that for titanium coverages up to 4ML the titanium growths in a layer-by-layer mode, and for higher coverages its growth mode changes to a Stranski-Krastanov mode. The detailed analysis of the XPS peaks of Si 2p and Ti $2p_{3/2}$ proved that there is no chemical reaction between the silicon and titanium at room temperature.

Titanium silicide formation by thermal annealing was investigated for n-type Si(111) and n-type Si(100) substrates. The clean silicon crystal was covered with 20ML of Ti and then thermally annealed in steps up to $\sim 700°C$, in order to initiate the chemical reaction between titanium and silicon. After each annealing step the samples were studied with XPS, UPS and LEED in order to investigate the interdiffusion process, titanium silicide

phase transformations, valence band evolution and the surface orientation of the formed structures.
The analysis of the XPS spectra show that the high temperature promotes the interdiffusion between silicon and titanium, and that the titanium silicide formation takes place. The formed silicides are disordered on both Si(111) and Si(100) surfaces, because no LEED pattern was observed.
The thermally annealed samples were studied with TLM to investigate the electrical properties of the formed contact. The samples were annealed in order to form C49 and C54 $TiSi_2$ phases and the formed titanium silicide phases were confirmed by GIXRD. The samples were TLMed and the measurement revealed that both C49 and C54 silicides form a good ohmic contact to silicon and the specific contact resistance is very low (lower than $0.18 m\Omega \cdot mm^2$). The analysis of the mechanical contact revealed that the titanium silicides have very good adhesion to silicon and no peeling effects were observed.
The titanium silicide crystal phases were studied ex-situ by GIXRD. The Ti/Si sample was annealed up to $700°C$ in order to form C54 $TiSi_2$, its surface was studied by XPS, UPS and LEED, and then it was measured ex-situ with GIXRD. The C54 $TiSi_2$ was identified, and it was possible to assign the C54 phase to a corresponding XPS peaks. The detailed analysis of the XPS peaks with fitting based on GIXRD measurements enabled to distinguish different titanium silicide phases. The XPS Si 2p peaks were fitted with doublets that represent the spin orbit split of Si 2p into Si $2p_{1/2}$ and Si $2p_{3/2}$ states. The fitted doublets differ in binding energy position and the position of the doublet corresponds to the different titanium silicide phases. This method allows to distinguish the titanium silicide phases (according to the doublet position) and their amount (according to the doublet intensity) using only the XPS spectrum of Si 2p.

The above described experiments with the thermal annealing of Ti/Si bilayers proved that the titanium silicides are suitable materials for low resistivity, ohmic contacts. Unfortunately the very high formation temperature of the contact makes them practically unusable in back side metallization process. That is why the room temperature titanium silicide formation by ion beam mixing was a subject of further investigations.
The IBM experiments were performed using the Ar^+ ion beam directed normal to the sample surface. The titanium coverages were as low as 20ML, so that it was possible to use for IBM an ion gun with ion kinetic energies up to only 5.0keV. During all the IBM experiments the kinetic energy of Ar^+ ions ranged from 1.30keV – 3.0keV.
The ion beam mixing was performed on both Si(111) and Si(100) substrates and during the IBM process the samples were examined with XPS, UPS and LEED. The behaviour

of the XPS Si 2p and Ti $2p_{3/2}$ peaks during the IBM process is the same as during the thermal annealing. Also no LEED pattern was observed, what is expected, because the ion bombardment disturbs the structure of the target material.
IBM was also performed on Si substrates covered with different Ti coverages (from 10ML to 20ML) and bombarded with different Ar^+ kinetic energies (1.30keV – 2.30keV). The purpose of the experiments was to find out how the Ti thickness and the ion energy influences the titanium silicide formation. The analysis of the XPS and UPS spectra shows that the higher the Ar^+ kinetic energy, the faster the titanium silicide transforms into a stable C54 $TiSi_2$ phase, and the higher the Ti coverage, the slower is the silicide phase transformation.
The electrical properties of the contact formed by the IBM of Ti/Si bilayers were examined by TLM. The electrical contact has good ohmic properties and the contact resistance is almost the same as in the case of the thermally annealed Ti/Si bilayers. The adhesion is as good as it was observed for thermally annealed samples.
The influence of argon, which was implanted during the IBM process, was investigated by comparing two samples: the first one was IBMed, the second one was IBMed and annealed at $400°C$ for $12min$ in order to remove the implanted argon. The TLM measurements show that there is no difference between the two contacts and the implanted argon has therefore no influence on the quality of the electrical contact. The mixing rate of the IBMed Ti/Si system with Ar^+ at 1.30keV was obtained experimentally and compared to the mixing rate values obtained from the calculations based on a compound formation model for IBM. The value of the experimentally obtained mixing rate ($k_{exp} = 0.647nm^4$) is similar to the calculated value of the mixing rate in the ballistic mixing regime ($k_{ball} = 0.46nm^4$), which suggests the ion mixing takes place in the ballistic mixing mode. Thermal spikes are not expected during the IBM and the interface mixing is driven by collision cascades. The squared thickness of the ion mixed Ti/Si interface changes linearly with the ion dose and IBM in this case is a diffusion–controlled process. It means the titanium silicide formation and the growth of the titanium silicide layer is not influenced by the kinetics of the chemical reaction between the titanium and the silicon. The growth speed of the titanium silicide layer depends only on the diffusion of the silicon into the titanium region.

A TRIM computer program was used to simulate the IBM of the Ti/Si interface. With the simulations for different Ar^+ energies and different Ti coverages it was possible to obtain important data for every experimentally studied Ti/Si system, such as sputtering yields, projected ion ranges of implanted argon ions/atoms and the argon distribution in the target, distributions of the energy absorbed by target atoms, ionization process,

distribution of the collision events in the target and more. The simulation results gave better understanding of the IBM process and enabled the analysis of phenomena that are not possible to be studied experimentally.

The surface roughness of the IBMed and annealed samples was investigated ex-situ by means of noncontact AFM. The purpose of these studies was to find out how the ion beam of argon influences the surface morphology and how the morphology of the thermally annealed Ti/Si system differs from the IBMed Ti/Si system. Four Ti/Si samples were prepares and the C54 titanium silicide was formed on their surfaces using different methods: IBM at different Ar^+ kinetic energies and thermal annealing. All the studied surfaces were very smooth (surface roughness average always $S_a < 0.85nm$), but the annealed sample was the roughest. It was discovered that the ion beam of Ar^+ at 1.30keV – 2.30keV smoothens the surface features, which is called an ion beam smoothing effect. On the surface of the thermally annealed Ti/Si sample pronounced grains were formed. The grain formation process is very well visible at the temperature of $700°C$, but it also appears at $350°C$. The grain formation results in higher surface roughness in comparison to IBMed samples.

In the previously described experiments the titanium silicides were formed by thermal annealing or by ion beam mixing. But also Thermally Assisted Ion Beam Mixing (TAIBM) was performed, which involved annealing and IBMing of samples at the same time. Since the purpose of this work was to form titanium silicides at temperatures lower than $400°C$, the temperature of $200°C$ was chosen for the TAIBM experiment. The IBM was performed with the Ar^+ at 1.30keV. During the process the sample surface was investigated with XPS and UPS. The results of the measurements show that there is no difference between the room temperature IBM and the TAIBM at the $T = 200°C$. The temperature of $200°C$ is to low to support the intermixing of Ti/Si bilayers and to speed up the titanium silicide phase transformation and its contribution to the whole process in negligible.

The IBM of Ti/SiO_2/Si interface was also investigated. The interface was formed by room temperature deposition of titanium (20ML) onto a silicon substrate covered with a native SiO_2 layer. The IBM was performed for different Ar^+ kinetic energies: 1.30keV, 1.80keV, 2.30keV and 3.00keV. During the IBM experiment the samples were examined with XPS with the focus on Si 2p, Ti $2p_{3/2}$ and O 1s binding energy regions. The ion energy of 1.30keV is not high enough to support the intermixing at SiO_2/Si interface

and therefore no ion beam mixing phenomenon is observed. The analysis of the XPS Ti $2p_{3/2}$ peak suggests the formation of Ti_xO_y during the ion bombardment. Argon energies $E_{kin} > 1.30keV$ are high enough to initiate the silicon diffusion into the titanium region and the titanium silicide formation takes place. The oxygen is removed at the beginning of the IBM process and no Ti_xO_y is observed.

The purpose of this work was to form titanium silicides at room temperature and this goal was achieved by applying an ion beam mixing method. Good properties of the electrical contact formed by IBM and its good adhesion to silicon make IBM a good equivalent to thermal annealing.

Bibliography

[1] *The Scanning Probe Image Processor (SPIP). User's and Reference Guide to the SPIP computer program, Version 3.2.* http://www.imagemet.com, 2004.

[2] David Adams. FitXPS 2.12 - the XPS fitting program, University of Aarhus, download location: http://www.sljus.lu.se/download.html.

[3] A. Arranz and C. Palacio. The room temperature growth of Ti on sputter-cleaned Si(100): Composition and nanostructure of the interface. *Surface Science*, 588:92–100, 2005.

[4] Friedhelm Bechstedt. *Principles of Surface Physics.* Springer, 2003.

[5] F. Besenbacher, J. Bøttiger, S.K. Nielsen, and H.J. Whitlow. Long-range ion-beam mixing in Cu:Al. Influence of interfacial oxide. *Appl. Phys. A*, 29:141, 1982.

[6] K. Bhattacharjee, S. Bera, D. K. Goswami, and B. N. Dev. Nonoscale self-affine surface smoothing by ion bombardment and the morphology of nanostructures grown on ion-bombarded surfaces. *Nuclear Instruments and Methods in Physics Research*, B:524–532, 2005.

[7] W. Bolse. Mechanisms of ion beam induced atomic mixing in solids. *Materials Science and Engineering A*, 253:194–201, 1998.

[8] W. Bolse. Atomic transport in thin film systems under heavy ion bombardment. *Surface and Coatings Technology 158 - 159*, pages 1–7, 2002.

[9] W. Bolse. Interface modification by swift heavy ions. *Radiation Measurements*, 36:597–603, 2003.

[10] W. Bolse and B. Schattat. Atomic mixing in thin film systems by swift heavy ions. *Nuclear Instruments and Methods in Physics Research B*, 190:173–176, 2002.

[11] W. Bolse and B. Schattat. Atomic transport in hot ion tracks. *Nuclear Instruments and Methods in Physics Research B*, 209:32–40, 2003.

[12] W. Bolse, B. Schattat, and A. Feyh. Modification of thin-layer systems by swift heavy ions. *Appl. Phys. A*, 77:11–15, 2003.

[13] D. Briggs and M. P. Seah. *Practical Surface Analysis, Second Edition, VOLUME 1 - Auger and X-ray Photoelectron Spectroscopy.* Wiley, 1990.

[14] R. Butz, G. W. Rubloff, and P.S. Ho. Chemical bonding and reactions at Ti/Si and Ti/oxygen/Si interfaces. *J. Vac. Sci. Technol. A (1)*, 2, 1982.

[15] R. Butz, G. W. Rubloff, T. Y. Tan, and P. S. Ho. Chemical and structural aspects of reaction at the Ti/Si interface. *Physical Review B*, 30, number 10:5421–5434, 15 Nov 1984.

[16] S. A. Chambers, D. M. Hill, F. Xu, and J. H. Weaver. Silicide formation at the Ti/Si(111) interface: Diffusion parameters and behavior at elevated temperatures. *Physical Review B*, volume 35, number 2:634–640, 15 Jan 1987-I.

[17] L. A. Clevenger, C. Cabral, R. A. Roy, C. Lavoie, J. Jordan-Sweet, S. Brauer, G. Morales, K. F. Ludwig, and G. B. Stephenson. Formation of a crystalline metal-rich silicide in thin film titanium/silicon reactions. *Thin Solid Films*, 289:220–226, 1996.

[18] M. del Guidice, J. J. Joyce, M. W. Ruckman, and J. H. Weaver. Silicide formation at the Ti/Si(111) interface: Room-temperature reaction and Schottky barrier formation. *Physics Review B*, volume 35 number 12:6213–6221, 15 Apr 1987-II.

[19] J. Desimoni and A. Traverse. Model for compound formation during the ion-beam mixing. *Physical Review B*, Volume 48, Number 18:13266–13272, 1 Nov 1993-II.

[20] S. Dhar, Y. N. Mohapatra, and V. N. Kulkarni. Compound formation under local thermal spikes during ion-beam mixing: Model and its experimental verification. *Physical Review B*, Volume 54, Number 8:5770–5776, 15 Aug 1996-II.

[21] M. Ekman and V. Ozolins. Electronic structure and bonding properties of titanium silicides. *Physical Review B*, volume 57, number 8:4419–4424, 15 Feb 1998-II.

[22] J. Erlebacher, M. J. Aziz, E. Chason, M. B. Sinclair, and J. A. Floro. Spontaneous Pattern Formation on Ion Bombarded Si(001). *Physical Review Letters*, volume 82, number 11:2330–2333, 1999.

[23] B. Fahrid and R. W. Godby. Cohesive energies of crystals. *Physical Review B*, Volume 43, Number 17:14248–14250, 15 Jun 1991-I.

[24] D. Fink and L. T. Chadderton. Ion-Solid Interaction: Status and Perspectives. *Brazilian Journal of Physics*, volume 35, number 3B:735–740, 2005.

[25] D. Flamm, F. Frost, and D. Hirsch. Evolution of surface topography of fused silica by ion beam sputtering. *Applied Surface Science*, 179:95–101, 2001.

[26] Lucille A. Giannuzzi and Fred A. Stevie. *Introduction to Focused Ion-Beams; Instrumentation, Theory, Techniques and Practice.* Springer Science + Business Media, Inc., 2005.

[27] I. Goldfarb, G. Cohen-Taguri, S. Grossman, and M. Levinshtein. Equilibrium shape of titanium silicide nanocrystals on Si(111). *Physical Review B*, 72(075430):1–6, 2005.

[28] D. K. Goswami and B. N. Dev. Nanoscale self-affine surface smoothing by ion bombardment. *Physical Review B*, 68, 2003.

[29] H. K. Henisch. *Semiconductor contacts. An approach to ideas and models.* Oxford University Press, 1984.

[30] S.B. Herner, V. Krishnamoorthy, A. Naman, K.S. Jones, H.-J. Gossmann, and R.T. Tung. Morphology of $TiSi_2$ films on Si formed from co-deposited Ti and Si. *Thin Solid Films*, 302:127–132, 1996.

[31] G. Huges, D. Carty, and A. A. Cafolla. Core level photoemission studies of the interaction of pentacene with the Si(111) (7x7) surface. *Surface Science*, 582:90–96, 24 Feb 2005.

[32] Tobias Jarmar. *High-Resolution Studies of Silicide-films for Nano IC-Components.* PhD thesis, Uppsala Universitet, 2005.

[33] H. Jeon, C. A. Sukow, J. W. Honeycutt, G. A. Rozgonyi, and R. J. Nemanich. Morphology and phase stability of $TiSi_2$ on Si. *J. Appl. Phys. 71 (9)*, pages 4269–4276, 1 May 1992.

[34] J. L. Jordan-Sweet. Synchrotron X-ray scattering techniques for microelectronics-related materials studies. *IBM J. RES. DEVELOP*, Vol. 44, No. 4:466–471, 4 Jul 2000.

[35] S.-J. Kim, M.-A. Nicolet, R.S. Averback, and D. Peak. Low-temperature ion-beam mixing in metals. *Physical Review B*, Volume 37 Number 1:38–49, 1 Jan 1988.

[36] Charles Kittel. *Introduction to Solid State Physics, 8th edition.* John Wiley & Sons, Inc, 2005.

[37] Daniel Kraft. *Präparation und Charakterisierung von Dünnschichtmaterialsystemen für die Rückkontaktbildung bei polykristallinen CdTe-Dünnschichtsolarzellen.* PhD thesis, Technische Universität Darmstadt, 2004.

[38] R. Larciprete, M. Danailov, A. Barinov, L. Gregoratti, and M. Kiskinova. Thermal and pulsed laser induced surface reactions in Ti/Si(001) interfaces studied by spectromicroscopy with synchrotron radiation. *Journal of Applied Physics*, volume 90, number 9:4361–4369, 1 Nov 2001.

[39] S. J. Lee, D. Y. Kim, and T. W. Kim. Formation of C54 $TiSi_2$ thin films by using high-temperature sputtering and rapid thermal annealing. *Journal of Materials Science*, 39:3203–3205, 2004.

[40] Michael Leitner. Bulk-type Manganese Oxide Films on Pd (100): Morphology and Structure, 2006.

[41] X.-P. Li, D. M. Ceperley, and Richard M. Martin. Cohesive energy of silicon by the Green's-function Monte Carlo method. *Physical Review B*, Volume 44, Number 19:10929–10932, 15 Aug 1991-I.

[42] V.G. Lifshits, A.A. Saranin, and A.V. Zotov. *Surface phases on silicon. Preparation, Structures and Properties.* John Wiley & Sons, 1994.

[43] H. Lüth. *Surfaces and Interfaces of Solid Materials.* Springer, 1995.

[44] K. Maex and M. van Rossum. *Properties of Metal Silicides.* INSPEC, the Institution of Electrical Engineers, London, 1995.

[45] M. A. Makeev, R. Cuerno, and A.-L. Barabasi. Morphology of ion-sputtered surfaces. *Nuclear Instruments and Methods in Physics Research B*, 197:185–227, 2002.

[46] R. W. Mann, L. A. Clevenger, P.D. Agnello, and F. R. White. Silicides and local interconnections for high-performance VLSI applications. *IBM J. RES. DEVELOP.*, Vol. 39, No 4:403–417, Jul 1995.

[47] L. F. Mattheiss and J. C. Hensel. Electronic structure of $TiSi_2$. *Physical Review B*, volume 39, number 11:7754–7759, 15 Apr 1989-I.

[48] Glen L. Miles, Randy W. Mann, and John E. Bertseh. $TiSi_2$ phase transformation characteristics on narrow devices. *Thin Solid Films*, 290:469–472, 1996.

[49] V. Milinović. *Ion-beam mixing of Fe/Si bilayers.* PhD thesis, Georg-August-Universität zu Göttingen, 2005.

[50] Winfred Mönch. *Electronic structure of metal-semiconductor contacts.* Kluwer Academic Publishers, 1990.

[51] Winfred Mönch. *Semiconductor Surfaces and Interfaces.* Springer-Verlag, 1993.

[52] S. Morita, R. Wiesendanger, and E. Meyer. *Noncontact Atomic Force Microscopy.* Springer, 2002.

[53] A. Mouroux, S. L. Zhang, S. Nygren, M. Östling, and C. S. Petersson. Enhanced formation of the C54 phase of $TiSi_2$ by an interposed layer of molybdenum. *Appl. Phys. Lett.*, 69:975–977, 12 Aug 1996.

[54] Michael Nastasi, James W. Mayer, and James K. Hirvonen. *Ion-Solid Interactions. Fundamentals and applications.* Cambridge Solid State Science Series, 1996.

[55] K. Nordlund and R. S. Averback. Point defect movement and annealing in collision cascades. *Physical Review B*, volume 56, number 5:2421–2431, 1 Aug 1997-I.

[56] K. Nordlund, M. Ghaly, R. S. Averback, M. Caturla, T. Diaz de la Rubia, and J. Tarus. Defect production in collision cascades in elemental semiconductors and fcc metals. *Physical Review B*, volume 57, number 13:7556–7570, 1 Apr 1998-II.

[57] D.J. O'Connor, B.A. Sexton, and R.St.C Smart. *Surface Analysis Methods in Material Science.* Springer-Verlag, 1992.

[58] The official website of the Surface Science Group of the Karl-Franzens University Graz. http://surface-science.uni-graz.at.

[59] The online Periodic Table of Elements. http://www.webelements.com.

[60] G. Otto, G. Hobler, and K. Gärtner. Defect characterization of low-energy recoil events in silicon using classical molecular dynamics simulation. *Nuclear Instruments and Methods in Physics Research B*, 202:114–119, 2003.

[61] Jian Hua Ouyang, Xin Sheng Zhaoa, Ting Li, and Da Cheng Zhang. Direct measurement of the etching rates on Si (111) and silicon dioxide surfaces in 40% ammonium fluoride aqueous solution via atomic force microscopy. *Journal of Applied Physics*, 93, number 7:6, 1 april 2003.

[62] R. Pastorelli, C. Bottani, L. Miglio, M. Iannuzzi, and A. Sabbadini. Brillouin scattering of $TiSi_2$: elastic constants and related thermodynamic parameters. *Microelectronic Engineering*, 55:129–135, 2001.

[63] H. Paulus, T. Bolse, and W. Bolse. Smoothing, compaction, mixing, sputtering and dewetting of semimetal- and halogenide-coatings by swift heavy ion irradiation. *Nuclear Instruments and Methods in Physics Research B*, 245:117–120, 2006.

[64] F. Richter, E. Bugiel, H. B. Erzgräber, and D. Panknin. Formation of titanium silicide during rapid thermal annealing: Influence of oxygen. *J. Appl. Phys. 72 (2)*, pages 815–817, 15 Jul 1992.

[65] B. Schattat and W. Bolse. Fast heavy ion induced interface mixing in thin-film systems. *Nuclear Instruments and Methods in Physics Research B*, 225:105–110, 2004.

[66] P. V. Serba and Yu. F. Bilnov. Mechanism of lattice relaxation in the theory of ion beam mixing. *Nuclear Instruments and Methods in Physics Research B*, 160:231–234, 2000.

[67] P. Süle, M. Menyhard, and K. Nordlund. What is the real driving force of bilayer ion beam mixing? *Nuclear Instruments and Methods in Physics Research B*, 226:517–530, 2004.

[68] A. M. Taubenblatt and C. R. Helms. Silicide and Schottky barrier formation in the Ti-Si and the Ti-SiO_x-Si systems. *J. Appl. Phys.*, 53(9), 1982.

[69] R. M. Tromp, G. W. Rubloff, and E. J. van Loenen. Low temperature material reaction at the Ti/Si(111) interface. *J. Vac. Sci. Technol. A (3)*, 4:865–868, 1986.

[70] R. T. Tung. Chemical Bonding and Fermi Level Pinning at Metal-Semiconductor Interfaces. *Physical Review Letters*, volume 84, number 26:6078–6081, 26 Jun 2000.

[71] J. Vähäkangas. Initial growth of Ti on Si. *Physical Review B*, volume 33, number 12:8716–8723, 15 Jun 1986.

[72] Lucia Vitali. *Growth Phenomena of Thallium and Phosphorus on Si(111) and Ge(111).* PhD thesis, Karl-Franzens Universität Graz, 2000.

[73] A.T.S. Wee, A.C.H. Huan, T. Osipowicz, K.K. Lee, W.H. Thian, K.L. Tan, and R. Hogan. Surface and interface studies of titanium silicide formation. *Thin Solid Films*, 283:130–134, 1996.

[74] D.P. Woodruff and T.A. Delchar. *Modern Techniques of Surface Science - Second Edition.* Cambridge Solid State Science Series, 1994.

[75] T. H. Yang, K. S. Chi, and L. J. Chen. Formation of Ti silicide nanocrystals in the amorphous interlayers in ultrahigh-vacuum-deposited Ti thin films on (001)Si. *Journal of Applied Physics*, 98, 034302:1–6, 2005.

[76] J. F. Ziegler. The Stopping of Energetic Light Ions in Elemental Matter. *J. Appl. Phys / Rev. Appl. Phys.*, 85:1249–1272, 1999.

[77] James Ziegler. The website of the SRIM computer software package, http://www.srim.org.

List of Figures

2.1 The chemical reaction sequence of the titanium silicides. 4

2.2 Two crystal phases of the $TiSi_2$: the base centered orthorhombic C49 silicide phase a) and the face centered orthorhombic C54 silicide phase b). . . 4

2.3 The picture [54] presents the possible ion-solid interactions. The R_p is the projected range of a single ion. 6

2.4 The path of an energetic ion in a solid during an ion implantation process. The picture shows the total ion path R and the projected ion range R_p. As the ion moves through the solid it collides into the stationary target atoms, which changes its direction. 8

2.5 The graphical interpretation of the Ion Beam Mixing (IBM) at the interface of two materials. 9

2.6 Target configuration assumed for the ion beam mixing model for compound formation [19]. Both A and B layers are the infinite reservoirs of atoms (C_A and C_B are the atomic concentrations of A and B atoms). J_1 is the diffusion flux according to the 1. Fick Law of Diffusion, and J_2 is the flux caused by the chemical reaction rate k for the A_aB_b compound. X is the thickness of the mixed layer. 11

3.1 Tilted quartz microbalance and its projection (ellipse) 18

3.2 Mean free path of the electrons as a function of their kinetic energy [43] . . 20

3.3 Schematic drawing of the LEED system [72]. A beam of electrons is directed on the crystal surface. The diffracted beams are collected on a fluorescent screen (the LEED pattern is observed). 22

3.4 Derivation of the Bragg Equation: $2dsin\theta = n\lambda$ 24

3.5 Image of an AFM cantilever approaching the surface (a) and the optical method for detection of the console bending (b) [40] 26

3.6 The illustration of the contact resistance measurement by the TLM method 27

3.7 SCIENTA Lab in 2007 28

3.8 SCIENTA UHV System. 28
3.9 Ion current measurement in SCIENTA Lab 32
3.10 Ion energy loss on ionization as the function of the target depth 33
3.11 Recoil energy loss on ionization as the function of the target depth 33
3.12 Ion current as the function of the filament position (in horizontal and vertical direction). 34
3.13 SPECS Lab in 2007 35
3.14 SPECS UHV System 36
3.15 Ion current as the function of the argon pressure, emission 10.00mA (SPECS UHV system). 39

4.1 The sputtering yield vs. the sputtering angle (a) and the Ar ion range vs. the sputtering angle (b), obtained from the TRIM code. The target material is defined as 15Å of SiO_2 on the 45Å of Si. The ion dose is 100000 Ar ions and the ion energy is $1.0keV$. The density of the SiO_2 is set to $2.533g/cm^3$ [59]. 41
4.2 LEED pattern of the Si(111)-(7x7) surface (E=60eV). 42
4.3 Ti growth on Si(111) at room temperature. XPS spectra of the Si 2p and Ti $2p_{3/2}$ regions taken for different Ti coverage. 43
4.4 Ti growth on Si(111) at room temperature. The XPS Si 2p and Ti $2p_{3/2}$ peak heights normalized to 1 and plotted against the Ti coverage (in monolayers). 43
4.5 The evolution of the Si 2p and Ti $2p_{3/2}$ XPS peaks during the thermal annealing of the Ti/Si(111) interface (Ti coverage: 20ML). 44
4.6 The average XPS peak shifts of the Si 2p and Ti $2p_{3/2}$ during the thermal annealing of the Ti/Si(111) interface (Ti coverage: 20ML). 45
4.7 The ratio of the XPS Si 2p to Ti $2p_{3/2}$ peaks. It was calculated using the measured XPS peak areas and the atomic sensitivity factors. 46
4.8 UPS spectra of the thermally annealed Ti/Si(111) interface (Ti coverage: 20ML) 47
4.9 The evolution of the Si 2p and Ti $2p_{3/2}$ XPS peaks during the thermal annealing of the Ti/Si(100) interface (Ti coverage: 20ML). 48
4.10 The ratio of the Si to Ti concentration during the thermal annealing of the Ti/Si(100) interface. The atomic concentration ratio was calculated using the measured XPS peak areas and the atomic sensitivity factors. 49

4.11 The XPS peak shifts of the Si 2p and Ti $2p_{3/2}$ during the thermal annealing of the Ti/Si(100) interface (Ti coverage: 20ML). RT stands for 'room temperature'. 49
4.12 UPS spectra of the thermally annealed Ti/Si(100) interface (Ti coverage: 20ML) 50
4.13 XPS survey spectra of the annealed Ti/Si(100) sample. Annealing temp. 700°C, annealing time: 20min, Ti coverage: 90.5ML. The Si/Ti atomic concentration ratio is 1.96. 52
4.14 XPS Si 2p and Ti 2p spectra of the annealed Ti/Si(100) sample. Annealing temp. 700°C, annealing time: 20min, Ti coverage: 90.5ML 52
4.15 UPS spectra of the annealed Ti/Si(100) sample. Annealing temp. 700°C, annealing time: 20min, Ti coverage: 90.5ML 53
4.16 GIXRD spectra of the annealed Ti/Si(100) sample. Annealing temp. 700°C, annealing time: 20min, Ti coverage: 90.5ML 54
4.17 Fitted XPS Si 2p spectra of the annealed Ti/Si(100) sample (annealing temp. 700°C, annealing time: 20min, Ti coverage: 90.5ML). Si 2p fitted with two doublets that correspond to the different titanium disilicide phases: 99.1eV - C54 $TiSi_2$, 98.80eV - C49 $TiSi_2$. 56
4.18 The fitted Si 2p XPS spectra of the thermally annealed Si/Ti(111) sample at lower temperatures (up to $\sim 520°C$). 57
4.19 The fitted Si 2p XPS spectra of the thermally annealed Si/Ti(111) sample at high temperatures (570°C and 650°C). 58
4.20 TLM results of the Ti/Si(100) annealed to 350°C (Ti coverage: 90.5ML). The specific contact resistance of the interface is $\rho_c = 0.72 m\Omega \cdot mm^2$. . . . 59
4.21 GIXRD spectra of the annealed Ti/Si(100) sample (12min at 720°C). C49 $TiSi_2$ phase was identified as the dominant phase. 61
4.22 GIXRD spectra of the annealed Ti/Si(100) sample (18min at 720°C). C54 $TiSi_2$ was identified as the dominant phase. 61
4.23 TLM results of the C49 $TiSi_2$/Si interface prepared by thermal annealing at 720°C for 12min of the in-situ prepared 90.5ML-Ti/Si(100) interface. The GIXRD spectra of the sample is presented in Fig. 4.21. The specific contact resistance is $\rho_c = 0.12 m\Omega \cdot mm^2$. 62
4.24 TLM results of the C54 $TiSi_2$/Si interface prepared by thermal annealing at 720°C for 18min of the in-situ prepared 90.5ML-Ti/Si(100) interface. The GIXRD spectra of the sample is presented in Fig. 4.22. The specific contact resistance is $\rho_c = 0.18 m\Omega \cdot mm^2$. 62

4.25 The stopping power of Ar penetrating the Si obtained from the TRIM code. The stopping power plots are presented for high kinetic energies of Ar (a) and for ion energies up to 5.0keV (b). The IBM ion kinetic energy range that was used in this work is marked in (b). 64
4.26 The stopping power of Ar penetrating the Ti obtained from the TRIM code. The stopping power plots are presented for the high Ar kinetic energies (a) and for the ion energies up to 5.0keV (b) IBM ion kinetic energy range that was used in this work is marked. 64
4.27 Projected Ar range vs. the Ar kinetic energy in Si (a) and in the Ti (b). . . 65
4.28 Ion beam mixing of the 20ML–Ti/Si(111) bilayers at room temperature with the Ar beam at 1.30keV normal to the target surface. The XPS spectra show how the Si 2p and the Ti $2p_{3/2}$ change with the ion dose. . . 67
4.29 The XPS peak shifts of the Si 2p and Ti $2p_{3/2}$ during the IBM of the Ti/Si(111) interface (Ti coverage: 20ML) at room temperature. Ar beam is normal to the surface, Ar kinetic energy is $E_{kin} = 1.30keV$. 67
4.30 The evolution of the valence band of the Ti/Si(111) sample during the IBM process at room temperature (irradiation with Ar^+ ions at the kinetic energy of 1.30keV, normal to the surface). 68
4.31 Ion beam mixing of the 20ML–Ti/Si(100) bilayers at room temperature with the Ar beam at 1.30keV normal to the target surface. The XPS spectra show how the Si 2p and the Ti $2p_{3/2}$ change with the ion dose. . . 69
4.32 The XPS peak shifts of the Si 2p and the Ti $2p_{3/2}$ during the IBM process of the Ti/Si(100) interface (Ti coverage: 20ML) with Ar ions at 1.30keV, bombarding the sample at normal incidence. 69
4.33 The evolution of the valence band of the Ti/Si(100) sample during the IBM process at room temperature (irradiation with Ar^+ ions at the kinetic energy of 1.30keV, normal to the surface). 70
4.34 Ion beam mixing of the 20ML–Ti/Si bilayers at room temperature with the Ar beam at 1.80keV normal to the target surface. The XPS spectra show how the Si 2p and the Ti $2p_{3/2}$ change with the ion dose. 72
4.35 Ion beam mixing of the 20ML–Ti/Si bilayers at room temperature with the Ar beam at 2.30keV normal to the target surface. The XPS spectra show how the Si 2p and the Ti $2p_{3/2}$ change with the ion dose. 72
4.36 XPS peak shits of the Si 2p and the Ti $2p_{3/2}$ during the room temperature IBM process for different Ar^+ energies. 73

4.37 The evolution of the valence band of the Ti/Si(100) sample during the IBM process at room temperature (irradiation with Ar^+ ions at the kinetic energy of 1.80keV and 2.30keV, normal to the surface) 74
4.38 The comparison of the XPS spectra showing the Si 2p and the Ti $2p_{3/2}$ peaks taken for the samples irradiated with the ion dose of $29.6\times10^{15} ions/cm^2$ and for different Ar^+ ion energies (1.30, 1.80 and 2.30keV). 75
4.39 XPS fitting of the Si 2p, the 20ML–Ti/Si(100) sample bombarded with Ar^+ at 1.30keV, the ion dose $29.6 \times 10^{15} ions/cm^2$. 75
4.40 XPS fitting of the Si 2p, the 20ML–Ti/Si(100) sample bombarded with Ar^+ at 1.80keV, the ion dose $29.6 \times 10^{15} ions/cm^2$. 76
4.41 XPS fitting of the Si 2p, the 20ML–Ti/Si(100) sample bombarded with Ar^+ at 2.30keV, the ion dose $29.6 \times 10^{15} ions/cm^2$. 76
4.42 The comparison of the UPS spectra taken for the samples irradiated with the ion dose of $29.6 \times 10^{15} ion/cm^2$ and for different Ar^+ ion energies (1.30, 1.80 and 2.30keV). 77
4.43 Si 2p and the Ti $2p_{3/2}$ XPS spectra of the Ti/Si(100) sample IBMed with the Ar^+ ions at 1.30keV. Titanium coverage is 15ML. 78
4.44 Si 2p and the Ti $2p_{3/2}$ XPS spectra of the Ti/Si(100) sample IBMed with the Ar^+ ions at 1.30keV. Titanium coverage is 10ML. 79
4.45 XPS peak shits of the Si 2p and the Ti $2p_{3/2}$ during the room temperature IBM process for different titanium coverages (10-20ML) at constant Ar^+ energy of 1.30keV. Substrate: Si(100). 79
4.46 The evolution of the valence band of the Ti/Si(100) sample during the IBM process at room temperature with Ar^+ at 1.30keV. Ti coverage is 15ML and 10ML. 80
4.47 The comparison of the XPS spectra of the Si 2p and the Ti $2p_{3/2}$ peaks taken for the samples irradiated with the ion dose of $\phi = 29.6\times10^{15} ions/cm^2$ at 1.30keV, but for different Ti coverage: 20ML, 15ML and 10ML on Si(100). 81
4.48 The fitted XPS spectra of the Si 2p for the 20ML–Ti/Si(100) sample. The ion dose $\phi = 29.6 \times 10^{15} ions/cm^2$ and the Ar^+ energy $E_{kin} = 1.30keV$. . . 82
4.49 The fitted XPS spectra of the Si 2p for the 15ML–Ti/Si(100) sample. The ion dose $\phi = 29.6 \times 10^{15} ions/cm^2$ and the Ar^+ energy $E_{kin} = 1.30keV$. . . 82
4.50 The fitted XPS spectra of the Si 2p for the 10ML–Ti/Si(100) sample. The ion dose $\phi = 29.6 \times 10^{15} ions/cm^2$ and the Ar^+ energy $E_{kin} = 1.30keV$. . . 83

4.51 The comparison of the UPS spectra taken for the samples irradiated with the ion dose of $29.6\times10^{15} ions/cm^2$ at 1.30keV, but for different Ti coverage: 20ML, 15ML and 10ML on Si(100). 84
4.52 The results of the TRIM simulations presenting the sputtering yield (Y) vs. the sputtering angle (a), and the total target displacements vs. the sputtering yield (b). The target material was titanium and it was bombarded with the Ar^+ ions at 1.30keV, 1.80keV and 2.30keV. 85
4.53 Projected argon range (Ar^+ bombarding the titanium surface) as a function of the sputtering angle. The plot obtained by the means of the TRIM code. 86
4.54 The percentage of the backscattered argon ions as a function of the sputtering angle. The graph was obtained by the TRIM code. 87
4.55 TRIM calculations of the sputtering yield and the projected ion range for different Ti/Si systems, that were studied experimentally. 88
4.56 Argon ion/atom distribution in the target for the constant Ti coverage (20ML) but different Ar^+ energy (a) and for the constant Ar^+ energy of 1.30keV and the different titanium coverage (b). The graph was obtained by the TRIM code. 88
4.57 Energy from ions absorbed by the target atoms calculated with the TRIM code. The graphs show the calculations for the same Ti coverage of 20ML and different ion energies, and the same ion energy (1.30keV) but different Ti coverage. 90
4.58 Ion energy loss on phonons (a) and recoil energy loss on phonons (b) calculated for the three different Ar^+ kinetic energies (1.30keV, 1.80keV and 2.30keV) for the IBMed 20ML–Ti/Si bilayers. 91
4.59 Ion energy loss on phonons (a) and recoil energy loss on phonons (b) calculated for the different titanium coverages (20ML, 15ML and 10ML) for the Ti/Si system IBMed with Ar^+ at 1.30keV 91
4.60 Ion energy loss on ionization (a) and recoil energy loss on ionization (b) calculated for the three different Ar^+ kinetic energies (1.30keV, 1.80keV and 2.30keV) for the IBMed 20ML–Ti/Si bilayers. 92
4.61 Ion energy loss on ionization (a) and the recoil energy loss on ionization (b) calculated for the different titanium coverages (20ML, 15ML and 10ML) for the Ti/Si system IBMed with Ar^+ at 1.30keV 92
4.62 Energy loss for ions and recoils. 93

4.63 Replacement collisions calculated for the IBMed Ti/Si system for the constant titanium coverage of 20ML, but the different Ar^+ energy (a) and for the constant Ar^+ energy, but the different Ti coverage (b). 94
4.64 XPS spectra of the Ta 4f and the O 1s taken during the depth profiling of the Ta_2O_5/Ta sample. 98
4.65 Depth profile of the Ta_2O_5/Ta sample showing the XPS peak heights of the Ta $4f_{7/2}$ and the O 1s as a function of the sputtering time. 99
4.66 Depth profiles of the 20ML–Ti/Si interface IBMed with the Ar^+ at 1.30keV with different ion doses: $9 \cdot 10^{14} Ar/cm^2$(a), $1.5 \cdot 10^{15} Ar/cm^2$(b), $2.5 \cdot 10^{15} Ar/cm^2$(c) and $3.5 \cdot 10^{15} Ar/cm^2$ (d). 100
4.67 Interface variance of the mixed Ti/Si bilayers as the function of the ion fluence. 101
4.68 The distribution of the energy absorbed by the target atoms from ions (a) and the distribution of the collision events (b) during the bombardment of the Ti/Si system with the Ar^+ ion beam at 45° to the target surface. . . . 102
4.69 XPS (a) and TLM (b) measurements of the 20ML–Ti/Si sample IBMed at room temperature with the Ar^+ at 1.30keV. Ion dose was $\phi = 29.6 \cdot 10^{15} ions/cm^2$, substrate: n-type Si(100). 104
4.70 The XPS (a) and the TLM (b) measurements of the 20ML–Ti/Si sample IBMed at room temperature with the Ar^+ at 1.30keV, and then annealed at 350° for 12min. Ion dose was $\phi = 29.6 \cdot 10^{15} ions/cm^2$, substrate: n-type Si(100). 105
4.71 The XPS spectra of argon on the surface of the IBMed (Ar^+ at 1.30keV, $\phi = 29.6 \cdot 10^{15} ions/cm^2$) and annealed ($400°C$ for $12min$) 20ML–Ti/Si(100) bilayers, taken before and after the thermal annealing. 106
4.72 The XPS (a) and the TLM (b) measurements of the 20ML–Ti/Si sample IBMed at room temperature with the Ar^+ at 1.30keV. Ion dose was $\phi = 1.1 \cdot 10^{16} ions/cm^2$, substrate: n-type Si(100). 107
4.73 The 3D view of the surface of the thermally annealed sample (no. 1) with the C54 $TiSi_2$ on Si(100). 108
4.74 AFM images of the C54 $TiSi_2$/Si(100) samples, where the C54 phase was formed by: thermal annealing at 700°C for 4.0min (no. 1), IBM with Ar^+ 2.30keV (no. 2), IBM with Ar^+ 1.30keV (no. 3), IBM with Ar^+ 1.30keV + annealing at $350°C$ for 10min (no. 4). 109

4.75 A TRIM simulation result showing the energy distribution of the ion-beam-induced displaced target atoms reaching the surface. The atoms with the energy lower than 4.8eV (surface binding energy) cannot leave the surface and do not contribute to the sputtering yield, but they contribute to the surface diffusion leading to smoothing. The simulation was performed for the Ar^+ ions bombarding the Ti/Si surface with the energy of 1.30keV and 2.30keV normal to the surface. The ion dose was 100000 ions. 111
4.76 The XPS spectra of the Si 2p taken during the TAIBM at 200°C (a) and taken during the room temperature IBM. The substrate is 20ML–Ti/Si(100), the Ar^+ energy is 1.30keV. 113
4.77 The XPS spectra of the Ti $2p_{3/2}$ taken during the TAIBM at 200°C. The substrate is 20ML–Ti/Si(100), the Ar^+ energy is 1.30keV. 114
4.78 Peak shifts of the XPS Si 2p and the Ti $2p_{3/2}$ peaks during the room temperature IBM and during the TAIBM at 200°C. The substrate is 20ML–Ti/Si(100) and the Ar^+ energy is 1.30keV. 114
4.79 The valence band evolution of the TAIBMed 20ML–Ti/Si(100) (Ar^+ at 1.30keV, T=200°C) obtained be the means of UPS. 115
4.80 Depth profile of the Ti/SiO_2/Si system formed by the room temperature deposition of the 20ML of titanium onto the Si(100) substrate covered with the native SiO_2 layer. 116
4.81 XPS spectra of the IBMed (Ar^+ at 1.30keV) Ti/SiO_2/Si system: Si 2p (a), Ti $2p_{3/2}$ (b,) O 1s (c), and the analysis of the peak heights (d). 118
4.82 The XPS spectrum of the clean surface of the pure TiO_2 crystal, taken by Mag. Stephen Berkebile in SCIENTA Lab. 119
4.83 fitted 120
4.84 XPS spectra of the IBMed (Ar^+ at 1.30keV at 45° to the target surface) Ti/SiO_2/Si system: Si 2p (a), Ti $2p_{3/2}$ (b,) O 1s (c), and the analysis of the peak heights (d). 121
4.85 XPS spectra of the IBMed (Ar^+ at 1.80keV normal to the target surface) Ti/SiO_2/Si system: Si 2p (a), Ti $2p_{3/2}$ (b,) O 1s (c), and the analysis of the peak heights (d). 122
4.86 XPS spectra of the IBMed (Ar^+ at 2.30keV normal to the target surface) Ti/SiO_2/Si system: Si 2p (a), Ti $2p_{3/2}$ (b,) O 1s (c), and the analysis of the peak heights (d). 123

4.87 XPS spectra of the IBMed (Ar^+ at 3.00keV normal to the target surface) $Ti/SiO_2/Si$ system: Si 2p (a), Ti $2p_{3/2}$ (b,) O 1s (c), and the analysis of the peak heights (d). 124
4.88 The distribution of the energy absorbed by the target atoms during the IBM of the $Ti/SiO_2/Si$ with Ar^+ at different kinetic energies at normal incidence. 125
4.89 The distribution of the replacement collisions during the IBM of the $Ti/SiO_2/Si$ with Ar^+ at different kinetic energies at normal incidence. 126
4.90 The argon distribution after the IBM of the $Ti/SiO_2/Si$ with Ar^+ at different kinetic energies at normal incidence. 126
4.91 The 3D argon distribution after the IBM of the $Ti/SiO_2/Si$ with Ar^+ at 1.30keV at normal incidence. 127
4.92 The final 3D argon distribution after the IBM of the $Ti/SiO_2/Si$ with Ar^+ at 3.0keV at normal incidence. 127

Acknowledgments

It would not have been possible to write this doctoral thesis without the support and help of the kind people around me.

Above all, I would like to thank my supervisor Prof. Falko P. Netzer for his constant support and patient guidance, not to mention his scientific advice, which kept me moving towards my goal.

I would like to acknowledge the technical and scientific support of Dr. Paul Ganitzer, Dr. Oliver Häberlen and Dr. Daniel Kraft from Infineon Technologies in Villach. The fruitful discussions we had were a great source of good ideas and motivation for me. I would like to thank also for their active participation and support in some measurements (TLM, GIXRD). The financial support of Infineon Technologies, Villach, was essential for this dissertation project and is gratefully acknowledged.

Also, I would like to give my thanks to all Members of the Surface and Interface Physics Group - dear Professors, Colleagues and fellow Students. Their support and friendship were invaluable on both an academic and a personal level, for which I am very grateful.

Thank you everyone!